Short-term Climate Variability in the mid-Miocene:

A Micropalaeontological and Sedimentological Investigation of a High-Resolution Maar Lake Sediment near Hindon, East Otago, New Zealand

A thesis

submitted in partial fulfilment

of the requirements for the degree

of

Master of Science in Earth Science

at

The University of Waikato

by

NOEL WILLIAM BATES

THE UNIVERSITY OF
WAIKATO
Te Whare Wānanga o Waikato

2018

Abstract

Maars are deep, steeply-sloped, small-diameter craters formed by phreato-magmatic eruptions. Phreatomagmatic eruptions result when rising magma intersects a body of water such as an aquifer. Maars often form deep closed-basin lake systems that become repositories for detrital material from the local environment. Tens of metres of detritus representing thousands of years of accumulation may be anoxically-preserved in maar lake sediments for millions of years.

The Hindon Maar Complex (HMC) is located in East Otago, on the South Island of New Zealand. The HMC hosts the highest-resolution mid-Miocene climate archive in the Southern Hemisphere. The date of its formation (14.6±0.1 Ma) coincides with the mid-Miocene climate transition (MMCT), a unique period when global temperatures were decreasing following an anomalous short-lived peak at the mid-Miocene climate optimum. Sensitivity to atmospheric pCO_2 levels and the confluence of the three main Milankovitch orbital cycle minima caused the Antarctic ice sheet (AIS) to advance and retreat. Concurrently, the Antarctic circumpolar currents (ACC) and atmospheric circumpolar westerlies also underwent latitudinal shifts while interacting with warm subtropical currents in the vicinity of vestigial Zealandia. With little rain-shadow effect over the low-lying land mass and exclusively ocean between the latitudes of Zealandia and the polar ice cap, the Hindon Maar Complex was ideally placed in the mid-latitudes to experience and record the subtle climate changes that resulted.

An 18.5 m core drilled from Hindon Maar #1 contained ~9.5 m of highly organic lake sediments with varying concentrations of biosiliceous microfossils. Physical properties of the core (magnetic susceptibility, gamma attenuation density, and spectrophotometry) measured using a Geotek multi-sensor core logger identified two lithofacies distinct from each other at ~5.7 mcd. High resolution mm-scale surveys of core split surfaces revealed core attributes that corroborated the Geotek findings. The lower facies is black laminated sapropelic material throughout while the upper facies is dark brown diatomite that exhibits light laminae and bedding structures related to turbidite mass flow events.

An age-depth model was developed by measuring lamina-couplet thickness in 10 lake sediment samples throughout the core. The lake sediments in the HMC M1-2 core represent ~10,400 years of deposition. The lamina-couplet thickness also identifies a boundary between depositional environments in the vicinity of 6.5 mcd, where deposition below represents a high annual flux of organic material to the lake, while deposition above represents biosiliceous deposition and much reduced flux of organic material.

51 approximately-equidistant lake sediment samples were subjected to FTIRS and BioSi wet chemistry compositional analyses and siliceous microfossil smear slide surveys. All analyses identify a change in deposition environment at ~6.5 mcd, from sediments with high organic input with some terrigenous material and few biosiliceous microfossils to sediments with reduced organic and terrigenous input and copious biosiliceous material.

Changes in the biosiliceous microfossil assemblages upcore were used to infer surface water pH changes. Changes in diatom abundance were indicative of access to nutrients sequestered in the profundal zone of the meromictic lake. Accessibility to nutrients was equated to climates that would promote or inhibit the transfer of nutrients from monimolimnion to mixolimnion across the chemocline. Therefore, changes in the lake sediment deposit were equated to climate-driven changes in the meromictic lake dynamics.

This Hindon Maar #1 lake sediment deposit represents two main climate-driven depositional environments. Warm wet climate conditions that promoted deciduous forest growth and inhibited nutrient accessibility in the lake transitioned over ~1300 years (~6.5 to 5.7 mcd) to windy, cool and dry climate conditions that shifted the range of the forests away from the HMC and allowed nutrients sequestered in the lake to become accessible to diatom algae, increasing the productivity of the lake.

The climates represented in the HMC M1 lake sediments are then projected back to the latitudinal shifts of the ACC and circumpolar westerlies, driven by the expansion and retreat of the AIS during the MMCT.

Acknowledgements

I first want to enthusiastically thank my supervisor, Beth Fox, for her exuberance, vision, and support during this project and in the years before when, I recognised a while ago, she was ‘planting the seed’ of the idea. Thanks as well to my secondary supervisor, Christina Riesselman, for her enthusiasm and methodical approach. I must also thank my fellow MSc colleagues, Caitlin Murphy and Francis Garrity for their work in the field and collaboration afterwards. Many thanks to the Neehof family, who allowed unprecedented access to their land and housed us while we were in the drilling phase.

The technical and administrative support required for this project has been huge and must be acknowledged. For those in Dunedin, thanks to Daphne Lee for the incredible amount of time and effort she has expended to help us with this project, Bob Dagg for sorting the Geotek, and Dee Roben, Ray Marx, and Damian Walls for arranging vehicles and access to facilities. At the University of Waikato I have been fortunate to have been trained, accommodated, and tolerated in so many labs and on so many pieces of equipment by Janine Ryburn, Barry O’Brien, Helen Turner, Renat Radosinsky, Annette Rogers, Bruce Patty and Jenny Stockdill. Special thanks also to Cheryl Ward for helping pull it all together. If there is anyone else who does not see their name here but thinks it should be, you are probably right, and I blew it.

I must also extend thanks to the University of Waikato for awarding me scholarships that funded my graduate study. It was much appreciated.

And to my neighbour, Vivienne Cassie Cooper, the original algal explorer, thank you for appreciating my research. I never thought I would see the day that someone would get overwhelmed by high resolution diatom microscopy.

My greatest gratitude is reserved for my family, Jeweleigh, Bailey and Charlotte, who have supported me and tolerated the time that I have given to my academic pursuit instead of them, so that it may pay off later. Thank you, wholeheartedly.

I dedicate this to my Mom, who passed in a merciful way before this project could be completed. That’s all I have to say about that.

Table of Contents

List of Figures

List of Tables

Chapter 1

Introduction

1.1 Background

In 2007 an aeromagnetic survey was jointly conducted by Glass Earth (New Zealand) Ltd and the Otago Regional Council across ~12,900 km^2 of eastern Otago, and when the survey data was made public in 2011, a cluster of four sub-circular areas of high magnetism in the Hindon region was recognised as potentially being maar diatremes (Christie *et al.*, 2012). Subsequent geophysical surveys performed by Bowie (2015) and colleagues from the Department of Geology, University of Otago confirmed that this was a complex of maars, two of which contain evidence of lake sediments above the diatremes.

Maar lake sediments are characteristically biogenic and carbonaceous laminae of seasonal to annual resolution, the properties of which have been used to draw conclusions about the environment during deposition and changes in climate during the evolution of the lake (Cohen, 2003; Lindqvist & Lee, 2009; Ojala *et al.*, 2012; Fox *et al.*, 2015; Dräger *et al.*, 2016). Syn-depositional volcanism in the Hindon Maar Complex (HMC) has been dated to ~14.6 Ma, i.e. mid-Miocene, International: Langhian Stage, New Zealand geological timescale: Lillburnian Stage (Kaulfuss *et al.*, 2018).

High resolution lacustrine palaeoclimate data from the mid-Miocene are rare. The sediments in the HMC are the first mid-Miocene maar lake deposits discovered in the Southern Hemisphere. The HMC deposits present a unique research opportunity to learn about the local environment in that time and region of Zealandia and to contribute to the sum of global palaeolimnological and palaeoclimate data.

1.2 Study Area

Hindon is located on the South Island of New Zealand, in the Otago region ~25 km NW of Dunedin CBD (Figure 1.1). The Hindon Maar Complex is situated at 45°45'-47'W longitude and 170°14'-17'E latitude, an area of ~16 km^2. The extent and orientation of the maar diatremes is shown in Figure 1.2. The HMC is located in a flat pastoral sub-circular depression of approximately 1100x600 m, surrounded by a low ridge with gently sloped sides (Figure 1.3).

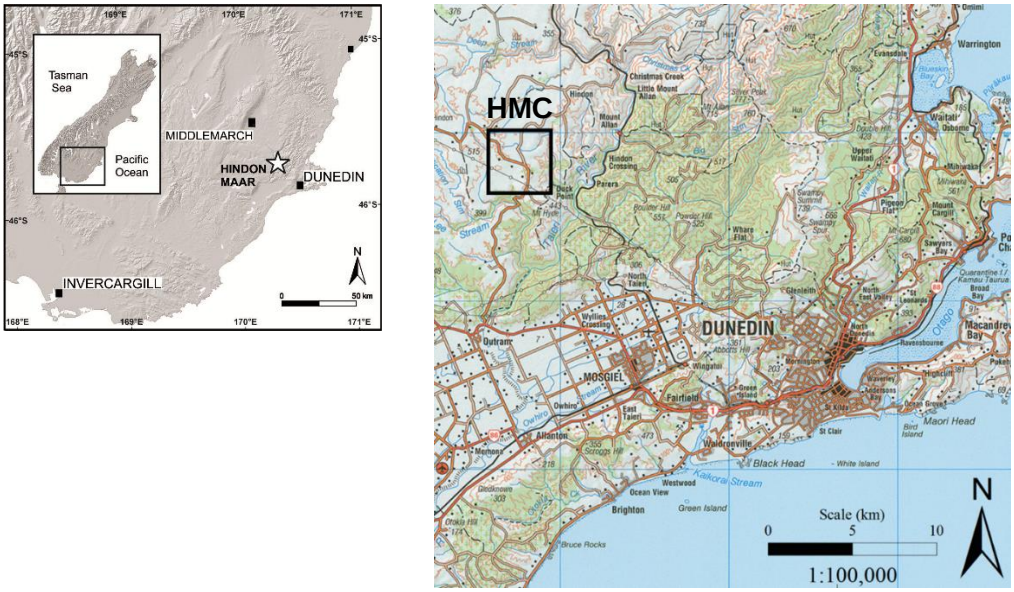

Figure 1.1: Location of the Hindon Maar Complex (Bowie, 2015; Möller *et al.*, 2017).

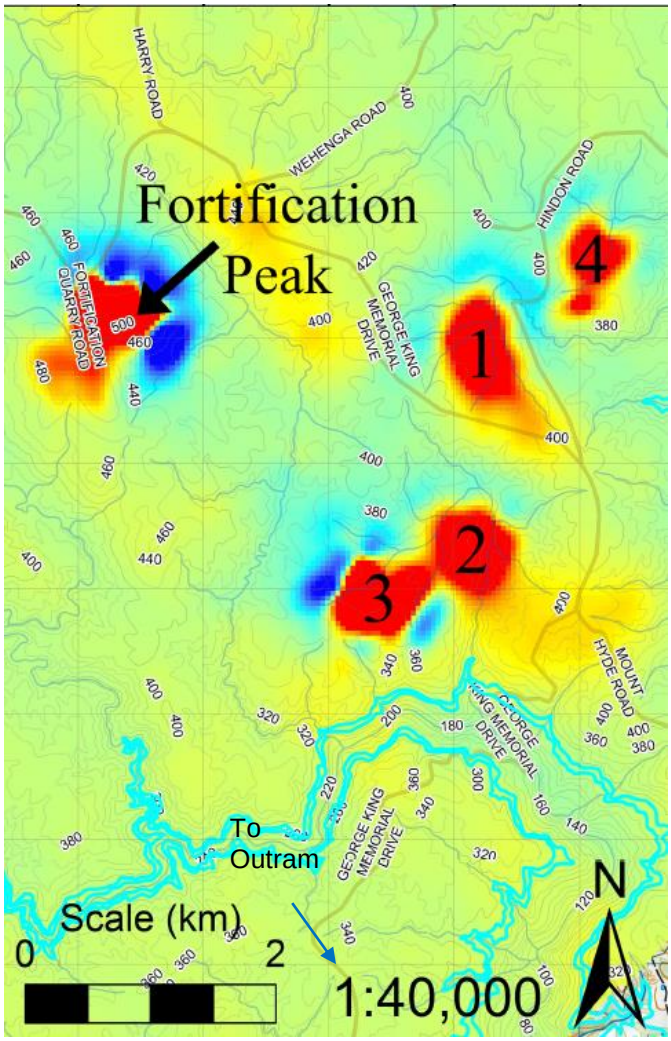

Figure 1.2: The maar diatremes (1-4) of the Hindon Maar Complex relative to Fortification Peak. Adapted from the Glass Earth (New Zealand) Ltd and the Otago Regional Council aeromagnetic survey data (Bowie, 2015).

Figure 1.3: HMC Maar 1 field area, July 2016.

The focus of this thesis is the lake sediment deposit in Maar 1, with data and observations being gleaned from a drill core. This sediment core is henceforth designated HMC M1-2 (Hindon Maar Complex, Maar #1, Core 2).

1.3 Research Aims and Objectives

There is a paucity of high-resolution mid-Miocene lacustrine deposits, especially in the Southern Hemisphere. There are several highly-resolved maar lake sediments deposits of Quaternary-age but few Neogene deposits, and the majority of examples of this deposit type are concentrated in the Northern Hemisphere. The primary aim of this research is to contribute climate proxy data from a high-resolution lacustrine deposit that is unique in its age and location. In order to achieve this aim, this project seeks to fulfil the following objectives:

1. Determine the sedimentology of the deposit.
   - Compile a core description and facies analysis.

2. Determine the composition and physical properties of the maar lake sediments.
   i) Use Geotek multi-sensor core logger (MSCL) to determine core:
      a) Magnetic susceptibility.
      b) Gamma attenuation density.
      c) Reflectance (L*a*b*)
      d) High resolution red-green-blue (RGB) colour
   ii) Determine ratio of total organic carbon content, total minerogenic content, and total inorganic biogenic content.

3. Determine the character and quantities of any inorganic biosiliceous microfossils, and record anomalies of interest

4. Collate the information from all datasets to infer processes that account for changes upcore through the lake deposits, and subsequently draw conclusions about changes in the environment during the evolution of the lake.

1.4 Thesis Outline

1.4.1 Chapter 2: Literature Review

This chapter reviews literature pertaining to the geology of the Hindon Maar Complex, the formation of maar lake sediment deposits, and utilisation of physical properties of lacustrine deposits and their microfossil assemblages in palaeoenvironmental studies.

1.4.2 Chapter 3: Methods

This chapter recounts the field methods for core acquisition and preparation for physical-property analysis. It also describes the core-sampling and processing methods required to conduct compositional analyses, produce representative smear slides, and consistently survey the biosiliceous microfossil assemblages.

1.4.3 Chapter 4: Results

This chapter presents data acquired from multiple analyses performed on a core drilled from Maar #1 in the HMC. The findings are laid out in the following order:

Sedimentological Analyses

Includes a stratigraphic log based on the split core sections and the field notes for the HMC Maar #1 (M1) sediment deposit, a core description with focus on the lake sediments, and data acquired by processing the lake sediments through a Geotek multi-sensor core logger (MSCL). The Geotek analyses include magnetic susceptibility, gamma density, L*a*b* reflectance, and RGB colour intensity.

Composition and Biogenic Silica Analyses

Presents Fourier transform infrared spectroscopy (FTIRS) results for the HMC M1 lake sediments, which partitioned the sediments into relative wt% of total organic carbon (TOC), biogenic silica (BioSi), and Otago Schist country rock. This section also includes absolute wt% BioSi results from molybdate-blue spectrophotometry.

Biosiliceous Microfossil Surveys

Semi-quantitative data is given for the micro-organisms found in significant abundance in the HMC M1 lake sediments.

1.4.4 Chapter 5: Discussion

This chapter considers the sum of all data acquired and discusses how they may be used to interpret the depositional evolution of the crater lake in Maar #1 of the HMC. It offers interpretations regarding changes in climate that would account for shifts in the character of the lake sediments throughout the deposit.

1.4.5 Chapter 6: Conclusion

This chapter summarises the findings of this thesis and identifies future research opportunities related to the Hindon Maar Complex.

Chapter 2

Literature Review

This chapter presents a review of studies pertaining to the regional and local geology of the Hindon Maar Complex and the processes and conditions in which similar lake sediment deposits have accumulated. Studies that relate to the mid-Miocene palaeoclimate and the palaeocology of the HMC during its formation (~14.6 Ma) are also presented. The chapter concludes with studies that use the physical properties and microfossil assemblages of lake sediments to infer palaeoenvironmental and climate processes that contributed to the characteristics found in the deposit.

2.1 Geology

2.1.1 Regional Geology and Tectonic Setting

The HMC is hosted in Otago Schist country rock (Bowie, 2015; Kaulfuss *et al.*, 2018). Otago Schist is a low-grade greenschist and is part of the Haast Schist Group (Mortimer, 1993), a long metamorphic belt oriented along the Alpine Fault and extending in a broad band to the south east across Otago (Mortimer, 1993). Otago Schist originated from metagreywacke-rich sandstones of the Rakaia Terrane, the older terrane in the Torlesse Composite Supergroup, which accumulated along the Gondwana margin from the late Permian to the early Triassic (Bishop & Turnbull, 1996; Adams *et al.*, 2013; Martin *et al.*, 2013). During the Triassic Rangitata Orogeny, the Rakaia Terrane was juxtaposed in a compressional regime with the Caples Terrane, an accretionary wedge also of late Permian to early Triassic age, possibly originating from high latitudes of the Southern Hemisphere (Mortimer, 1993; Ito *et al.*, 2000; Adams *et al.*, 2013). The HMC is located in the Rakaia Terrane, ~6-7 km northeast of the Caples-Rakaia contact (Bishop & Turnbull, 1996)

Metamorphism from the early Jurassic followed by uplift and cooling through the late Cretaceous resulted in Otago Schist overprinting the contact of the Caples and Rakaia Terrane (Mortimer, 1993; Bishop & Turnbull, 1996). Extensional forces in the Cretaceous during the rifting of Zealandia from Gondwana created NE and NW-trending faults. Extensive marine transgressions and planation of the land surfaces through the mid-Oligocene created the Waipounamu Erosion Surface (Upton *et al.*, 2014).

Uplift from the late Oligocene to early Miocene, combined with lowering of the eustatic sea level due to the growth of polar icecaps after the mid-Miocene, raised the Waipounamu Erosion Surface (WES) above sea level (Zachos *et al.*, 2001; Upton *et al.*, 2014). In the early Pliocene, the transition of the South Island Alpine Fault motion from strike/slip to transpressional initiated a prolonged period of orogeny and uplift that continues to present day (King, 2000). Late Neogene and Quaternary orogeny deformed inland expanses of the WES, creating NE-oriented ridges, some of which have since been eroded (Craw *et al.*, 2012).

The mid-Miocene HMC is located in an area of low relief east of the Rock and Pillar range and west of the Taieri River (Figure 2.1). This places it in the present-day catchment of the Taieri River, as is the Oligocene-Miocene (O/M) Foulden Maar which is located near Middlemarch, ~25 km northwest of the HMC (Craw *et al.*, 2012; Jones *et al.*, 2017). Projecting the locations of both the Foulden Maar and HMC into a Taieri River palaeo-catchment study (Craw *et al.*, 2016) showed that the catchment has included both eruption sites since at least the mid-Miocene. As the Taieri River catchment was evidently established on the planed WES prior to Pliocene deformation, it is reasonable to assume that the catchment area included the Foulden Maar site during the O/M transition when the Foulden Maar eruption occurred. The Foulden Maar deposit remains intact even though it existed prior to the aforementioned regional uplift and orogenic events, and has experienced up to ~120 m of erosion (Jones *et al.*, 2017). As they are in geographically close proximity and in the same drainage regime, maar lake deposits in the mid-Miocene HMC are expected to have undergone similar post-depositional erosion as those at the Foulden Maar, albeit to a lesser degree as the HMC eruptive activity occurred ~8.5 Ma after that of the Foulden Maar.

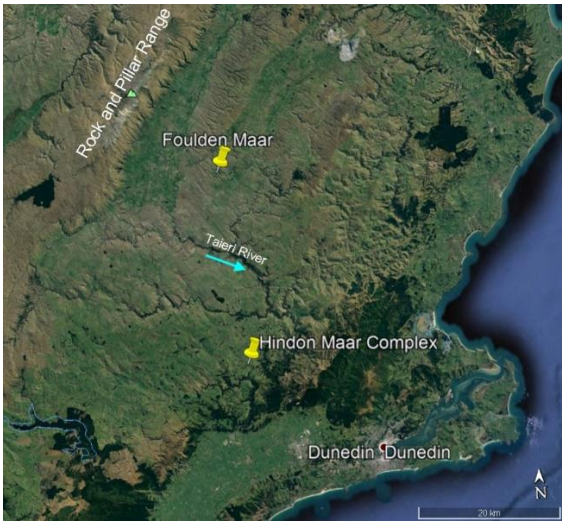

Figure 2.1: Location of Hindon Maar Complex and Foulden Maar. The blue arrow shows flow direction in Taieri River (annotated Google Earth image).

2.1.2 Volcanism

The HMC forms part of the Waipiata Volcanic Field (WVF), an assemblage of small, sub-aerial, monogenetic eruption craters and cones that was active from ~25.0-8.9 Ma (Németh & White, 2003; Coombs *et al.*, 2008; Jones *et al.*, 2017). The WVF is a part of the Dunedin Volcanic Group, along with the Dunedin Volcano Complex (DVC) and the Alpine Dyke Swarm (northwest Otago, outside the boundaries of Figure 2.2) (Németh & White, 2003). The volcanic features are generally aligned in NE-NW directions, mirroring the regional fault trends. Lava composition in the WVF ranges from basaltic to alkaline/sub-alkaline (Németh, 2001).

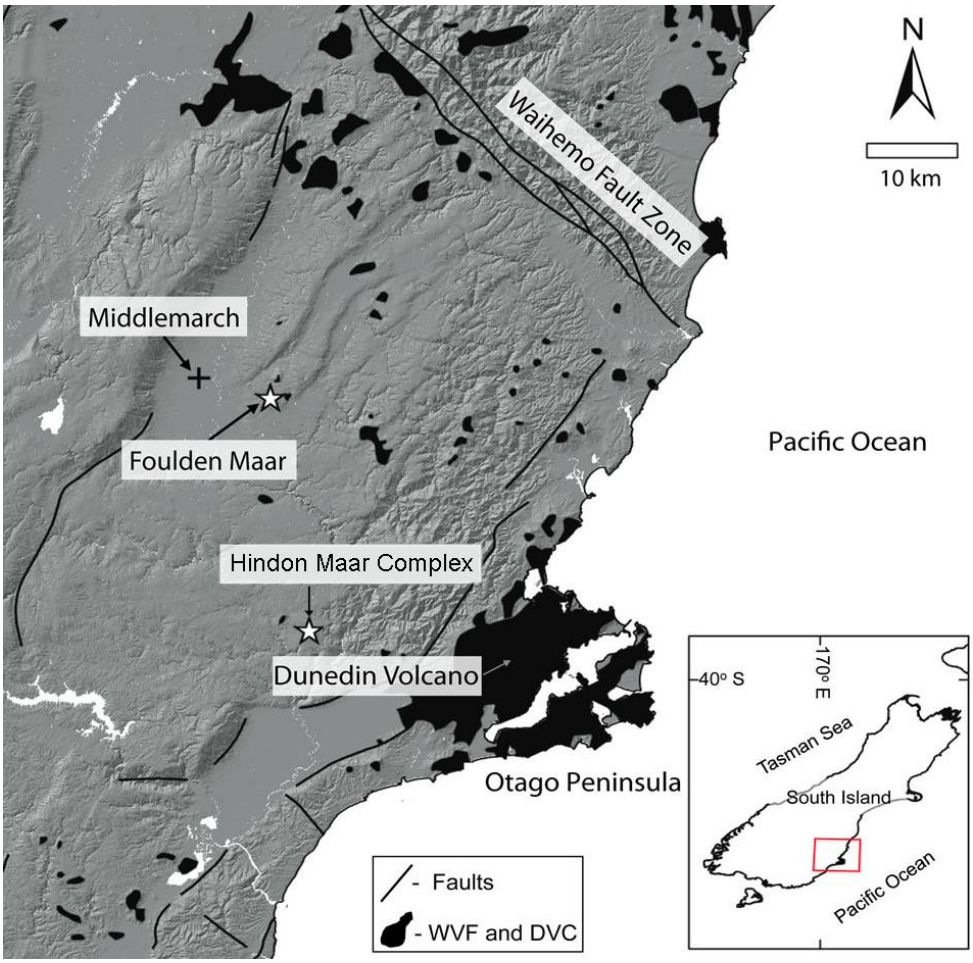

Figure 2.2: Location of the Hindon Maar Complex and other components of the Waipiata Volcanic Field (WVF) (adapted from Jones *et al.*, 2017).

The ~55 volcanic features in the WVF have been classified by Németh and White (2003) into three vent types. Type 1 vents consist primarily of feeder dykes, lava lakes, and/or lava flows that remain from the original monogenetic volcano, with little evidence of accompanying pyroclastic material (Németh & White, 2003). Type 2 vents are also associated with individual monogenetic volcanoes, but are associated with pyroclastic rocks and little evidence of lava. They are the product of phreatomagmatic eruptions. Most Type 2 vents are overlain by pyroclastic deposits rich in spatter, signalling a reduction in explosivity when the water supply

which would otherwise cause a phreatomagmatic eruption has been exhausted. The pyroclastic deposits may incorporate accidental lithics from the original overlying Cenozoic sediments. This indicates that the Cenozoic sediments had been emplaced prior to commencement of volcanic activity, although many tens of metres of rock have since been eroded from the syn-eruptive surface (Németh & White, 2003).

Type 3 vents consist of multiple Type 1 and 2 vents coalesced into a vent complex consisting of maars, tuff rings and scoria cones, as well as extensive lava flows and lakes. Pyroclastic deposits are typically stratigraphically low in Type 3 vent complexes, with scoriaceous deposits from strombolian-style eruptions higher in the stratigraphy, followed by or accompanying effusive lava flows (Németh & White, 2003).

2.1.3 Hindon Maar Complex

The HMC consists of the remnants of four maar eruption craters. Maars are steep-sided cone-shaped volcanic craters that have progressively been blasted downwards into country rock (Lorenz, 1986). They are initially formed by phreato-magmatic subsurface explosions caused by intrusion of mafic magma into a body of water or an aquifer (Lorenz, 2003; White & Ross, 2011). The maar eruption model presented by Lorenz (2003) consists of rising magma intersecting a water body, causing a series of phreatomagmatic explosions. This develops a root zone which then penetrates downward along its feeder dyke, leaving very steep sides, the edges of which collapse, forming the diatreme cone shape (Figure 2.3) (Lorenz, 2003).

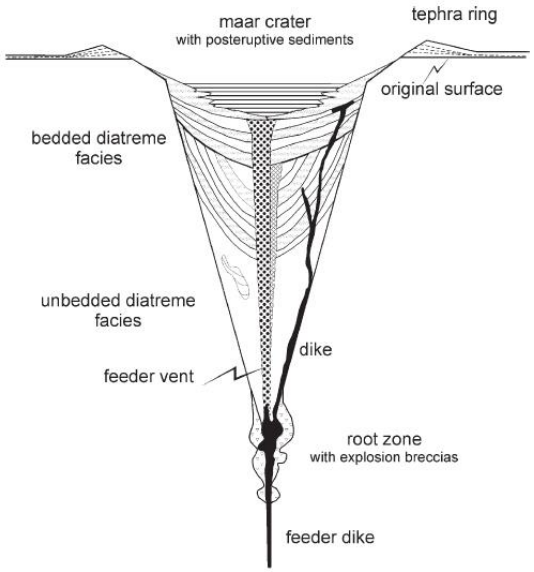

Figure 2.3: Generic post-eruptive configuration of a maar/diatreme capped with varved lacustrine sediments (Lorenz, 2003).

Valentine and White (2012) proposed a revised model in which explosive molten fuel-coolant interactions (MFCIs) begin at *any* level where water pressure is below the critical pressure of water, resulting in several brecciated subsurface zones but still ultimately forming a cone-shaped diatreme due to the fact that more volume of country rock will be blown out at shallower depths, as they have decreased lithostatic load. In either case, the post-eruptive result is typically a circular crater of 100-2000 m diameter, with steep sides to depths from 10s of metres to 300 m, surrounded by a circular tephra-ring up to 100 m high (Lorenz, 2003). The tephra ring will typically have a steeper inner slope than outer slope (30-35° vs. 5-15°, relatively), and its composition can include a high proportion of country rock fragments (up to 80% around the Westeifel maars in Germany) (Lorenz, 1986, 2007).

Jordan *et al.* (2013) studied tephra-ring deposits to determine that the large (>3 km diameter) Purrumbete maar in SE Australia had a multi-event formation history involving the interception of several smaller shallow maar craters (with varying phreatomagmatic eruption styles, from wet to dry) by a later deeper maar eruption. Blaikie *et al.* (2014) sought to elucidate the range of eruption styles that can occur in different maars within a volcanic maar complex by utilising gravity and magnetic survey data to develop geophysical models of the underlying diatremes. Studies such as these show that the evolution of maar volcanoes can be complex and may in fact not be exclusively monogenetic (Jordan *et al.*, 2013; Blaikie *et al.*, 2014).

The 2007 aeromagnetic survey (Figure 1.2) shows four maars in close proximity to each other (Christie *et al.*, 2012). Although they do not appear to have coalesced, there has been substantial erosion (Jones *et al.*, 2017). Evidence of coalescence at the syn-depositional surface may have been lost. In 2015, members of the Department of Geology at the University of Otago undertook a geophysical investigation of the HMC (Bowie, 2015). The results show that the HMC includes elements of vent Types 2 and 3, as defined by Németh and White (2003) (See above, Section 2.1.2 Volcanism).

Magnetic and microgravity surveys were conducted for all four maars. Due to time constraints, only Maar #1 was surveyed by seismic reflection. The seismic reflection survey shows that Maar #1 has a typical maar-type subsurface diatreme-structure and volcaniclastic infill overlain with lake sediments. Interpretations based on the magnetic and microgravity surveys are that Maar #2 has pyroclastic basalt and schist overlying a basalt diatreme, the Maar #3 diatreme includes some lake sediments and an effusive basanite lava deposit signalling cessation of

phreatomagmatic eruptive activity, and the remains of Maar #4 consist of a diatreme with a basaltic ring dyke and a lava flow (Bowie, 2015).

2.2 Maar Lakes

2.2.1 Maar Lake Evolution

Cessation of phreatomagmatic eruptive activity when water is still available can cause a lake to form above the maar diatreme within weeks (Pirrung *et al.*, 2008). Early-post-eruptive activity includes shallowing of the steep slope angle of the upper diatreme by mass flows of breccia and country rock from the steep sides into the crater, infilling the centre of the diatreme (Lorenz, 2003; White & Ross, 2011; Valentine & White, 2012). The slope angle eventually reaches an equilibrium, and the crater then begins to accumulate sediments at a background-sedimentation rate determined by environmental factors (detrital and algal inputs, tephra ring sediments washed in by precipitation, aeolian sedimentation) (Lorenz, 2003; Pirrung *et al.*, 2008; White & Ross, 2011). A study of the Alaskan Ukinrek East Maar that formed in 1977 showed that it took less than 30 years for the slopes to reach a natural (for the local geology) 35° angle of repose (Pirrung *et al.*, 2008).

Intersection of the maar through an aquifer means that the crater often floods quickly, as was witnessed during historic eruptions at Ukinrek (1977, Alaska) and Rotomahana (1886, New Zealand) (Pirrung *et al.*, 2008; White & Ross, 2011). The last eruption of the Ukinrek West maar occurred in the morning, and a shallow lake had formed in the crater by the afternoon (Pirrung *et al.*, 2008). Within 5 years the lake had evidence of phytoplankton, while the lake level slowly continued to rise over the first 13 years until it reached that of the present day (Pirrung *et al.*, 2008). Similar timescales could be expected for the HMC maar lakes.

Once physical and chemical conditions of the lake water permit, a lacustrine habitat becomes established (Cohen, 2003). Maar lakes host distinct ecosystems in both the lacustrine environment and around the inner slope of the tephra ring (Lee *et al.*, 2009; Lindqvist & Lee, 2009; Kaulfuss *et al.*, 2010; Reichgelt, 2015; Kaulfuss *et al.*, 2018). Zolitschka *et al.* (2015) stated that geological influence on depositional processes in individual varved lake catchments are generally stable during the lifetime of a lake.

Maar lake beds are often anoxic due to the small surface area vs depth of the lake, a physical characteristic that tends to develop a permanent thermocline between warmer surface water and cold profundal water (Cohen, 2003). The thermocline prevents dissolved oxygen from reaching the lakebed, and decomposition of detritus that settles on the lakebed depletes any dissolved oxygen that was

available below the thermocline (more on this process below in Section 2.2.2 Meromictic Lakes) (Cohen, 2003). Maar lakebed deposits generally remain largely undisturbed and, as the underlying diatreme compacts and subsides, may accumulate over 100 m of varved biogenic and minerogenic detritus, the character and proportions of which may be used as proxies for palaeoclimate (Pirrung *et al.*, 2003; Suhr *et al.*, 2006; Lorenz, 2007; Fox, 2014; Zolitschka *et al.*, 2015). Pirrung *et al.* (2003) noted that maar lakes not only offered excellent preservation for fossils but also protect the deposit itself through times of tectonic uplift. This is evident in the Foulden Maar deposit, as the maar lake was closer to sea level at the O/M boundary but is now positioned at about 300 m a.s.l. without incurring significant deformation (Lindqvist & Lee, 2009; Martin *et al.*, 2013; Jones *et al.*, 2017). Maars within the HMC have experienced similar tectonic forces and the diatreme structures appear to have remained intact (Bowie, 2015).

2.2.2 Meromictic Lakes

The physical characteristics of maar lakes (relatively deep depth, small diameter, often intersect a groundwater supply/aquifer) makes them particularly susceptible to thermal stratification (Cohen, 2003; Boehrer *et al.*, 2017). Thermal stratification is the vertical segregation of the lake into distinct zones by differential density of the warm surface waters (epilimnion) from the deep cold profundal waters (hypolimnion) (Figure 2.4) (Henry, 1913; Cohen, 2003; Boehrer *et al.*, 2017). The depth range at which the zones are separated from each other is called the thermocline (Birge, 1904; Smith & Smith, 2014).

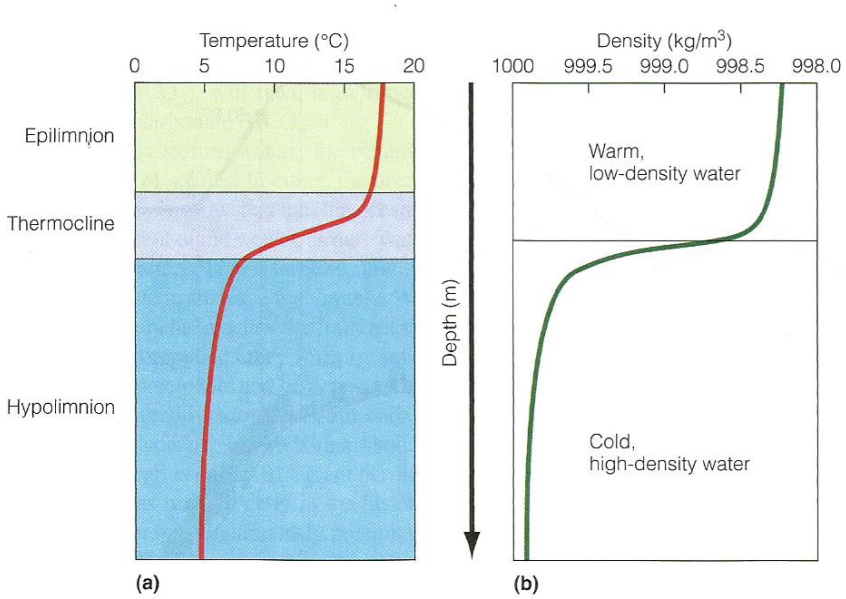

Figure 2.4: A generic example of thermal stratification in a lake (Smith & Smith, 2014).

When a lake is stratified, dissolved oxygen and nutrients are unable to pass freely across the thermocline (Birge, 1904). Organic matter (leaves, algal and animal remains) settles to the lakebed and decomposes, and the nutrients are sequestered beneath the thermocline (Birge, 1904). Decomposition of the organic material depletes residual dissolved oxygen (DO) in the hypolimnion (Birge, 1904; Henry, 1913). DO is unable to mix or diffuse down into the hypolimnion in sufficient amounts to support aerobic decomposition, so the hypolimnion becomes anoxic and unable to support aerobic organisms (Birge, 1904). As a consequence, aerobic benthic organisms (e.g. molluscs, polychaete worms) are excluded from the hypolimnion during the time that it is anoxic, so detrital material is left undisturbed, accumulating as thin laminae (Cohen, 2003). If the thermocline breaks down (e.g. by seasonal cooling of surface waters, or wind-wave agitation of the water column down to the depth of the thermocline), nutrients from below and dissolved oxygen from above would be able to mix throughout the water column (Henry, 1913), allowing benthic organisms to re-inhabit and disturb the sediments as long as sufficient DO was available.

A meromictic lake is one in which a permanent thermocline exists (Cohen, 2003). Rather than an epilimnion and hypolimnion divided by a thermocline, a meromictic lake has a mixolimnion and monimolimnion divided by a chemocline (Figure 2.5) (Boehrer *et al.*, 2017).

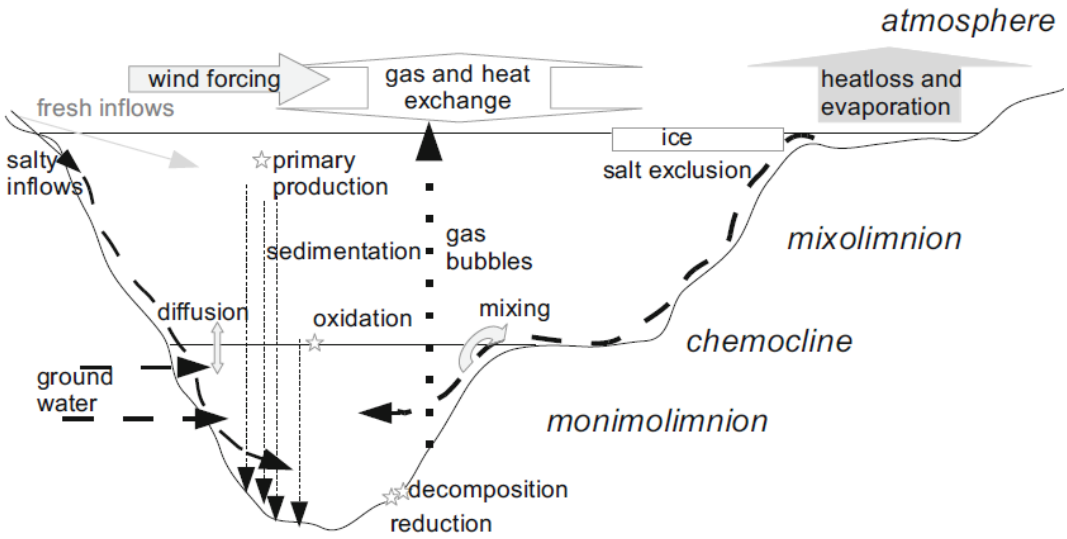

Figure 2.5: Terminology and basic processes in a meromictic lake (Boehrer *et al.*, 2017).

Small deep lakes are often meromictic, as there is insufficient wind-wave agitation to add sub-surface orbital energy to break down the chemocline (Cohen, 2003). Meromixis also persists as it is unusual for water in the mixolimnion to be able to cool sufficiently for its density to equalise with the cold dense water in the monimolimnion (Cohen, 2003). Tropical lakes are also meromictic due to the water

surface receiving a relatively constant influx of solar radiation that keeps the mixolimnion warm and low-density (Smith & Smith, 2014).

Because of isolation by the permanent chemocline in meromictic lakes, the mixolimnion and monimolimnion each have chemical characteristics distinct from each other (Boehrer *et al.*, 2017). However, nutrients sequestered in the monimolimnion can be exchanged with the mixolimnion if the depth of the chemocline is reduced (Boehrer *et al.*, 2017). This can happen by an influx of cold groundwater or by cooling of the mixolimnion. Subsequently, turbulent convective currents in the mixolimnion can “shave” nutrients off the top of the chemocline and redistribute them to the biota near the surface (Boehrer *et al.*, 2017).

The lakes that formed in the HMC are assumed to have been meromictic by the prevalence of unbioturbated laminated lake sediments throughout the deposits (Kaulfuss *et al.*, 2018). This is consistent with their assumed depth, cold groundwater supply (assuming intersection with an aquifer), and small surface areas with surrounding tephra rings which would have greatly reduced the ability of winds to generate wave energy. Many meromictic maar lake sediments have been studied for palaeoenvironmental reconstructions, including sites in Germany (Brauer & Negendank, 1993; Sabel *et al.*, 2005; Herrmann, 2010), China (Mingram *et al.*, 2004; Hu *et al.*, 2015), and New Zealand (Lee *et al.*, 2016; Fox *et al.*, 2017; Möller *et al.*, 2017; Kaulfuss *et al.*, 2018).

2.3 Studies of Mid-Miocene Climate

2.3.1 Global Studies

Global climate followed a general pattern of cooling from the Oligocene-Miocene boundary through the Holocene. However, the mid-Miocene saw a reversal in this trend (the mid-Miocene Climatic Optimum, or MMCO, ~17.0-14.7 Ma) (Zachos *et al.*, 2001). The age of the HMC (14.6±0.1 Ma) coincides with the mid-Miocene climate transition (MMCT) from the MMCO to the extended cooling trend (Zachos *et al.*, 2001; Holbourn *et al.*, 2015).

Figure 2.6 shows the HMC formation relative to the MMCO peak (pale orange band), using global deep-sea oxygen isotope records as temperature proxies (Zachos *et al.*, 2001). The HMC formed at a time when the Antarctic ice sheet (AIS) had been established by the early Oligocene after initiation of the Antarctic Circumpolar Current (ACC) following the opening of the Drake Passage (Coxall & Wilson, 2011). However, the extent of the AIS in the early to mid-Miocene was

variable and perhaps ephemeral, and a Northern Hemisphere ice sheet had not yet formed (Zachos *et al.*, 2001; Levy *et al.*, 2016).

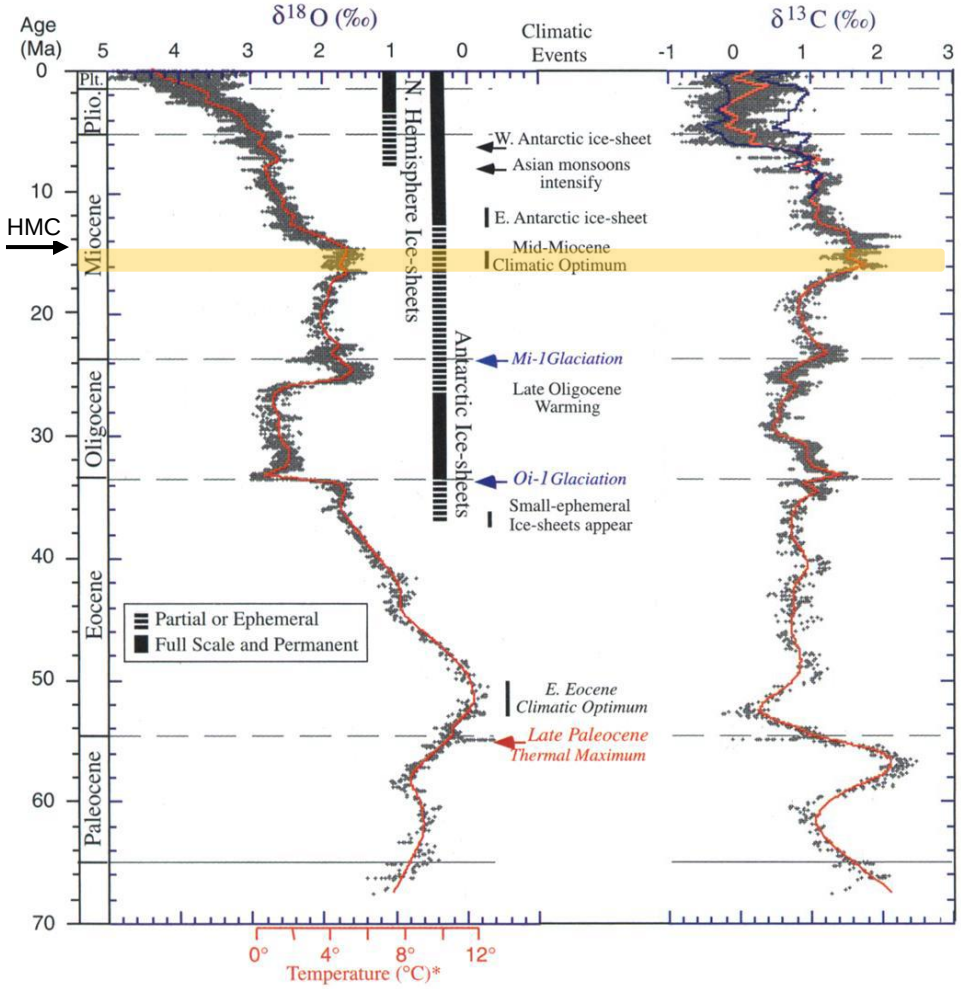

Figure 2.6: Global deep sea oxygen and carbon isotope records from DSDP core analyses. MMCO range represented by pale orange band. The temperature scale is calibrated for ice-free oceans so it applies no later than 35 Ma. Vertical bars indicate ice coverage (see legend) relative to the Last Glacial Maximum. Dashed line represents ≤50%; Solid line represents >50% (adapted from Zachos *et al.*, 2001).

Many studies have independently recognised and corroborated the mid-Miocene episode of global warming. Isotope records derived from deep marine cores have been used to determine the timing of changes in global ice coverage (Miller *et al.*, 1991; Naish *et al.*, 2001; Liebrand *et al.*, 2011; Beddow-Twigg, 2016); global carbon cycling and meridional heat flux by deep sea currents (Flower & Kennett, 1994; Pälike *et al.*, 2006; Holbourn *et al.*, 2015); and primary production and atmospheric pCO_2 (Knorr & Lohmann, 2014). However, understanding the processes driving the global climate shifts at the initiation of and transition from the MMCO has been difficult. Commencement of the MMCO has been attributed to increased atmospheric pCO_2 and increased oceanic acidity caused by the

voluminous Columbia River Basalt Group lava flows (Foster *et al.*, 2012; Holbourn *et al.*, 2015). While this may have been a factor, the timing of the volcanism is too late for it to have been the primary cause (Holbourn *et al.*, 2015). The transition from the MMCO to cool climate conditions has been attributed to alteration of deep ocean circulation by tectonic activity (Hamon *et al.*, 2013); a decrease in atmospheric pCO_2 due to an increase in global carbon burial (Zhang *et al.*, 2013); or an orbital change that resulted in an insolation pattern conducive to ice sheet formation and glaciation cycles (Holbourn *et al.*, 2015).

The various changes in the characteristics of the Earth's orbital patterns have long been recognised as major climate-drivers. The oscillations were recognised by James Croll early in the 20th century and later clarified by Milutin Milankovitch, who developed the theory that the Earth's surface temperatures vary latitudinally in regular and predictable ways due to periodic changes in Earth's orbital path and axis angle, now called Milankovitch cycles (Figure 2.7) (Milankovitch, 1941). These cycles have been correlated to sea level and palaeotemperature by the oxygen isotope $\delta^{18}O$ record, where ^{18}O is biogenically incorporated from sea water into the calcareous tests of marine foraminifera found in deep sea drilling cores (Emiliani & Geiss, 1959; Shackleton, 1967). Linkage of $\delta^{18}O$ to ice sheet cover extends back to at least the past 40 Ma (Zachos *et al.*, 1997; Zachos *et al.*, 2001; Miller *et al.*, 2005).

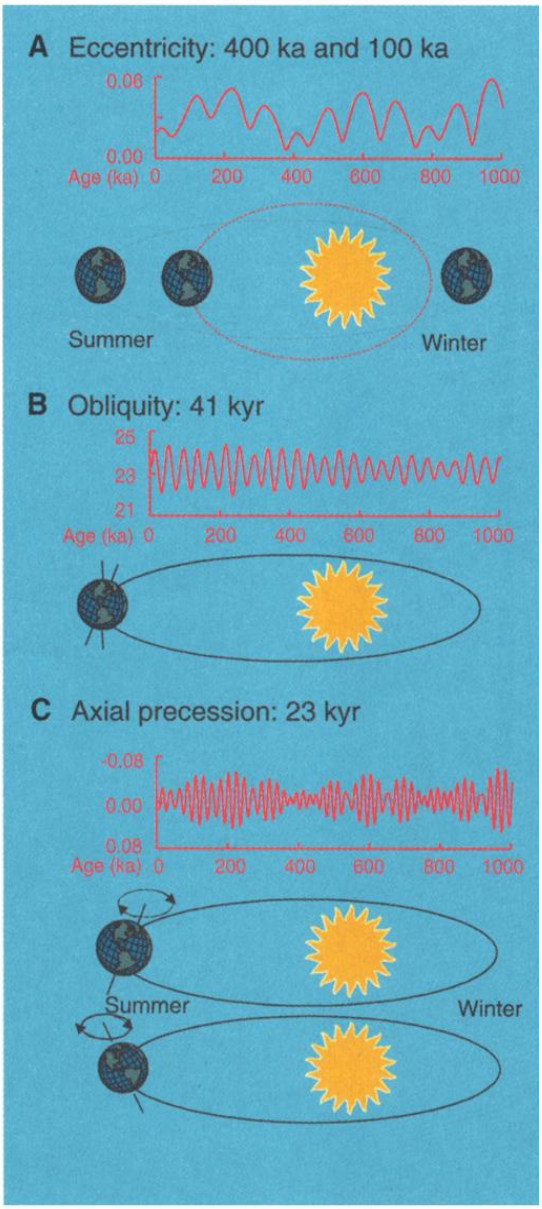

Figure 2.7: Orbital Milankovitch cycles. A. eccentricity; B. obliquity; C. precession (Zachos *et al.*, 2001).

Three orbital Milankovitch cycles are commonly recognised (Figure 2.7) (Zachos *et al.*, 2001). Eccentricity of the orbital path of the Earth around the Sun has a periodicity of ~100 ka, and in that time the orbital path

transitions from more circular to more elliptical, influencing the amount of seasonal solar insolation by ~30% (Figure 2.7A) (Zachos *et al.*, 2001; Nichols, 2009). Obliquity is the angle of Earth's axis relative to a pole normal to the orbital plane (or its tilt), and it oscillates from ~21.5° to ~24.5° over ~41 ka (Figure 2.7B, presently at ~23.5°) (Zachos *et al.*, 2001; Nichols, 2009). Precession is the circular 'wobble' of the Earth's axis every ~22 ka (Figure 2.7C) (Zachos *et al.*, 2001; Nichols, 2009). Together the interaction of Milankovitch orbital cycles changes the intensity and distribution of solar energy incident upon the Earth's surface (Milankovitch, 1941). The phase of the cycles in combination with the peaks and troughs in the different cycles results in modulation of their overall effect on insolation, and in the Quaternary has resulted in glacial/interglacial cycles (Shackleton, 1967).

A study using a drill core proximal to the AIS (~30 km offshore from Southern Victoria Land, Antarctica) concluded that the AIS was very sensitive to changes in orbital cycles and atmospheric pCO_2 during the mid-Miocene (Levy *et al.*, 2016). It found that MMCO/MMCT glaciations/deglaciations were aligned with 100 ka orbital eccentricity cycles, while the extent of AIS advance and retreat was modulated by atmospheric pCO_2 (Levy *et al.*, 2016). Maximum AIS retreat occurred when eccentricity maxima were accompanied by high pCO_2 ($\geq$500 ppm), while maximum AIS advance was evident when eccentricity minima occurred while atmospheric pCO_2 was <400 ppm (modelled) (Levy *et al.*, 2016). This study placed the time of maximum ice sheet advance at a period of low orbital eccentricity, between 14.6 and 14.7 Ma, within the date-range for the formation of the HMC (Levy *et al.*, 2016; Kaulfuss *et al.*, 2018). That time period coincided with atmospheric pCO_2 of ~280 ppm, as reported by Levy *et al.* (2016) based on multi-proxy evidence.

Milankovitch cycles during the HMC (shaded area) are shown in Figure 2.8. The HMC formation (14.6$\pm$0.1 Ma) occurred when the three orbital cycles converged near their minima, resulting in a time of low insolation (Laskar *et al.*, 2004).

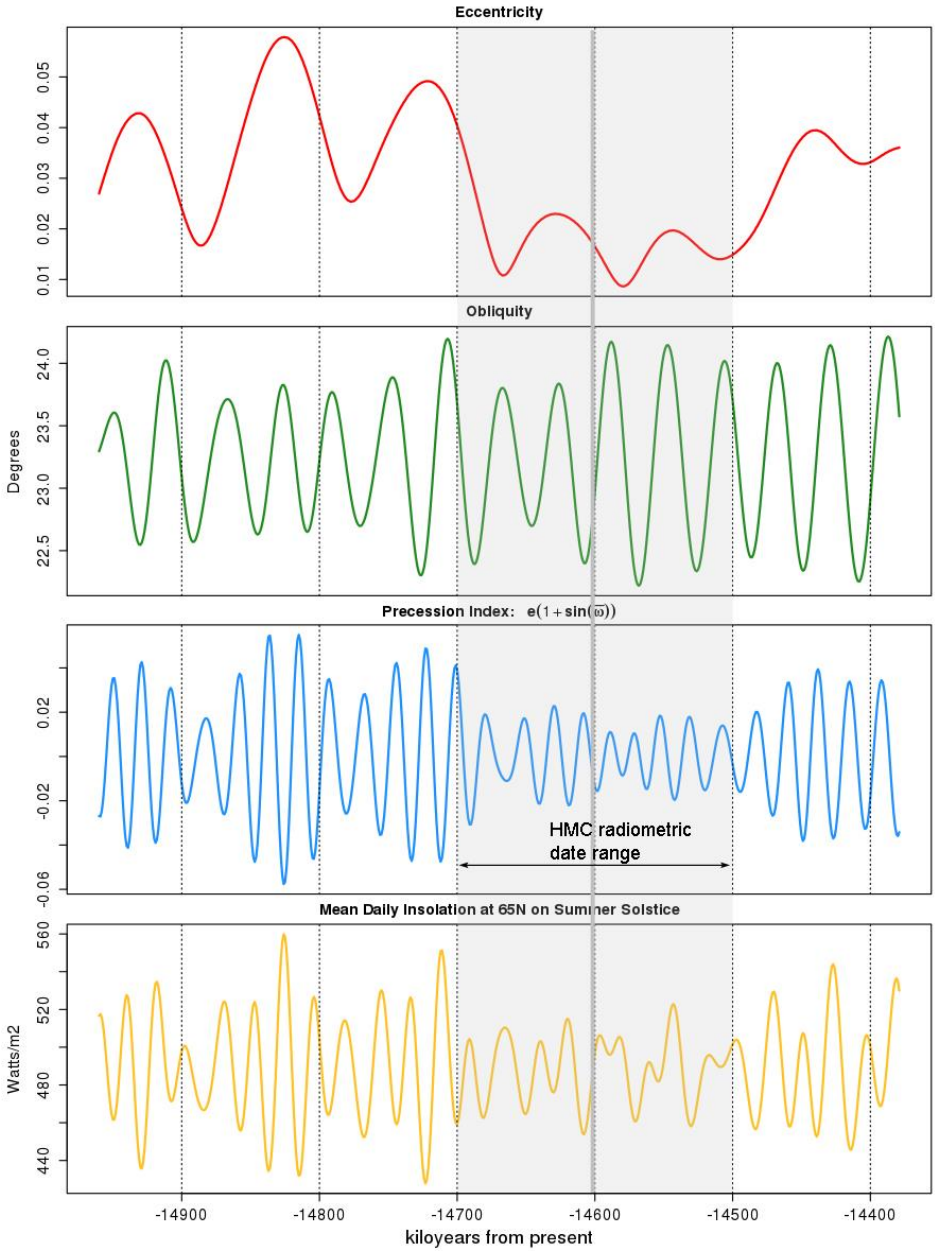

Figure 2.8: Milankovitch cycles at the time of the HMC formation (14.6±0.1 Ma) (adapted from Laskar *et al.*, 2004).

2.3.2 New Zealand Studies

New Zealand-focussed studies encompassing the mid-Miocene, the time of the HMC formation, primarily involve palaeobotanical investigations of lacustrine and lignite deposits on the South Island (Field *et al.*, 2009; Reichgelt *et al.*, 2016b; Prebble *et al.*, 2017; Kaulfuss *et al.*, 2018). Palaeobotany-based temperature estimates for the Dunedin Volcano and Kaikourai Valley indicated cooler mean annual temperatures during the MMCT, which Reichgelt *et al.* (2016b) postulated could be due to strengthening of the ACC and northward progression of the Sub-Antarctic Front. Palynological analyses of mid-Miocene New Zealand samples provided palaeotemperature estimates that mirrored global deep sea oxygen and carbon isotope values (Field *et al.*, 2009).

Prebble *et al.* (2017) mined the New Zealand FRED-database (Fossil Record Electronic Database) to compile terrestrial fossil pollen and spore data acquired as early as 1946 for comparison with 70 modern analogues of the fossil data in order to build a climate model for the past 34 Ma. The findings were compared with regional and global climate drivers and proxies (Figure 2.9). The time period in which the HMC was formed and deposited is identified with a vertical orange-dashed rectangle (within the Lillburnian Stage). The Prebble *et al.* (2017) study included a suite of samples from the HMC/Dunedin region from the Lillburnian Stage. As part of the study, palaeo latitude data was also extrapolated. This showed the HMC location was ~2° further south when it was formed (Prebble *et al.*, 2017).

Correlation of the HMC origin with the global benthic foraminifera oxygen isotope temperature-proxy (Figure 2.9D) shows that formation of the HMC occurred early in the MMCT, after the MMCO peak. Figure 2.9A displays the mean summer, annual, and winter temperatures in ranges bounded by the warmest and coldest 20% of the samples in each Stage. The upper bound of the mean annual temperature in the Lillburnian Stage is the highest of the dataset, at ~20.7°C vs. ~18.6°C at the end of the Pleistocene. There is also little seasonality between the mean summer and winter temperatures during the Lillburnian. After the middle Miocene seasonality increases substantially, from a difference of ~6°C between the upper 20% of the summer/winter data to a difference of ~11°C in the Castlecliffian Stage. Figure 2.9C is a fossil pollen-based estimate of the mean annual precipitation (MAP), bounded above and below by determinations from the wettest and driest 20% of the samples, respectively. Precipitation through the Lillburnian averaged between ~1600 and 1900 mm, with low variability. Precipitation variability increased once uplift began to occur on the South Island at the end of the Miocene (Figure 2.9C).

Cooke *et al.* (2008) studied foraminifera in an intermediate water marine core (acquired from the southwest margin of the Challenger Plateau in the Tasman Sea) to determine palaeotemperatures of several deep ocean currents in the region. Unfortunately, the core had a disconformity from ~15.9-13.46 Ma which excludes data that could be directly correlated to the HMC formation (Cooke *et al.*, 2008). The data that was acquired did generally corroborate global seawater temperature trends (Cooke *et al.*, 2008).

Based on palaeobotanical data and reviews of previous studies, New Zealand climate at ~50°S latitude during the MMCO was recorded as subtropical, with MATs ~10°C warmer than present coastal MATs (Pole, 2014).

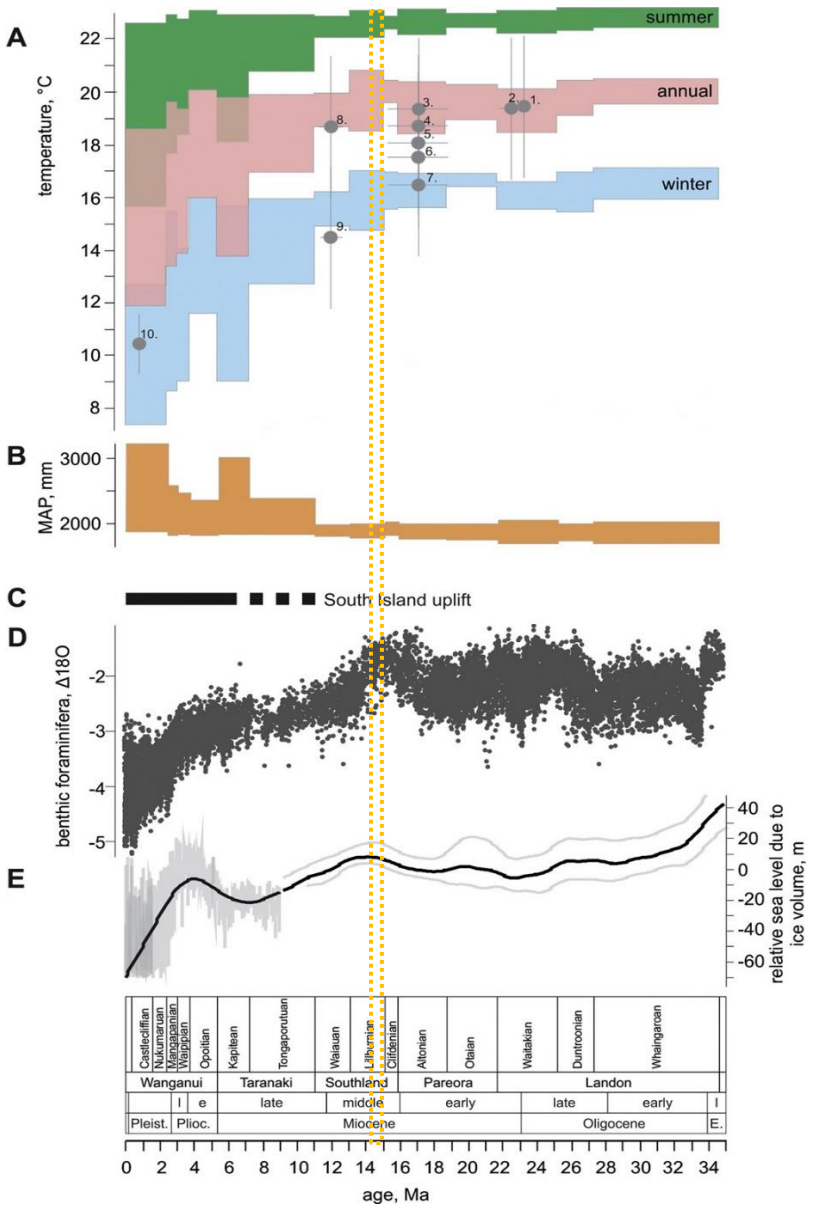

Figure 2.9: Summary of New Zealand pollen-based climate model with regional and global climate proxies. HMC=orange-dashed rectangle. **A.** Summary of New Zealand palynologically-based estimates for temperature and precipitation alongside regional and global climate proxy data. Green=mean summer temperature, bounded above by mean of warmest 20% of samples and below by coldest 20%. Pink=mean annual temperature. Blue=mean winter temperature. **B.** Mean annual precipitation, bounded by wettest and driest 20% of samples. **C.** Summary of South Island compressional tectonics. **D.** Global benthic $\delta^{18}O$‰. **E.** Estimated sea level based on ice volume. (adapted from Prebble *et al.*, 2017).

Orbital cycles have been used to infer palaeoclimate conditions at Foulden Maar on the South Island, New Zealand, during the O/M transition and Mi1 deglaciation event. Foulden Maar formed in similar fashion to maars in the HMC (Fox, 2014). Drilling yielded a composite core of ~110 m of lake sediments, representing ~100 ka of deposition (from ~23.03-22.93 Ma) (Fox, 2014). Both obliquity and precession frequencies were recognised in the lamina-thickness changes and density changes upcore, confirming that the lamina-couplets were true annual varves (Fox *et al.*, 2016). Varved sediments enabled the development of an age

model that was cyclostratigraphically correlated with global climate proxies (i.e. benthic foraminifera oxygen and carbon isotope studies), making it possible to determine that there was strong ocean-atmosphere coupling in the mid-latitudes of the Southern Hemisphere during the Mi1 deglaciation (Fox *et al.*, 2016). Further study revealed a low-latitude-associated sub-precessional orbital insolation cycle that appeared later in the deposit (Fox *et al.*, 2017). Earlier deposition was influenced more by polar-associated obliquity orbital cycles (Fox *et al.*, 2017). Latitudinal shifts of the circumpolar westerly wind currents in the vicinity of the mid-latitude Foulden Maar seem to have influenced the characteristics of its deposit (Fox *et al.*, 2017).

As mentioned in Section 2.1.1 Regional Geology and Tectonic Setting, the Foulden Maar is ~25 km northwest of the HMC. Although temporally separated by ~8.5 Ma, both sites are high-quality fossil repositories (or *Lagerstätten*) hosting thousands of years of evidence attributed either directly to the local environment or indirectly by the physical characteristics of the deposits (Lindqvist & Lee, 2009; Kaulfuss *et al.*, 2010; Fox *et al.*, 2016; Fox *et al.*, 2017; Kaulfuss *et al.*, 2018). The Foulden Maar and HMC were formed in very similar geological circumstances, at important Neogene transitions from global thermal maxima to cooling climates.

2.4 Hindon Maar #1 Palaeoecology

Discovery of the Hindon Maar Complex is relatively recent. Even so, two articles relating the geology and palaeoecology of the lake deposits in the HMC have recently been published (Möller *et al.*, 2017; Kaulfuss *et al.*, 2018).

Möller *et al.* (2017) examined over 550 fossil angiosperm leaves from the upper sediments of Hindon Maar #1 for evidence of insect herbivory. The leaves represented two types of forests: deciduous species in the tephra ring soils proximal to the maar lake, and evergreen podocarp species in the distal soils developed on Otago Schist (Möller *et al.*, 2017). Palaeobotanical analyses by Pole (2014) showed that the warm wet climate in the Otago region transitioned to dry and fire-prone at times during the mid-Miocene.

Kaulfuss *et al.* (2018) presented the geology and palaeontology of HMC from outcrops, samples from an excavation pit, 2.5 m-deep hand auger samples and two exploration drill cores from Maar #1 (~39 m) and Maar #3 (~30 m). Though the depths vary slightly, the units represented in the Maar #1 core correlate with those in the HMC M1-2 (~18 m) core acquired for this thesis. Assemblages of limnic microfossils, allochthonous macroflora, arthropods, teleost fish (including a freshwater eel species), and the first pre-Quaternary bird feathers in New Zealand

are inventoried (Kaulfuss *et al.*, 2018). The study finds that lacustrine deposition took place in a meromictic environment and that there is little evidence of alteration of the sediments or fossils by diagenetic processes, with an exception being the absence of calcareous organisms (Kaulfuss *et al.*, 2018). The forest on the lake margins is dominated by several species of *Nothofagus* (e.g. Southern Beech) but the surrounding forest was generally *Nothofagus*/podocarp/mixed broadleaf ecosystem (Kaulfuss *et al.*, 2018). The MMCO/MMCT HMC macrofloral assemblage is different, warmer, and may be of higher diversity than that of the O/M boundary Foulden Maar (Kaulfuss *et al.*, 2018).

2.5 Palaeoenvironmental Analysis of Lacustrine Deposits

2.5.1 Physical Properties

This section presents background information regarding the analyses used to discern some of the physical properties of the HMC M1-2 lake sediments. Many of physical property analyses were completed using a Geotek Multi-Sensor Core Logger (MSCL). Physical property measurements performed on the Geotek MSCL are acquired quickly and are non-destructive.

Magnetic Susceptibility

Magnetic susceptibility (MS) is a measure of the magnetic response that a material has when subjected to a magnetic field of known strength (Nowaczyk, 2002). Changes in climate cause variation in weathering and erosional processes, the results of which can be recognised by changes in sedimentation patterns and sediment composition. (Nowaczyk, 2002). Terrigenous sediment commonly includes magnetic minerals, and changes in sediment composition can be seen by variation in the sediment magnetic susceptibility (Nowaczyk, 2002).

There are three principal types of response by a material to an applied magnetic field (Geotek, 2012). Ferromagnetic material has a strong (or high positive) magnetic response and retains part of the magnetism after the applied magnetic field is removed (Geotek, 2012). Paramagnetic material has a weak (or low positive) magnetic response and retains no magnetism when the applied magnetic field is removed (Geotek, 2012). Diamagnetic material responds by generating a weak negative magnetic field that is immediately lost when the applied magnetic field is removed (Geotek, 2012).

In all cases, the measured MS of a bulk sample is the net response of all the minerals in that sample (within the applied magnetic field) (Fox, 2014). The strong positive MS of ferromagnetic minerals in a sample can be negated by the weak

response of diamagnetic minerals in the same sample if the concentration of the former is very low and latter very high. Ferromagnetic minerals are common in terrigenous sediments while biogenic materials are generally diamagnetic (Fox, 2014). Changes in MS upcore along with sedimentological observations can thus be used to infer the relative contributions of terrigenous vs biogenic material. For example, MS was used in combination with the density of Foulden Maar sediments to determine the relative contributions of minerogenic and biogenic sediment (Fox *et al.*, 2017).

Gamma Attenuation Density

The bulk density of a sediment is dependent upon the density of the minerals in the sediment combined with the porosity of the sediment (Geotek, 2012). The material filling the sediment pore spaces (usually air or water) also affects the bulk density. When using the Geotek MSCL system, sediments should undergo bulk density analysis while saturated with water.

Gamma attenuation density is measured by measuring the attenuation of gamma rays (reduction in intensity) as they pass through the sediment sample (Zolitschka *et al.*, 2002). Gamma rays of a known intensity are focussed into a narrow beam through a sample of known volume (calculated using the cross-sectional area of the beam and the core thickness measurement) and are sensed on the opposite side by a detector (Geotek, 2012). To ensure the detector does not sense erroneous background radiation, it is calibrated to sense only gamma rays with the specific energy of the gamma ray source (in this case, 0.662 MeV) (Geotek, 2012). The gamma ray intensity sensed by the detector is compared to that of the source, the difference reflecting how much of the signal was attenuated by the sediment sample (Geotek, 2012). High-density materials attenuate more of the signal than low-density materials, and this attenuation is then used to determine the bulk density of the material (Geotek, 2012).

Density is commonly utilised in palaeoelimnological and palaeoenvironmental studies in a similar manner as MS (Cohen, 2003). Siliceous terrigenous sediments often host high-density minerals (e.g. magnetite, titanomagnetite) while marine and lacustrine biogenic sediments are constructed from low-density materials such as silica and carbonate and exclude heavy minerals (Fox, 2014; Fox *et al.*, 2017).

Colour

The colour of sediments can be a general reflection of the composition (Martínez-Carreras *et al.*, 2010). For example, light-coloured sediments may have a high percentage of biosiliceous or carbonate material, or may be composed of

terrigenous minerals that have a higher silica content (quartz, feldspars). As is the case for MS and density, changes in the colour of sedimentary deposits are indicative of changes in sediment weathering, erosion, and transport characteristics, all of which are evidence of changes in climatic and environmental processes from the sediment source to sink. The human eye may not be able to detect the subtleties in colour variation, and it is difficult to subjectively describe colour consistently. However, digital spectroscopic colour analyses are able to quantify the sediment colours into data which can be presented in co-ordinate systems such as CIE L*a*b* reflectance and RGB intensity (Geotek, 2012).

CIE L*a*b* Reflectance

The L*a*b* colour co-ordinate system was developed by the Commission Internationale de l'Eclairage (International Commission on Illumination) (Geotek, 2012). This system splits the colour information into luminosity (L*), green-red hue (a*), and blue-yellow hue (b*) in a way that is meant to simulate colour as it is perceived by the human eye (Ohta & Robertson, 2006). The L* represents the darkest black as 0 and the brightest white as 100 (Ohta & Robertson, 2006). The a* green-red hue represents green as negative values and red as positive values, with greater intensity represented by higher integer values (Ohta & Robertson, 2006). Similarly, the b* hue represents blue as negative values and yellow as positive values. For both a* and b*, 0=neutral grey (Ohta & Robertson, 2006).

RGB Intensity

The red, green, and blue channels of the RGB co-ordinate system are employed to reproduce images on viewing devices (Fox, 2014). Black is represented by values of zero for each channel, while white is the maximum value (Fox, 2014). All other hues are represented by varying values in each of the three channels (Fox, 2014). RGB data can be used to understand sedimentation and palaeoclimatic processes. For example, Jakobsson *et al.* (2000) used the RGB colour values at manganese peaks in an Arctic Ocean deep sea core to develop a transfer function which was then used to correlate RGB peaks with glacial/interglacial deep sea $\delta^{18}O$ variation during the Pleistocene. At Foulden Maar, analysis of L*a*b* and RGB co-ordinate system data and other physical properties revealed changes in biosiliceous sediments that reflect primary production rates, and highlighted multiple Milankovitch cycles as climate drivers at the O/M boundary (Fox *et al.*, 2016; Fox *et al.*, 2017).

Composition

The proportion of total organic carbon (TOC), biogenic silica (BioSi), and total inorganic carbon (TIC) in a lacustrine sediment deposit can be used to infer environmental or climatic forcings that contributed to changes in sedimentation throughout the evolution of the lake (Rosén *et al.*, 2011). TOC consists of organic remains from autochthonous ecological activity and allochthonous detritus washed or blown into the lake from adjacent forests (Cohen, 2003). BioSi is present in siliceous organisms such as diatoms (siliceous tests, or valves), freshwater sponge remains (spicules, or scleres), and siliceous spherical resting spores (stomatocysts, statospores, or simply 'cysts') of chrysophycean golden brown algae (Smol *et al.*, 2002). TIC represents minerogenic compounds found in terrestrial sediments.

Fourier Transform Infrared Spectroscopy

Individual chemical analyses have typically been performed to determine the proportion of the TOC, BioSi, and TIC components in sediment samples. However, recent studies have demonstrated that the proportions (wt%) of TOC, BioSi, and TIC can be quickly and simultaneously ascertained in minute samples using Fourier transform infrared spectroscopy (FTIRS) in combination with partial least squares regression (PLSR) (Fellman *et al.*, 2010; Rosén *et al.*, 2011; Meyer-Jacob *et al.*, 2014a).

The basic principle relies on the quantum mechanical behaviour of molecules to absorb infrared radiation at energies specific to their composition (Rosén *et al.*, 2011). The absorbance energies recorded for the samples are compared against a locally-derived site-specific FTIRS calibration model developed using synthetic sediments of varying proportions (Meyer-Jacob *et al.*, 2014a). Ultimately, absorbance peaks correspond to the concentrations of the components in the sediments (Rosén *et al.*, 2011).

A FTIRS calibration model specific to the Hindon Maar Complex sediments was developed by F. Garrity using synthetic sediments derived from activated carbon as a pure example of TOC, food-grade diatomaceous earth as a pure example of BioSi, and Otago Schist as a local example of terrigenous material (Garrity, 2017). FTIRS results for Garrity's HMC Maar #3 lake sediments showed useful variation upcore which he was then able to equate to changes in wind intensity that modified the quantity of terrigenous input (Garrity, 2017).

Biogenic Silica by Wet Chemical Digestion

Biogenic silica is a measure of the amorphous silica content (or biogenic opal) in sediments and represents the abundance and variability of siliceous primary

productivity in a palaeolake (Conley & Schelske, 2002; Meyer-Jacob *et al.*, 2014a). Diatom frustules are typically the main source of siliceous evidence of primary productivity, but sponge spicules can dominate at times, and silica-walled statospores of chrysophycean cysts contribute a small quantity of BioSi as well (Ragueneau *et al.*, 1996; Meyer-Jacob *et al.*, 2014a).

BioSi is soluble in alkaline solutions, a physical property that has been utilised as a means to remove and isolate BioSi from sediment samples, and thus determine their contribution (DeMaster, 1981; Mortlock & Froelich, 1989). Wet chemical digestion techniques involve soaking samples in a base of a specific strength (varies with different methods, from 1% Na_2CO_3 to 1 M NaOH) and volume, at a specific temperature, and removing small aliquots after specified lengths of time (Mortlock & Froelich, 1989; Conley & Schelske, 2002). BioSi wt% content of each aliquot is measured by a spectrophotometer and plotted against time since digestion began (Figure 2.10) (DeMaster, 1981). The y-intercept for the slope of the line drawn through the BioSi wt% data-points represents the wt% of silica extracted (DeMaster, 1981).

The wet chemical digestion method was further refined and standardised by Mortlock and Froelich (1989), using a moderate strength base (2 M Na_2CO_3). This study of the HMC M1-2 lake sediment deposit utilised a procedure prepared by Mucciarone (2003) which calls for a 0.1 M NaOH solution. The specifics of Mucciarone's method will be presented in Chapter 3: Biogenic Silica Wet Chemical Analysis.

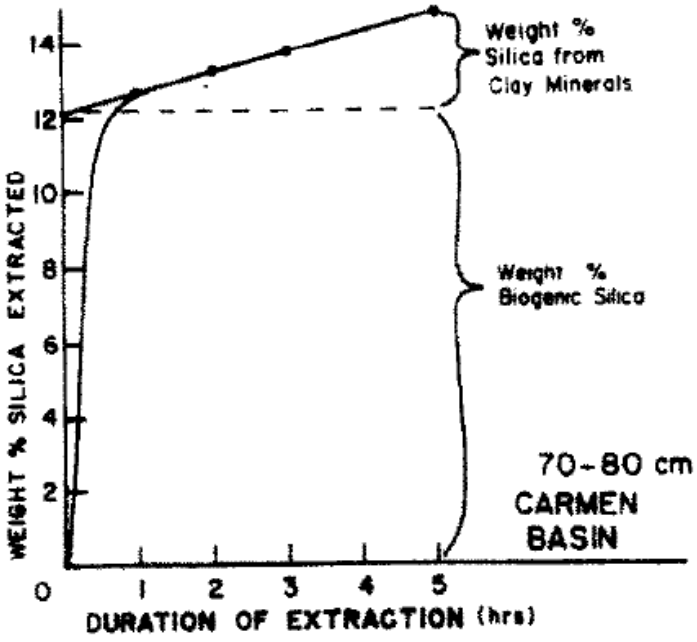

Figure 2.10: BioSi wt% extracted vs time of extraction (curve) (DeMaster, 1981).

2.5.2 Analyses of Biosiliceous Microfossils

“The present is the key to the past” – that is the principle of uniformitarianism (Hutton, 1788).

This section presents studies regarding biosiliceous assemblages in lacustrine deposits and the palaeoenvironmental information that can be acquired from them. Siliceous microorganisms take up silicic acid from aqueous environments and utilise it to biochemically construct skeletal elements in the form of amorphous biogenic opal, a hydrated silica mineraloid (Round *et al.*, 1990). The value of these microfossils is their global extent (they can be found virtually anywhere where water is at least occasionally present) and the resistance of their amorphous silica to environmental chemical weathering, leaving them well preserved for palaeontological investigations (Smol & Stoermer, 2010). The exception is in alkaline environments in which BioSi dissolves, as mentioned above in Section 2.5.1 Physical Properties: Composition.

Diatoms as Palaeoenvironmental Indicators

Diatoms are unicellular eukaryotic algae comprised of a hard hydrated silica dioxide frustule encompassing and surrounded by organic matrix (Battarbee *et al.*, 2002). The frustule consists of two overlapping parts called thecae (informally called valves) which fit together like a box and lid, one half being slightly smaller (hypotheca) than the other (epitheca), with siliceous girdle bands (or copulae) between them (Figure 2.11) (Smol & Stoermer, 2010). They range in size from 5 to 2000 μm (Round *et al.*, 1990). Fossil diatom flora were diverse in the Miocene, and many Miocene diatom taxa are similar to extant diatom species (Battarbee *et al.*, 2002).

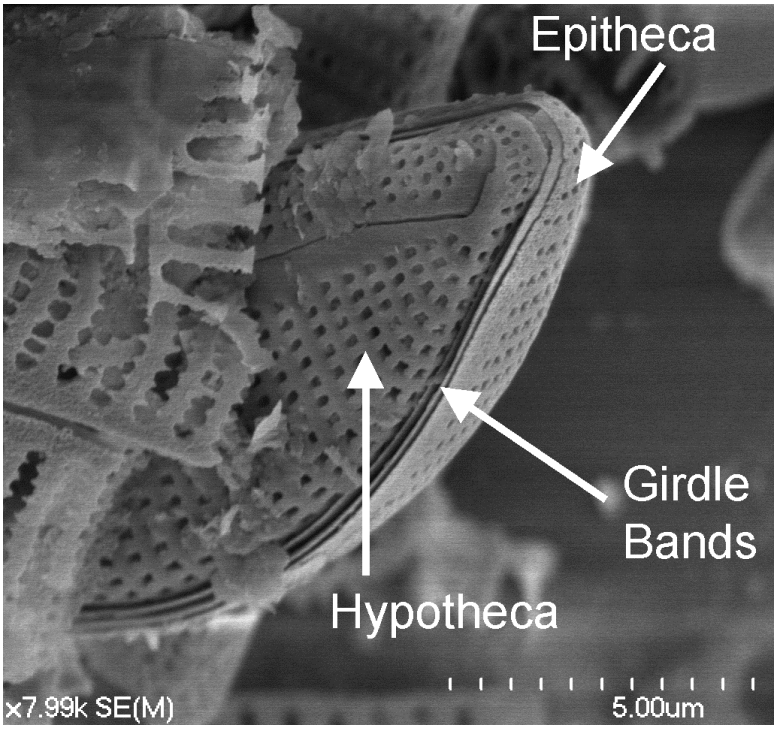

Figure 2.11: Intact frustule of a pennate diatom from HMC M1-2 (this study), 8000x magnification.

Diatoms are globally ubiquitous in any environment where moisture is present (Round *et al.*, 1990). Diatoms have been found in a wide variety of archives utilised for environmental reconstruction, including river channel deposits, freshwater and marine sediments, and even tephra deposits (Smol & Stoermer, 2010; Van Eaton *et al.*, 2013).

Contemporary diatom communities are extremely sensitive to the environmental conditions in which they live (e.g. pH, nutrient availability, water depth) (Gasse, 1994; Smol & Stoermer, 2010). In the 1930s it was recognised that diatom species could be classified by pH preference, from alkalibiontic (pH>7), alkaliphilous (pH just above ~7), indifferent (pH=7), acidophilic (pH just below ~7), and acidobiontic (pH<7 with optimum distribution around 5.5) (Battarbee *et al.*, 2010). Diatoms are especially sensitive to nutrient availability (Hall & Smol, 2010). They respond quickly to changes in nutrient flux by increased/decreased abundance of the species in the diatom assemblage, and by changes in habitat distribution (planktonic, epiphytic, epilithic, epipelic, etc.) (Hall & Smol, 2010). They are also characterised by taxon-specific sensitivity to changes in nutrient concentration and ratios of various nutrients (Hall & Smol, 2010).

Diatom-based interpretations are best combined with those of multiple other proxies when reconstructing a palaeoenvironment (Juggins, 2013). For, example, Newnham *et al.* (2004) utilised diatom data along with tephrochronology, radiometric dating, palynology, and physical characteristics of sediments taken

from Lake Omapere, Northland, New Zealand to draw conclusions regarding Quaternary climate changes. Diatom data from a MMCT planar-bedded lacustrine deposit in the McMurdo Dry Valleys of Antarctica were employed along with radiometric dating, palynology, palaeobotany, and arthropod palaeontology to determine that the Antarctic lake was permanently ice-free until at least ~13.85 Ma during the MMCT, well after the HMC formed (Lewis *et al.*, 2008).

Use of diatoms as palaeoenvironmental proxies has not been without issues. Historical inconsistencies when classifying diatoms and later updates in taxonomic naming conventions has led to multiple names or synonyms being assigned to many species (Round *et al.*, 1990; Smol & Stoermer, 2010). Regarding dissolution, attempts have been made to account for this in alkaline and/or saline environments (Lewin, 1961; Ryves *et al.*, 2009). Researchers have conducted experiments and statistical analyses in an attempt to develop a dissolution index in order to quantify the error between diatom-dissolution-based salinity estimates and historical salinity measurements (Ryves *et al.*, 2006). Their findings were that increasing dissolution leads to increasing errors by overestimation or underestimation of salinity (Ryves *et al.*, 2006).

Chrysophycean Cysts as Palaeoenvironmental Indicators

Chrysophycean cysts are the silica-walled resting stage in the life cycle of chrysophytes, a unicellular golden-brown flagellated alga (Kristiansen & Preisig, 2011). Also referred to as stomatocysts or statospores, the cysts are typically spherical or obovate and range in size from ~3-35 μm (Sandgren, 1991).

A single pore is the distinguishing feature of all cysts (Sandgren *et al.*, 1995). The pore may or may not be surrounded by an elevated collar, and the cyst surface may be smooth or ornamented with thickened features such as scabrae verrucae or conula (small projections); spines; reticula (ridges); indentations such as psilae and depressions; fossae (grooves) (Duff *et al.*, 1995).

Very few cyst morphotypes have been linked with the chrysophyte algal taxa that produced them (Zeeb & Smol, 2002). Without this link, early work to associate cysts with environmental conditions saw the cysts assigned with artificial generic designations based on their morphology (Nygaard, 1956). As the number of morphotypes grew, a set of standards for their description was developed by the International Statospore Working Group (ISWG) (Sandgren *et al.*, 1995). By the ISWG standards, the cyst morphotypes were assigned numbers and archived with SEM and LM images (Sandgren *et al.*, 1995). There are over 300 published cyst morphotypes by the ISWG in two volumes (Duff *et al.*, 1995; Wilkinson *et al.*, 2002),

although a more recent article places that figure at >800 based on reviews of subsequent research (Soroczki-Pinter *et al.*, 2014). Figure 2.12 shows an as-of-yet unassigned cyst morphotype from this study.

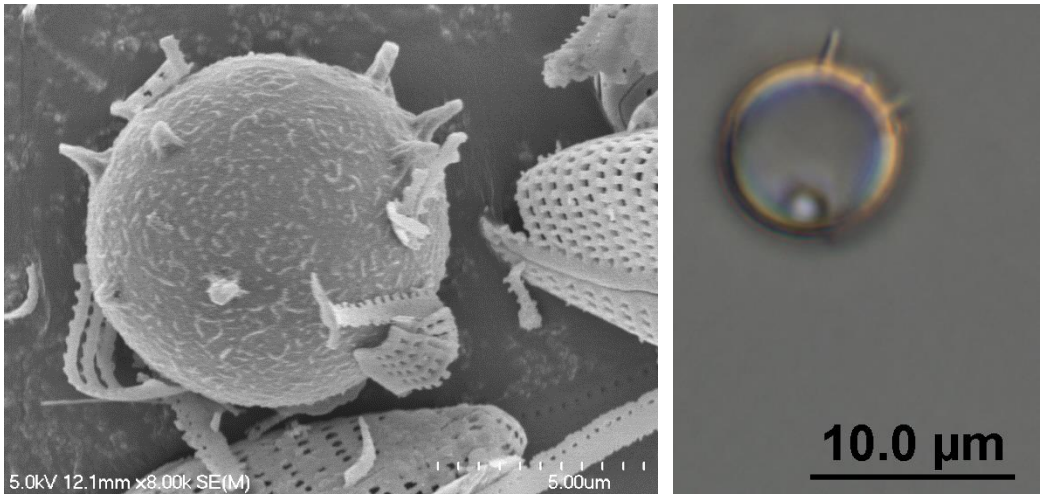

Figure 2.12: Scanning electron microscope (SEM) (left) and differential interference contrast (DIC) light microscope (LM) (right) images of an unassigned spined chrysophycean cyst found in HMC M1-2 lake sediments (this study).

Chrysophytes are typically found in oligotrophic and somewhat acidic lakes, often in cold environments or unpredictable climates (Zeeb & Smol, 2002). A decrease in cyst abundance vs diatoms as lakes become eutrophic has been used to infer that chrysophyte algae are poor competitors in high nutrient environments (Zeeb & Smol, 2002). Much research involving cysts has been in Arctic, Antarctic, and alpine lakes and ponds (Zeeb & Smol, 2002). For example, Kamenik and Schmidt (2005) related the dates of ice break-up and spring mixing in alpine lakes with changes in cyst assemblages, and correlated the timing of cyst assemblage changes to glacial advances. However, some work has involved cysts in tropical climates such as lake sediments in Costa Rican (Zeeb *et al.*, 1996), a Caribbean mangrove swamp (Rull & Vegas-Vilarrúbia, 2000), and an African thermal spring (Piątek *et al.*, 2009).

The mainly-planktonic algae will sometimes form stratified populations at depth (Smol, 1988). The presence of cysts in individual bands of laminated sediments has been used as evidence of annual autumnal deposition of varved sediments (Smol, 1988).

Rybak *et al.* (1991) surveyed 50 lakes in Ontario to equate groups of cyst morphotypes with lake water characteristics. The data showed that alkalinity (and pH) and trophic status were the main factors determining cyst morphotype assemblages (Rybak *et al.*, 1991). The study also noted that identification of cyst morphotypes requires considerable taxonomic expertise, and misidentification of

cyst morphotypes may be one of the largest sources of error in analyses involving fossil cysts (Rybak *et al.*, 1991).

Freshwater Sponge Spicules as Palaeoenvironmental Indicators

Freshwater sponge species are exclusive to the order Spongillida of the class Demospongiae, characterised by the use of silica in the formation of skeletal components, similar to the way diatoms use silica to form frustules (Penney & Racek, 1968; Frost, 2002). As such, sponge spicules, or scleres, are typically well preserved in lacustrine sediments (Cohen, 2003). Manconi and Pronzato (2002) provide a comprehensive review of the freshwater Spongellidae family.

There are three main types of spicules for freshwater sponges. Megascleres are the largest skeletal components of sponges (from ~100-450 μm long) and provide sponges with structure (Frost, 2002). Megascleres can be smooth or spined, with pointed or blunt apices (Frost, 2002). Microscleres are skeletal components of similar form to megascleres but are of smaller size (~8-130 μm long) and act to stiffen the sponge structure (Frost, 2002). Gemmuloscleres are specialised spicules that are typically smaller and often dumbbell-shaped, and, in life, are assembled closely together to form a gemmule (Cohen, 2003). A gemmule is an asexual reproductive structure that is often generated when the sponge is under environmental stress such as under conditions of hot temperatures or desiccation (Frost, 2002). In describing the value of spicules in palaeolimnological studies, Harrison (1988) emphasised that identification of sponges to species-level was the ideal. Gemmuloscleres are most valuable for taxonomic identification of sponges as they exhibit the most morphological differentiation between species (Harrison, 1988; Cohen, 2003).

Harrison (1988) and Poirrier (1969) grouped freshwater sponges based on their tolerance for conditions such as lentic or lotic habitat, light intensity, pH, siltation, bicarbonate concentration, and conductivity. Harrison (1988) has also equated the absence of photophilic sponge spicules in a lake sediment core to overgrowths of macrophytes shading the benthic littoral zone.

Cumming *et al.* (1993) surveyed sponge spicules and chrysophycean cysts in a variety of lake water conditions to assess their viability as indicators of lacustrine salinity. Sponges in the survey had little tolerance for salinity and were rarely found in lakes in which salinity exceeded 1 gL^{-1} (Cumming *et al.*, 1993). Sponge spicules have been used to track meandering river channel migration in the Holocene in Brazil, by the lentic or lotic preferences of sponge species found in a floodplain sediment core (Kuerten *et al.*, 2013).

Chapter 3

Methods

This chapter details the steps taken to acquire and preserve the HMC core, and describes how the core sections were prepared for MS, density, spectrophotometric analyses and digital imaging on the Geotek MSCL. It then specifies the work done to manually survey the core splits, develop an age-depth model using lamina-couplet thickness measurements, and collect small core samples at ~20 cm intervals to be processed for FTIRS and BioSi wet chemistry compositional analyses. Finally, this chapter presents the methods used to isolate the biosiliceous microfossils and determine their species assemblage and abundance information throughout the core.

3.1 Core Acquisition and Preparation for Analysis

3.1.1 Drilling

Drilling in the Hindon Maar Complex took place in July and November 2016 by three graduate students (F. Garrity, C. Murphy, and myself) and our academic supervisor, Dr Bethany Fox. Both campaigns utilised the University of Waikato's trailer-mounted hydraulically-operated rotary drilling rig, originally designed and equipped to reach 30 m depth in non-lithified sediment (Figure 3.1).

Figure 3.1: The University of Waikato "Lone Star" rotary drilling rig.

In the first campaign (July 2016) we used a rotary hollow-flight auger system with an SPT-type (standard penetration test) percussion sampling method (a 140 lb hammer). The method was largely unsuccessful as fine wet sediments (lake sediments or clayey silt soils) agglomerated in the auger flights and would not allow the flights to transfer sediments to the surface. The sampling method using the SPT percussion hammer was also an issue, as it was unable to penetrate the compacted lake sediments at greater depths. Some core was retrieved (sum total of ~11 m from four drilling sites, maximum depth of ~10 m) but we were unable to achieve our goal of drilling to the full depth capability of the rig.

Prior to the second campaign (November 2016), the drill rig was heavily modified to operate as a direct circulating-mud rotary drilling system with an inner continuous core-sampling barrel. The drilling system uses rotating hollow rods with an annular drill bit on the end, with drilling fluid pumped down the inside of the drill rods and out through ports at the end of the drill bit. The drilling fluid keeps the drill bit cool and transports the cuttings back to the surface through the annular space between the outside of the drill rods and the sides of the drill hole (Figure 3.2).

Figure 3.2: Assembling the hollow rotary drill outer tube assembly (drill bit not yet installed). Note angled outer processes (bottom of photo), which create slightly wider hole diameter for space between the outer diameter of the drill rods and the drill hole to return mud and cuttings to the surface. Photo includes N. Bates (author, left), F. Garrity (centre), and C. Murphy (right). Photo by Dr B. Fox.

The HMC November 2016 drilling campaign succeeded in acquiring two cores of lake sediments through to the basal sediments, as well as four cores of shallower penetration that were either of poor quality (highly fragmented or missing core intervals, collected while learning the new drilling method) or did not intersect lake sediments. The viscosity of the industry-grade drilling mud was excess to the requirements of the lake sediments (and was washing core away), so farm service water was successfully utilised instead. The pH and hardness of the drilling mud and the water was tested in the field with paper test-strips. The hardness for both was 35 ppm, while the pH was ~9 for the mud vs ~5 for the service water.

The cores were field labelled according to the drilling sites from which they were acquired (Figure 3.3), using the following nomenclature: HMN M1-2 = Hindon Maar November, Maar #1, Drilling site #2 (this study). For this study I have altered the HMN prefix to HMC, for Hindon Maar Complex.

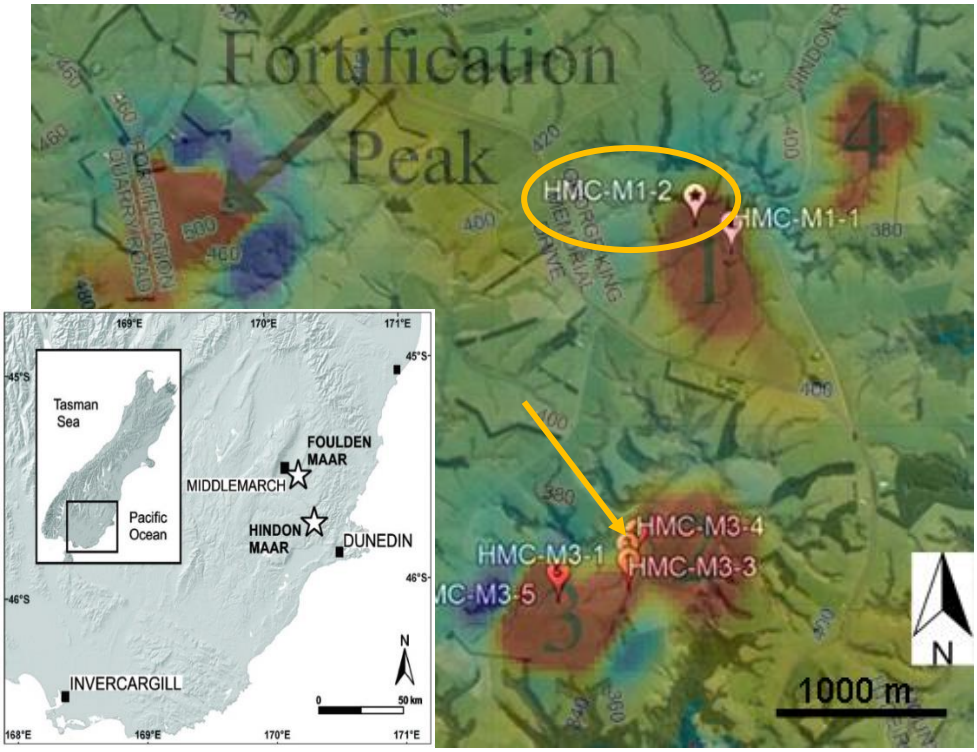

Figure 3.3: November 2016 drilling locations in the HMC; oval around HMC M1-2 core location for this study; arrow showing HMC M3-3 core location for concurrent study by Garrity (2017) (adapted from Google Earth; Bowie, 2015; Kaulfuss & Moulds, 2015).

During the drilling process, the core sample collection barrel would retrieve 1.5 m lengths of core 63.5 mm in diameter. At the bottom of the continuous core sampling barrel is an 8 cm-long cylindrical cutting shoe called a core catcher. Intervals of core were transferred from the sample barrel to longitudinally-split 65 mm OD PVC liners cut to ~1.0 m lengths. The contents of the core catcher were rarely retrieved intact, so they were placed in labelled plastic sample bags and stored with their associated core sections, either inside the liner or in the storage box. The core

sample liner sections were labelled with estimated field depths and core observations were written in a field log book. The core sections were placed in thick-walled flexible plastic tubing, heat-sealed shut, labelled, and placed in corrugated cardboard core boxes. The core boxes were stored at ~2-4°C in the University of Otago core storage refrigerator at the earliest opportunity.

3.1.2 Core Preparation for Analyses

The HMC core samples remained in the University of Otago core storage refrigerator until mid-January 2017, when F. Garrity and I were scheduled to conduct Geotek analyses. Whole core analysis was initially performed on the core sections (magnetic susceptibility and gamma attenuation density). With little variation in the lake sediments and the whole core sections surrounded with mm-scale mud-coating, the whole core Geotek data is deemed to be of nominal value.

I then split the core sections lengthwise using the University of Otago core splitting saw (a modified wet tile-cutting rotary saw) at the Sawyer's Bay facility a few kilometres north of the University campus. Because our core diameter didn't quite fit supports on the saw table, the resulting core splits were not perfectly bisected. Thickness at one end was often different than the thickness at the opposite end (Figure 3.4). Some core sections also had inter-core thickness (CT) discrepancies (Figure 3.5). Intact core-catcher samples that had been bagged and placed in the liners in the field were split in place.

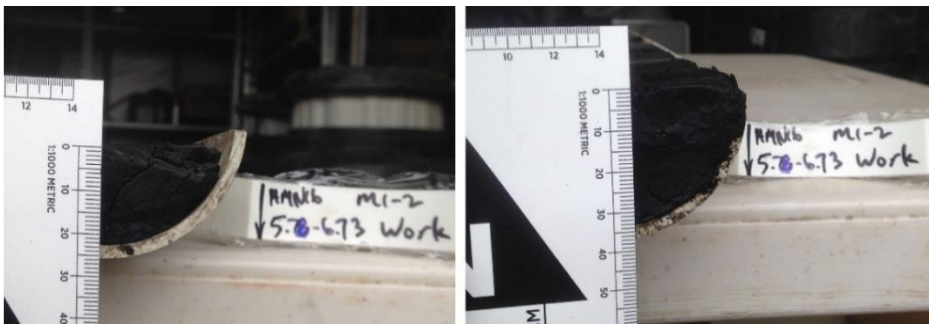

Figure 3.4: Differential core thickness (CT) of HMC M1-2 Core Section #6 from one end to the other after splitting with core saw. CT on left is ~23 mm; CT on right is ~33 mm.

Figure 3.5: Example of uneven core split surface within a HMC M3-3 core section.

The core saw left shredded PVC and thick muddy cuttings of core material on the core split faces. I gently washed the PVC debris and mud off of the core split surfaces with low-pressure potable water and a small (~30 mm-wide) paint brush. I drained the core splits of excess water taken on by the washing process, then double-wrapped them with cling film. The core splits were individually labelled “Work” and “Archive”, then heat-sealed in labelled thick-walled plastic tubing, and placed in two-tiered core storage boxes.

Once the split core Geotek analyses were complete, the core sections were re-wrapped as described above, shipped to the University of Waikato, and stored at ~2-4°C in the University of Waikato core storage refrigerator.

3.2 Physical Property Analyses

3.2.1 Geotek Analyses

The Geotek Multi-Sensor Core Logger (MSCL) used in this study is shown in Figure 3.6, as it is installed at the Department of Geology at the University of Otago. Core splits are advanced along the rails from right to left via the core pusher as they undergo analysis by the instruments attached to the core logger. The core pusher is under computer control in concert with a laser sight so that precise length measurements can be recorded.

It was vital to the accuracy of core length and thickness measurements that the rails, pusher, and the ends and bottom of the PVC core liners be kept clean of sediment and mud build-up. The cleanliness of these components was assessed at the addition of each core section.

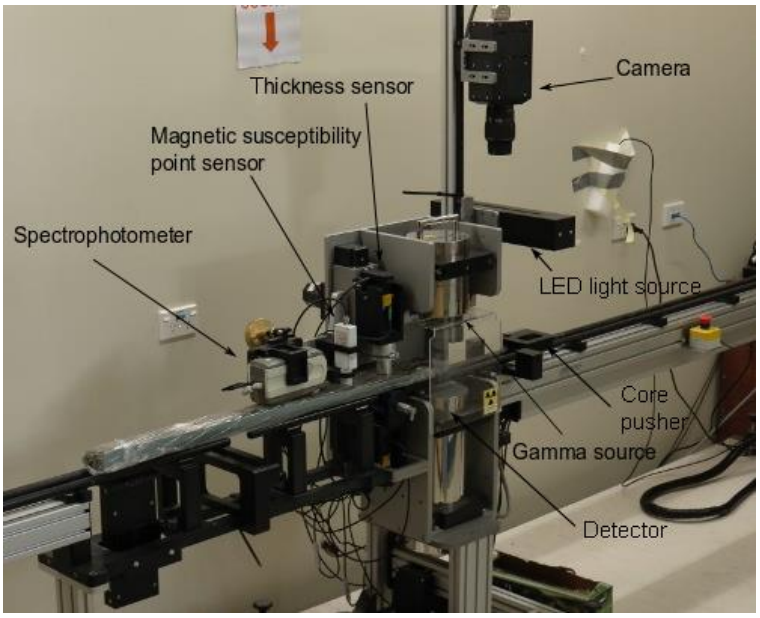

Figure 3.6: Overview of the Geotek MSCL and its analysis instruments, at the Department of Geology at the University of Otago (adapted from Fox, 2014)

Prior to scanning, a visual core description and sketch was done for each core section (on hardcopy). Magnetic susceptibility (MS), gamma attenuation density (GAD), and CIE L*a*b* spectrophotometry data were collected at 0.5 cm intervals. RGB digital imaging was done at 50 μm intervals. The MS, core thickness, and spectrophotometer instruments are all mounted on an armature (the Z motor assembly) that moves vertically to place the instruments against the core split surface during analysis. All Geotek core analysis activities plus the visual core description notes were recorded in digital log spreadsheets (3.2.1 in Appendix).

Magnetic Susceptibility

MS measurements are sensitive to changes in temperature (Geotek, 2012). For this reason, core splits were brought into the Geotek room and left with the core storage box lids removed for ~24 hours before they were scheduled to be analysed so that their temperature would equilibrate with that of the room. The Geotek instruments were also started immediately at the start of the day to allow them time to stabilise for ~15 minutes while the gamma attenuation density calibration was being performed (see Gamma Attenuation Density below).

MS measurements on core splits are done as a point measurement by inducing a low intensity magnetic field directly at the core split surface (Geotek, 2012). The magnetic field was applied by an oscillator circuit within a Bartington point sensor (MS2E) which produces a low-intensity 2 kHz alternating magnetic field (Figure 3.6) (Geotek, 2012). The response of any magnetically-susceptible material within a ~1 cm-range of the point sensor will change the oscillator frequency, which is translated into a MS value by the instrument (Geotek, 2012).

The MS point sensor would occasionally become slightly contaminated after being in contact with soft sediments. Diligence and care was taken to wipe the sensor as necessary. The HMC M1-2 lake sediments were firm and were not prone to transfer material onto the sensor.

Gamma Attenuation Density

The lake sediment core splits were placed on the Geotek between the lead-shielded gamma ray source and lead-shielded proton detector to determine the bulk GAD of the material (Figure 3.6) (Geotek, 2012). The gamma ray source is a 10 milli-curie Caesium-137 capsule that emits energy at 0.662 MeV (Geotek, 2012). Gamma rays are focused into a beam through a collimator set at 2.5 or 5.0 mm diameter (we used 5.0 mm for this study) (Geotek, 2012). The detector consists of a scintillator (a crystal that emits flashes of light when protons are incident upon it)

and an integral photomultiplier tube that amplifies the scintillator emissions and converts them into electronic pulses (Geotek, 2012).

To determine the bulk density of a material, the gamma ray beam of known diameter and known energy emits protons at a known flux through the sample material (Geotek, 2012). Any protons not scattered by interactions with electrons in the sample material are sensed by the detector (Geotek, 2012). The detector unit generates electronic pulses that are continuously sent to a counter, the period and rate of which are inversely proportional to the bulk density of the sample (Geotek, 2012). The Geotek software uses the count period and rate to calculate bulk density values in g/cc (grams per cubic cm).

Caesium has a relatively short half-life (30.2 years), and the decay in radioactivity is measurable by the detector unit even over short time intervals (Geotek, 2012). For this reason, a calibration sequence was performed at the beginning (AM) and end (PM) of every day in which GAD analysis was carried out.

A diagram of the calibration section is shown in Figure 3.7. It is housed inside a tube of the same material and wall thickness as the core split liners (in this case, 3 mm-thick PVC) to mirror the scatter-effect of the sample. Inside the tube is a 'stepped' aluminium block of various known thicknesses. We first filled the calibration section about halfway with water to reflect saturated bulk core split sample.

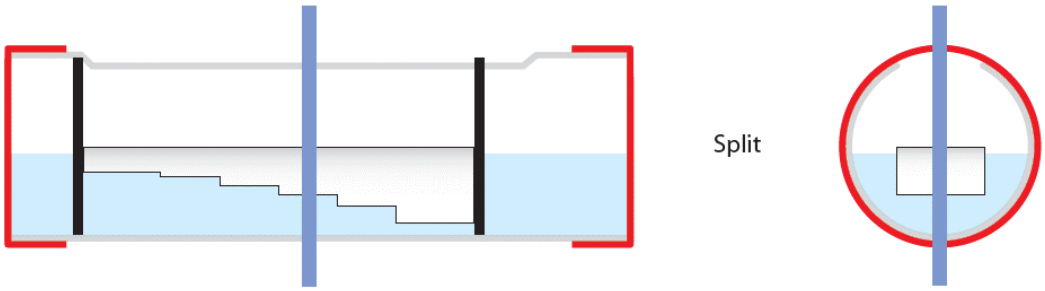

Figure 3.7: GAD calibration section, filled with enough water (blue) to evacuate all air from underneath the aluminium calibration block (Geotek, 2012).

We placed the calibration section on the Geotek rails with the thickest section of the stepped aluminium block positioned between the gamma ray source and the detector. We then opened the collimator from the source and recorded the counts registered across three intervals of 30 seconds for each step-thickness of the aluminium block. The mean counts for each thickness were plotted as an average thickness*density vs the natural log of the detected counts per second (Figure 3.8) (Geotek, 2012). The x^2, x, and y-intercept coefficients in the AM and PM calibration graphs (equated to A, B, and C in the inset box) were averaged and entered into

the Geotek processing panel so that the Geotek software could make the necessary adjustments to the data.

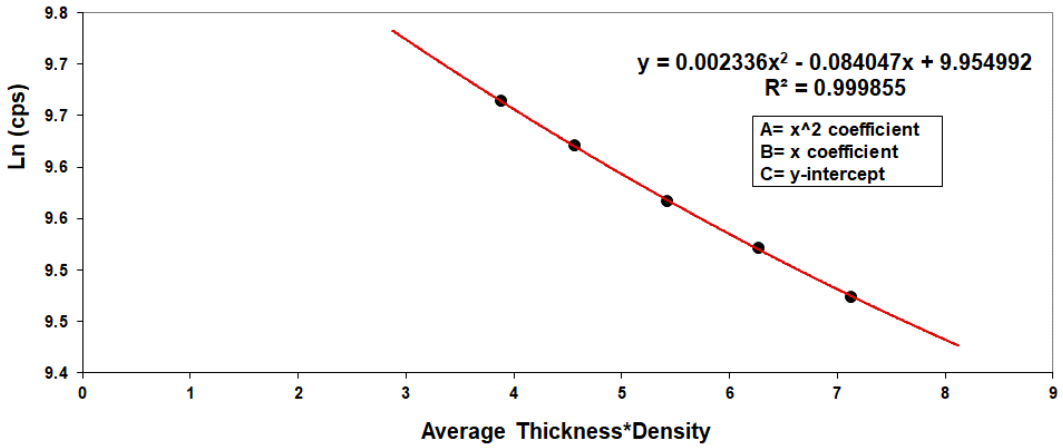

Figure 3.8: GAD calibration plot from HMC M1-2, Core Sections #1-9 (this study).

The GAD calculation requires the thickness of the core split sample at each measurement. A core thickness (CT) measurement instrument is fastened to the Z motor assembly that lowers and raises the instruments over the core split surface. As with the MS sensor, at times the tip of the CT instrument that contacts the core split surfaces would require a wipe to clean residue off of it.

The CT instrument also required calibration for each Geotek session. A calibration sequence would be initiated once a plastic cylinder of known diameter was placed on the Geotek rails under the CT instrument. On at least three occasions I mistakenly calibrated the CT instrument against core split surfaces rather than the plastic cylinder. Once the issue was recognised, the core split sections that were used for the CT calibrations were measured with a scaled-calliper at the core interval originally used. The measurements were recorded in the Geotek log file so that they could be used for the corresponding core split sections during data processing (3.2.1 in Appendix). None of the known CT calibration issues are associated with the HMC M1-2 lake sediments in this study.

*CIE L*a*b* Reflectance Spectrophotometry*

The Geotek spectrophotometer is a Konica Minolta CM2600D model (Geotek, 2012). It was supplied with an 8 mm diameter 'mask' over the aperture to isolate the desired area for measurement (Geotek, 2012). The spectrophotometer is mounted to the Z motor assembly (Figure 3.6). The aperture of the spectrophotometer is placed on the surface of the core splits to consistently manage the illumination it emits against the core split surface as it performs its analysis (Geotek, 2012). Light wavelengths from 360-740 nm can be detected by

the spectrophotometer (slightly into the ultraviolet and infrared ranges beyond the light range of 400-700 nm visible to humans) (Geotek, 2012).

The spectrophotometer must first be calibrated before use. A zero calibration is done with nothing under the aperture. A white (high) calibration is done with a calibration cap installed over the aperture, and a Z motor assembly calibration is done to ensure the aperture is able to make contact with core split surfaces as they vary in height. At times the core split surface height was below the range of the Z motor assembly and the aperture was not in contact with the core split face. Spectrophotometer data at those isolated areas was deleted during the data reduction phase (see Core Surveys and Data Reduction, below).

At each sample location, the spectrophotometer emits three flashes from separate xenon light sources at different angles to the core split surface in order to measure light in the diffuse 'back-scattered' spectrum, specular 'reflected' spectrum (gloss, shine), and the ultraviolet spectrum (Geotek, 2012). The Geotek software can display the spectral data in several colour systems. We chose the L*a*b* colour coordinate system as it is meant to represent how the human eye perceives colour. Henceforth, the L*a*b* suite is referred to as reflectance, L* is luminosity, while the a* and b* data are hues.

High-Resolution RGB Imaging

A line-scan camera and light bar are mounted on the Geotek MSCL directly above the rail to the right of the gamma ray source (Figure 3.6). Light that enters the camera lens goes through a beam splitter (Geotek, 2012). The beam splitter separates the light into three paths which then pass through a dichroic colour interference filter (Geotek, 2012). The filter ensures there is minimal overlap between the three split beams (Geotek, 2012). The beams then fall upon red, green and blue (RGB) detectors (Geotek, 2012). The camera uses three separate high-resolution (2048 pixel) charge-coupled devices (CCDs) to individually capture the RGB spectra (Geotek, 2012). The actions of the camera and the laser-sighted core pusher are coordinated by the Geotek to digitally construct high resolution images of 200 pixels/cm (or 50 μm/pixel) with sufficient precision down the length of the core that a scale can be digitally added to each core image afterwards (Figure 3.9) (Geotek, 2012).

The height of the camera and light bar are individually adjustable so that the depth of field and light intensity can be optimised for core split sections of different colours and surface textures. The colour balance on the camera is set by first placing a white calibration tile on the core split surface directly under the camera and

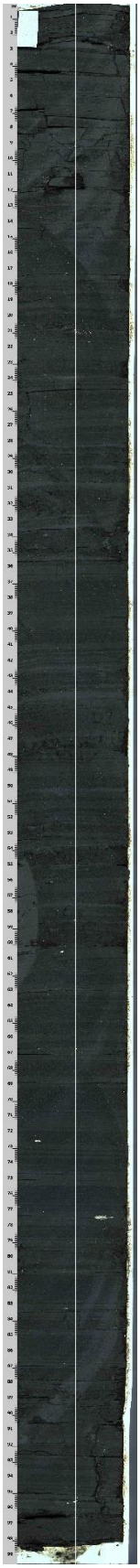

Figure 3.9: HMC M1-2 Core Section #8, with cm-scale at left.

adjusting the lens focus, aperture size and exposure time, and light bar intensity and height to maximise the RGB signals at the CCDs (Geotek, 2012). Then the dark balance is set with the lens cap installed on the camera (Geotek, 2012).

We partitioned the core sections from our six drill cores into groups of similar colours (e.g. “Black Cores”: dark lake sediments, “Blue-grey cores”: basal micaceous sandy silts) to minimise the lighting adjustments that would be required if the length of each drill core was analysed separately. For the dark HMC lake sediments, it was necessary to have the light bar at maximum intensity and lowered close to the core so that enough light would reflect from the core split surface to the RGB detectors in the camera.

The width of the high resolution images was digitally cropped to just outside of the outer edge of the core split liner. The core split surface width selected to determine RGB values was digitally constrained to ~3-4 cm across the longitudinal centre of the 6.35 cm-wide core split, avoiding the ‘core drag’ and disruption at the outer edges. A small piece of 18%-grey tape was placed at the top left of each core split section so that they images may later be correlated to others, but the light intensity that was required left the tape ‘washed out’ (Figure 3.9). Afterwards, cm-scales were digitally added to the left margin of each core split section image, beginning with zero at the top of each section (3.2.1 in Appendix).

Core Surveys and Data Reduction

I surveyed high resolution digital images of the HMC M1-2 lake sediment core splits at 1 mm intervals. I first used Microsoft Paint to add a line down the centre of each core split image (Figure 3.9). The Paint software displays the cursor position on a vertical ruler next to the image, beside the cm-scale that had previously been digitally-added to the left margin of the image. The cursor was moved down the centreline one millimetre at a time, and core attributes present at that interval (e.g. black/dark laminae, light laminae, dark homogeneous sediments, missing core, drilling mud injection into gaps in core, etc.) would be marked in a

spreadsheet cell as ‘1’ if present and left empty if not present (3.2.1 in Appendix).

The sum of the Geotek data were converted to an Excel file, to which was added the results from the core attribute surveys of the HMC M1-2 lake sediments. Data was discarded at depths in which missing core, gaps, or drilling mud injections were identified in the surveys. Intervals were inserted into the data spreadsheet to represent the length of the contents of the core catcher at drill rod breaks (recall at end of 3.1.1 Drilling). All data reduction and subsequent data analysis use this composite Geotek/core split survey data spreadsheet as a source (3.2.1 in Appendix).

I created the depth model by correlating the field notes and the drilling rig depths with the equivalent core section intervals in the composite Geotek/core split survey data. The depths are reported hereafter as metres composite depth (mcd).

Data for each Geotek analysis dataset were compared to the associated core split images. Data were excised adjacent to core termini, mud injections, or cracks and gaps where it was seen to have affected the results. Some colour data were also discarded where the spectrophotometer was not in contact with the core split surface during the analysis due to low local relief of the core split surface (e.g. Figure 3.5).

Initial plots of the density results showed a large deviation at ~10.5 mcd. This depth corresponds to a core section break. The density calculation is dependent on the Geotek core thickness measurement, and the CT measurement deviated at that depth as well (Figure 3.10).

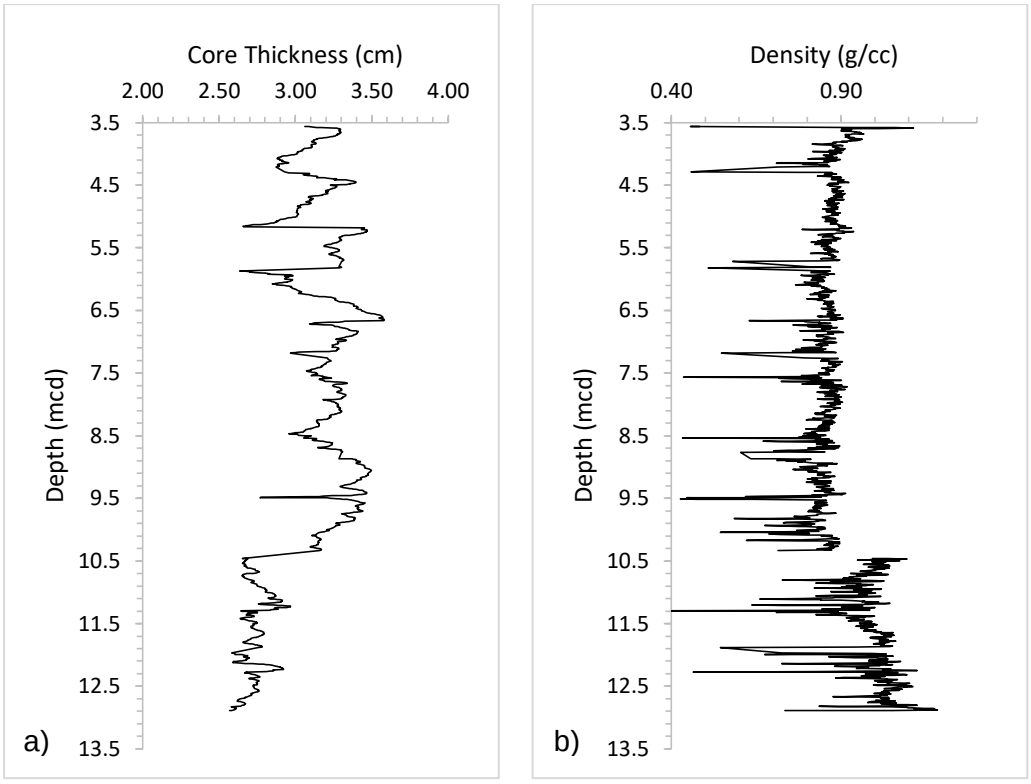

Figure 3.10: Original data for; a) core thickness; b) density, prior to data reduction.

The Geotek analysis log shows that all data above 10.5 mcd (8 core sections) were acquired in one session while all data below 10.5 mcd (3 core sections) were acquired in a later one. I unwrapped 4 core sections from the first session and 2 core sections from the second session. I borrowed a precision digital calliper from the Physics department, accurate to 0.01 mm, to measure the core split thicknesses in two locations on each of the 6 core sections. I subtracted the thickness of the PVC core liner (3 mm) from the measurement (as is done in the Geotek CT data processing). Core sections from the first session consistently measured thickness values that were an average of 0.315 cm lower than the Geotek measurements. Conversely, core sections from the second session consistently measured an average of 0.360 cm higher than the Geotek measurements. Each of those average values was then applied to their respective core sections as an adjustment factor for all CT data. At the intervals where the core sections had been measured with the digital calliper, the recalculated CT measurements were typically within ~0.04 cm (range of 0.003 to 0.09 cm) of the digital calliper measurements.

The Geotek density data was reprocessed with the aforementioned CT adjustments (Figure 3.11). The transition from the core break at ~10.5 mcd is much less prevalent, and the data trends match across the transition (density increasing from below 10.5 mcd to above). Hence, this study employs the data acquired by using the adjusted CT values.

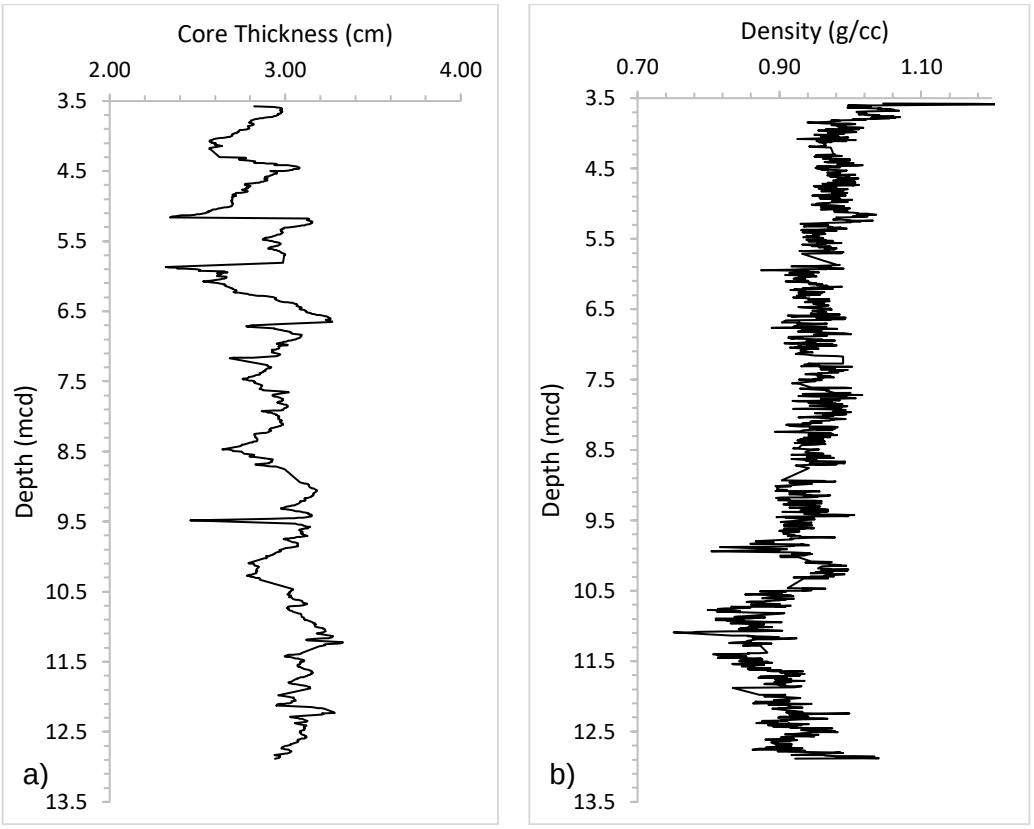

Figure 3.11: Adjusted data for; a) core thickness; b) density, after data reduction.

3.2.2 Lamina-couplet Thickness

I undertook a lamina thickness survey to develop an age-depth model for the duration of the lake sediment deposit. One ~3.5-5.5 cm sample was excised from each of the 11 working core halves of HMC M1-2 lake sediments with a cylindrical soil-sampling ring. Each sample was taken from an interval of laminated core that was uninterrupted by mud injections or other disruptions. The sample thickness was immediately measured with a digital calliper accurate to 0.01 mm.

I had previously observed that laminae were much more visible when core samples were dry. Consequently, I dried the samples at 50°C for a minimum of 24 hours. Assuming the laminae were indicative of a seasonal or annual deposition pattern, they were counted and were recorded as a number of lamina-couplets. The pre-measured length of each corresponding sample was divided by the lamina-couplet count to arrive at an average mm/couplet-value which was then assumed to be characteristic for that section of core. The mm/couplet value for each of the 11 core sections was recorded on an Excel spreadsheet, from which calculations were made to estimate the total time of the HMC M1-2 lake sediment deposition (3.2.2 in Appendix).

Some of the digital core split images showed evidence of turbidite deposits. Turbidites are mass flows of material into the core sample area and do not

represent background sedimentation which normally contributes to the laminated bedding in the deposit. In total, 13 turbidites were observed and their depth contribution was subtracted from the total prior to calculating the age-depth model figures.

3.2.3 Collecting Core Samples

Lake sediments comprise ~10 m of the ~18.5 m HMC M1-2 drill core. In consultation with Dr B. Fox, I took core samples every ~20 cm for a total of 51 samples. The samples were extracted from undisrupted core segments, and care was taken to avoid including drilling mud-injection gaps, or cuttings residue which was common at the outer circumference of the core. A razor blade was used to make two parallel slices perpendicular to the laminae (i.e. along the core length) ~10 mm long and ~10 mm apart. A flat-bladed screwdriver was then used to lever out a block of core ~8 mm deep (~0.8 cm^3). Each sample was sealed in a sample bag labelled with a unique sample number and an estimated field depth. The razor blade and screwdriver tip were rinsed with distilled water and wiped with a clean paper towel between every sample to avoid cross-contamination. Also, the razor and screwdriver blades cut the laminae best when they were pre-wetted with distilled water just before use. The 51 samples were placed in a sample storage refrigerator kept at 2-4°C until required for analyses.

3.2.4 Composition

FTIRS

Fourier transform infrared spectroscopy, as described in Section 2.5 Composition, was undertaken by my colleague, F. Garrity, on similar lake sediments from HMC Maar #3 with some promising results. Under Garrity's tutelage, I undertook this analysis as well.

Samples for the FTIR spectrometer are wafer-shaped pellets prepared from a measure of finely ground sample combined with a measure of spectroscopic-grade potassium bromide (KBr) (Meyer-Jacob *et al.*, 2014b). Both components are oven dried prior to sample preparation (Meyer-Jacob *et al.*, 2014b).

F. Garrity found that the dark lake sediment samples prepared at the sample:KBr mass amount specified by the normal IR procedure (10:100 mg) generated results that were off-scale low. This was due to the high absorbance of the dark lake sediments, which left low intensities of IR light reaching the detector. This has occurred in another study with similar sediments (Meyer-Jacob *et al.*, 2014b). It was necessary to decrease the sample:KBr ratio by reducing the sample mass

from 10 mg to 1 mg. When combined with 100 mg of KBr, the sample:KBr ratio = 0.01.

I homogenised ~30 mg of each oven-dried sample with a mortar and pestle, cleaning the equipment with ethanol between samples. Then 1 mg aliquots were carefully weighed out, and 100 mg of KBr was added to each of the aliquots. The samples were kept in desiccators until they could be pelletised.

The sample and KBr powders are formed into pellets in a small hydraulic press. It is a technical exercise to successfully press an unblemished homogeneous pellet without it cracking or breaking on removal from the press, or being unevenly distributed. Figure 3.12 shows an example of a failed pellet attempt (left) and a successful one (right). Pellets that were not suitable were reground into powder with a mortar and pestle then re-pressed until an ideal pellet was formed.

Figure 3.12: HMC M1-2 sediments rendered into FTIRS pellets. NB16 is unsuitable while NB17 is ideal.

Biogenic Silica Wet Chemical Analysis

Biogenic silica (BioSi) wt% was determined by a long-employed alkaline BioSi-dissolution method (Figure 2.10) and carried out following the procedure developed by Mucciarone (2003). The procedure, as it was performed for this study, will be summarised here in brief.

For each daily sample cohort, two sets of 10 calibration standards were made. Each standard was measured thrice via a Shimadzu UV-1800 spectrophotometer. The readings were used to generate calibration curves against which the samples would be compared by linear regression. Values for the R^2-value (coefficient of determination) for the calibration curves used in my analyses ranged from 0.9998 to 1.0. In this analysis, the R^2-value is indicative of the accuracy of the pipetting technique.

The same 51 HMC M1-2 lake sediment samples used for the FTIRS analysis were used for this BioSi wet chemical analysis. The samples were oven-dried at 50°C for at least 24 hours, then manually homogenised into fine grains with a mortar and

pestle. For samples that had higher BioSi content according to the FTIRS analysis, 7.0±1.0 mg was measured for each. For the remaining samples, 10.0±1.0 mg was measured out. All BioSi samples were placed in labelled centrifuge tubes, to which 40 ml of 0.1 M NaOH alkaline solution was added to perform the BioSi digestion.

The samples were shaken and placed in a pre-heated hot water bath set at 85°C, and the time of immersion was recorded. The samples were agitated every 30 minutes then placed back in the hot water bath. After digesting for 2 hours (from time of initial immersion in the hot water bath), the samples were spun in a centrifuge at 4000 rpm for 3 minutes. A pipette was used to withdraw a 0.25 ml aliquot from each sample and add it to a vial. A total of 4.75 ml of Elix (deionised water) was added to each vial (total volume=5.0 ml). The sample centrifuge tubes were then re-agitated and placed back in the hot water bath. This process was repeated at the third and fourth hours of digestion while continuing to agitate the samples every 30 minutes.

Once all of the hourly aliquots had been taken, 2 ml of Molybdate reagent was added to each vial. After no less than 10 minutes but no more than 30 minutes, 3 ml of Reducing solution was added to each vial. The vials were capped, agitated, and left for 3 hours (Figure 3.13).

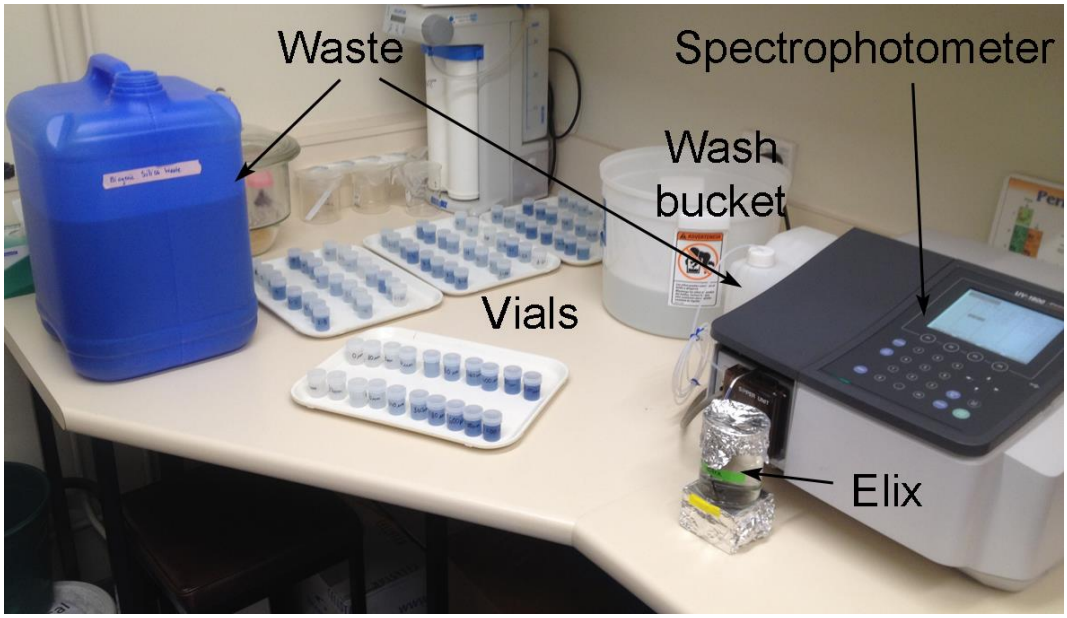

Figure 3.13: BioSi wet chemical digestion samples, waiting for analysis.

After 3 hours, each vial was analysed in turn via the Shimadzu UV-1800 spectrophotometer. The spectrophotometer uses a rotary positive-displacement pump to draw in a sample for analysis. Each vial was sampled three-to-four times, the results for each manually recorded on a readings sheet. Between each calibration and sample-hour set, the analyser was rinsed with copious volumes of Elix (Figure 3.13). The Elix rinse water was analysed to check the instrument for

drift. Rinse water tests were repeated until the analyser read at least three consecutive identical results. Any drift values (very slight drift was typical as analysis progressed) were recorded on the readings sheet.

Each analysis run of 24 included 3 replicates from that run, 2 replicates from a previous day's run, and 1 blank containing 0.1 M NaOH. The replicates allowed for inter- and intra-run comparisons. I endeavoured to include as many replicates as possible to ensure quality results.

Data reduction involved plotting all analysis results then discarding erroneous data. The remaining data as well as the mean and standard deviation for all test results for each sample are recorded in an Excel spreadsheet (3.2.4 in Appendix).

The HMC M1-2 lake sediments are known to host sponge spicules. Spicules are several magnitudes larger than diatom valves, with much lower surface-area-to-volume ratio. About midway through the analysis regime I was concerned that, even though the sediments had been crushed by mortar and pestle, the spicular biogenic opal may not fully dissolve during the alkaline digestion. The analysis was repeated with a 1.0 M NaOH solution on samples that had already been analysed using a 0.1 M NaOH solution. A comparison between the two results is shown below (Figure 3.14).

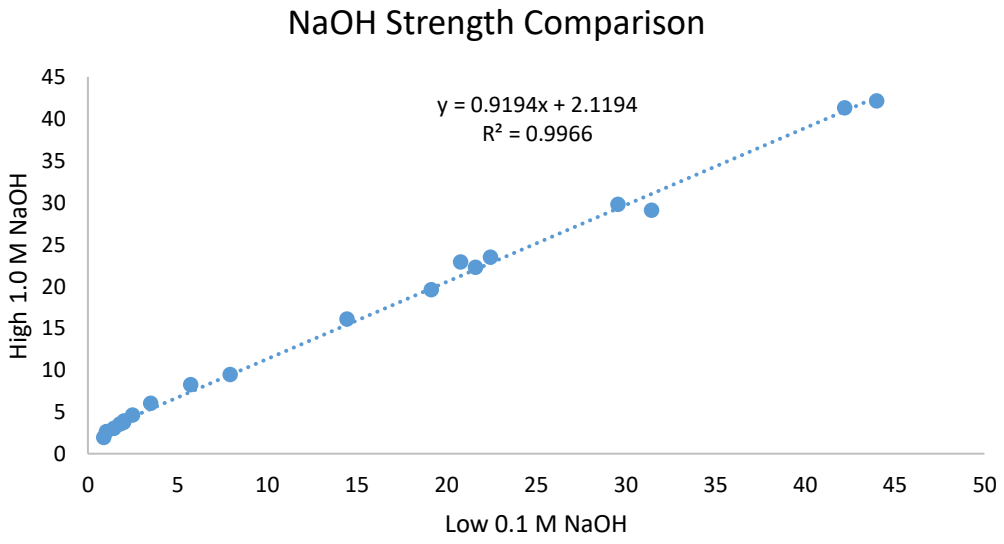

Figure 3.14: Cross-plot comparison of high strength 1.0 M NaOH vs low strength 0.1 M NaOH for digestion of BioSi in HMC M1-2 lake sediments.

Each data point in the cross-plot above is the BioSi wt% result from the high-strength and the low-strength digestion method for any specific sample. With a slope near 1 and an R^2-value of 0.9966 when plotted against each other, the difference between the high and low strength NaOH digestion solutions was not significant with respect to the BioSi wt% results. The decision was made to save

the trouble of working with and disposing of the high strength NaOH solution and continue as before. Homogenising the samples by mortar and pestle was an effective means of ensuring all biogenic silica was digested during the time allotted for in the procedure.

3.3 Biological Surveys

3.3.1 SEM Imagery

Scanning electron microscopy was undertaken to acquire high-quality, high magnification images of the suite of microfossils hosted by the HMC M1-2 lake sediments to aid in making positive species-level identifications. I used the Hitachi S-4700 cold field emission SEM at the University of Waikato, with the electron acceleration voltage set at 5.0 kV. Due to scheduling demand on the SEM, only an initial coarse survey was done on 10 unprocessed lake sediment samples at intervals ~1.0 m apart.

Dried samples were applied by a small spatula to double-sided tape on top of a 'stub' (~10 mm diameter). Each stub hosted two samples, one on a long strip of tape, one on a short strip (Figure 3.15). After the SEM technician coated the stubs with platinum in a vacuum, I surveyed the samples across the latitudinal midline of the stub, a path that bisected both samples across the middle. At a representative site for each sample an image was taken at 30x magnification, then at 250x magnification. After that, individual features (spicules, diatom valves, chrysophycean cysts) were sought out and imaged at magnifications that best captured the characteristics of the features.

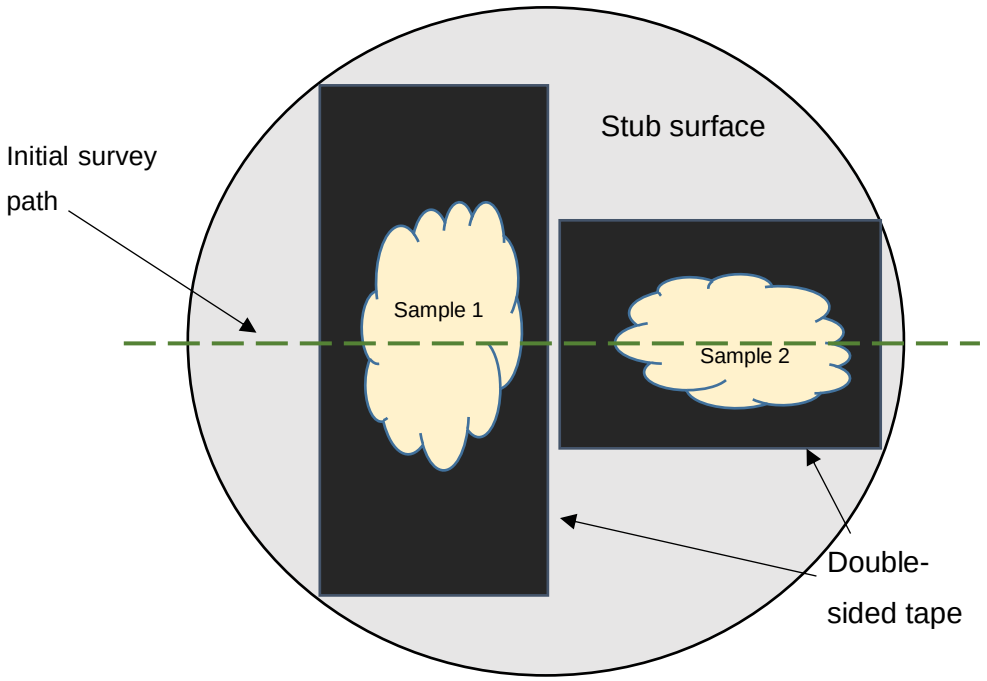

Figure 3.15: Sample set-up on top of ~10 mm diameter SEM stub.

SEM notes and survey results were summarised in an Excel spreadsheet. The spreadsheet and images from the surveys can be viewed in the 3.3.1 in Appendix.

3.3.2 Smear Slide Preparation

Several smear slide trials were conducted on two suites of samples during the course of this study. Sample suite 1 was the set of 10 lake sediment samples taken at ~1.0 m intervals that was employed in the SEM survey. It was also used to generate two investigatory smear slide trials meant to determine the sediment processing requirements for the HMC M1-2 lake deposit. As they were ultimately not the main source of data for this study they will not be discussed further, except to say that both surveys consistently showed that the top ~1/4 of the lake sediments had a high concentration of diatoms while the lower ~3/4 had a paucity of biosiliceous material, save sponge spicules at times. Observation notes and images taken down an ocular lens of a petrographic microscope are available in the 3.3.2 in Appendix.

Sample suite 2 was the set of 51 lake sediment samples taken at ~20 cm intervals. This suite was used for the FTIRS and BioSi wet chemical composition analyses, as well as the final high-resolution smear slide survey.

Some sediments from sample suite 2 were tested with 10% hydrochloric acid. The mixture was not reactive, so carbonates were deemed to be absent. The suite 1 smear slide surveys showed excessive organic material, so sample suite 2 sediments were treated with hydrogen peroxide (H_2O_2) to digest the organic matter.

Sample suite 2 was split into two groups (odd and even numbered) and processed at different times. For each of the odd-numbered samples, ~0.2 g was measured out on a digital scale and placed in a labelled glass 50 ml pottle (even-numbered samples that were processed later used 50% more sample: ~0.3 g, as there was only just enough biosiliceous material in some of the earlier odd-numbered samples). Without knowing the reactivity of these sediments in hydrogen peroxide, the H_2O_2 was added to the sample pottles in stages of increasing concentration, starting with 10 ml of 10% H_2O_2 in each. Reactivity was low, so the pottles were heated to increase the reaction rate (Figure 3.16). The optimal temperature to avoid excessive reactivity and frothing was found to be 60-65°C. The pottles were monitored often to ensure the pottles did not dry out, and they were manually agitated at every opportunity. H_2O_2 strength was eventually increased to 30%. Digestion was deemed to be complete when there was no evidence of foaming or bubbling of the mixture while heated.

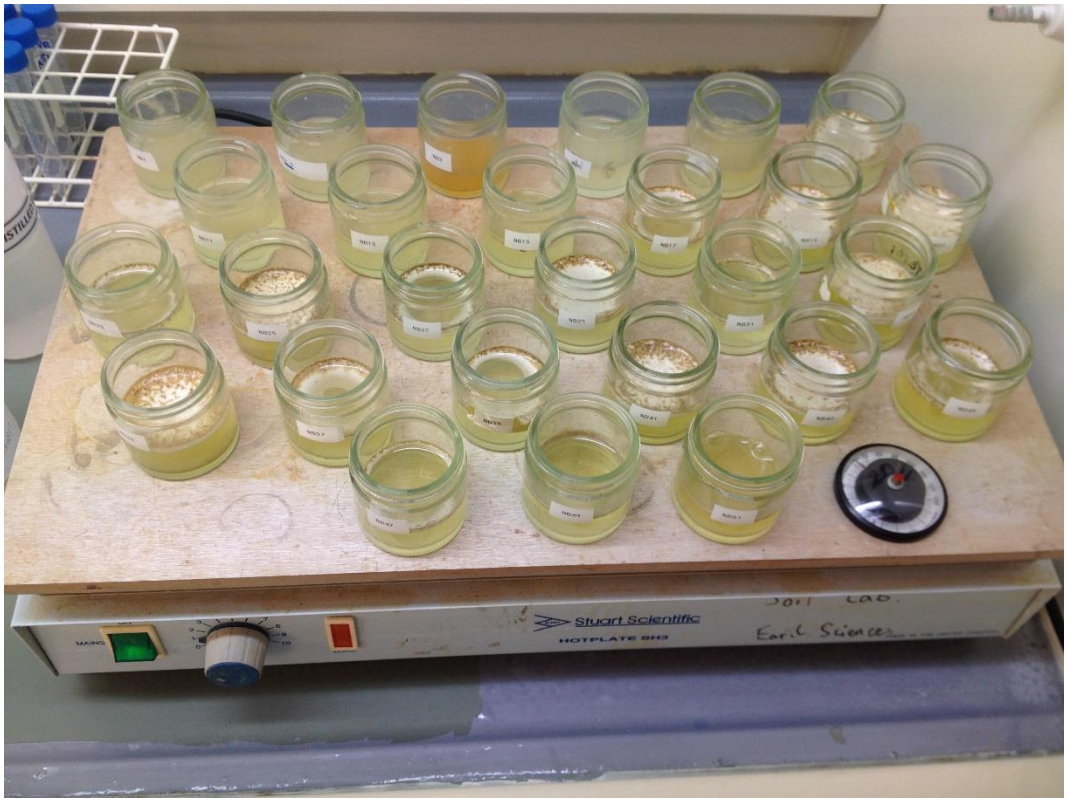

Figure 3.16: Hydrogen peroxide digestion of organics from the odd-numbered HMC M1-2 lake sediment samples, on a hot plate set at 60-65°C.

The contents of the pottles were decanted into labelled 15 ml Falcon tubes. Each Falcon tube was topped up to the 10 ml-mark with distilled water. They were spun in a centrifuge at 1500 rpm for 3 minutes, then disposable plastic 3-ml pipettes were used to extract as much of the supernatant as possible without agitating the biosiliceous material (Figure 3.17). The Falcon tubes were again filled to 10 ml with distilled water and manually agitated. The centrifuge/rinse process was repeated until it had been done a total of 4 times. Litmus paper test strips confirmed that the supernatant was ~6.0-6.5 pH. Water was extracted from the Falcon tubes until they were at the 4 ml level (even-numbered samples done later were left with 50% more volume; 6 ml).

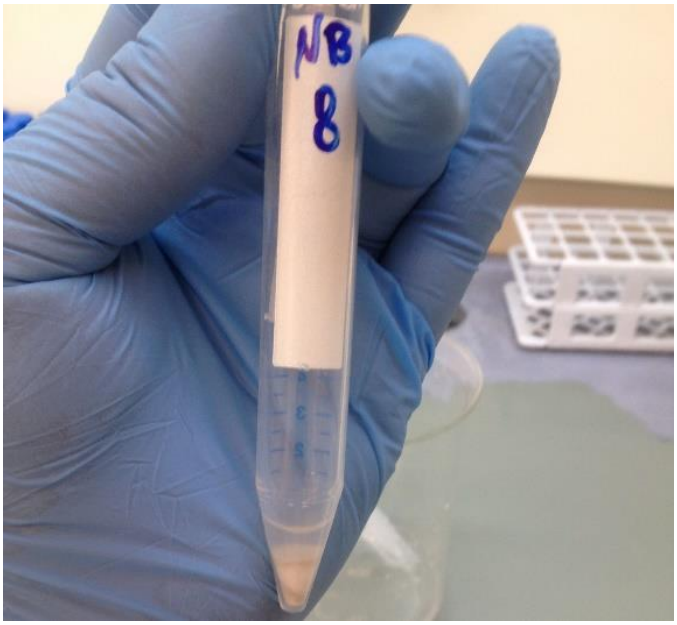

Figure 3.17: 15 ml Falcon tube with biosiliceous microfossils from Sample 8, post-digestion.

The preferred diatom concentration on the finished smear slides was 20-25 valves per field of view at 400x magnification (C. Riesselman, personal communication, August 17, 2017). The biosiliceous material at the bottom of the Falcon tubes was used in multiple trials and exploratory surveys to reach that concentration. The exploratory surveys revealed that the sediments had a diatom concentration demarcation between samples 16 and 17. Samples 17-51 could be used as they were in their Falcon tubes to make smear slides, while samples 1-16 required more dilution to achieve the ideal diatom valve/view concentration. Diluted 1-16 samples were created by first agitating the biosiliceous material in the Falcon tube with a disposable 3-ml pipette, then by adding one drop of the suspension into a new Falcon tube prefilled with 3 ml of distilled water. The diluted samples were labelled 1d-16d.

The diatom smear slides in this study were made by applying a suspension of biosiliceous material onto pre-treated 22x40 mm petrographic coverslips. A coverslip was pre-treated by first dipping it in an acid alcohol solution (1% HCl in ethanol) and gently blotting it with a fresh lint-free tissue to clean off oily residue. In early trials the diatom suspension would have a hydrophobic reaction when applied to the acid-dipped coverslips. The diatom suspension would draw up into a bubble and would not disperse across the coverslip surface. Consequently, I added a ‘distilled water rinse’ dip step which was successful in solving the hydrophobic issue. The final drying step avoided using tissues on the coverslip surface as lint had been noticed during microscopic survey trials on earlier slides. I held the coverslip vertically with forceps and wicked the distilled water off the

edge of the coverslip with a tissue, then used a Bunsen burner flame to carefully evaporate the remaining droplets.

To make a smear slide, I used a new disposable plastic 3-ml pipette to agitate the biosiliceous mixture in its Falcon tube until it was fully suspended, then drew in ~1 ml of mixture from within the suspension cloud. Before it had a chance to settle in the tip of the pipette, I released the desired number of drops onto the coverslip. I found that releasing the drops from a height of ~15-25 mm caused the drop to disperse evenly across the coverslip surface. Additional distribution on the coverslip was done with the tip of the pipette, after first emptying the excess back into the Falcon tube.

Diluted samples 1d-16d required 5 drops of the 3-ml diluted suspension on each coverslip. The undiluted samples 17-51 required 1 drop of the original suspension. To make surveys between these different concentrations comparable, a dilution factor was multiplied to the diluted 1d-16d survey results. I counted the number of drops it took to dispense 1 ml of suspension from a disposable plastic 3-ml pipette (22 drops), then applied that to the amount of the suspension that was used out of the 3 ml diluted suspension to arrive at a dilution factor of 13.2 (66 drops total/5 drops used). One exception is Sample 9d, from which the biosiliceous material was consumed during earlier trials. The 9d sample data is from an earlier trial slide made with 3 drops of suspension rather than 5. Its dilution factor is 22 (66 drops total/3 drops used). Consumption of the 9d sample during processing is the reason that I chose to increase the pre-digestion sample weight of the even-numbered samples which were done later. As stated above, the even-numbered cohort began digestion with samples of 50% greater mass than the earlier odd-numbered cohort (~0.3 g rather than ~0.2 g) and were stored in 50% more distilled water (6 ml rather than 4 ml).

Early attempts to quickly dry the suspension on the coverslips caused the water surface tension to draw the diatoms into a pile towards the centre of the droplet, making the slide unsuitable for surveying. The suspension was left overnight to dry on the coverslips placed in a plastic tray. The tray was covered with cling film to prevent dust from settling onto the coverslips. Two small vent holes were punched in the cling film at opposite ends of the tray so the moisture could evacuate from the tray. Once the coverslips were dry, the biosiliceous material was ‘stuck’ onto them by passing the back of the coverslip through a Bunsen burner flame three to four times.

Coverslips were mounted onto slides with Naphrax, a diatom-specific mountant with a high refractive index (minimum 1.74, vs ~1.5 for glass) to maximise the

contrast between the glass slide (silica) and the biosiliceous material. The slides were pre-treated with acid alcohol, then flame dried. The slides were preheated on a hotplate set at ~110°C. A glass-tipped rod was used to distribute a line of Naphrax along the middle of the long axis of the slide. A corner of a coverslip sample was rested on the slide, then the coverslip was dropped onto the Naphrax line with the biosiliceous suspension facing down. The coverslip was gently pressed to distribute the Naphrax across the warm slide and the entire underside of the coverslip, and to minimise the thickness of the Naphrax resin between the coverslip and the slide. The slide was then heated on the hotplate for 10-20 minutes to cure the Naphrax resin. Once the Naphrax had cured and cooled, the slide was ready for analysis.

3.3.3 DIC LM Imagery

The slide surveys were carried out using differential interference contrast light microscopy (DIC LM). DIC microscopy is an improvement over normal brightfield microscopy for viewing slides of unstained biosiliceous material because the technique enhances the features of the sample (Figure 3.18).

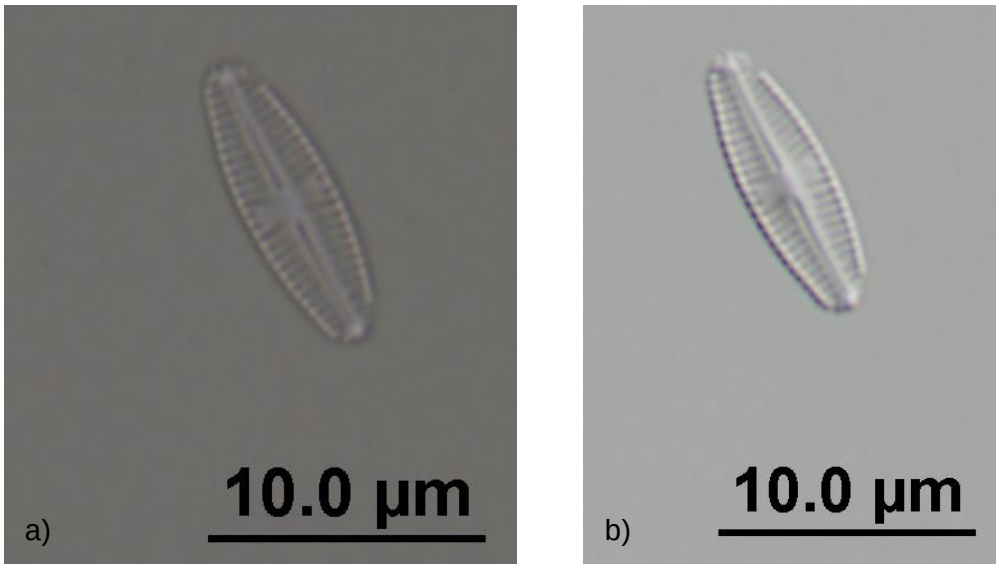

Figure 3.18: Identical view point in HMC M1-2, Sample 11: a) brightfield LM; b) DIC LM.

I used the Leica DMRE microscope in the Department of Biological Sciences at the University of Waikato. The microscope has a Leica DMRD camera system and imaging software integrated with it. I captured over 700 images between 100x and 1000x magnification, most of them at 400x magnification. They are available in the 3.3.3 in Appendix. The image file names reflect the sample number in the M1-2 lake sediments followed by an index number (E.g. image file name HMC M1-2-L11d-19 is the 19th image file captured from the HMC M1-2 lake sediment Sample 11d slide (a diluted sample)).

3.3.4 Slide Surveys

Slide surveys were carried out to enumerate the biosiliceous individuals in each of the 51 samples. The Leica DIC microscope was used for the surveys, using the 40x objective (400x magnification). I fashioned an Excel spreadsheet template so that survey results and notes for each slide could be recorded on its own sheet. I then developed a summary Excel spreadsheet in which the data from all 51 samples could be integrated (3.3.4 in Appendix).

Prior to enumerating the biosiliceous microfossils, I first did a DIC photo-survey of the odd-numbered sample slides to get accustomed to what I would be looking for. The images were used along with the SEM survey images to learn the names of the microfossil taxa.

Diatoms were provisionally identified to the species-level by using the 4 volumes of *Süsswasserflora von Mitteleuropa* as a primary information source (Krammer *et al.*, 2000). *The Diatoms* by Round *et al.* (1990), and the *Diatoms of the United States* website (https://westerndiatoms.colorado.edu/) were also employed (Spaulding *et al.*, 2010b). The diatom species found in this study were confirmed in January 2018 by Dr C. Riesselman of the Department of Geology at the University of Otago.

Diagnosis of the chrysophycean cyst morphotype numbers (recall Chrysophycean Cysts as Palaeoenvironmental Indicators) was by comparison with information found in both volumes of *The Atlas of Chrysophycean Cysts* (Duff *et al.*, 1995; Wilkinson *et al.*, 2002).

The slide surveys were conducted in a set pattern, using the micrometres mounted on the x- and y-axes of the microscope stage (Figure 3.19). I installed the sample slide on the stage, brought it into focus, then adjusted the slide on the stage until the focal point was at the top left corner of the cover slip (Figure 3.20). I noted the stage coordinates from the x,y micrometres, then moved the slide 3 mm into the cover slip along each axis. The stage micrometre positions were recorded on the survey spreadsheet as initial x,y coordinates at View #1 (V1) (Figure 3.20). I would count and record all microfossils within or intersecting the viewing area, then move the slide 5 mm sinistrally (to move the focal point to the right with respect to the cover slip) to View #2 (V2), repeat the survey, and move another 5 mm sinistrally. Upon completion of the last available view area at the right margin of the coverslip, I moved the slide up 5 mm (to move the focal point down with respect to the coverslip) then repeated the lateral pattern in the opposite direction. In this way, the 40x22 mm coverslip accommodated 32 survey areas (8x4).

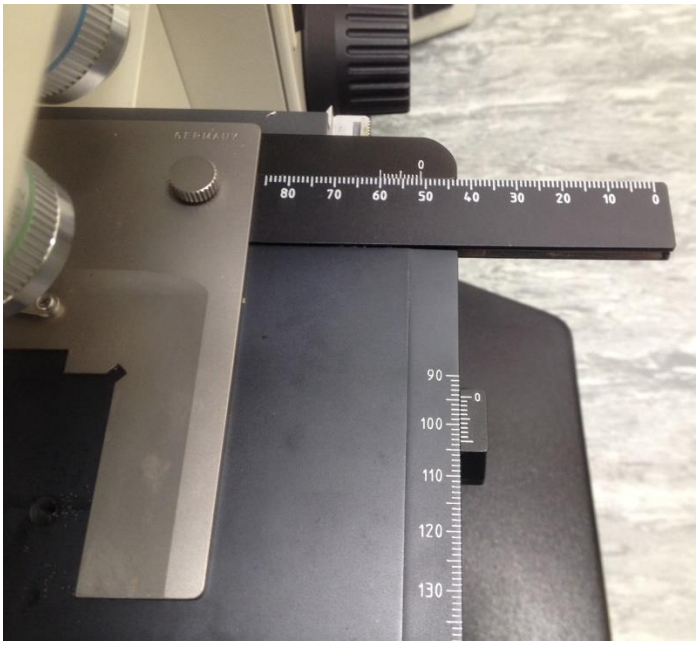

Figure 3.19: Leica DIC microscope stage micrometres.

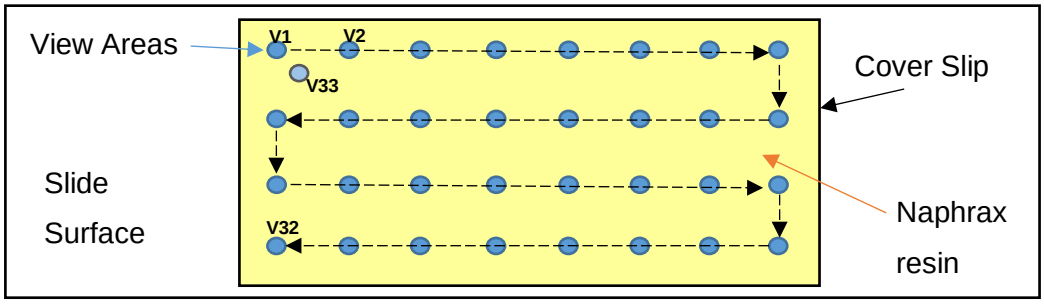

Figure 3.20: Plan view of a microscope slide, with view area survey pattern used in this study.

Dr C. Riesselman specified that, to be statistically valid, the minimum total diatom valve count per slide is 300 (C. Riesselman, personal communication, January 9, 2018). Partially dissolved diatom valves which maintained features that could distinguish them as individuals were included in the surveys. For example, the thickened central node left remaining after peripheral stria had been dissolved away is evidence of an individual valve, but fragments of the ends of valves are not and were consequently excluded (unless the fragment included the central node). I surveyed all 32 viewing areas on every sample slide, although I would stop if the diatom valve count reached a maximum of 600. If the diatom valve count did not reach 300 after 32 views but it had reached at least 150, I would do a second pass. The second pass started with the viewing area at 5 mm away from top left corner of the cover slip along the x- and y-axes (V33). The V33 coordinate was recorded in the spreadsheet, then the survey continued with 5 mm movements

between viewing areas, as before. Samples that reached diatom valve counts of <150 after the initial 32-view survey have hence been categorised as “Barren”.

Unique features (pollen, leaf cuticle, odd spicules) were recorded at the viewing area number in which they occurred. With the survey pattern as described above, one should be able to find features of note if the same microscope is used. The sample slide should get set up at the initial x,y-coordinate that is recorded on the spreadsheet, then proceed in 5 mm increments to the viewing area the feature was recorded in.

The data from the individual sample slide survey spreadsheets was aggregated in the Summary spreadsheet (3.3.4 in Appendix). The dilution factor calculation was applied to diluted samples 1d-16d to correct the diatom, cyst and spicule counts to values that reflect the actual concentrations. Each feature is reported as number of individuals per view.

Chapter 4

Results

This chapter presents data acquired from multiple analyses performed on the lake sediment deposit in the HMC M1-2 drill core. It begins with a description of the core and its various attributes then presents data acquired by various sensors on a Geotek multi-sensor core logger. Next are the results of FTIRS and BioSi wet chemistry analyses, then microscopic surveys of smear slides made with biosiliceous organisms sampled from 51 intervals throughout the core, and finally, an accounting of the species of diatoms present in the deposit that can aid in interpreting changes in the characteristics of the maar lake over time.

4.1 Core Description

The Hindon Maar Complex, Maar 1 Core 2 (HMC M1-2) reached ~18.5 m in depth. It encompasses the surficial soil horizons, the lake sediments, and the underlying basal sediments (Figure 4.1). As the lake sediments are the focus of this thesis, descriptions of the basal and overlying sediments will be brief.

Core descriptions are based primarily on core attribute surveys made from high-resolution images taken for each core section in millimetre increments (Core Surveys and Data Reduction). The descriptions are supplemented by information from field notes taken during core acquisition, and visual core descriptions recorded during split-core image processing on the Geotek MSCL. Results are described upcore, from the deepest sediments to the shallowest, emulating the deposition pattern as it occurred. Depths are reported as metres composite depth (mcd), which is the depth model I created using the Geotek MSCL data in combination with Geotek log notes and actual drill rig field depths.

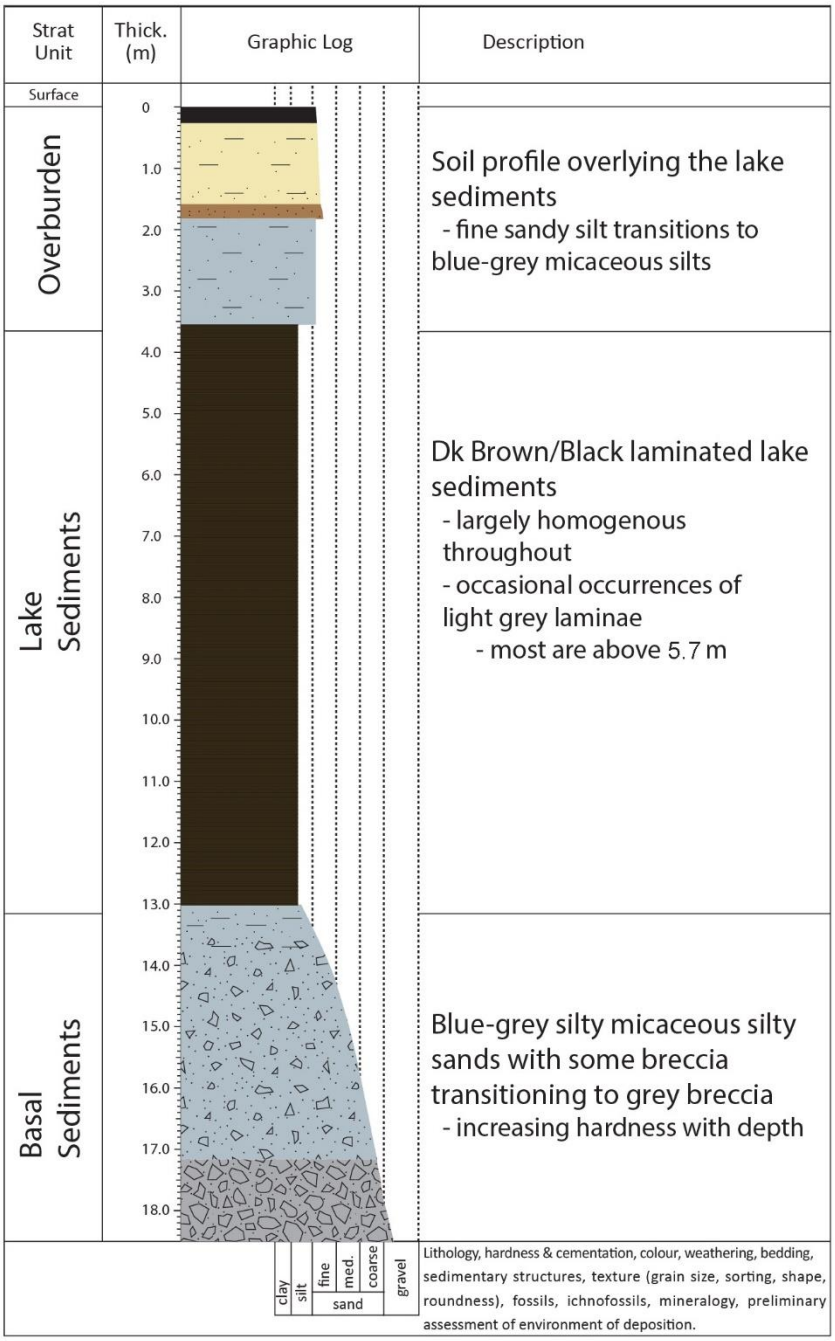

Figure 4.1: Graphic log of HMC-M1-2 core. Approximately 3.5 m of soil horizons over ~9.5 m of organic-rich lake sediments, with light/dark laminae couplets apparent between ~5.7 and 3.5 metres composite depth (mcd). Basal sediments are loose micaceous blue-grey sandy silts that transition to silty sands and finally to dark grey sandy breccia. Strength, proportion of Otago Schist country rock sands/fine gravels, and breccia-content increase with depth.

4.1.1 Basal Sediments

The basal sediments (~18.5–13.0 mcd) consist of ~5.5 m of massive dark-grey sandy breccia with fine gravel clasts consisting of Otago Schist country rock and altered volcanics (Figure 4.2a), transitioning upcore (Figure 4.2b) to poorly consolidated micaceous blue-grey sandy silt (Figure 4.2c). Approximately 50 cm of core was not acquired from the poorly consolidated sediments and is presumed

to have been washed out with the drill cuttings. Consequently there is a sharp contact with the overlying lake sediments, occurring at 13.01 mcd.

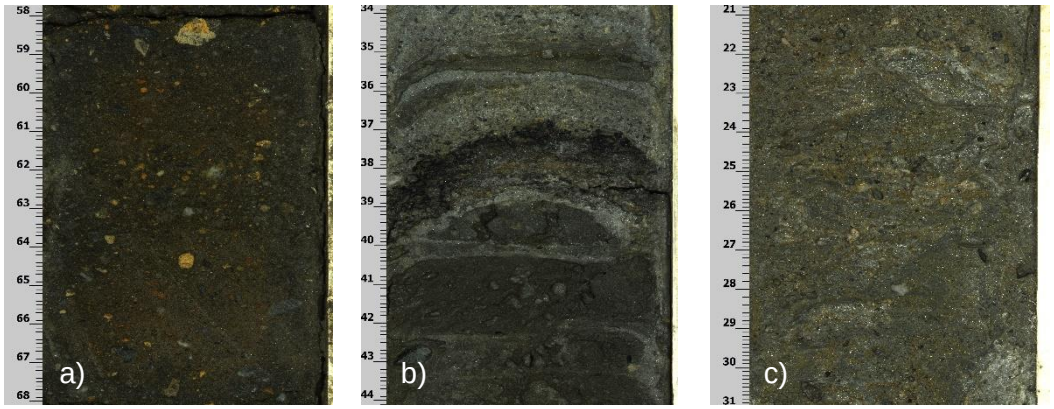

Figure 4.2: Representative sections of basal sediments. Scale is in cm from top of core section liner, while the depth given in this caption is in metres composite depth (mcd): a) ~18.0 mcd, highly consolidated dark grey sandy breccia with occasional gravel clasts (schist, quartz and altered-scoria clasts); b) ~15.4 mcd, massive well-consolidated dark grey sands transitioning upcore to poorly consolidated micaceous blue-grey sandy silts; c) ~13.75 mcd, poorly consolidated blue-grey micaceous sandy silt with granules of breccia and Otago Schist country rock.

4.1.2 Lake Sediments

The lake sediment interval is 9.45 m long, from 13.01 to 3.56 mcd. Visually the lake sediments consist of very dark brown carbonaceous laminae that would initially seem to be almost homogenous. However, above ~5.7 mcd the upper ~2.2 m of the lake sediments are slightly brighter and have light/dark laminae couplets. Consequently, I have divided the lake sediment deposit into two major lithofacies at 5.7 mcd:

- DLCS, dark laminated carbonaceous sapropel, ~7.3 m of very dark brown laminated carbonaceous sediments (Figure 4.1 from 13.0–5.7 mcd, and Figure 4.3a).
- DLDA, dark laminated diatomite, ~2.15 m of dark brown organic-rich sediments with packets of light-dark lamina-couplets (Figure 4.1 from 5.7–3.56 mcd, and Figure 4.3b).

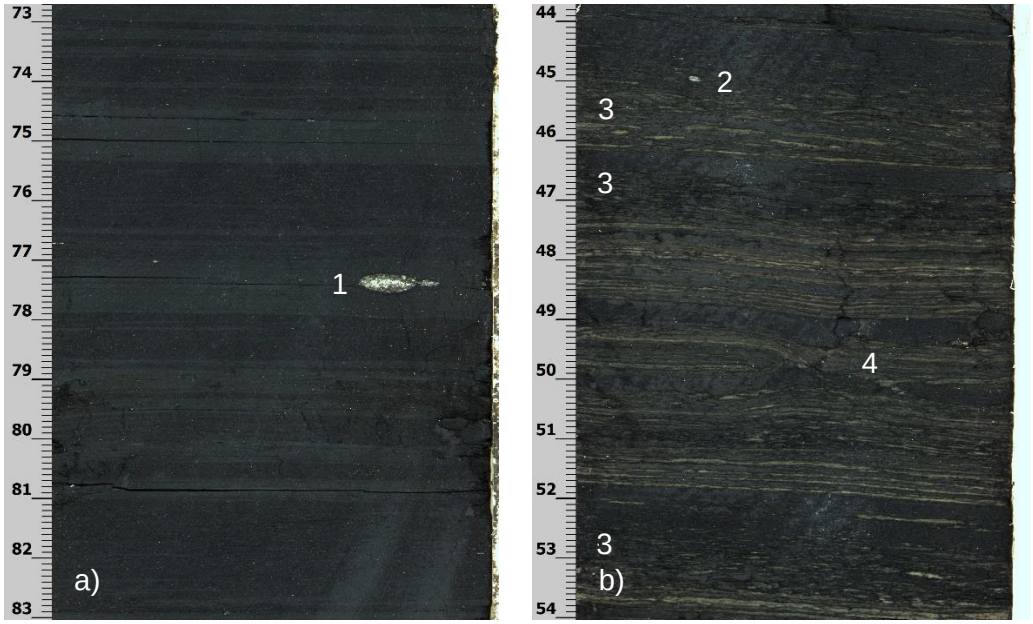

Figure 4.3: Representative intervals of lake sediments. Scale to right of each image is in cm from the top of the core section liner: a) ~8.35 mcd, DLCS facies with subtle brightness differences; b) ~4.0 m, DLDA facies alternating between dark and light/dark laminated sections. 1) a lens of coarse sands; 2) a terrigenous sediment clast; 3) examples of wavy bedding at 45-46 cm, 46.5-47 cm, and 52.5-53.5 cm; 4) disturbed section between 49.5 and 50.5 cm.

Dark Laminated Carbonaceous Sapropel (DLCS) Facies (13.0-5.7 mcd)

The DLCS facies (Figure 4.3a) is almost entirely very dark brown to near-black laminated carbonaceous organic material; i.e. a laminated sapropel (Schnurrenberger *et al.*, 2003). The DLCS is considered homogenous in that, although there are some subtle visual distinctions by which the laminar structure is evident, there is virtually no sustained amount of significantly lighter-coloured material that would denote a shift in sedimentation processes. From 13.0 to ~6.5 mcd, the dark organic laminae are interbedded with very thin bands (maximum one grain-diameter thick) of very fine sediments. The fine sediments between the thicker dark laminae vary upcore in depth and occurrence, from scattered muscovite flecks (~12.7-10.7 mcd), to muscovite flecks and light brown silt (~10.7 mcd), to dark brown very fine sand (~9.0 and ~6.9 mcd). Fine muscovite flecks are ubiquitous throughout the facies.

Isolated terrigenous sediment clasts are peppered throughout the DLCS facies. They are often equant, sub-angular to sub-rounded, in sizes ranging from very coarse sand to small granules. Figure 4.4 shows just such a clast (labelled “3”). They are most common between 11.3 and 10.4 mcd. The Core Attributes section includes a more detailed discussion on the occurrence of the sedimentological features observed in the HMC M1-2 core, including these terrigenous clasts.

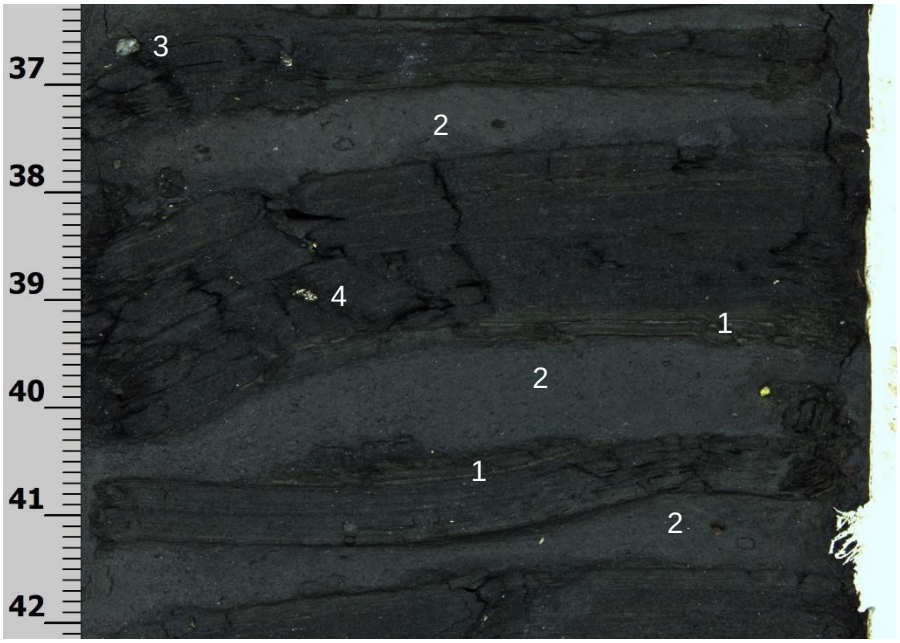

Figure 4.4: A segment of DLCS core from Core Section #6 corresponding to ~6.1 mcd. The scale on the left margin is centimetres from top of the core section liner. All core in this segment is classified as 'disturbed': 1) light laminae amongst the DLCS; 2) mud injections between segments of core, from the drilling process (data removed from depth model); 3) terrigenous sediment clast; 4) plastic liner shavings from core-splitting saw.

Lenses of terrigenous coarse sandy sediments occasionally appear in this facies. These lenses are generally ~2.0-22.0 mm wide and from ~0.6-4.0 mm thick, and cause minor distortion of the laminae above and below. Figure 4.3a includes an example of this type of structure (labelled "1"). These lenses appear irregularly but are particularly common in the interval 11.1-10.6 mcd. Intervals at which these lenses were found were also identified as having terrigenous sediment clasts and are included in that data set.

Light laminae are those which are distinctly brighter than the dark organic material. There are some very isolated occurrences of mm-scale light grey laminae in the DLCS. An example from ~6.1 mcd is shown in Figure 4.4 (labelled "1").

Observation of other macro-characteristics approaching the upper extent of the DLCS facies is confounded somewhat by fragmentation and deformation of segments of the core due to the drilling process, either by mechanical forces or by injection of drilling mud/cuttings between laminae that separates the core into cm-scale chunks and distorts the structure. Much of the core in the ~11.3-10.4 mcd interval is fragmented, and core from ~7.5-5.9 mcd has a high amount of disturbance. These attributes have been included in the core survey, as well. Three mud injection layers are shown Figure 4.4 (labelled "2"). All core segments shown in that figure are classified as 'disturbed'.

All of these features, and additional ones that follow, are further discussed below in the Core Attributes section.

Dark Laminated Diatomite (DLDA) Facies (5.7-3.56 mcd)

The DLDA facies is dark brown laminated carbonaceous and diatomaceous sediment. It is distinguished from the DLCS facies by the presence of centimetre-scale packets of light/dark laminae couplets occurring at decimetre-scale intervals (Figure 4.3b and Figure 4.5) (Schnurrenberger *et al.*, 2003). Like the DLCS facies, it also has muscovite flecks throughout.

Light laminae are common throughout the DLDA facies. Figure 4.3b and Figure 4.5 show examples of the light laminae. They occur at irregular intervals in almost equal measure in the three core sections that contain the 2.15 m of DLDA sediments.

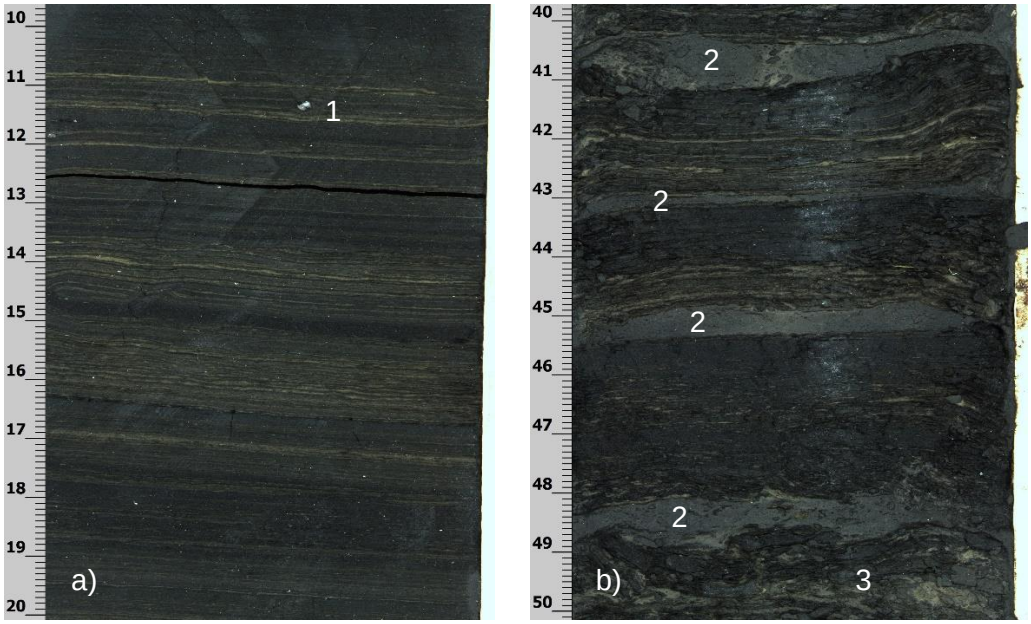

Figure 4.5: Segments of DLDA core. Scale on left margin in centimetres below top of core liner; a) light laminae in Core Section #5, at ~5.3 mcd; b) wavy bedding between mud-injection layers in Core Section #4, at ~4.65 mcd. 1) A sediment clast; 2) mud-injections; 3) Disturbed bedding.

Wavy bedding is observed often in the DLDA facies. Wavy bedding refers to bedding that has mm-to-cm-scale wavelengths of sub-mm-to-mm amplitude. Some examples of wavy bedding are shown in Figure 4.5b, between the mud injections (labelled “2”). Wavy bedding is especially common in Core Section #4, from ~5.1-4.3 mcd.

Individual terrigenous sediment clasts and lenses of coarse sediments, as described earlier, are found in the DLDA facies very infrequently. Figure 4.5a shows one of the sediment clasts (labelled “1”).

Disturbed bedding occurs in the DLDA facies. An example of disturbed bedding in this facies is shown at the bottom of Figure 4.5b (labelled “3”) as well as in Figure 4.3b between ~49.5 and 50.5 cm (labelled “4”).

Core Attributes

In the figures that follow, a blue line has been drawn at 5.7 mcd to show the depth of the boundary between the two lithofacies. The DLCS facies is below the blue line (13.5 to 5.7 mcd) and the DLDA facies is above (5.7 to 3.5 mcd).

Figure 4.6-4.8 show the prevalence of various attributes observed at mm-scale in the high resolution images of the split core sections. The mcd used to plot each attribute is the calculated midpoint of the each of the 11 lake sediment core sections (Table 4.1).

Table 4.1: Depth (mcd) ranges and midpoints of the HMC M1-2 core sections that contain lake sediment deposits. The blue line identifies the transition zone from the DLCS to the DLDA facies.

Litho-facies	Core Section	Metres Comp. Depth		Mid-core (mcd)
		Sec. top	Sec. btm	
DLDA	Sec. 3	3.561	4.287	**3.9**
	Sec. 4	4.288	5.173	**4.7**
	Sec. 5	5.174	5.843	**5.5**
DLCS	Sec. 6	5.844	6.661	**6.3**
	Sec. 7	6.662	7.564	**7.1**
	Sec. 8	7.565	8.541	**8.1**
	Sec. 9	8.542	9.492	**9.0**
	Sec. 10	9.493	10.42	**10.0**
	Sec. 11	10.421	11.295	**10.9**
	Sec. 12	11.296	12.269	**11.8**
	Sec. 13	12.27	13.01	**12.6**

The percent-occurrence of each attribute is calculated from the number of millimetres in which the attribute was observed in relation to the total length (mm) of that section of core. The number of sand lenses is an exception in that the reported result is a direct count of sand lenses per core section (Figure 4.8b).

Of the areas of core having light laminae (Figure 4.6a), almost all (99%) occur in the DLDA lithofacies (above 5.7 mcd). This is also the case with both the wavy (93%) and dipped laminae (100%) (Figure 4.6b and c). The light laminae accounts for ~43-50% of the core throughout the upper facies.

The DLDA facies is where 93% of the wavy laminae are found. ~33% of the DLDA facies consists of wavy laminae, but most (over 70% of the wavy laminae) occur between ~4.3 and 5.2 mcd (core section #4). Correlating the light and wavy laminae in the upper facies shows that 69% of the wavy laminae are also light laminae. The DLCS lithofacies has occasional occurrences of wavy bedding, most of which are found between 9.18 and 9.36 mcd (core section #9).

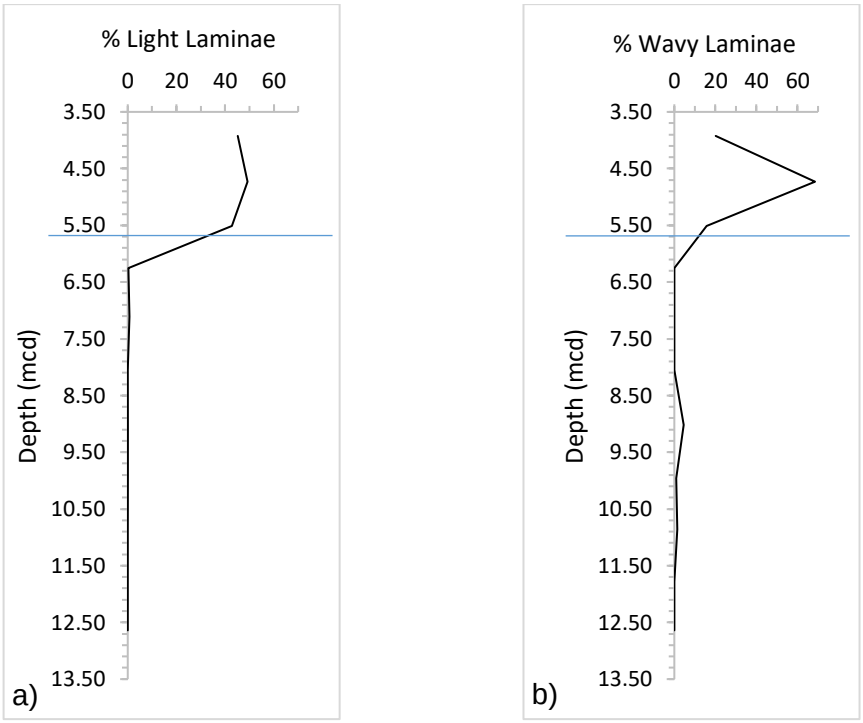

Figure 4.6: Depths at which light and wavy laminae occur in the 11 split core sections. Depth value for each core section is mcd at midpoint of that section (Table 4.1): a) percent of core section that is composed of light laminae; b) percent of core section composed of wavy laminae.

Fragmented laminae were observed exclusively within the carbonaceous DLCS lithofacies (Figure 4.7a). After increasing from 35% at the deepest core to a maximum of 53% in the 11.3-10.4 mcd range, the percentage of each core section that was fragmented generally decreased upcore until near zero from Core Section #6 (midpoint 6.3 mcd) and above.

Dark homogeneous sediments are occasional and occur in both the DLDA and DLCS lithofacies (Figure 4.7b). About 63% of the thickness of these are found in the DLDA facies, increasing upcore to a maximum of 4.1% of total core thickness in Core Section #3. In the DLCS facies, only Core Section #8 (midpoint 8.1 mcd) contains some homogeneous sediments (1.7%).

Terrigenous sediment clasts are defined in this study as individual minerogenic siliciclastic sediment clasts of at least coarse sand grain size (>0.5 mm), as per the Udden-Wentworth grain-size classification scheme. This excludes the ubiquitous muscovite flecks. Clasts were enumerated by identifying each millimetre of core in which they were present (Figure 4.7c), either as individual or multiple clasts or as lenticular sand lenses, as discussed earlier in Chapter 3: Core Surveys and Data Reduction. Any number of terrigenous sediment clasts in a one-millimetre interval of core identified that single interval as having sediment and it would contribute to the “% Sediments” in that core section. Terrigenous sediment presence increases in abundance from 3.4% at the base of the lake sediments to a maximum of 9.6%

in Core Section #11 (midpoint 10.9 mcd). From that point the abundance generally declines down to 0.9% at ~4.7 mcd, then rises in Core Section #3 (the top of the lake sediments) to 2.7%.

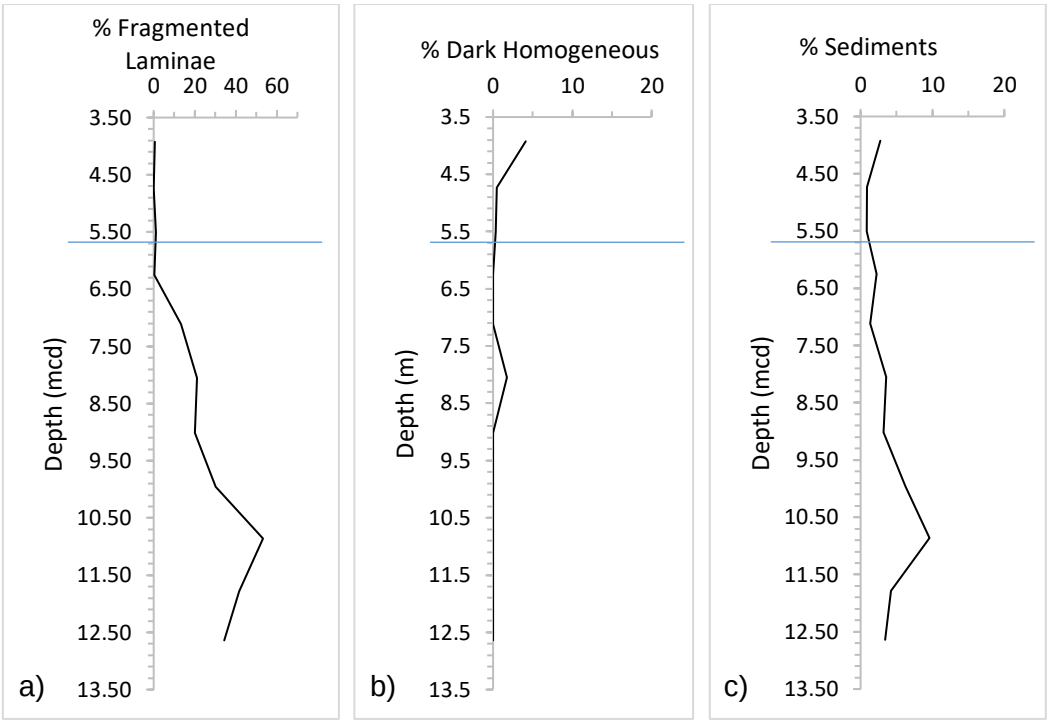

Figure 4.7: Depths at which laminae that are fragmented, homogenous, or where isolated coarse sediment clasts occur. Depths determined as shown in Table 4.1: a) percent of core section that consists of fragmented core material; b) percent of core section composed of homogenous black sediments; c) percent of core section that has coarse grains of siliciclastic sediments.

Lenticular coarse sand deposits were observed in the lake sediments almost exclusively in the DLCS lithofacies (although one was observed in the DLDA lithofacies, near the top of Core Section #3). Each individual sand lens was recorded for the core section in which it occurred (Figure 4.8a). From the base of the lake sediments, sand lenses increased in abundance to peak at 12 in Core Section #11 (midpoint of 10.9 mcd) then generally reduced in number upcore, with the exception of Core Section #8 (midpoint of 8.1 mcd) where 6 were found.

Moving upcore, the percent of lake sediments that were classified as disturbed (Figure 4.8b) was between 3 and 15% from 12.6-8.1 mcd, then rose above 50% for the top two core sections of the DLCS facies (Core Sections #6 and #7, representing core between ~7.6 and 5.8 mcd). In the upper DLDA facies, the highest occurrence of disturbed sediments is 28% in Core Section #4, decreasing to 7% in Core Section #3.

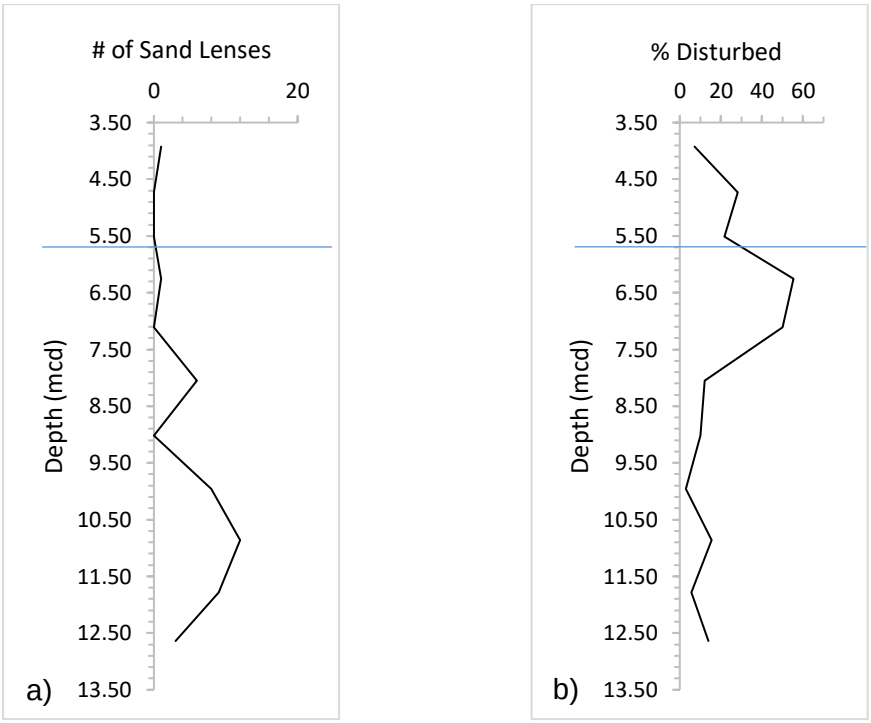

Figure 4.8: Depths at which sand lenses and disturbed bedding occurs. Depths determined as shown in Table 4.1: a) number of sand lenses per core section; b) percentage of core section that consists of disturbed core.

Lamina-couplet Thickness

I undertook lamina thickness measurements in order to build an age-depth model for the deposition of the HMC M1-2 lake sediments (3.2.2 Lamina-couplet Thickness). The results are summarised in Table 4.2.

Table 4.2: Summary of age-depth model estimates based on averaged laminae-couplet measurements from each of the HMC M1-2 lake sediment deposit core sections (11). Green dashed line distinguishes boundary between two unique couplet-thickness zones. The blue line identifies the transition zone between the lower DLCS and the upper DLDA lithofacies, as determined by the core description.

	Core Section	Depth sampled (mcd)	Ave. Couplet thickness (mm)	Estimated Deposit Time	Ave. Est. Time btwn Smear Slide Smpls.	Ave. Est. Time in ea. Smear Slide Smpl.
DLDA	Sec. 3	3.83	0.67	3250 years	275 years	12 years
	Sec. 4	5.06	0.69			
	Sec. 5	5.55	0.66			
	Sec. 6	6.16	0.63	1300 years		
DLCS	Sec. 7	6.90	1.33	5850 years	170 years	7 years
	Sec. 8	7.73	0.94			
	Sec. 9	9.02	1.11			
	Sec. 10	10.12	1.07			
	Sec. 11	10.76	1.23			
	Sec. 12	11.64	1.01			
	Sec. 13	12.61	1.05			

There is a distinct change in lamina-couplet thickness between Core Sections #7 and #6 (green dashed line in Table 4.2 (blue line shown for reference to the DLCS/DLDA lithofacies contact region)). The average couplet thickness is ~1.09 mm from 13.0-6.5 mcd (the top of Core Section #7). From 6.5-3.56 mcd the average couplet thickness is ~0.66 mm. These accumulation rates are reasonable

when compared with values reported in a varve database compilation which found that varve thickness (akin to laminae couplet thickness) for 95 studies ranged from 0.07-27.30 mm while the mean and median thickness was 1.00 and 1.84 mm respectively (Ojala *et al.*, 2012). I made the assumption that lamina-couplets are analogous to annual deposition. In that case, the length of the core in Core Sections #7-13 would take ~5850 years to accumulate while the length of the core in Core Sections #3-6 would take ~4550 years, for a total of ~10400 years to deposit the 9.45 m of HMC M1-2 lake sediments.

51 small core samples (to make smear slides) were taken at regular intervals throughout the core; 34 from 12.97 to 6.66 mcd (the thick laminae sections), and 17 from 6.66 to 3.56 mcd (the thin laminae sections). The average gap between samples in the thick and thin laminae sections is 18.5 and 18.2 mm, respectively. Consequently, the average timespan is ~170 years between samples in Core Sections #7-13, and ~275 years between samples in Core Sections #3-6. The smear core samples were approximately 8 mm long with respect to the length of the core. At the estimated average rates of deposition, each sample in Core Sections #7-13 encompassed an average timespan of ~7 years, while samples in Core Sections #3-6 crossed an average timespan of ~12 years.

4.1.3 Overlying Sediments

Due to the drilling method, core for the initial ~1.47 metres of drill depth was not recovered intact. Soils from that depth range are thus described from the field notes.

From 3.60 to 3.56 mcd, there is a disrupted contact between the top of the lake sediments and the base of the overlying unit. The lake sediments are intruded by a band of light-coloured terrigenous sediments and pebble-sized clasts of Otago Schist, which is bedded sub-horizontally within the top of the DLDA. The overlying unit from 3.56 to ~2.0 mcd consists of medium-brown micaceous sandy silts (Figure 4.9a) with occasional laminar structure and some sub-angular to sub-rounded pebbles of weathered schist and carbonaceous material, grading upcore to grey-brown micaceous silt and finally to blue-grey micaceous sandy silt (Figure 4.9b). There is an abrupt transition to firm light brown-grey fine silty micaceous sand at ~2.0 SB depth, with occasional bands of coarse sands/small schist pebbles from ~2.0 to ~1.6 mcd (Figure 4.9c).

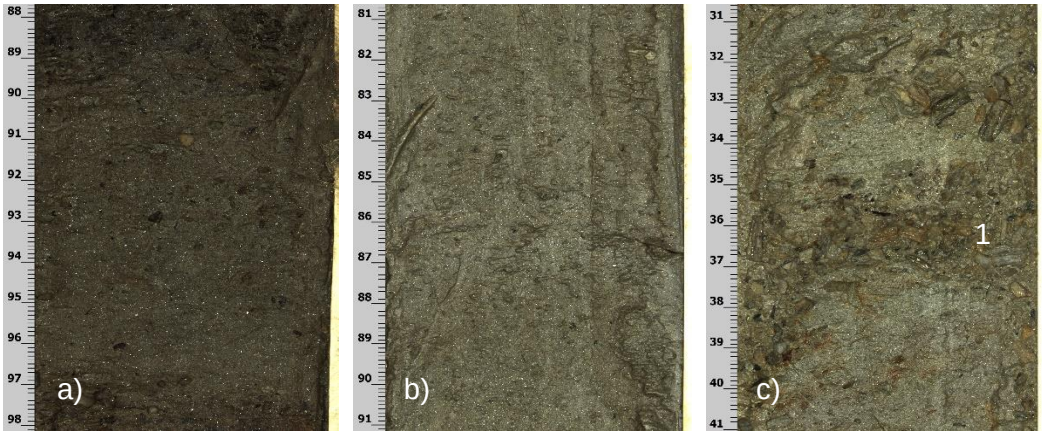

Figure 4.9: Representative intervals of sediments overlying the lake sediments. Scale is in cm from top of core section liner:: a) ~3.45 mcd, dark brownish-grey micaceous silty sands with sub-angular to sub-rounded pebbles of weathered schist and carbonaceous material; b) ~2.3 mcd, blue-grey micaceous sandy silt; c) ~1.8 mcd, light brown-grey fine silty micaceous sand with downward-curved band of coarse schist grains ("1", starting from the right margin between ~35 and 37 cm).

At ~1.5 mcd the profile transitions to yellowish gold fine sandy silt, the top ~25 cm of which is dark brown topsoil to the surface.

4.2 Geotek MSCL Results

In total, seventeen 1-metre sections of core were acquired from HMC M1-2. They were split and prepared as described in 3.1.2: Core Preparation for Analyses to be analysed by the Geotek multi-sensor core logger (MSCL). Analyses included magnetic susceptibility (MS), gamma attenuation density (GAD), and colour spectrophotometry capable of rendering results in a variety of colour classification systems such as Munsell values, two CIE (acronym for French phrasing of International Commission on Illumination) numerical colour methods (L*/a*/b* and X/Y/Z), RGB colour, and spectral values for every 10 nm wavelength-increment in the visible light range (between 360 and 740 nm).

The results which are of significance for this project and presented here are the MS, GAD, CIE L*/a*/b*, and RGB colour data relating to the lake sediments (Core Sections #3-13). The near-homogeneous darkness of the lake sediments mean that spectral data has little variation. Data analysis by the other colour classification systems adds little value so these results have been excluded.

A blue line at 5.7 mcd in each graph marks the depth of the transition zone between the lower DLCS and the upper DLDA lithofacies.

4.2.1 Magnetic Susceptibility

The range of magnetic susceptibility of the lake sediments is restricted to between -5.0 and 4.0 SI units x 10^{-5} (Figure 4.10). MS generally rises and falls ('bulges') upcore from base to ~5.7 mcd, then declines slightly at ~4.1 mcd. Fine-scale and

decimetre-scale variance decreases upcore. The variance is lowest above 5.7 mcd, in the DLDA facies. MS increases somewhat over the final ~0.6 m of lake sediments, above 4.1 mcd.

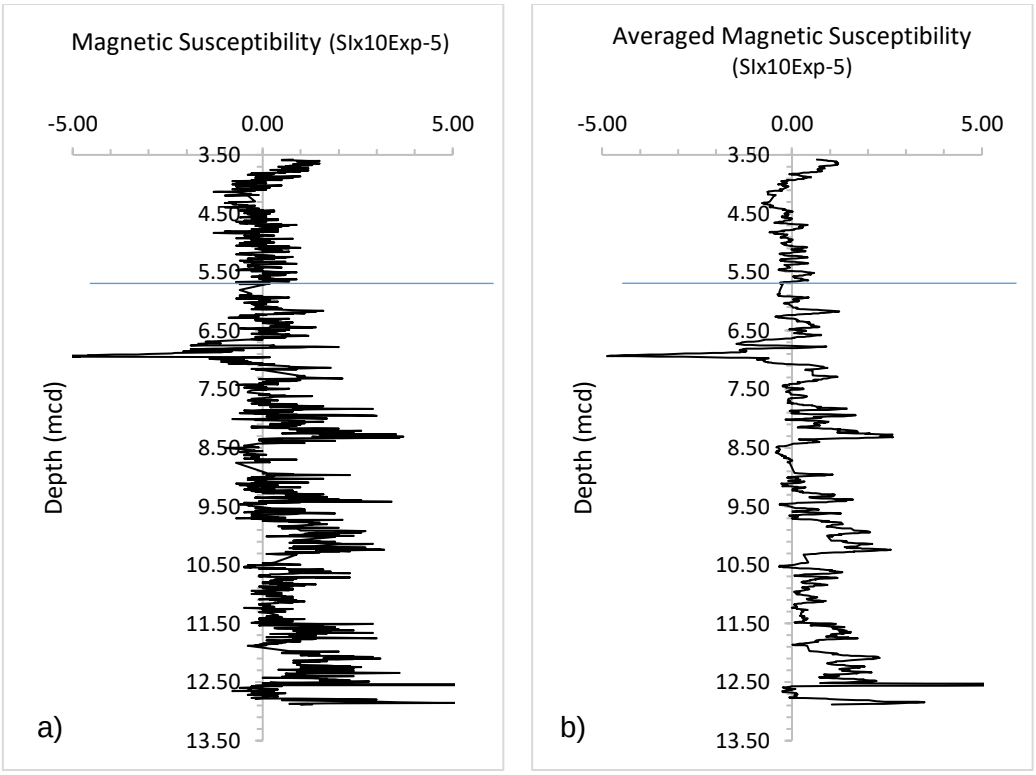

Figure 4.10: Magnetic susceptibility data in SI units x 10^{-5} for lake sediment split cores: a) individual data points; b) 7-point running average.

There is an anomalous spike at 12.54 mcd (reaching as high as 20 x 10^{-5} SI units, outside the scales displayed in Figure 4.10). There are three bulges at which MS increases abruptly then trends back down. They occur from ~12.5 to 12.2 mcd, ~10.6 to 9.8 mcd, and ~8.4 to 8.1 mcd. A two minor bulges may be evident from ~9.4 to 9.2 and ~7.5 to 7.2 mcd.

Between ~7.05 and 6.80 mcd there is a dip indicating a net diamagnetic effect. This interval spans the upper part of Core Section #7 between 39.5 and 14.5 cm from the top of the core section liner (Figure 4.11). The lowest MS readings (-5.0 x 10^{-5} SI) occur at the 28 cm mark on the scale (corresponds to 6.93 mcd). There are no obvious visual distinctions between the lake sediments in the low-MS region and the adjacent sediments above and below. Biogenic material is usually diamagnetic. As will be shown later in 4.3.2 Biogenic Silica Wet Chemistry Results, biosiliceous material is not prevalent at this depth. The dip could occur due to a reduction in ferromagnetic or paramagnetic terrigenous input, but the absolute value of -4.90 SI units x 10^{-5} is more indicative of an analysis error. I consider this data to be anomalous and have subsequently excluded it from consideration.

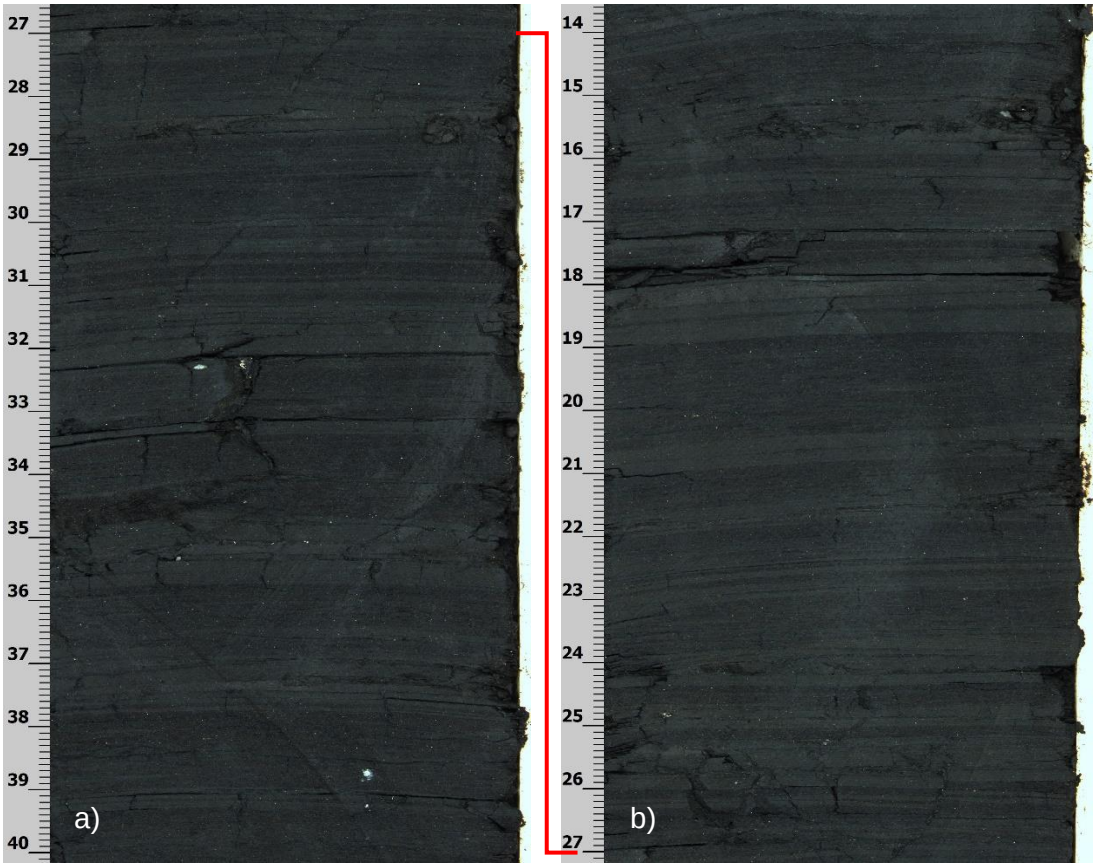

Figure 4.11: Segment of Core Section #7 that spans the low MS data. Scale on left margin is in cm from top of core section liner. The red line shows how the two sections are joined: a) ~7.05 – 6.92 mcd; b) ~6.92 – 6.80 mcd.

4.2.2 Density

The density of the lake sediments decreases from the base to ~10.9 mcd, and then generally increases upcore until a sharp increase over the top ~40 cm of the lake sediments (Figure 4.12).

There is a density bulge between ~10.5 and 9.9 mcd, at the base of the generally gentle increase. It correlates with an increase in magnetic susceptibility (the second of three MS bulges) in the DLCS facies (Figure 4.13). The MS and density datasets have some similarities (inside of blue translucent rectangles) in that there is a slight decrease in values from base to ~10.8 mcd, a general increase from ~10.5 to 9.9 mcd, a minor bulge and decrease from ~9.4 to 9.0 mcd, and an increase in values above ~4.1 mcd. However, MS and density generally diverge from each other in the remaining regions.

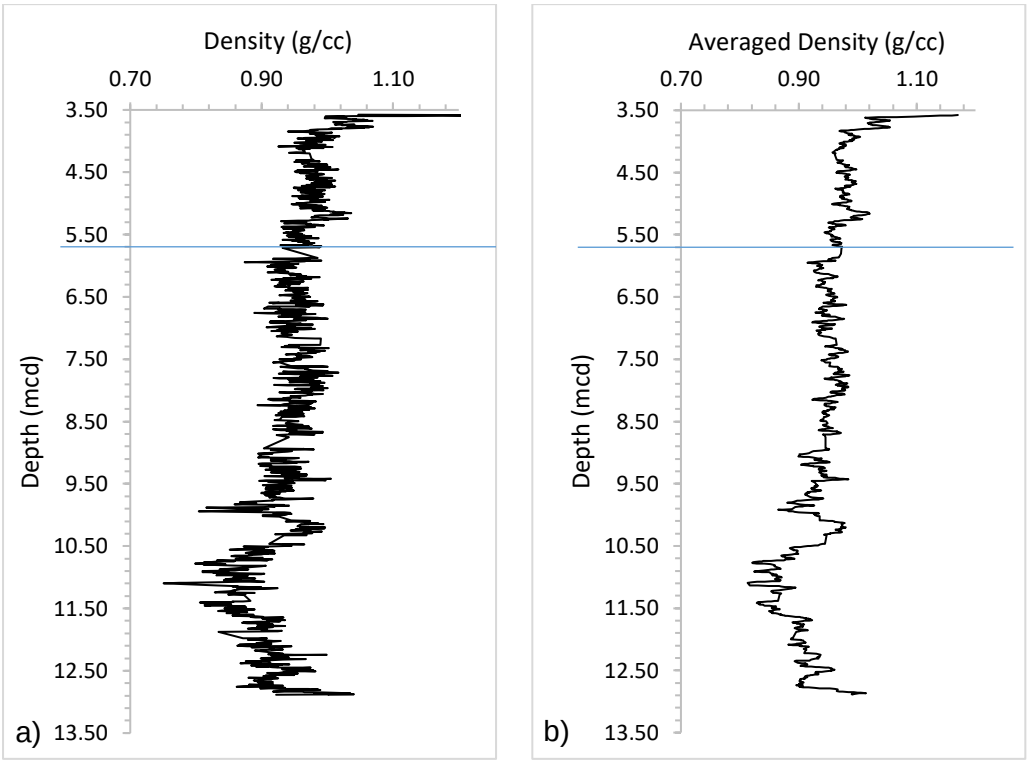

Figure 4.12: Density data in grams per cubic centimetre for lake sediment split cores: a) individual data points; b) 7-point running average.

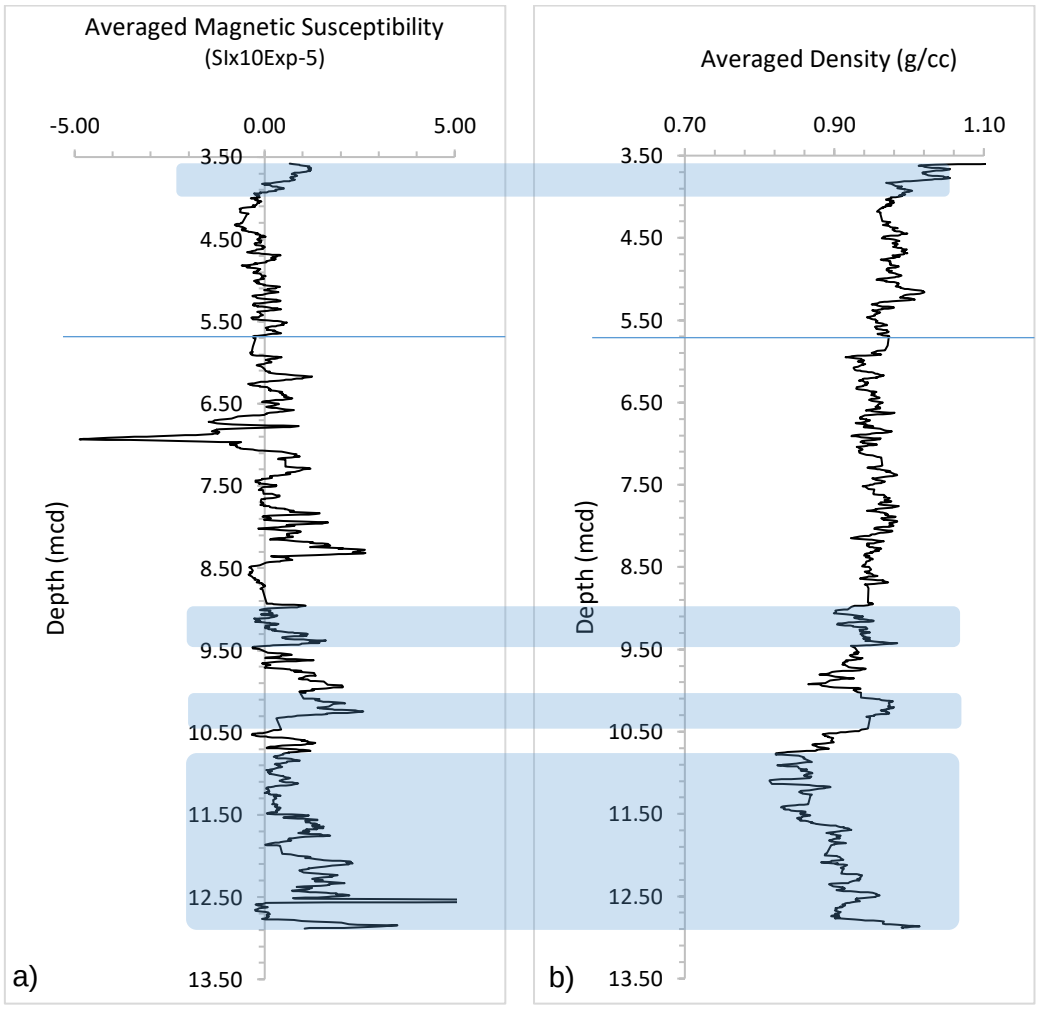

Figure 4.13: a) Average MS data compared to b) average density data. Blue bands highlight similar data trends. In unmarked regions they generally diverge.

4.2.3 CIE L*/a*/b* Reflectance

This colour space classification deals primarily with light of visible wavelengths. Reflected light from the split core surface is partitioned into three coordinate groups of data (Figure 4.14). The ranges on the x-axes are as narrow as possible in order to display the subtle variation in the HMC M1 lake sediments. The L* group represents the brightness of the sample, where 0 is black and 100 is diffuse white. The a* group is the net green-to-red value, in which green is represented by negative values while red values are positive. The b* group is similar to the a* group except that negative values are blue and positive values represent yellow. The L*a*b* data as a group will be referred to as “reflectance”. The L* component of that group will be termed “luminosity”, while a* and b* are hues.

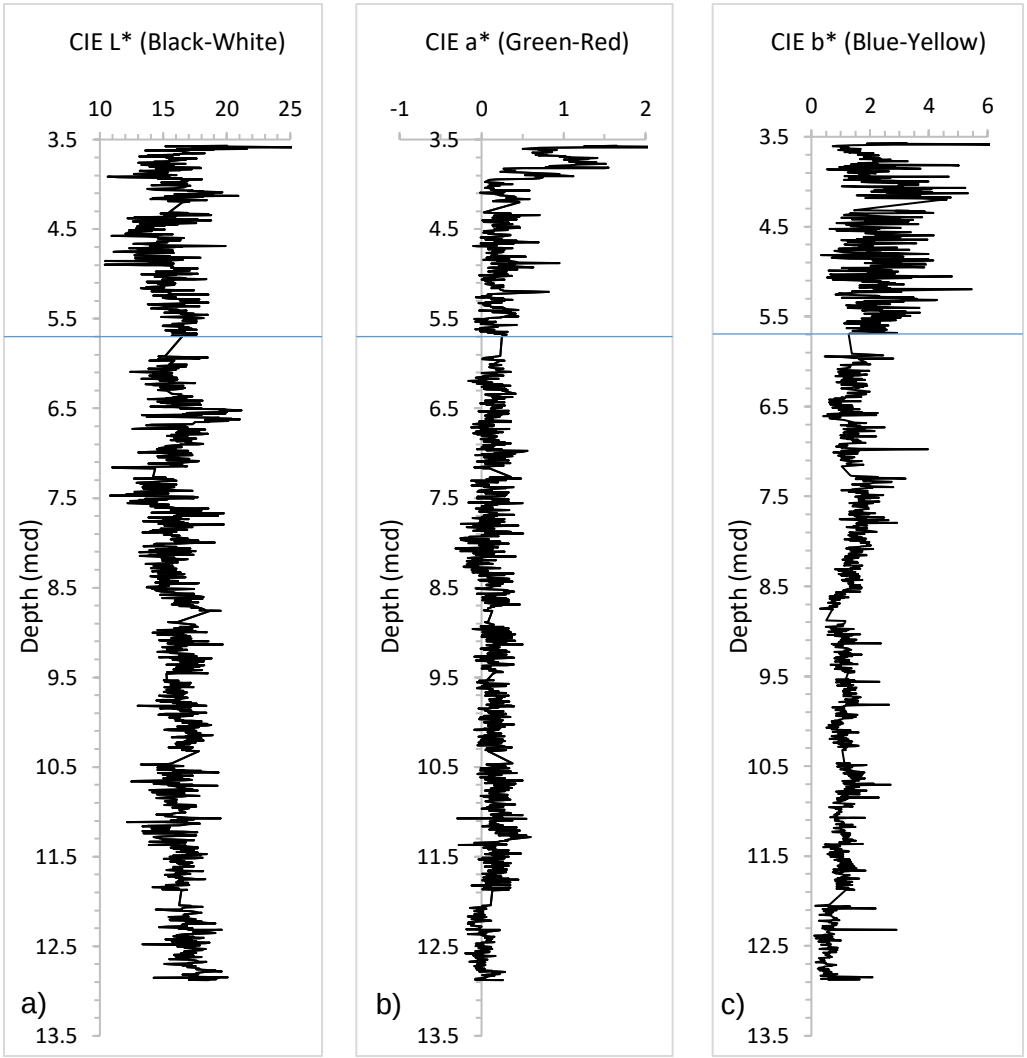

Figure 4.14: CIE L*/a*/b* colour data for HMC M1-2: a) CIE L* brightness; b) CIE a* green-red; c) CIE b* blue-yellow.

The reflectance data showed very little upcore variation through the DLCS facies. Luminosity (CIE L*, Figure 4.14a) generally decreases upcore. There is some

metre-scale variability in the values with a final uptick in brightness at the top of the lake sediments.

The green-red value (CIE a*, Figure 4.14b) is near neutral (0) at the base of the lake sediments and increases slightly at ~12 mcd. It remains at about the same slightly positive (red) value until ~4.0 mcd. At that point it alternates between the positive and negative directions twice as it increases to the top of the lake sediments.

The blue-yellow value (CIE b*, Figure 4.14c) tends to increase slightly upcore from the base to ~5.7 mcd with centimetre-scale and slight metre-scale variation. Above 5.7 m the b* values increase by a small step and become much more variable at the centimetre-scale. They peak around 4.1 mcd then decline slightly until just before the top of the lake sediments where some of the lighter sediments from the overlying unit has been incorporated into the top of the DLDA facies.

99% of the light/dark lamina-couplets are found above 5.7 mcd, the depth which divides the DLDA and DLCS lithofacies (see Section 4.1.2 Lake Sediments). The CIE colour values were averaged for the each facies (Table 4.3). The standard deviation for each was calculated as well.

Table 4.3: Averaged CIE colour space values for DLDA and DLCS lithofacies.

Depth (mcd)	CIE colour values					
	L* Ave	*L* StDev*	a* Ave	*a* StDev*	b* Ave	*b* StDev*
DLDA	15.7	*1.86*	0.3	*0.36*	2.3	*1.03*
DLCS	16.2	*1.39*	0.1	*0.14*	1.2	*0.46*

The average L* value was 15.7 in the DLDA facies while in the DLCS it was 16.2. On its own this would indicate that the upper facies of the core is less bright than the lower facies, although visually it is not. The average b* value almost doubled from 1.2 to 2.3, indicating that the DLDA has more yellow colour than the DLCS. Upon observation, light laminae in the DLDA facies have a yellowish grey hue. Doubled b* hue values in the DLDA facies combined with the L* brightness data indicate net brighter appearance of the DLDA.

4.2.4 RGB Colour

The red-green-blue colour intensity data are shown in Figure 4.15. The RGB data closely emulates the luminosity data (Figure 4.14a) in pattern and depths at which variability changes. The separate RGB components keep approximately the same deviation from each other in the DLCS facies and variability is lower. This is most evident at core discontinuities in the Geotek data (e.g. 12.0, 10.4, and 9.5 mcd) – the three colour components are generally parallel across the core break.

The variability increases in the DLDA facies in core intervals where light laminae are present. The output from each RGB channel diverges in the DLDA facies, with the red and blue data recording data that correlates to their respective a* and b* reflectance counterparts. The red channel has the strongest reaction to the presence of light laminae above 5.7 mcd.

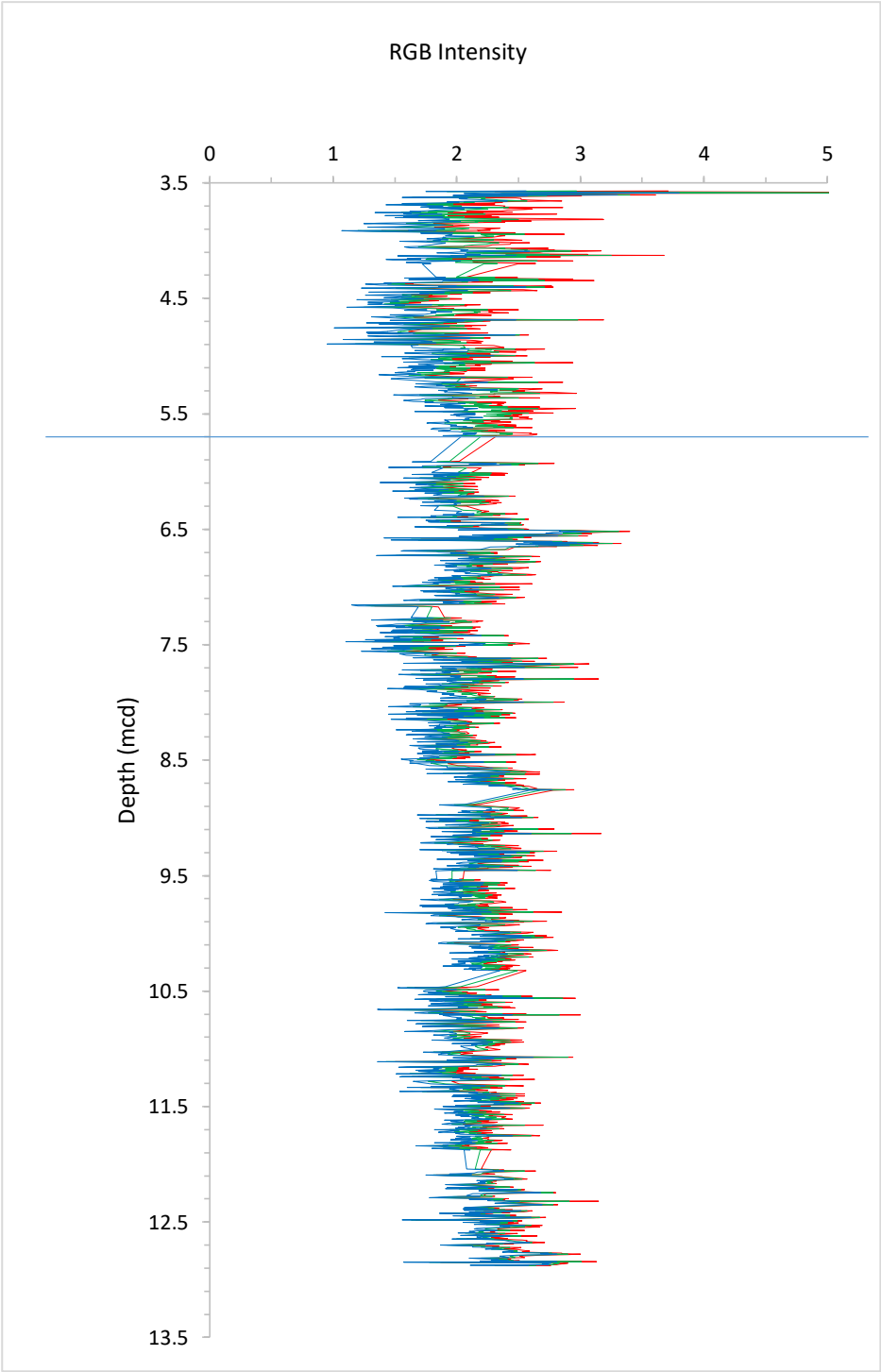

Figure 4.15: RGB colour data for the HMC M1-2 lake sediments.

4.3 Composition Analyses

Biogenic silica (BioSi, or biogenic opal/hydrated silica) content in the HMC M1-2 lake sediments is an important proxy for the presence of siliceous organisms that build their skeletal components from silicic acid in the water (DeMaster, 1981; Mortlock & Froelich, 1989). Two composition analyses were conducted for this project: Fourier transform infrared spectroscopy (FTIRS) and molybdate-blue wet chemical analysis for BioSi wt% (3.2.4 Composition).

4.3.1 Fourier Transform Infrared Spectroscopy Results

For each of the HMC M1-2 lake sediment samples analysed by FTIRS, data were generated that show the proportions of three specified constituents: total organic carbon (TOC), biogenic silica (BioSi), and Otago Schist from the sample location (Figure 4.16). For each sample/depth, the sum of the wt% of the three components is 100%.

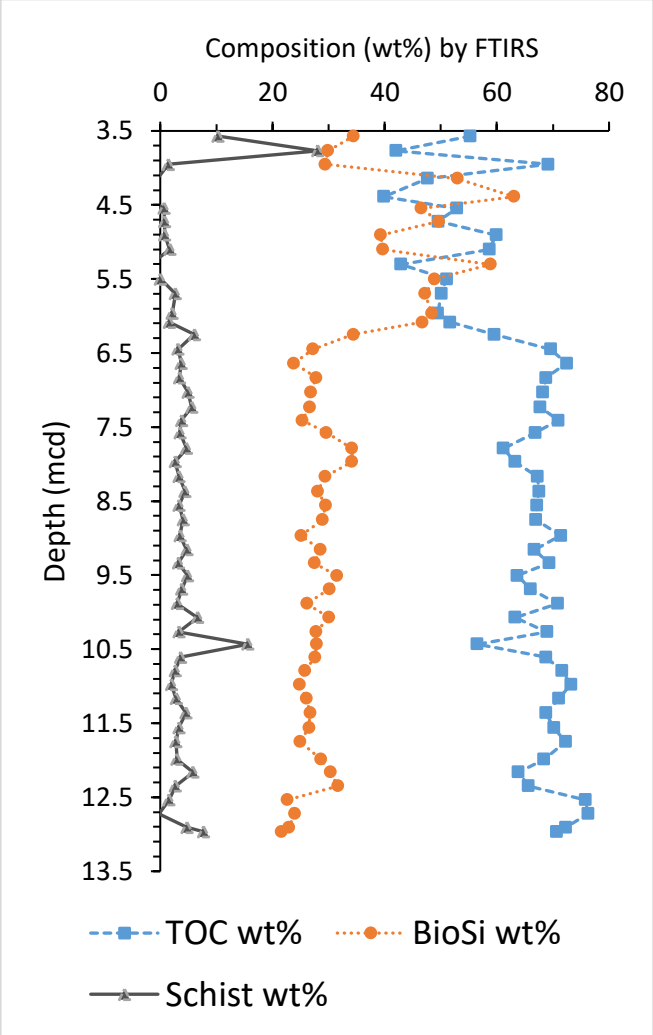

Figure 4.16: FTIRS normalised weight-% composition of total organic carbon (TOC), biogenic silica (BioSi), and Otago Schist-components (Schist) in the HMC M1-2 lake sediments.

From core base to ~6.3 mcd the TOC component accounts for the majority of the lake sediments (65-75 wt%). Across this interval, the BioSi component ranges between ~24 and 34 wt% while the schist remains low, between ~3 and 6 wt%. An exception occurs at ~10.4 mcd where the proportion of schist increases to 15.7 wt% at the expense of TOC which drops to 56.5 wt%.

From 6.3 to ~4.0 mcd the BioSi component increases sharply at the expense of the percentage of TOC. These components vary between ~40 and 60 wt% in inverse proportion. The schist component decreases further to <3 wt%.

The top 0.5 m of the lake sediments show a reduction in the BioSi component resulting initially in a complimentary increase in TOC wt%. In the sample just below the top of the lake sediments (3.77 mcd) the schist component spikes from 1.5 to ~28 wt%, with a corresponding reduction in TOC and BioSi. Above this, the wt% of the schist component declines, though not to its former low levels, and TOC and BioSi concomitantly increase.

4.3.2 Biogenic Silica Wet Chemistry Results

BioSi wet chemical spectroscopy was completed on the same samples used in the FTIRS analysis, generating results in absolute wt%. These results reflect the actual wt% of the sample that is composed of biogenic silica rather than a proportional wt% comparison between three assigned components, as in the FTIRS results. The results for the HMC M1-2 lake sediments are shown in Figure 4.17a.

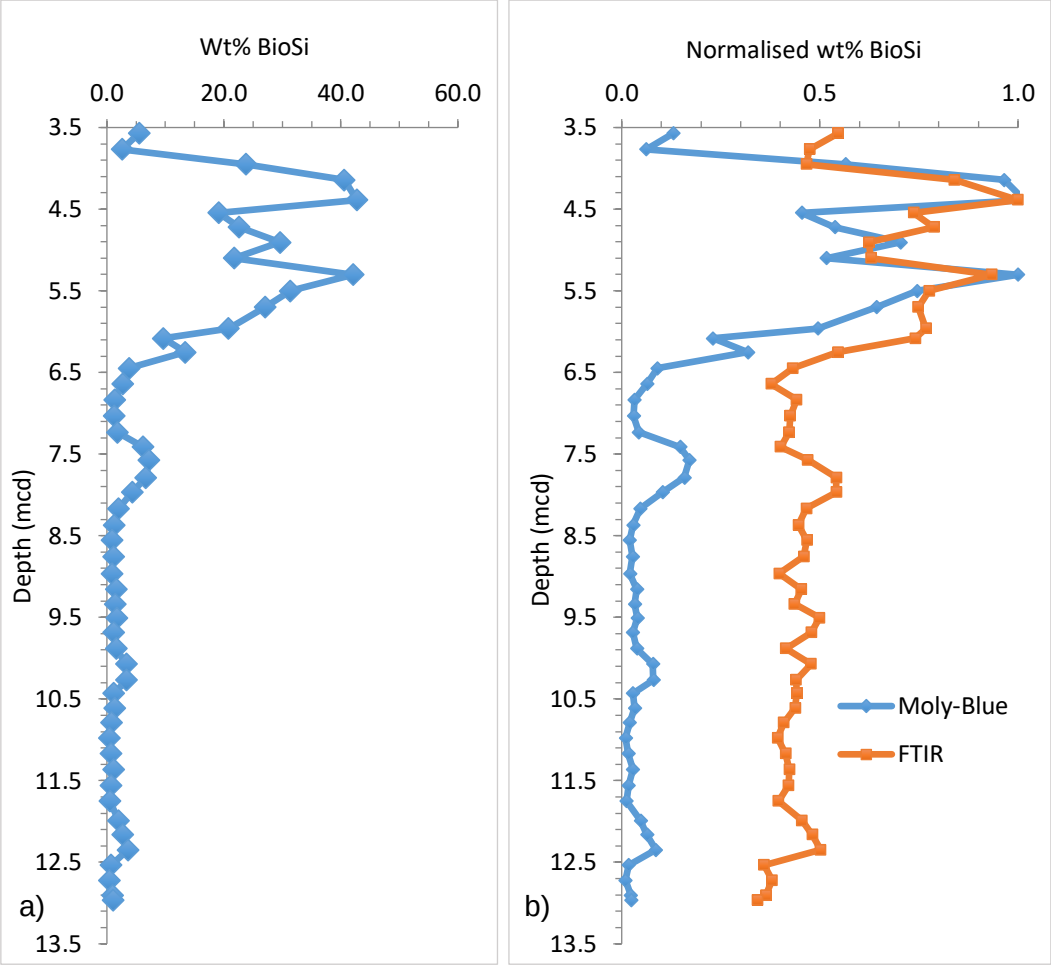

Figure 4.17: a) Moly-blue BioSi wet chemistry results in wt% for HMC M1-2 lake sediment deposit; b) Normalised Moly-blue and FTIRS BioSi wt% results.

Normalised results for the FTIRS and Moly-blue BioSi datasets are shown in Figure 4.17b. The Moly-blue BioSi results closely parallel those of the FTIRS analysis BioSi results albeit with significantly lower values below 6.5 mcd where BioSi-wt% is low. Both datasets show small increases around 12, 10, and 8 mcd. They increase sharply above 6.5 mcd. Where normalised data is >0.6, the two datasets are more closely comparable. Both also show a dip in BioSi between 5.3 and 4.0 mcd and a sharp reduction just below the top of the lake sediments.

4.4 Smear Slide Descriptions

Smear slides of the 51 lake sediment samples were surveyed for inorganic material that remained after digestion of organics in hydrogen peroxide (as described in 3.3.2 Smear Slide Preparation). Samples from ~6.5 to 3.5 mcd had a much higher abundance of inorganic biogenic material relative to the rest of the core – this material was too concentrated to make useable smear slides so these samples required dilution. The diluted smear slides were surveyed according to the same standards as the non-diluted slides, then a dilution factor was applied to the data

(as described in 3.3.2 Smear Slide Preparation) which made it directly comparable to the non-diluted smear slide data. The calculated values are reported here.

Diatom valves were by far the dominant feature (Figure 4.18). Other microfossil types included chrysophycean cysts (spherical stomatocysts with siliceous walls); a variety of freshwater sponge spicules (megascleres, gemmuloscleres, and siliceous nodules); and, although not studied in depth for this project, pollen grains and occasional fragments of leaf cuticle material.

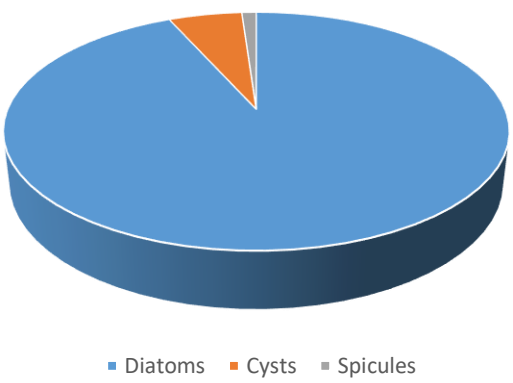

Figure 4.18: Contribution of individual diatom valves, chrysophycean cysts, and freshwater sponge spicules to the biosiliceous content of the HMC M1-2 lake sediment deposit.

4.4.1 Diatoms

Individual diatom valves were inventoried at 400x magnification using the differential interference contrast (DIC) light microscopy (LM) technique (3.3.3 DIC LM Imagery). They were recorded by abundance at species level for each of the 51 smear slides throughout the lake sediment deposit. Species were identified as per the sum of taxonomic diatom identification criteria used by Round *et al.* (1990), Krammer *et al.* (2000), later studies such as that regarding *Sellaphora* by Wetzel *et al.* (2015), and confirmed by C. Riesselman (personal communication, January 9, 2018). The total abundance of all diatom valves is presented here as average number of diatom valves per microscope view (dv/view) at 400x magnification (Figure 4.19). At 400x magnification the view is a circle of ~0.6 mm diameter, or ~0.28 mm^2.

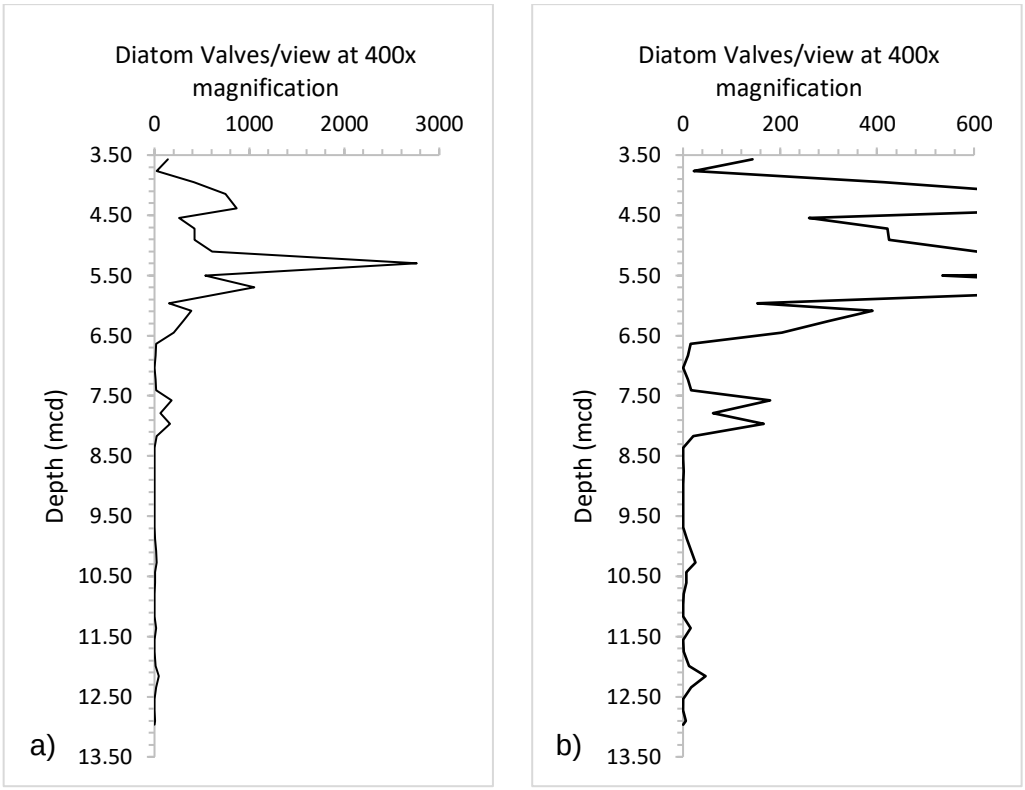

Figure 4.19: Average diatom valves/view (dv/view) at 400x magnification, shown at two different diatom valves/view scales: a) range of diatom valves/view from 0-3000 to display all results; b) range of diatom valves/view reduced to 0-600 to better display variations at low concentrations in sediment core depths <7.0 mcd.

The graph in Figure 4.19a shows the full range of diatom concentrations across the entire lake sediment interval. Displaying the very high abundance of ~2750 dv/view at 5.3 mcd visually compresses the variation shown by lower-concentration samples that occur at deeper depths. Therefore, the results are displayed in Figure 4.19b with a truncated 'Diatom valve/view' scale (0-600 valves) that effectively excludes the highest concentration results but better highlights the variation at lower concentrations.

Diatoms are generally scarce below 6.5 mcd, but this interval includes several zones in which diatom concentrations increase (Figure 4.19b). These are at depths of ~12.1, 11.4, and 10.3 mcd (~15-45 dv/view) and from ~8.2 to 7.4 mcd (~60-180 dv/view). Diatom abundance increases sharply from 6.5 mcd, with peaks of 1052 dv/view at 5.7 mcd and 2763 dv/view at 5.3 mcd. There is a relative reduction in diatom abundance between ~5.1 and 4.5 mcd (250-450 dv/view) before a final peak of 750-850 dv/view between ~4.4 and 4.1 mcd. The diatom concentration drops sharply at ~3.8 mcd before recovering slightly to 143 dv/view at the top of the lake sediments.

The pattern of diatom concentration variability throughout the lake sediments is similar to that shown by the two biogenic silica analyses. The three datasets are shown together in Figure 4.20. Initial attempts to display normalised results for the

three datasets were less than ideal. Normalising the dv/view data with the dv/view-maximum-value (at 5.3 mcd) skewed all other dv/view data to low values that suppressed the variability relative to the FTIRS and Moly-blue BioSi-wt% results, especially below 6.5 mcd. Instead, all diatom dv/view results were divided by 20 to bring them into the range of the BioSi wt% scale while maintaining the original pattern. This method renders the BioSi wt% scale useless with respect to the diatom dv/view data, but that is of little relevance as the goal is to visually compare the plotted datasets.

All but one diatom data point is displayed within the 0-70% range shown in Figure 4.20a. The missing data point is the highest dv/view peak at 5.3 mcd, where the adjusted value is 138. The graphs do show that the three different datasets have very similar patterns of abundance throughout the HMC M1-2 lake sediment deposit. Abundance increases sharply above 7.0 mcd and decreases between ~5.1 and 4.5 mcd and at ~3.8 mcd before a final uptick at the top of the lake sediments.

To better display variations in the low concentration region below 7.0 mcd, Figure 4.20b displays data in the 0-20% range. This range excludes the FTIRS data but similarities between it and the Moly-blue BioSi dataset were established earlier (Figure 4.17b). Small abundance peaks in the diatom-based dataset correlate with Moly-blue BioSi peaks at ~12.1, 11.4, and 10.3 mcd, as does the more sustained peak from ~8.4 to 7.4 mcd.

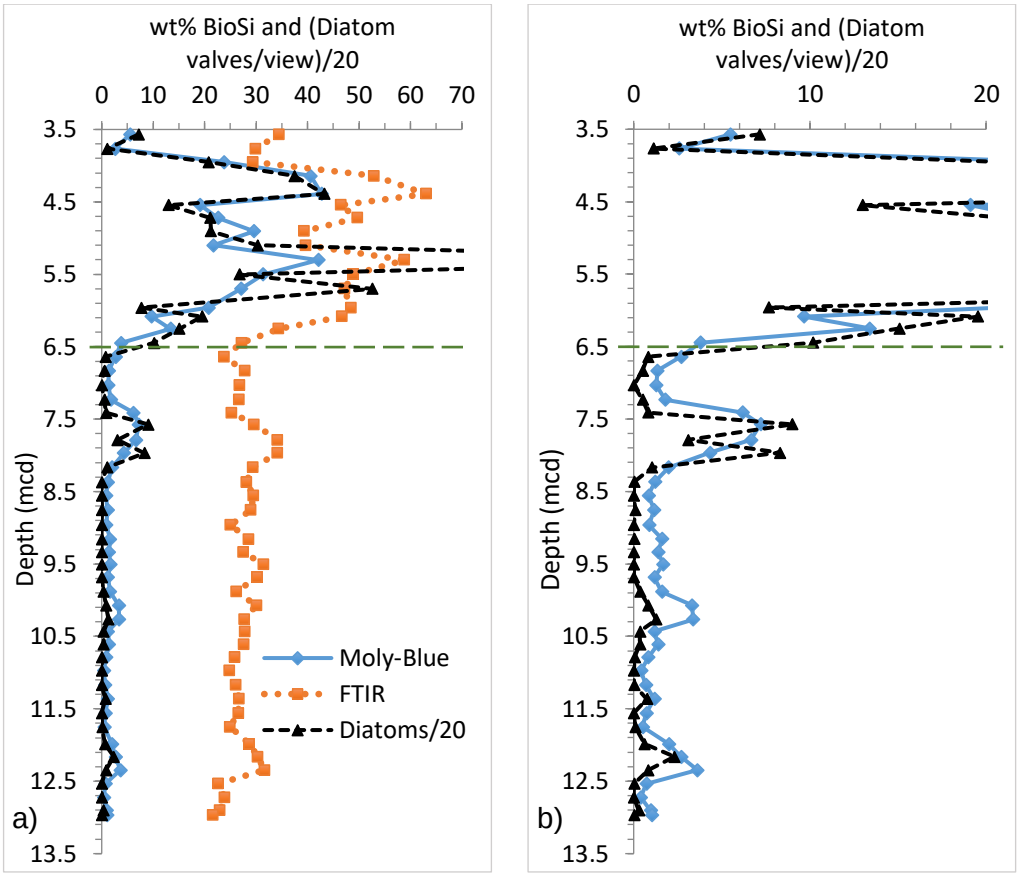

Figure 4.20: Comparative BioSi analyses result graphs with relative diatom concentration change throughout the HMC M1-2 lake sediments, shown at two different scales. The diatom valve/view results were divided by 20 to bring them into a comparable range with the BioSi wt% results. Dashed green line at transition zone between Diatom Poor (DP) lower biofacies and Diatom Rich (DR) upper biofacies: a) 0-70% range displays all but the highest diatom/view result (5.3 mcd offscale high at 138); b) 0-20% range better displays variations at low concentrations in sediment core depths <7.0 mcd.

Results for the multiple biologically-focussed analyses show a distinction at ~6.5 mcd between the lower and upper sediments of the HMC M1-2 lake sediment deposit. This depth corresponds to the junction between Core Section #7 and #6. This also correlates to the findings of the laminae couplet thickness analysis (Table 4.2), where the laminae couplet thickness differs in core sections above and below 6.5 mcd (~0.66 mm above and ~1.09 mm below). Two major biofacies can be assigned from the sum of the data. As the origin of the BioSi is strongly correlated with the concentration of diatoms in the lake sediments, the biofacies designations are as follows:

- **Diatom-poor (DP)** biofacies from 13.0 to 6.5 mcd, and;
- **Diatom-rich (DR)** biofacies from 6.5 to 3.56 mcd.

A dashed green line on the following graphs (as well as Figure 4.20) identifies the transition zone separating the lower DP biofacies from the upper DR biofacies.

4.4.2 Chrysophycean Cysts

Chrysophycean cysts are silica-walled statospores that are generated during the life cycle of chrysophycean algae, commonly known as golden brown algae (Smol, 1988). Chrysophycean algae are typically planktonic and common in cool oligotrophic lakes (Smol, 1988) Individual chrysophycean cysts were inventoried at 400x magnification using the differential interference contrast (DIC) light microscopy technique. They were recorded by abundance of morphological types as per the standards of the International Statospore Working Group (ISWG) (Wilkinson *et al.*, 2002) for each of the 51 smear slides throughout the lake sediment deposit. Chrysophycean cysts have rarely been positively associated with the chrysophyte algae from which they were formed. Subsequently, by the ISWG standards, chrysophycean cyst morphological types are given numerical designations (Sandgren *et al.*, 1995; Last *et al.*, 2001; Wilkinson *et al.*, 2002). Studies surveying these cysts determine the numeric designation for cysts observed in the study material by comparison with the ISWG morphotypes (Smol, 1988; Sandgren, 1991).

The cyst morphotypes that comprised greater than 5% of the total observed are shown in Figure 4.21. The total abundance of chrysophycean cysts is presented here as average cysts/view (Figure 4.22).

Cyst 1/29/46 (hereafter referred to as Cyst 1) and Cyst 9/120/189 (hereafter referred to as Cyst 9) are amongst a group of cyst morphotypes that are morphologically identical (spherical, with no collar) and differ only in size when observed by light microscopy techniques. Each group has minor distinctions in pore geometry but these can only be discerned by SEM, so size is the criterion by which these groups have been classified.

Cyst 1 (Figure 4.21a and b) is of the small variety, $\leq$ 5.9 μm. Cyst 9 (Figure 4.21c and d) is of medium size (6–8.9 μm). Cyst 156 (Figure 4.21e and f) is also of medium size (7–10 μm) and has a short conical collar around the pore that is rounded at the outside edge. The collar in the SEM image (Figure 4.21e) is presumed to show effects of weathering since deposition. Cyst 384 (Figure 4.21g and h) is small (4.5–7.7 μm) and spherical, with a wide conical collar and small conulae (projections) scattered over the surface.

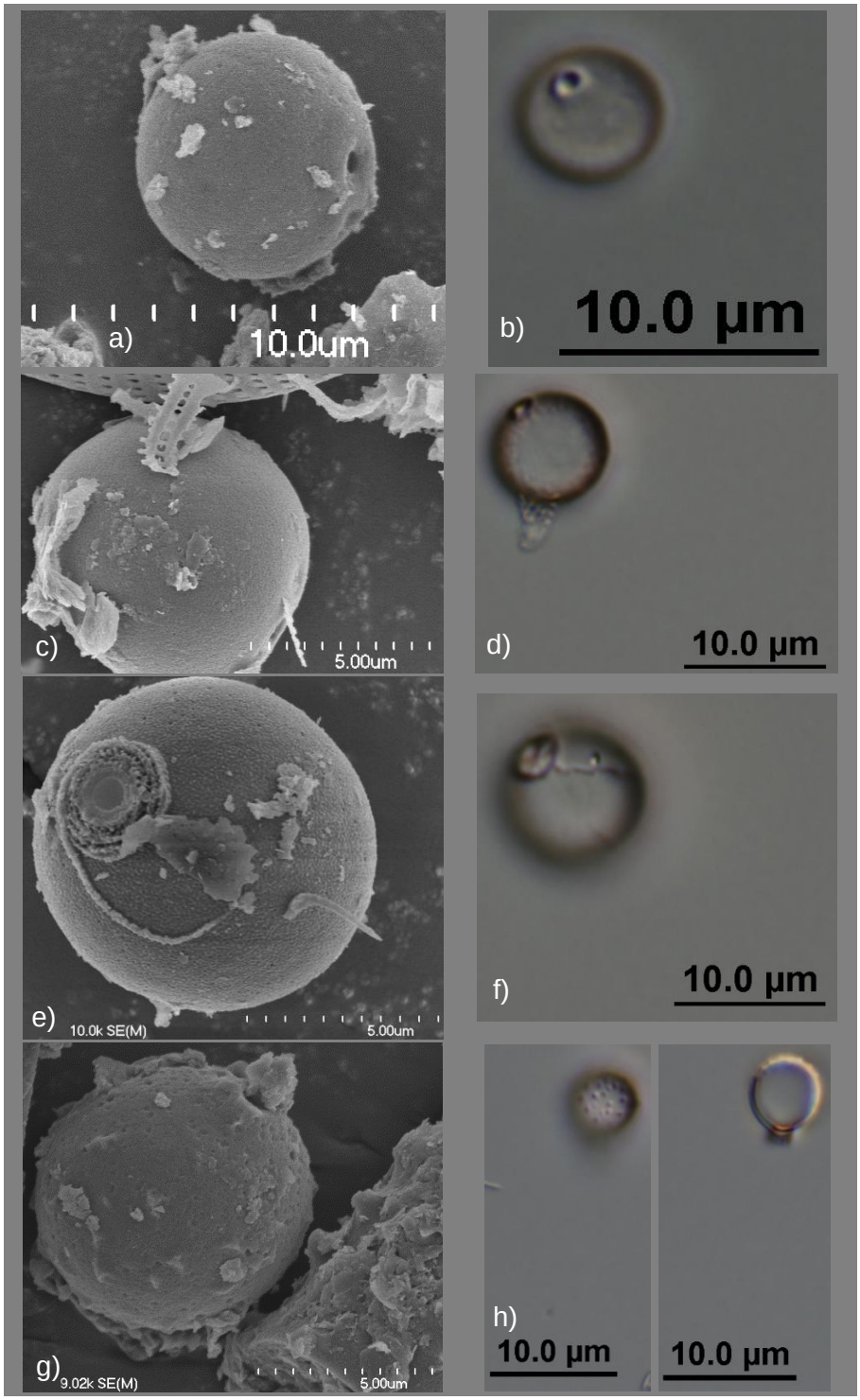

Figure 4.21: Images of chrysophycean cysts, via SEM at left and DIC LM at right: a) and b) Cyst morphotype 1/29/46; c) and d) Cyst morphotype 9/120/189; e) and f) Cyst morphotype 156; g) and h) Cyst morphotype 384: two different focal planes of same individual in LM showing; (left) surface conulae (projections) and; (right) cross section with collared pore.

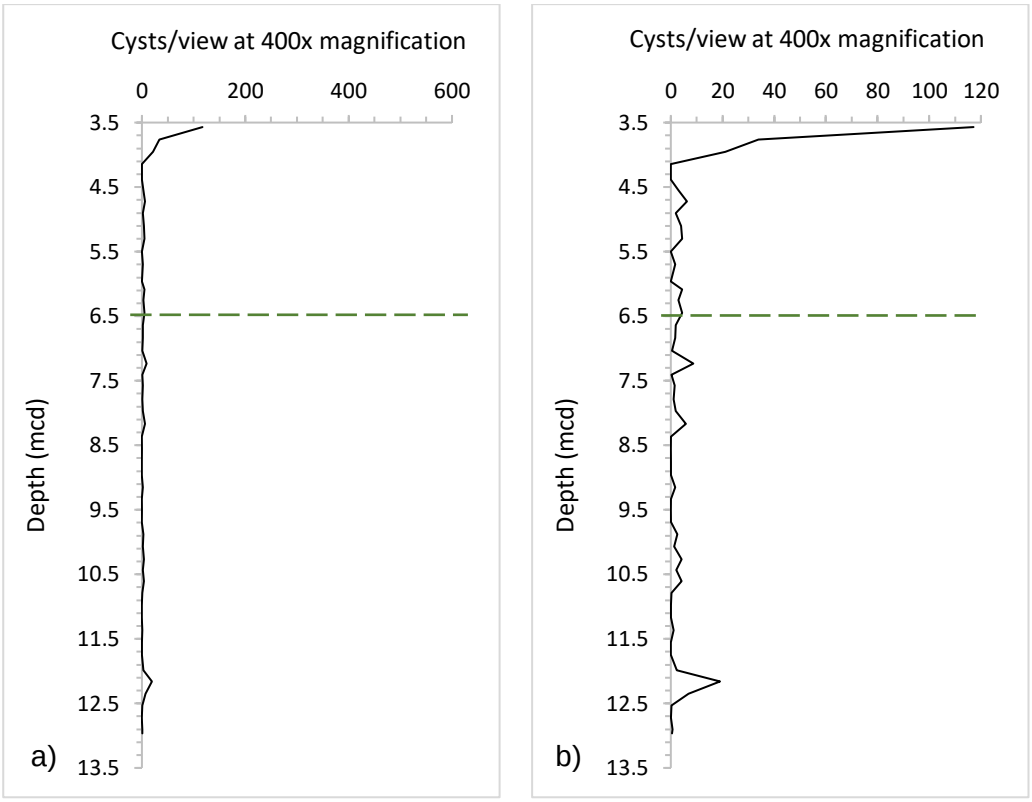

Figure 4.22: Cysts/view at 400x magnification in the HMC M1-2 lake sediment deposit: a) 0-600 range of cysts/view, to be visually comparable with the low-range diatom valves/view in Figure 3.4.1b; b) 0-120 range of cysts/view showing variability in cyst abundance throughout the lake sediment deposit.

In comparison to diatom valves, chrysophycean cysts are a minor component in the overall abundance of biosiliceous material (Figure 4.22a). The concentration of chrysophycean cysts is variable and alternates between presence and absence. The greatest abundance occurs above 4.0 mcd, where the concentration increases from zero to 120 cysts/view over the uppermost 0.5 m of lake sediments (Figure 4.22b). At depth, the highest peak is around ~12.2 mcd, with several small peaks at other depths upcore. One peak at ~10.2 mcd coincides with a small diatom peak, while increases at ~8.2 and 7.2 mcd occur just below and just above the diatom peak in that region, which is at ~8.4 to 7.4 mcd.

The abundances of the four most common cyst morphotypes is shown in Figure 4.23. Cyst 1 contributes the greatest proportion to the total cyst concentrations at depths below ~4.2 mcd. Near the top of the lake sediments at ~4.0 mcd, Cyst 384 is the first to increase in abundance relative to the other types. In the overlying sample (~3.8 mcd) Cysts 1, 9 and 156 abruptly increase in abundance while Cyst 384 declines. This is the depth at which diatom concentration drops sharply (Figure 4.19b). Cysts 1, 9 and 156 are at their greatest abundance at the top of the lake sediments.

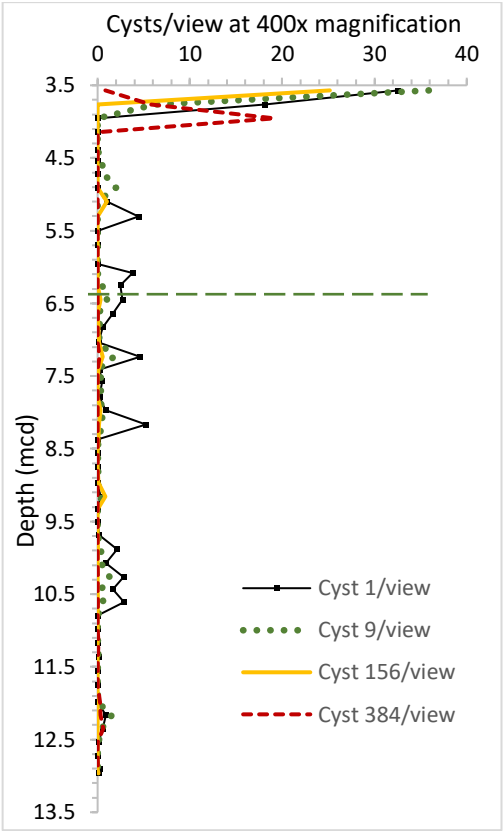

Figure 4.23: Cysts/view at 400x magnification for four morphotypes (1, 9, 156, and 384) that each comprise more than 5% of the total cysts in the HMC M1-2 lake sediment deposit.

4.4.3 Freshwater Sponge Spicules

The siliceous spicules of freshwater sponges (*Porifera* → *Demospongiae* → *Spongillidae*) were inventoried at 400x magnification using the differential interference contrast (DIC) light microscopy technique (3.3.3 DIC LM Imagery). Fig. 4.24 includes several examples of them.

Large (2 mm diameter) intact gemmules of *Spongilla* (Lamarck) were found in HMC Maar #1 by Kaulfuss *et al.* (2018). The gemmuloscleres of Spongilla are curved with blunt apices (Manconi & Pronzato, 2002). However, gemmuloscleres of that description were not witnessed in this study.

The megascleres (Fig. 4.24c-e) do not possess characteristics that allow for taxanomic classification. However, the length and shape of the gemmuloscleres, and the absence of microscleres in the deposit, point toward *Umborotula bororensis* as the likely sponge species (Manconi & Pronzato, 2002; Ruengsawang *et al.*, 2017). The tips of *Umborotula sp.* gemmuloscleres are birotular, as seen in Fig. 4.24i and j (Manconi & Pronzato, 2002; Ruengsawang *et al.*, 2017). Partial dissolution of the biosiliceous material is thought to be the cause for the blunted form of the gemmulosclere apices in Fig. 4.24g and h.


a)
5.0kV 11.9mm x1.00k SE(M)
50.0um
b)
200 µm
c)
50.0 µm
d)
50.0 µm
e)
10.0 µm
f)
20.0 µm
g)
5.0kV 12.3mm x2.50k SE(M)
20.0um
h)
10.0 µm
i)
5.0kV 12.2mm x2.49k SE(M)
20.0um
j)
50.0 µm

Figure 4.24: (Previous page) Examples of freshwater sponge spicules in the HMC M1-2 lake sediments. Scales unique to each image. a) SEM image of spicule variety, 1000x magnification; b) DIC LM image of spicule variety at 100x magnification; c) thick-walled megascleres; d) thin-walled megascleres; e) filamentous megascleres; f) siliceous nodule; g) and h) SEM and DIC LM of gemmuloscleres with different apices (one rounded and one blunt); i) and j) SEM and DIC LM of birotular gemmuloscleres.

Extant examples of *Umborotula* are epiphytic, forming circular to irregular crusts on aquatic plant stems or on the underside of floating leaves (Manconi & Pronzato, 2002). *Umborotula bororensis* are presently found from southeast Asia to east Australia but are not found in New Zealand (Manconi & Pronzato, 2002).

The survey recorded the abundance of several spicule types (see Fig. 4.24): thick-walled megascleres (c), thin-walled megascleres (d), filamentous megascleres (e), siliceous nodules (f), and gemmuloscleres (g-j) for each of the 51 smear slides throughout the lake sediment deposit. The total abundance of all spicules is presented here as average spicules/view (Figure 4.25).

Spicules account for a small number of individuals per view due to the fact that they are physically many times larger than the diatom valves and chrysophycean cysts. Nevertheless, taking inventory of them in this way gives results that are consistent and comparable with the diatoms and cysts.

Spicules are the only component found at many depths in the absence of diatoms or chrysophycean cysts. With the exception of four samples in the upper diatom-rich zone, spicules are found throughout the sediments (Figure 4.25). When present, the concentration of spicules/view ranged from 0.05 to 5.90 (at ~12.7 and 7.0 mcd, respectively). The greatest consistent abundance of spicules occurs in the sediments between ~9.5 and 5.9 mcd. The two depth ranges with the lowest concentrations of spicules are from ~13.0 to 9.7 m and ~5.7 to 3.9 mcd. Like the chrysophycean cysts, the concentration of spicules increased over the upper 0.5 m of the lake sediment deposit.

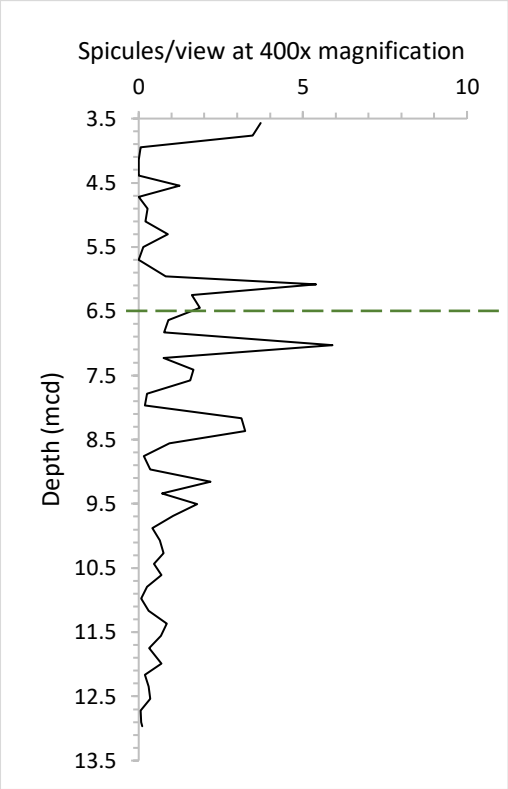

Figure 4.25: Total spicules/view throughout the HMC M1-2 lake sediment samples at 400x magnification.

4.4.4 Pollen

Although pollen abundance is not officially within the scope of this study, pollen grains were included in the notes taken during the smear slide surveys (Figure 4.26). Core sections in the DLCS/DP facies had a high occurrence of observed pollen grains compared to the upper DLDA/DR facies.

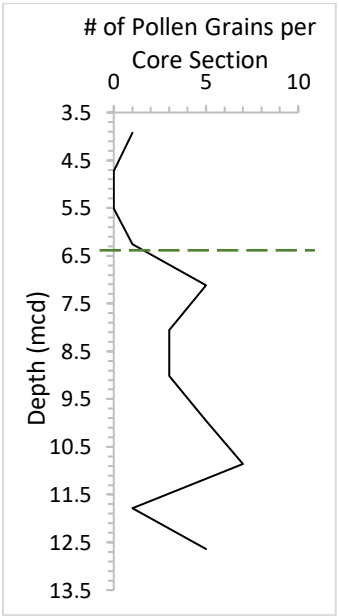

Figure 4.26: Number of pollen grains observed in each core section at 400x magnification.

4.5 Diatom Distribution by Species

Presented here are the diatom species that make up >2% of the total in any of the HMC M1-2 lake sediment smear slide samples in which survey counts reached values of >300 valves (which is the minimum required to be statistically significant: C. Riesselman, personal communication, January 9, 2018). They are listed in order of abundance in Table 4.4, with the source of taxonomic determination following in parentheses. Also shown are the percent-occurrence at which each species peaked and the metres composite depth at which the peak occurred.

Table 4.4 Diatom species of significance in the HMC M1-2 lake sediment deposit. Taxonomic designations from algaebase.org (Guiry & Guiry, 2018).

Diatom Species	Taxonomic Designation attributed to:	% of Total Diatoms	Peak %-Occurrence	Depth (mcd) of Peak %
Encyonema mesianum	(Cholnoky) Mann	97.33	99.86	4.39
Staurosirella lapponica	(Grunow) Williams & Round	1.26	85.76	11.99
Sellaphora saugerresii	(Desmazières) Wetzel & Mann	0.70	3.00	6.45
Rossithidium nodosum	(Cleve) Aboal	0.33	6.16	11.36
Gomphonema affine	Kützing	0.16	17.16	12.91
Achnanthes exigua var. elliptica	Hustedt	0.10	3.40	11.99

Encyonema mesianum is by far the most dominant species in the HMC M1-2 lake sediments. It accounts for 97.3% of all diatom valves surveyed. The next five diatom species make up the remaining 2.67% of the total. While low in total percent-occurrence, there are two species that are responsible for a significant proportion of the diatoms surveyed in the depths at which they peak. These are *Staurosirella lapponica*, which makes up ~86% of diatom valves at 11.99 mcd, and *Gomphonema affine* which peaks at ~17% at the base of the lake sediments (12.91 mcd). *Sellaphora saugerresii*, *Rossithidium nodosum*, and *Achnanthes exigua var. elliptica* have peak percent-occurrences of ~3 to 6%.

4.5.1 Encyonema mesianum

Encyonema mesianum (Figure 4.27) is an asymmetrical biraphid diatom species ~25-40 μm across. *Encyonema* species are widely distributed, typically temperate, and exist in a broad spectrum of environmental conditions (Wehr & Sheath, 2003). They are primarily benthic, being epilithic and epiphytic (often metaphytic), attaching by gelatinous matrices to substrates (Round *et al.*, 1990; Murakami *et al.*, 2009).

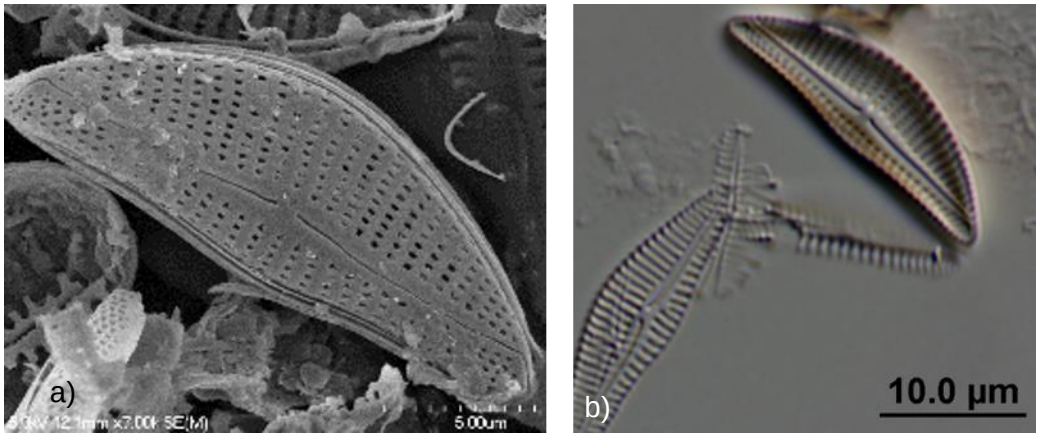

Figure 4.27: *Encyonema mesianum*, both images from the HMC M1-2 lake sediment deposit: a) SEM image from the top of the lake sediments, 7000x magnification; b) DIC LM image from sample at ~10.1 mcd, 1000x magnification.

E. mesianum are ubiquitous in the HMC M1-2 lake sediment deposit (Figure 4.28a). The proportion of *E. mesianum* is variable (~8-55%) at the base of the lake sediments (from 13.0 to 11.0 mcd) before becoming dominant (>90%) above ~10.6 mcd.

The concentration of *E. mesianum* (Figure 4.28b) is presented to show the abundance of the species for comparison to its percent-occurrence in the total diatoms at any given depth. The number of *E. mesianum* is very low until above ~6.5 mcd where they begin to account for a significant proportion of the sediments.

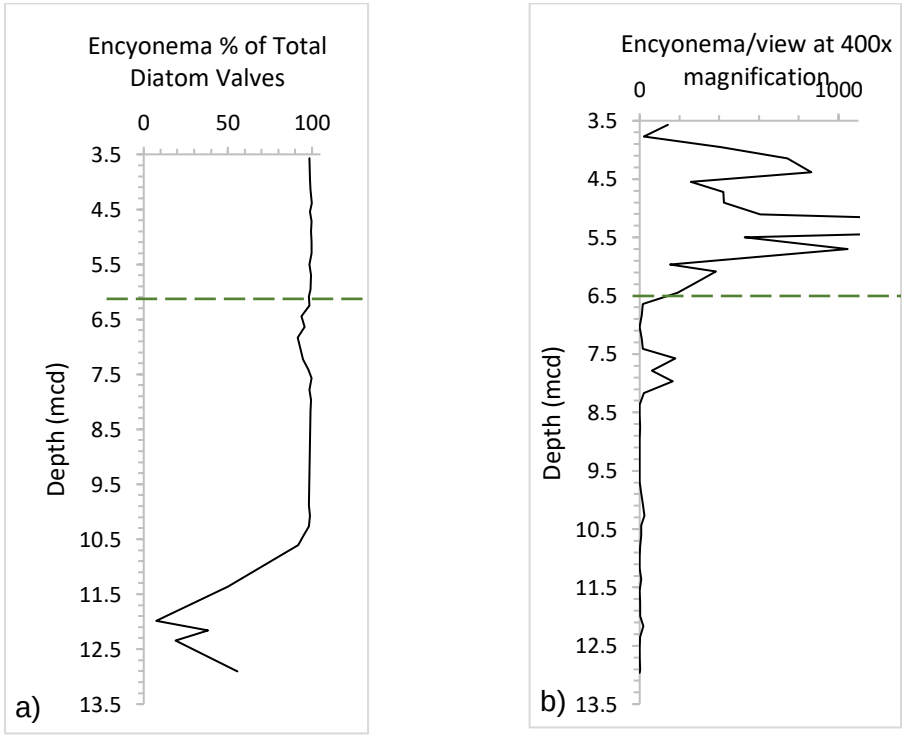

Figure 4.28: a) Percentage of total diatom abundance which is composed of *Encyonema mesianum* throughout the HMC M1-2 lake sediment deposit. b) Concentration of *E. mesianum* in dv/view at 400x magnification. Dv/view scale is reduced to show the variability at low values below 6.5 mcd. One missing data point of 2753 dv/view at 5.3 mcd.

Figure 4.29 further displays the dominance of the *E. mesianum* species as a contributor to the total diatom valves surveyed throughout the HMC M1-2 lake sediments. The plot for the concentration of *E. mesianum* is virtually identical to that of all diatoms observed in the deposit, with the exception of at ~12.2 mcd. At that depth the contribution of *E. mesianum* to the total is less than half.

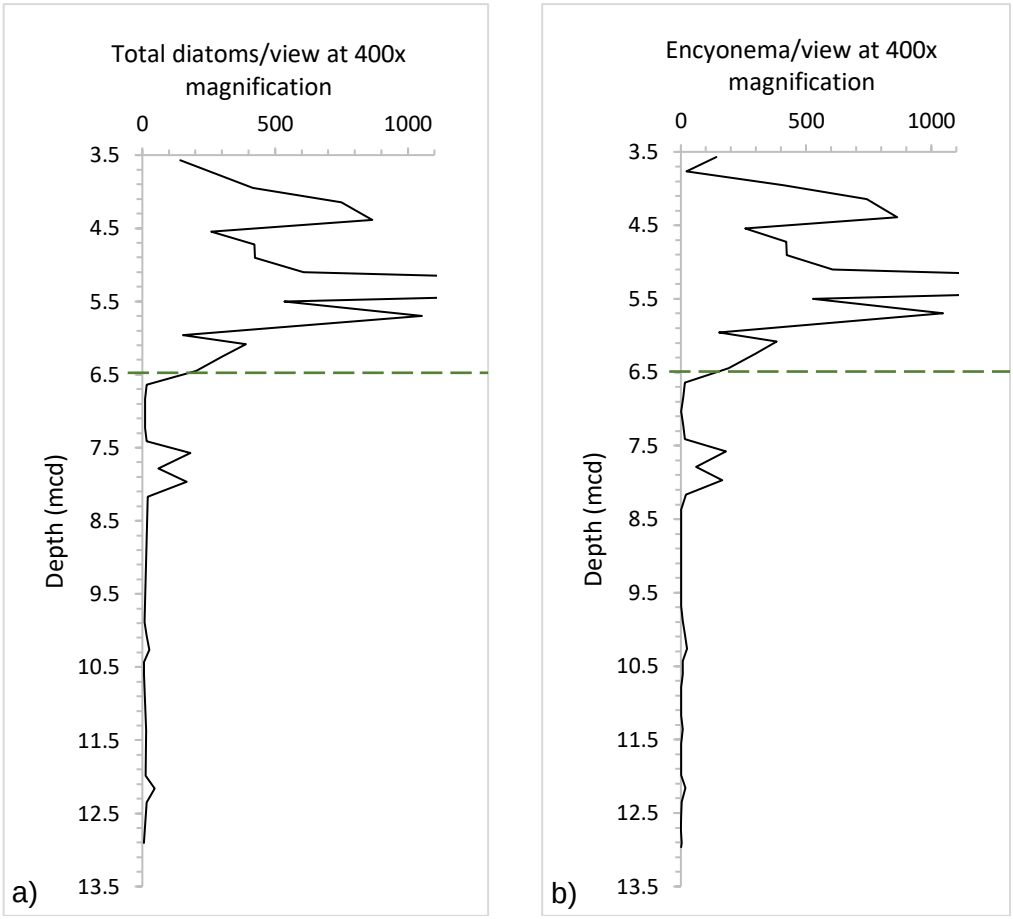

Figure 4.29: Comparison between concentration of a) all diatom valves observed, and; b) *E. mesianum*.

4.5.2 Staurosirella lapponica

Staurosirella lapponica (Figure 4.30) is a small bilaterally symmetrical araphid diatom species. It occurs in the HMC M1-2 lake sediments in the ~8-12 μm-size range. *S. lapponica* are episammic and epiphytic, attaching to benthic substrates in shallow lentic waters by short mucilaginous stalks or pads (Round *et al.*, 1990; Wehr & Sheath, 2003; Spaulding & Edlund, 2008; Murakami *et al.*, 2009). Studies record *S. lapponica* in cool waters to waters as warm as 30-40°C. At some locations in Iceland and Finland it has been found in waters with elevated pH (up to 8.6) and conductivity (up to ~500 μScm^{-1}) (EDDI; Fallu *et al.*, 2002; Owen *et al.*, 2008; Morales *et al.*, 2010), although it was classified by Haworth (1972) as being indifferent with regards to pH.

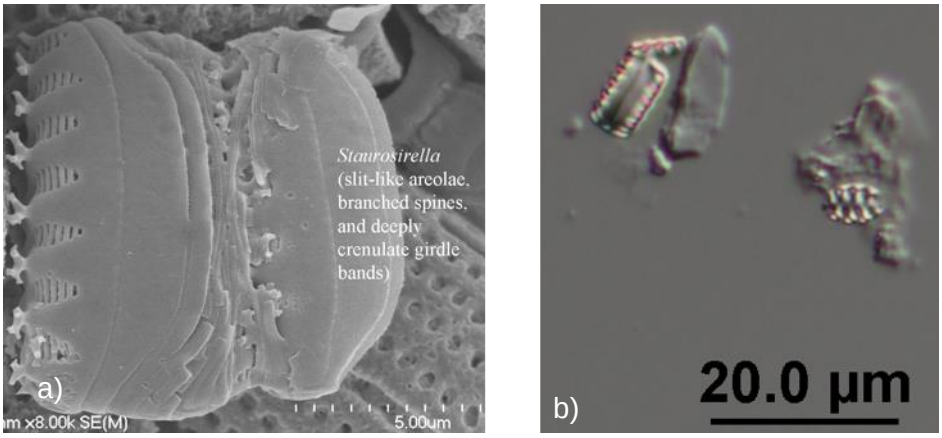

Figure 4.30: *Staurosirella lapponica*, both images from ~11.4 mcd in the HMC M1-2 lake sediment deposit: a) SEM image, 8000x magnification; b) DIC LM image, 400x magnification.

S. lapponica is the most abundant of the non-dominant diatom species present in the HMC M1-2 sediments (1.26%). Its distribution is restricted to depths below 11.3 mcd (Figure 4.31b). It ranges in percent-abundance from 26 to 85%, with the peak being at 12.0 mcd (Figure 4.31a).

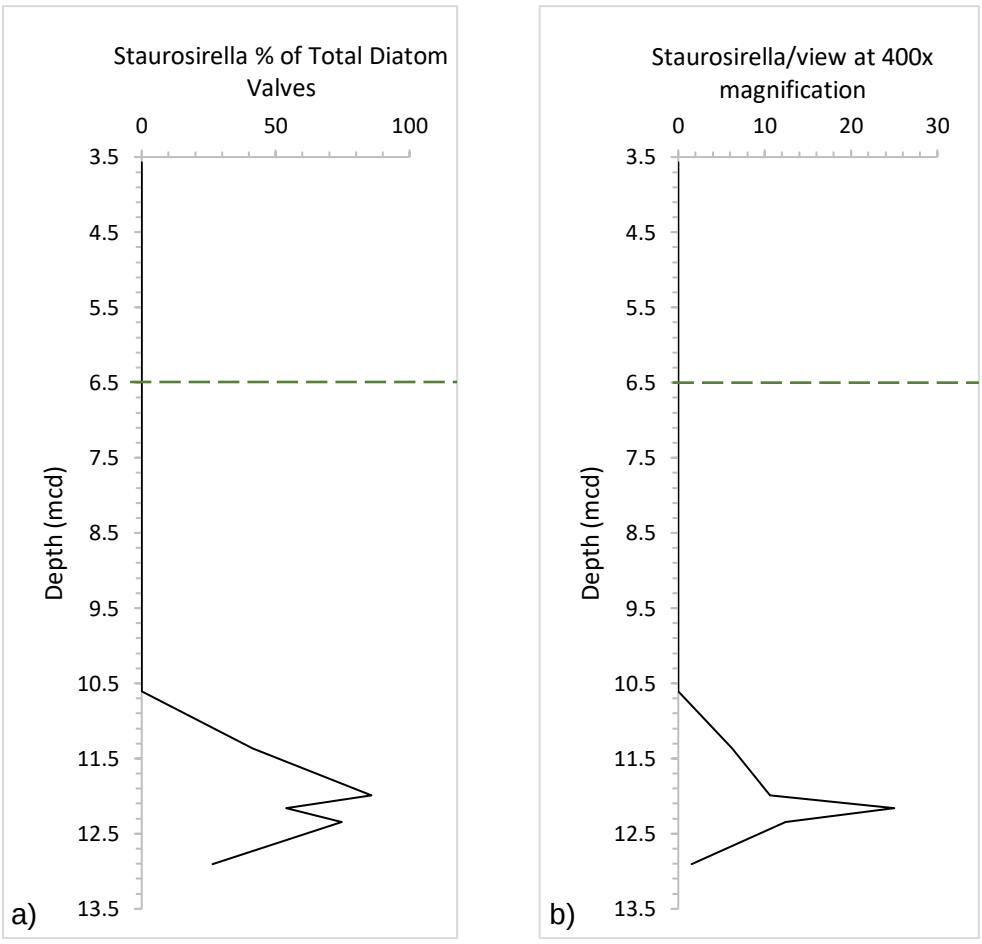

Figure 4.31 a) Percentage of total diatom abundance which is composed of *Staurosirella lapponica* throughout the HMC M1-2 lake sediment deposit; b) Concentration of *S. lapponica* in dv/view at 400x magnification.

4.5.3 *Sellaphora saugerresii*

Sellaphora saugerresii (Figure 4.32) is a small (10-12 μm) symmetrical biraphid species. It inhabits benthic substrates and tends to be alkaliphilous, being found in North American and European lakes having pH ranges from 7.1-8.0 and conductivity from 28 to 423 μScm^{-1} (EDDI; Spaulding *et al.*, 2010a; DPDC, 2017). It has been observed in association with *Staurosirella lapponica* in cooler outflows from alkaline springs (Owen *et al.*, 2008).

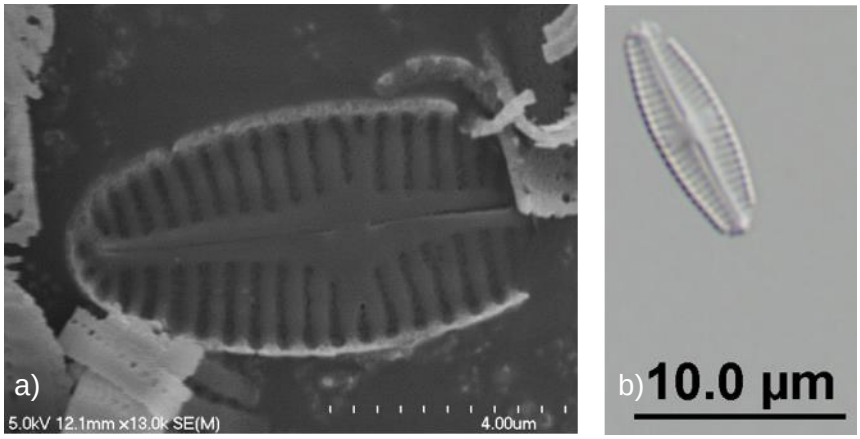

Figure 4.32: *Sellaphora saugerresii*, both images from the HMC M1-2 lake sediment deposit: a) SEM image from ~4.6 mcd, 13,000x magnification; b) DIC LM image from 5.5 mcd, 1000x magnification.

S. saugerresii makes up 0.7% of the total diatoms surveyed. Its distribution in the HMC M1-2 sediments is almost entirely above 6.5 mcd (Figure 4.33b). One sample at 6.45 mcd has >2% of *S. saugerresii* (3.0%) (Figure 4.33a).

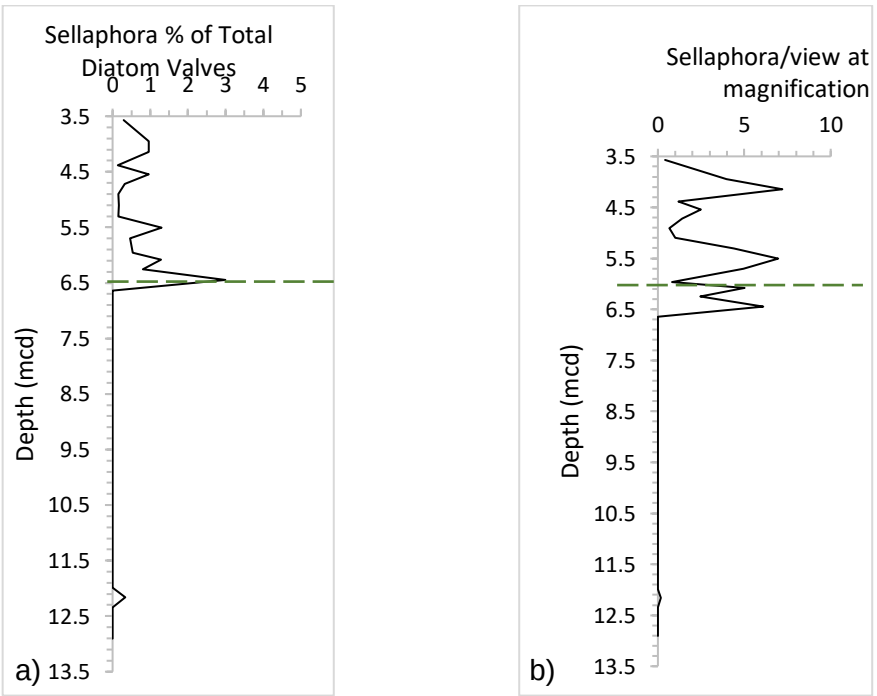

Figure 4.33: a) Percentage of total diatom abundance which is composed of *Sellaphora saugerresii* throughout the HMC M1-2 lake sediment deposit; b) Concentration of *S. saugerresii* in dv/view at 400x magnification.

4.5.4 Rossithidium nodosum

Rossithidium nodosum (Figure 4.34) is a small (9-12 μm) benthic monoraphid diatom that uses a mucilaginous stalk to attach itself to substrates (Spaulding *et al.*, 2010b). It has been recorded in cold oligotrophic waters, including lakes in northern Europe having low conductivity and pH ranges from 7.1 - 7.4 (EDDI; Spaulding *et al.*, 2010b).

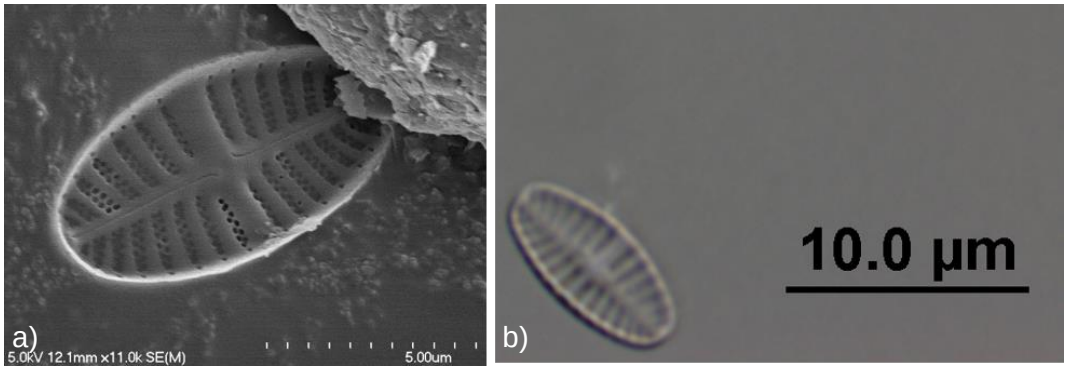

Figure 4.34: *Rossithidium nodosum*, both images from the HMC M1-2 lake sediment deposit: a) SEM image from the top of the lake sediments, 11,000x magnification; b) DIC LM image from ~4.7 mcd, 1000x magnification.

0.33% of the total diatoms surveyed in the HMC M1-2 lake sediment deposit consist of *R. nodosum*. Their concentration/view (Figure 4.35b) peaks at the same depths as *E. mesianum* in the DP biofacies, but drops off above ~6.1 mcd. The distribution of samples that contain >2% *R.nodosum* is exclusively in sediments deeper than 6.5 mcd (DLCS facies) and are clustered into two peaks, one between 12.35 and 10.61 mcd and another from 7.23 to 6.64 mcd. The peak of 6.16% occurs at ~11.4 mcd (Figure 4.35a).

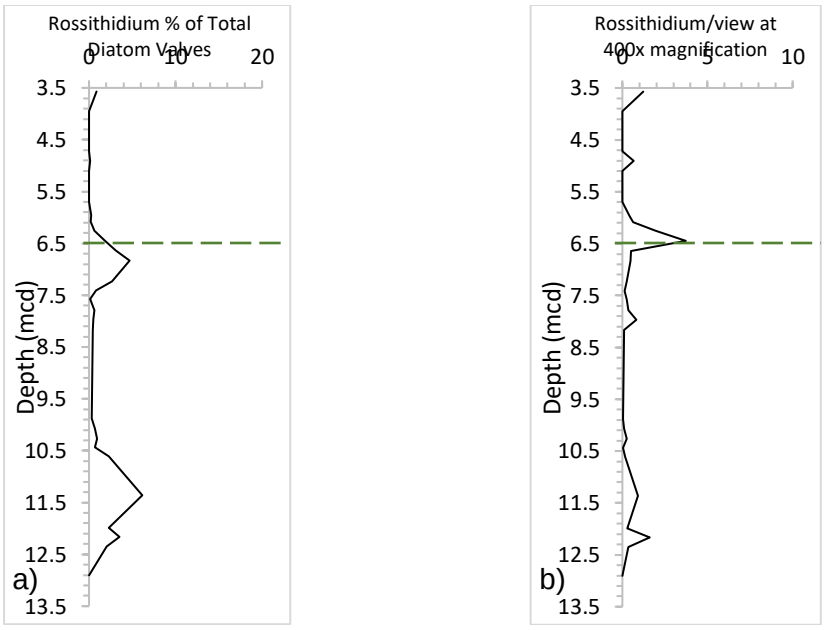

Figure 4.35: a) Percentage of total diatom abundance which is composed of *Rossithidium nodosum* throughout the HMC M1-2 lake sediment deposit; b) Concentration of *R. nodosum* in dv/view at 400x magnification.

4.5.5 Gomphonema affine

Gomphonema affine (Figure 4.36) is an asymmetrical biraphid diatom species ~70 μm in size. It is considered to be a haptobenthic species (hard bottom-surfaces) that attaches to substrates by mucilaginous stalks (Round *et al.*, 1990; Murakami *et al.*, 2009). It is a cosmopolitan species that has been observed in abundance ranges similar to the HMC M1-2 lake sediments in circumneutral (pH 6.5 - 7.5) lentic waters with low conductivity (Wehr & Sheath, 2003; Barinova *et al.*, 2010; Bere & Mangadze, 2014).

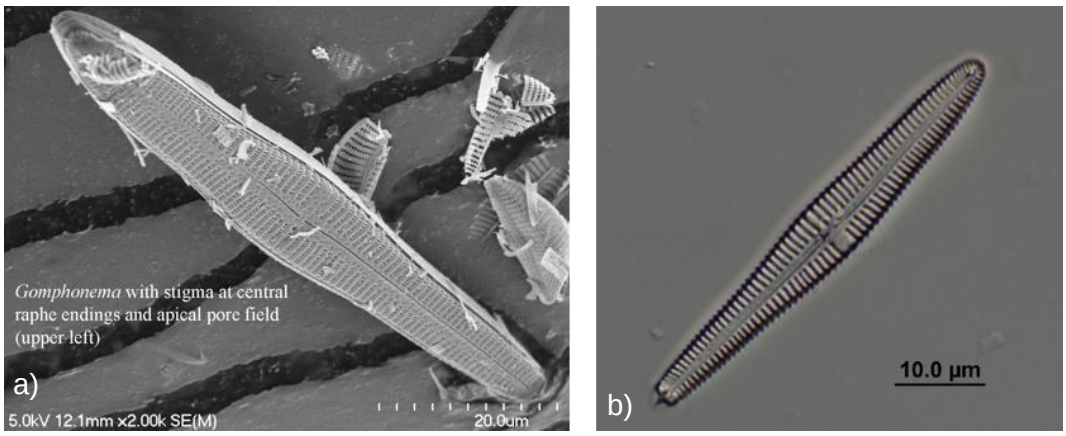

Figure 4.36: *Gomphonema affine*, both images from the HMC M1-2 lake sediment deposit: a) SEM image from ~4.6 mcd, 2000x magnification, includes some E. mesianum; b) DIC LM image from the top of the lake sediments, 1000x magnification.

G. affine occurs in very low abundance overall (0.16%), but it accounts for a significant percentage of the initial base lake sediments (17.16% at 12.9 mcd) (Figure 4.37b). Two other depths where this species is found above 2% are at 10.6 and 10.4 mcd (4.92 and 2.67% respectively). All other samples have less than 2% *G. affine*. In Figure 4.37a, the concentration of *G. affine* peaks at similar depths as *R. nodosum* and *E. mesianum*.

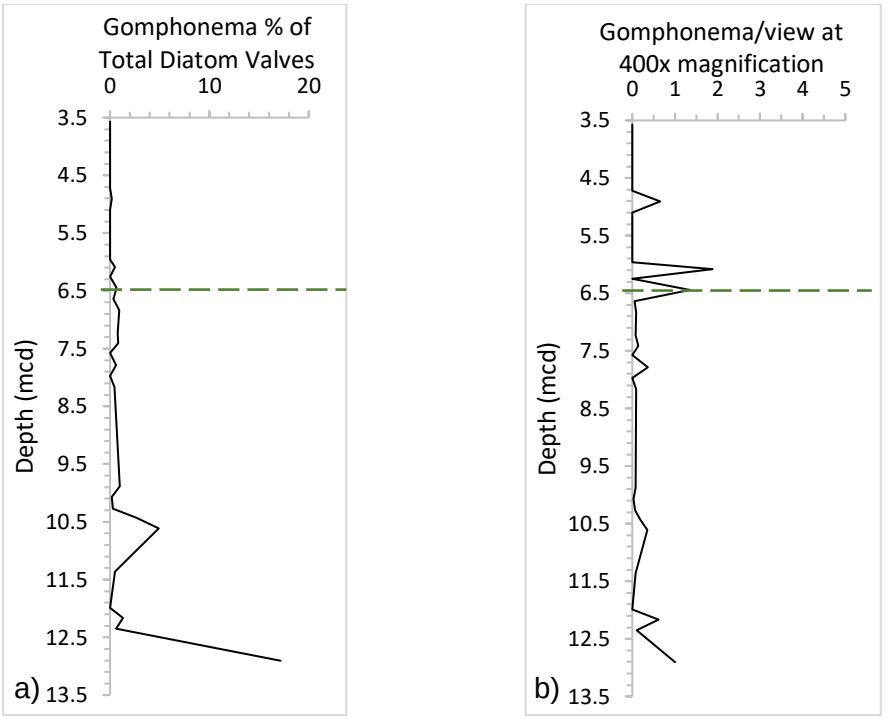

Figure 4.37: a) Percentage of total diatom abundance which is composed of *Gomphonema affine* throughout the HMC M1-2 lake sediment deposit; b) Concentration of *G. affine* in dv/view at 400x magnification.

4.5.6 Achnanthes exigua var. elliptica

Achnanthes exigua var. elliptica (Figure 4.38) is a benthic monoraphid diatom species ~20 μm in size. It is alkaliphilous, able to tolerate pH as high as 9.2 in lakes having very high conductivity (up to 13,500 μS/cm^{-1}) (EDDI; Haworth, 1972).

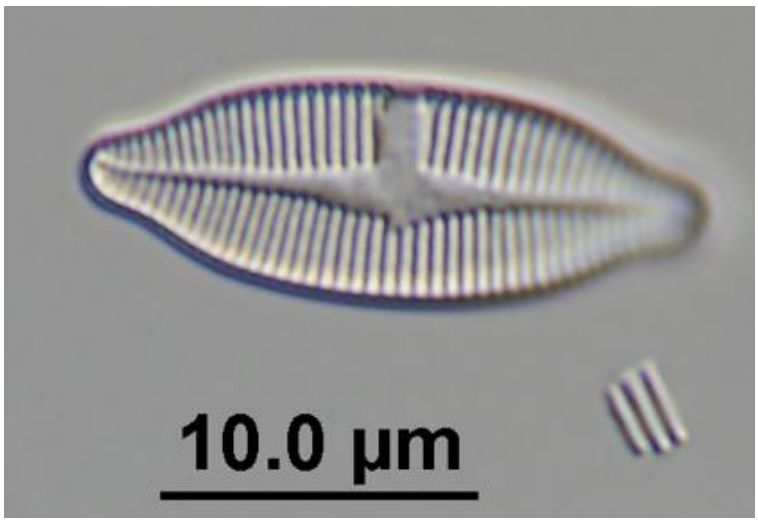

Figure 4.38: DIC LM image of *Achnanthes exigua var. elliptica* image from 5.5 mcd in the HMC M1-2 lake sediment deposit. 1000x magnification. Not found during surveys using SEM.

A. exigua var. elliptica contributes 0.10% of the total diatom abundance. There are two distinct peaks where the proportion of *A. exigua var. elliptica* exceeds 2% (Figure 4.39a). They are between 12.35 and 11.99 mcd (highest peak is 3.4%) and at 6.83 mcd. While the highest concentrations of *A. exigua var. elliptica* occur in

the DR biofacies (Figure 4.39b), they are a minor percent-contribution to the total diatoms due to the dominance of *E. mesianum*.

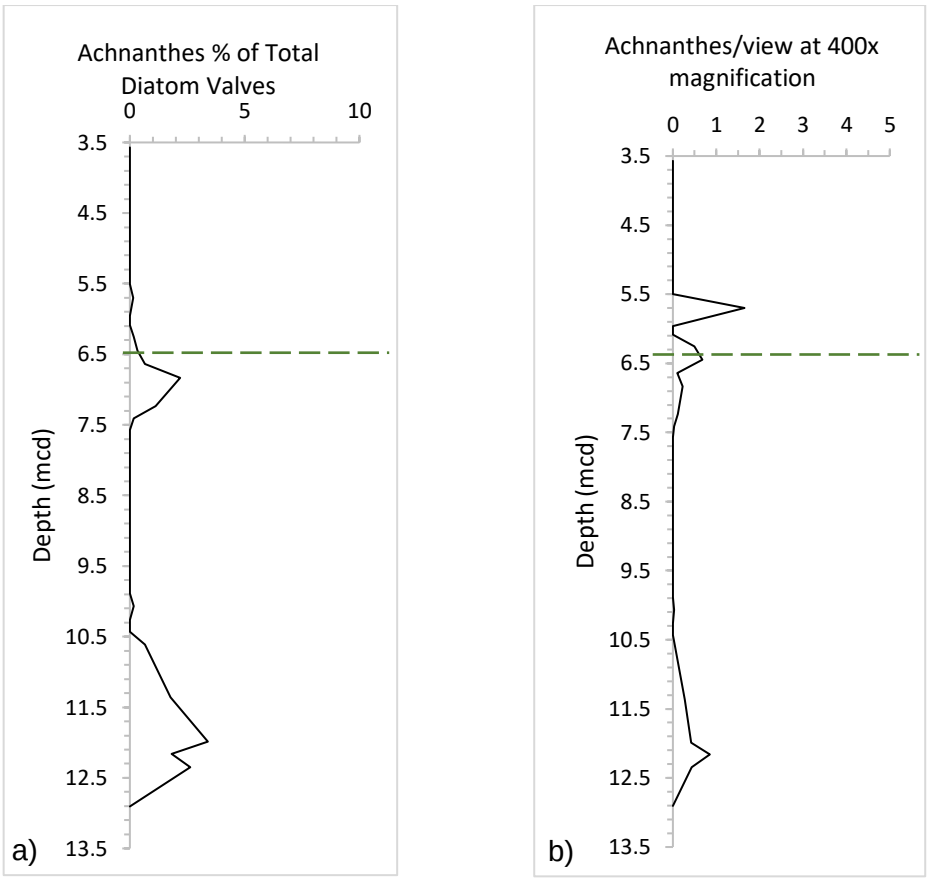

Figure 4.39: a) Percentage of total diatom abundance which is composed of *Achnanthes exigua var. elliptica* throughout the HMC M1-2 lake sediment deposit; b) Concentration of *A. exigua var. elliptica* in dv/view at 400x magnification.

Chapter 5

Discussion

This chapter will discuss uncertainties in the datasets which are not addressed in Chapter 3. The results will then be synthesised by sedimentological and biological characteristics in order to fashion an interpretation that identifies processes which account for changes in the character of the HMC Maar 1 lake sediment deposit from formation to fill.

5.1 Addressing Potential Issues

Issues that affect confidence in the data acquired for this study are addressed here.

5.1.1 Age Model Uncertainties

The 14.6±0.1 Ma absolute age estimate for the Hindon Maar Complex was obtained by palynomorph analysis and $^{40}Ar/^{39}Ar$ radiometric dating of the groundmass sample from a basanite boulder field in Maar #3 (Kaulfuss *et al.*, 2018). Previous palynological studies of the fossiliferous lake sediments in the HMC had constrained the upper age limit to the early Miocene (~16-23 Ma) (Kaulfuss & Moulds, 2015).

The eruptive period that generated all four maars in the HMC is thought to have been geologically short, possibly within a timespan of weeks or months (Kaulfuss *et al.*, 2018). Maar lake sediments can accumulate after a few hundreds to thousands of years after eruptive activity has ceased (Pirrung *et al.*, 2003; Pirrung *et al.*, 2008). The basanite boulder field is thought to have been emplaced in the maar complex near the end of the eruptive period that caused the formation of the entire HMC (Kaulfuss *et al.*, 2018). Consequently, the 14.6±0.1 Ma absolute age for the Maar #3 lake sediments adjacent to the boulder field, and by extension, Maar #1, is considered to be a reasonable estimate, therefore this study regards the HMC M1-2 lake sediment deposit to be mid-Miocene in age. Additional palynological analysis of these lake sediments is currently being undertaken to further corroborate their age. Radiometric dating on the volcaniclastic upper diatreme deposits at the base of the lake sediments may yet be done in the future.

The age-depth model presented in Table 4.2 is based on the number of lamina-couplets manually counted in dried core samples originally of ~35-55 mm length (when damp) (3.2.2 Lamina-couplet Thickness). I consider the age-depth model to be a reasonable estimate when assuming that laminae in lacustrine sediments

often reflect annual deposition intervals, especially where light and dark laminae alternate as consequence of an annual diatom bloom followed by seasonal deposition of detrital plant matter. Further support for the age-depth model is that the calculated lamina-couplet thicknesses are reasonable when compared to a review of varved deposits (Ojala *et al.*, 2012). One uncertainty in the age-depth model would originate from the couplet thickness measurements in the very dark sediments in Core Sections #7-13. Where the upper Core Sections #3-6 had laminae couplets that readily separated when dry, laminae in the dark sapropelic core were more difficult to differentiate from each other. It is possible that some laminae were missed in those counts, meaning that the calculated lamina-couplet thickness would be falsely high in this model.

Ideally, multiple thin-sections from samples of Core Sections #7-13 would be made, with the laminae orientation perpendicular to the long axis of the slides. Microscopic examination would reveal all of the laminae. However, this was outside the scope of this study. Nonetheless, in this study, ~290 mm of the ~5600 mm of dark laminated core in Core Sections #7-13 were analysed for laminae thickness, representing ~5% of all the total dark core sections. In that amount of sample length, the few laminae that could have been missed would not have a significant enough effect on the age model estimate to alter the findings of this study.

5.1.2 Disturbed Split Core

About 20% of the total core length is classified as ‘disturbed’, meaning core that is thought to have been deformed from its *in situ* condition by the drilling process (Figure 4.8 and Table 5.1). A high percentage of Core Sections #6 (upper half) and #7 (lower half) are highly segmented and deformed by mud injections (>50%). This makes bedding subtleties impossible to view in those intervals. If bedding structures were originally present, they could not be recognised in the core due to the condition it was in after drilling. Core Sections #6 and 7 are in the vicinity of the major facies transition zones so important sedimentological data has likely been lost. Nonetheless, there are sufficient Geotek physical property data adjacent to the disturbed regions to maintain adequate continuity, and the compositional and biological data are unaffected by disturbed core condition.

5.1.3 Geotek Density Analysis with Dry Split Core Sections

At <1.0 gcm^{-3}, the baseline bulk density for the HMC M1-2 sediments is very low. The sediments are high in sapropelic organic material which is characteristically of low density, but certainly not so low they would float in water in the condition they

were it while being processed, as these values would indicate. Upon return from performing Geotek analyses at the University of Otago and reviewing the data, I realised that the split core sections are meant to be water-saturated when analysed, to better emulate *in situ* conditions in the deposit. This is usually managed by misting some distilled water onto the split surface until the pore spaces are full. These core splits had not been prepared in that way so the density results have skewed low. However, as the mistake was consistently repeated, I believe that the relative pattern of changes in the density data over the length of the core is representative of actual density changes in the core. Density is the only physical property significantly affected by the core sections being not completely saturated.

5.1.4 FTIRS Data

Raw data acquired using the Fourier transform infrared spectroscopy technique (FTIRS) underwent post-analysis data processing by Spectrum Quant quantitative analysis software. During data processing, the raw data were compared against a three-component model (TOC, BioSi, and Otago Schist) developed for the specific purpose of determining the composition of HMC maar lake sediments by F. Garrity, another University of Waikato MSc candidate.

For each of the 51 HMC M1-2 lake sediment samples, the Spectrum Quant software generated results for the abundance of the three components, reported in wt%. When added together for each individual sample, the wt% values for the three components totalled from 96.97 to 136.24 wt%, which, left as it is, is not credible. Without having personally been involved with the development of the comparison model or the software parameters used to process the data, it is difficult for me to say what might be the cause of the issue. However, from my observations, it would seem that the results are either roughly being normalised by the program, or other components in the sediments that are not TOC, BioSi, or Otago Schist are erroneously being assigned to one or more of the three components, causing the total to be well over 100 wt% at times.

Absolute (wt%) FTIRS analysis results have been reported by other studies as having high correlation with classic wet chemistry-derived BioSi wt% values (Rosén *et al.*, 2011; Meyer-Jacob *et al.*, 2014a). The model and data processing software used in this study report the results as normalised rather than absolute values. Comparison of the FTIRS BioSi results with those acquired through classic alkaline dissolution wet chemistry (4.3.2 Biogenic Silica Wet Chemistry Results) shows that the FTIRS results, while showing a similar pattern of variability, are consistently higher. This study considers the wet chemistry BioSi wt% results to be absolute and accurate.

I have consequently normalised the FTIRS results for this study so the samples in the FTIRS dataset may be directly compared with each other. FTIRS data are considered as relative indicators of compositional change rather than absolute values.

5.1.5 Dissolution Effects on Diatom Data

There is evidence of dissolution of the biosiliceous material throughout the deposit, especially at depths below ~6.5 mcd. Several sponge megascleres exhibit circular corrosion pitting (Figure 5.1).

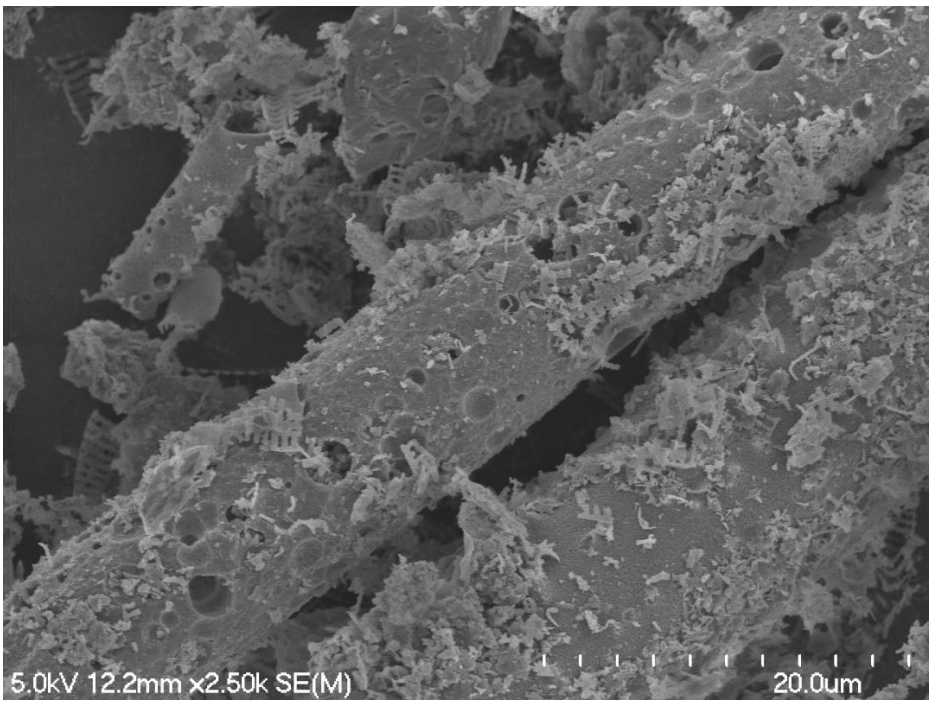

Figure 5.1: SEM micrograph (2500x magnification) of sponge spicule dissolution (large cylindrical megascleres) and *Encyonema* diatom valves (fragments on spicule surfaces) showing corrosion effects at ~7.8 mcd. There is pitting on the spicules, and the diatoms are missing all but the features most proximal to the centre of the valves.

Diatom valves show a range of corrosion effects, from widened areolae (Figure 5.2) to loss off all but the thickest central raphe nodule (Figure 5.3). As described in 3.3.4 Slide Surveys, the remaining central nodules of diatom valves were enumerated during the microscopic surveys. Some diatom valve data have most likely been completely lost to dissolution. Thin-walled diatoms such as *Encyonema* are more susceptible to dissolution than thicker-walled diatoms such as *Staurosirella* (4.5.2 *Staurosirella lapponica*). Differential dissolution rates of diatom species can result in a bias towards the more resistant species, potentially having significant consequences for palaeoenvironmental and palaeoecological studies (Ryves *et al.*, 2009). This study recognises that dissolution has occurred to varying degrees, especially below ~6.5 mcd. The dominant diatom throughout all but the deepest sediments in this study is a thin-walled *Encyonema* species. However, in

samples that showed the highest amount of dissolution, many central nodules and raphe fissures of *Encyonema* remained to be enumerated. Therefore, I consider dissolution effects to ultimately have little bearing on the findings of this study.

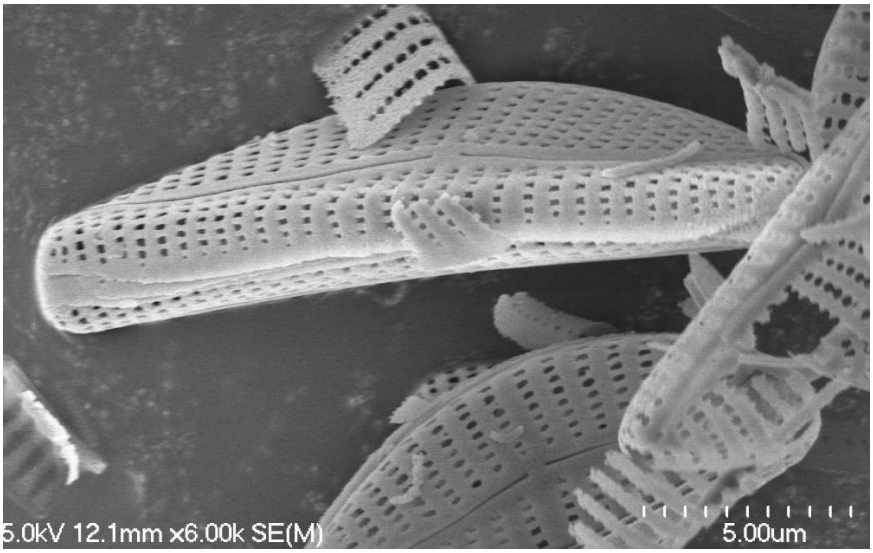

Figure 5.2: SEM micrograph (6000x magnification) of two intact *Encyonema* frustules at ~4.6 mcd, each having both valves (the epitheca and the hypotheca) and cingulum (mantle bands where the valves are joined). Partial dissolution has slightly widened the areolae.

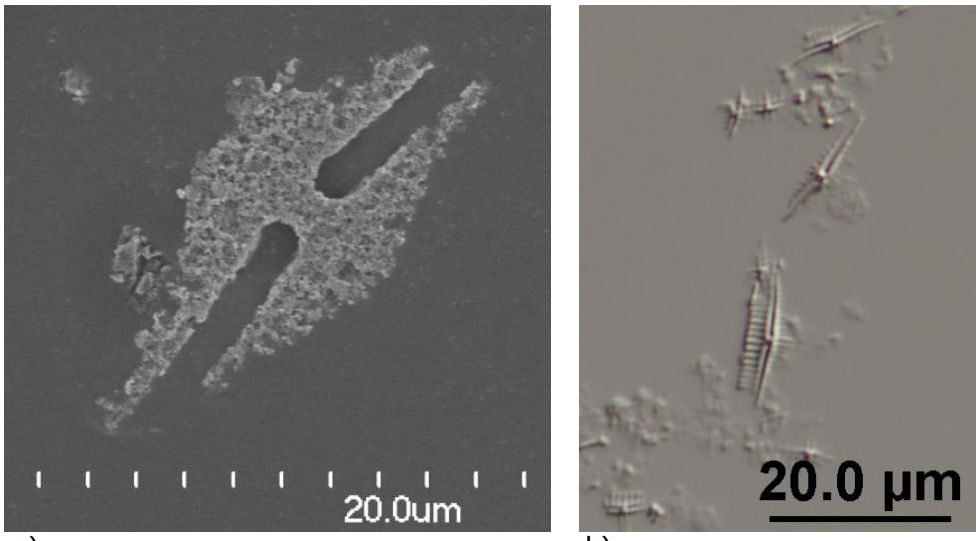

a) b)

Figure 5.3: Severe dissolution of diatom valves; a) SEM micrograph (2500x magnification) of central nodule of a large biraphid diatom valve at ~13.0 mcd; b) DIC light micrograph (400x magnification) of the central nodules and raphe fissures of *Encyonema* valves at ~10.3 mcd.

5.2 Facies Analysis Procedure

As discussed in Chapter 4, it is clear that the 9.45 m HMC M1-2 lake sediment deposit can be divided into two major facies based on most of the sedimentological, physical (Geotek), compositional (FTIRS and BioSi molybdate-blue wet chemistry) and biological datasets generated for this study. However, the facies boundary depth differs between the sedimentological and physical datasets (5.7 mcd) and the compositional and biological datasets (6.5 mcd). I have consequently separated the discussion of the facies into two broad sections: Physical Facies (Section 5.3) and Biological Facies (Section 5.4). The reason that the depth difference exists between the distinct sedimentological and the biological divisions will be discussed in Section 5.5 Evolution of the Lake Environment.

5.3 Physical Facies

The sedimentological and physical properties of the HMC M1-2 lake sediments transition from one major facies to another at 5.7 mcd. This depth corresponds to a boundary between drill-rod runs, where a full core sample barrel is removed and another length of drill rod and an empty core sample barrel is inserted. The interval from 5.72-5.80 mcd consists of the crumbled contents of the core catcher, which is an 8 cm-long cutting shoe that is installed at the bottom/inlet-end of the core sample barrel (holds the lower-most interval of the drill run). Additional material (to 5.87 mcd) was excluded from the Geotek results due to fracturing and disturbance that is common for core at these boundary points. Within this 15 cm gap the sedimentation pattern changed enough that distinct light laminae not commonly observed below that depth were deposited in relatively high abundance above it. I selected 5.7 mcd as the depth of the facies boundary as it was the first interval of intact core where Geotek data could be utilised to demonstrate the change between the two sedimentation patterns.

The physical facies are:

- **Dark Laminated Carbonaceous Sapropel** (DLCS, from 13.01 to 5.7 mcd, representing ~7150 years of deposition).

- **Dark Laminated Diatomite** (DLDA, from 5.7 to 3.56 mcd, representing ~3250 years of deposition).

In this study, core attributes are sedimentological observations of the surfaces of the core split sections. They are plotted as individual graphs in Chapter 4 Core Attributes, and are provided here as Table 5.1.

Table 5.1: Summary of core attributes (in percent-occurrence) surveyed in core sections containing HMC M1-2 lake sediments. The blue line shows the boundary between the DLCS and DLDA facies.

Depth (mcd)		Core	Calc. mid-	Percent-Occurrence of Attribute in Core Section						# of Sand
Sec. top	Sec. btm	Section #	depth mcd	Light Lam	Wavy	Frag/crack	Drk hmog	Seds	Disturbed	Lenses
3.56	4.29	**3**	**3.9**	45.2	20.2	0.6	4.1	2.7	7.2	2.5
4.29	5.17	**4**	**4.7**	49.2	68.5	0.0	0.5	0.9	28.2	0.0
5.17	5.84	**5**	**5.5**	42.7	15.7	1.0	0.3	0.8	21.7	0.0
5.84	6.66	**6**	**6.3**	0.2	0.0	0.2	0.0	2.2	55.4	2.5
6.66	7.56	**7**	**7.1**	0.7	0.0	13.2	0.0	1.3	50.1	0.0
7.57	8.54	**8**	**8.1**	0.0	0.0	21.2	1.7	3.6	12.1	15.0
8.54	9.49	**9**	**9.0**	0.1	4.5	20.0	0.0	3.2	10.0	0.0
9.49	10.42	**10**	**10.0**	0.1	0.9	30.3	0.0	6.3	2.9	20.0
10.42	11.30	**11**	**10.9**	0.0	1.5	53.3	0.0	9.6	15.5	30.0
11.30	12.27	**12**	**11.8**	0.0	0.0	41.6	0.0	4.3	5.7	22.5
12.27	13.01	**13**	**12.6**	0.0	0.0	34.3	0.0	3.4	14.0	7.5

5.3.1 Dark Laminated Carbonaceous Sapropel

The DLCS facies (13.01-5.7 mcd; the first ~7150 years of deposition) is characterised by black to very dark brown laminated carbonaceous organic sediments, horizontally-bedded, with flecks of muscovite distributed throughout. From 13.01 mcd (lake sediment base) to ~6.5 mcd the lamina-couplets average 1.09 mm thick, while from ~6.5 to 5.7 mcd the laminae couplets average 0.63 mm (Table 4.2). It is common for the thick organic laminae below 6.5 mcd to be interbedded with very thin bands (maximum one grain-diameter thick) of very fine sediments. The fine sediments vary upcore in composition and occurrence, from scattered muscovite flecks (Core Sections #13-11) to light brown silt (some in Core Section #11, associated with a "Barren Zone", which is discussed later in 5.4 Biological Facies), or dark brown very fine sand (Core Sections #9 and 7, also associated with "Barren Zones").

DLCS Core Attributes

Core attributes distinct to this facies are the tendency to fragment, the presence of isolated terrigenous sediment clasts, and the presence of coarse sand lenses. This facies is also distinguished by a paucity of light laminae or bedding structures.

Core fragmentation was originally surveyed in order to cross-check the Geotek analyses with the core condition, as the MS and density data are inaccurate on core that is not intact. However, the fragmentation data unexpectedly identified a distinction in the physical properties of the sediments. The propensity for the DLCS facies below ~6.5 mcd to fragment/fracture (Table 5.1 and Figure 4.7) is an indication of low ductility. Compaction increases in sediments at depth due to the weight of overlying sediments, compressing and packing them more tightly. Pore space and water content is reduced, decreasing the ductility of the sediments and increasing the tendency to fracture as a response to stress applied by the drilling

process (Selby, 1993; Maier *et al.*, 2013). The overlying DLDA facies does not tend to fragment. The distinguishing characteristic of DLDA is light diatomaceous laminae. This suggests that the diatomaceous laminae may play a role in the contrasting response to applied stress between the DLCS and DLDA facies sediments. This, and the fact that the top core section of the DLCS facies (#6) does not share this feature with the rest of the DLCS facies, will be discussed later in 5.5 Evolution of the Lake Environment.

Over 90% of the bedding which hosts terrigenous sediment clasts of coarse sand to small granule-size (as defined in Chapter 4 Core Attributes) is in the DLCS facies. No petrography or mineralogical analyses have been performed on the clasts, but their appearance (light grey and green with platy muscovite) suggests the majority are Otago Schist country rock (metamorphosed quartz and feldspar with muscovite and chlorite). They are often sub-angular to sub-rounded, are commonly found as isolated individuals, and they slightly deform the laminae above and below. Their occurrence and abundance generally correlates with that of the number of sand lenses.

Almost all sand lenses (39 of 40) discovered during the core split surveys were found in the DLCS facies (Table 5.1). Lenses of coarse sands have been attributed to faecal matter from waterfowl (Lindqvist & Lee, 2009; Kaulfuss & Moulds, 2015). As this core attribute is associated with a biological rather than a sedimentological process, it will be discussed below in Section 5.4 Biological Facies.

DLCS Geotek Data

Magnetic susceptibility is low and has low variability. The MS range in Figure 4.10 has been reduced in order to make the slight variability more visible. Increases in the absolute values and variability of magnetic susceptibility in lake sediments are typically indicative of increased minerogenic sediment content (Nesje *et al.*, 2000). While low, the MS of the DLCS facies (below 5.7 mcd) has greater absolute values and variability than that of the DLDA (above 5.7 mcd).

Gamma attenuation density measures the net density of all components in the sediments: terrigenous, organic, and biosiliceous. As in the MS graph, the density range in Figure 4.12: Density data in grams per cubic centimetre for lake sediment split cores: a) individual data points; b) 7-point running average. has been reduced to highlight the slight variability. The density of the DLCS facies is low, as would be expected with a sapropelic deposit having little terrigenous input.

CIE L*/a*/b* reflectance data (Figure 4.14) show little variation in the DLCS facies. For each reflectance dataset, the base lake sediment (13.01-12.0 mcd) was slightly

distinct from the core above: more luminous (L*), less red (a*), and less yellow (b*). The base lake sediments are in contact with the volcaniclastic upper diatreme infill. There has likely been some ion exchange between the sediments as well as reduction of ferric minerals incorporated into the earliest lake sediments.

The RGB colour (Figure 4.15) also shows little change in mean or variance throughout the DLCS facies. The dataset closely mirrors that of the L* luminosity (Figure 4.14a). This is unsurprising as each of the RGB channels includes a luminosity component.

DLCS Compositional Data

Fourier transform infrared spectroscopy (FTIRS) (Figure 4.16) shows that, below 6.5 mcd, the three major constituents of the DLCS facies each provide a relatively invariable contribution to the lake sediment deposit (High TOC, moderate BioSi, and low terrigenous material (modelled as Schist)). An exception is at ~10.4 mcd, where the FTIRS analysis indicates an increase in the terrigenous component (Schist). From 6.5 to 5.7 mcd the biogenic silica increases primarily at the expense of the total organic carbon but with some reduction in Schist, as well. This depth interval is between the Physical and Biological Facies boundaries mentioned in Section 5.2 Facies Analysis Procedure. This will be further discussed below in The DLCS Depositional Environment.

The BioSi wet chemistry results mirrored those of the FTIRS BioSi component, albeit biased to much lower absolute values (Figure 4.17). As stated in 4.3.2 Biogenic Silica Wet Chemistry Results, the BioSi wet chemistry results are regarded as the most accurate measure of BioSi wt% for this study.

The DLCS Depositional Environment

The aforementioned characteristics indicate that the DLCS facies accumulated in a quiet anoxic seasonally-varying depositional environment with high input of organic material. This is consistent with the very dark, thickly-laminated organic sediments that show no evidence of bioturbation by macro-organisms.

Once established, the DLCS depositional environment was relatively stable with little variation during the depositional period. This is consistent with the low variability in the L*a*b* reflectance and RGB colour intensity datasets. The colour datasets indicate a minor change just above the lake base at ~12.0 mcd. I take this to show progression from the initial post-eruptive deposition over the volcaniclastic deposits of the upper diatreme (~13.01-12.0 mcd) to the ‘steady-state’ conditions in which the rest of the DLCS facies accumulated.

The distinct separation of the thick black carbonaceous laminae by very thin laminae of terrigenous sediments (maximum one grain-diameter thick) indicates that deposition in the lake was likely an annual cycle. Organic material was added to the lake at the end of the growing season, and terrigenous fine sands were transported into the lake between the growing seasons. The likely source of the sediments was the weathered juvenile material and country rock (Otago Schist, i.e. the source of ubiquitous muscovite) constituents from the tephra ring that surrounded the maar crater lake.

Aside from this background terrigenous sedimentation, there was little bulk terrigenous or biogenic sediment input over the deposition-period, as the low MS and density values and FTIRS data attest. One exception is at ~10.4 mcd, where the FTIRS compositional data (Figure 4.16) show a sharp increase in the proportion of schist. A climate shift resulting in increased rainfall, aridification with increased winds, or small seismic events could have increased the background sedimentation from the inside of the tephra ring to the lake, depositing juvenile material and fragmented Otago Schist into the maar lake. Increases in the MS, density, L* luminosity, and RGB colour intensities at this depth (4.2 Geotek MSCL Results) are interpreted as increased lighter-coloured minerogenic input to the lake sediments and would seem to corroborate this event.

5.3.2 Dark Laminated Diatomite

In contrast to the DLCS, the DLDA facies (5.7 to 3.56 mcd; ~7150 to 10400 years since deposition began) is characterised by light diatomaceous laminae interbedded with dark brown laminated organic material. The brightness, thickness, and distribution of light laminae is variable throughout the DLDA. Lamina-couplet thickness averages 0.66 mm throughout (Table 4.2). This facies includes bedding structures such as turbidites and soft sediment deformation structures. As in the DLCS facies, muscovite flecks are found throughout.

DLDA Core Attributes

The distinguishing core attributes in the DLDA facies are the presence of light laminae, wavy bedding, and some dark homogenous sediments (Table 5.1). The DLDA has a dearth of fragmented beds, terrigenous sediment clasts, and sand lenses.

The variability of the distribution and thickness of the light diatomaceous laminae is here interpreted as annual variability in primary production in the maar crater lake. Years having higher primary productivity created thicker diatomaceous laminae.

I regard the diatomaceous sediments to be the reason that the DLDA facies shows evidence of soft sediment deformation as a response to applied stress, rather than brittle fracture as in the DLCS facies. When dry, the DLDA lake sediments readily separate at the diatomaceous laminae (the carbonaceous DLCS sediments do not easily delaminate). The siliceous tests of the laminated diatom deposits have not bonded together, allowing laminae to distort and deform when subjected to stress such as mud-injections or friction against the inner circumference of the core sample barrel (Figure 4.5b; note deformation of the laminae near mud-injections, and pulled-down laminae at core edges).

Wavy bedding is here defined as bedding having mm-to-cm-scale waveforms of sub-mm-to-mm amplitude. Over 90% of this material is in the upper DLDA facies (Table 5.1). Several instances of mm-scale wavy bedding in the DLDA are classified here as turbidites. Turbidites result from underwater gravity-driven mass flow events in which sediments move downslope as a turbulent flow (Nichols, 2009). Turbidites are normally graded, with the coarsest grains at the base and fining upwards. The turbidite deposition pattern in these sediments is characterised by mm-scale wavy lenticular deposits of light-coloured diatomaceous material in a dark matrix, darkening upwards to a black homogeneous 'cap' ("Dark homogeneous" attribute in Table 5.1). Two examples are shown between the green and orange lines in Figure 5.4. A mud-injection wedge is seen underneath them (labelled "1"). The turbidites range from ~5-20 mm thick. Thirteen turbidites were recorded, all in Core Sections #3-5, accounting for a total of 113 mm of turbidite sediments. As the sediments in turbidite deposits are added from outside the study area by mass flow events and, consequently, do not represent normal background sedimentation, the thickness of the turbidites was subtracted from the lamina-couplet thickness calculation used for the age-depth model (Table 4.2 and 3.2.2 in Appendix).

Some instances of cm-scale wavy bedding in DLDA Core Sections #3-5 were identified as soft sediment deformation (SSD). SSD in this facies is defined as slight deformation of the laminae while maintaining identifiable bedding across the width of the core. Figure 5.5 shows an example of SSD (yellow arrow, between red and green lines). I interpret the SSD in this situation to be deformation of *in situ* sediments caused by emplacement of the overlying turbidite. Because the sediments that underwent deformation were already in place, their contribution to the core thickness remains in consideration for the lamina-couplet thickness calculations (Table 4.2). A thick mud-injection band (labelled "1") is seen at the top and upper right margin of Figure 5.5, disrupting the laminae below it.

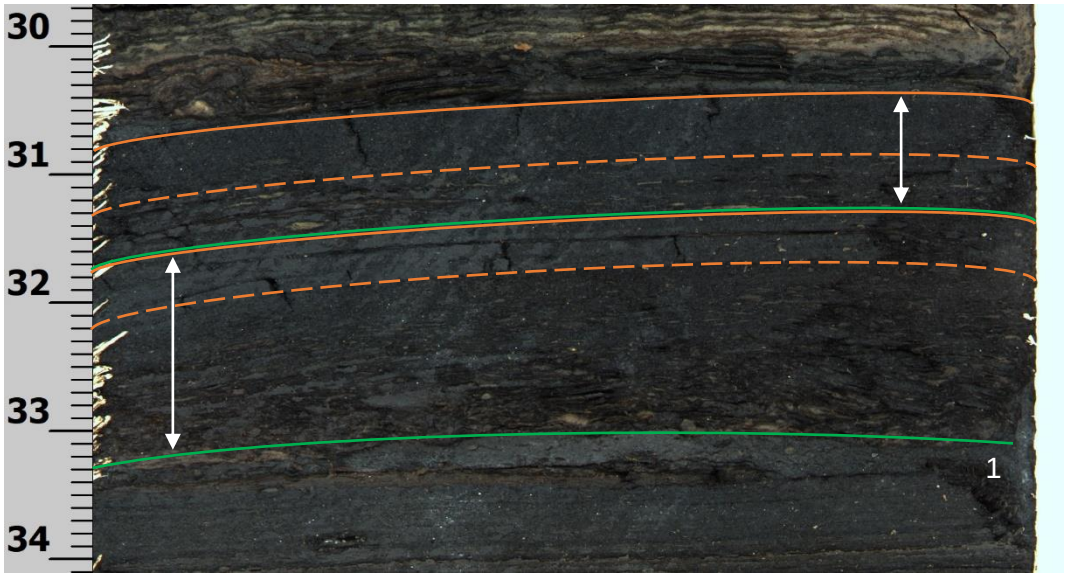

Figure 5.4: Two turbidites (white arrows) in a segment of Core Section #3 corresponding to ~3.85 mcd. Turbidites are bounded by a green line at the base and an orange line on top of the cap. The dashed orange line is the transition from wavy turbidite bedding to black homogeneous cap. A mud-injection wedge (labelled "1") is seen under the base of the lower turbidite. It thins out from right to left.

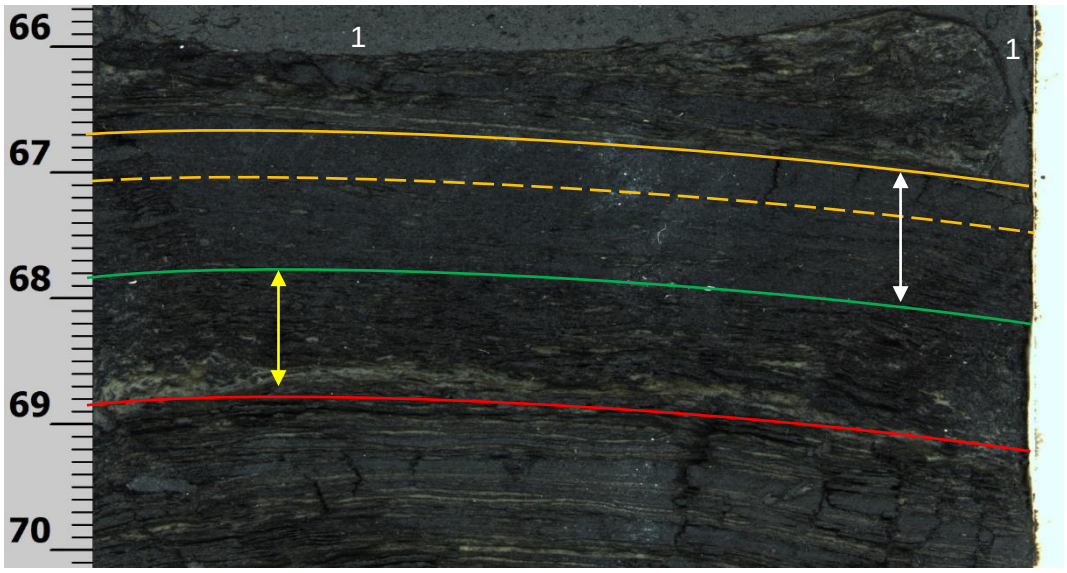

Figure 5.5: An example of soft sediment deformation (SSD) as a result of emplacement of an overlying turbidite in a segment of Core Section #4, corresponding to ~4.85 mcd. The SSD (yellow arrow) is bounded by a red line at the base and the green line of the overlying turbidite (white arrow). The turbidite is bounded as in the previous figure. A thick mud injection (labelled "1") is apparent across the top and along the right margin of the liner in the figure. It has deformed the underlying deposit.

The DLDA facies has few terrigenous sediment clasts or sand lenses. Over 50% of the terrigenous clasts that are in the DLDA facies are in the upper 25 cm of the lake sediments, as is the single DLDA sand lens. This, in conjunction with the Geotek datasets, signals a change in the depositional environment near the top of the lake sediment deposit.

DLDA Geotek Data

In the DLDA facies, the MS decreases and becomes less variable (Figure 4.10). The density increases and also becomes less variable (Figure 4.12).

Recall that the MS and density data were compared in Figure 4.13. Blue rectangles show where the MS and density values follow a similar pattern. Otherwise the patterns diverge, with density increasing slightly as the MS decreases. Increased contribution of biogenic silica relative to organic input is the likely cause for density increase where MS decreases. The density of biosiliceous diatom tests is ~1.98 gcm^{-3} (Hurd & Theyer, 1977). Diatomaceous deposits inherently have high fractional porosity (due to the resistance of irregularly shaped diatom valves to being tightly packed) which tends to reduce bulk density. However, at 5.30 mcd, the depth at which the FTIRS, the BioSi wet chemistry, and the diatom abundance analyses indicate peak diatom abundance, the Geotek density indicates an increase. Organic matter in the HMC M1-2 lake sediments is sourced from submerged macrophytes, animal and algal input, and plant detritus from forests surrounding the lake, which is then decomposed by biochemical processes in the lake. Such material is typically lower in density than biosiliceous remains formed from hydrated silica. In the HMC M1-2 lake sediments, the diatomaceous deposits are of higher density than the organic deposits.

CIE L*/a*/b* reflectance data (Figure 4.14) and the RGB colour intensity data (Figure 4.15) generally show greater variation in the DLDA facies than the DLCS. This is due to the presence of light-coloured laminae which characterise this facies.

At ~4.1 mcd there is a major departure from the general pattern of the DLDA deposit. The MS and density steadily increase across the top 50 cm of the lake sediments. The L*/a*/b* reflectance data increase sharply across the uppermost ~20 cm interval of the lake sediments. The RGB intensity decreased from ~4.1 to 3.9 mcd, then increased linearly up to ~3.6 mcd before increasing sharply across the top 5 cm. Recall from 4.1.3 Overlying Sediments that the top 5 cm of the lake sediments were intruded by some of the lighter-coloured overlying sediments. The rise in spectral data values are a response to the intrusion.

DLDA Compositional Data

FTIRS results (Figure 4.16) shows that the BioSi is a major component in the DLDA facies, primarily at the expense of the TOC proportion but the Schist proportion is reduced, as well. In the DLDA, the BioSi wt% increases to ~50-60wt% from ~25% in the DLCS, while the TOC decreases an amount that is about equal to the

increase of the BioSi. As discussed above in Section 5.1 Addressing Potential Issues, these values are somewhat notional. However, the pattern is consistent with the BioSi wet chemistry and biosiliceous survey datasets (Figure 4.20). Terrigenous input in the form of schist is further reduced compared to the DLCS facies, except in the last two samples at the upper ~25 cm of the lake sediment deposit. Here, the data indicate an increase in schist content near the end (top) of the lake sediment deposit. As the age-depth model has estimated the time between samples is ~275 years in the DLDA facies, the rise in schist input occurred during a ~300-600 year time span.

In the DLDA facies (above 5.7 mcd), the low terrigenous inputs appear to be inversely correlated to the BioSi wt% in the FTIRS data. Where terrigenous input is absent at ~5.3 mcd, the BioSi is at peak values near 60 wt%. Where some terrigenous material is present from ~5.1 to 4.55 mcd, the BioSi component decreases to ~40 wt%. When terrigenous input is absent again at 4.39 mcd, the BioSi reaches a peak high of 63 wt%. This pattern remains consistent in the uppermost lake sediments.

As in the DLCS facies, the BioSi wet chemistry results were much lower in absolute value, but the pattern reflected that of the FTIRS BioSi component (Figure 4.17), including the sharp decrease in BioSi at the top of the lake sediments. The decrease coincides with a sharp increase in terrigenous input recorded in the FTIRS samples.

The DLDA Depositional Environment

The environment in which the DLCS was deposited remained seasonal/annual and anoxic at the lakebed, preserving the laminae. Light laminae in the DLDA facies, and decreasing MS with increasing density, show that there was a shift to less organic input concomitant with increased inorganic biogenic silica accumulation.

Due to the large increase in diatomaceous material in the DLDA, I regard the presence of turbidites in the DLDA to be associated with the accumulation of benthic siliceous organismal remains (diatoms, sponge spicules, cysts of chrysophycean algae) upslope from the study site, in the photic zone nearer the shoreline. The accumulations must have periodically reached sufficient heights to become unstable and move downslope as mass flows, deforming the underlying lake sediments. Mass flow events may have also been initiated by seismic events or, if the accumulations were in shallow water, storm events that generated unusually high waves such that the storm wave base would interact with the accumulated diatomaceous sediments and make them unstable.

Another major sedimentological shift was occurring near the end of the lake sediment deposit, as evident by the deviation in all Geotek datasets from the general DLDA pattern across the top 50 cm. I interpret this to represent a swing back towards The DLCS Depositional Environment, with decreased biosiliceous input and increased organic input. There is an influx of terrigenous material recorded above 3.95 mcd by the FTIRS dataset. MS increases in those sediments towards DLCS values, a shift which I interpret as a response to the minerogenic terrigenous input as well as the reduction in biogenic silica. The density increases beyond that of the DLCS facies. The likely cause of this is relatively lower organic input and higher terrigenous input compared to the DLCS. The response of the L*/a*/b* reflectance data to the sedimentological shift across the top ~50 cm of lake sediments is disparate. The L* and b* data appear to be shifting to DLCS-type values, while the a* data deviate towards higher red values. This may be a characteristic of the late terrigenous sediment input. The fact that the a* values here are distinct from those that characterise the similar terrigenous input peak in the DLCS facies may be due to the reduced organic input in the DLDA facies relative to the DLCS facies, leaving a higher terrigenous:organic sediment ratio in the DLDA.

5.4 Biological Facies

The compositional and biological datasets for the HMC M1-2 lake sediment deposit show a biofacies transition at 6.5 mcd (Figure 4.20). There is little biosiliceous material in the sediments below 6.5 mcd, while above 6.5 mcd it is abundant. This depth corresponds to the middle of a core section, where a sample was taken 78 cm from the top of the core liner in Core Section #6 (sample 16, the first sample moving upcore that required dilution due to excess diatom valve concentration when making slides). It is not associated with a boundary between core sections or between drill-rod runs, as the physical facies division is. The compositional (FTIRS and BioSi wet chemistry) and biological (diatom, chrysophycean cyst, and sponge spicule surveys) datasets are all based on small samples taken at ~20 cm intervals along the length of the core. The transition from one biofacies to the other occurs at some point within the interval between the samples at 6.64 and 6.45 mcd (98 and 78 cm from the top of the Core Section #6 liner, respectively) (Figure 5.6).

The sources of BioSi in the lake sediment deposit are diatom valves, chrysophycean cysts, and freshwater sponge spicules. The chrysophycean cysts (henceforth simply 'cysts') have low abundance and thin walls, leaving them a minor component in their contribution to total BioSi (Figure 4.18). Sponge spicules were also few in number, but they are many times larger than diatom valves (megascleres are ~200 μm long while diatom valves average ~20 μm). Thus, a sponge spicule incorporates much more volume/mass of BioSi than a diatom valve. However, the BioSi analyses (both the FTIRS and wet chemistry) show a strong correlation with the diatom surveys (Figure 4.20) and little correlation with the cysts or the spicules (Figure 4.22 and Figure 4.25). I conclude that diatom valves account for the highest contribution of the biogenic silica in these sediments. Hence, the biological facies are designated:

Figure 5.6: Biofacies transition zone in Core Section #6, from 6.45 to 6.64 mcd (78 to 98 cm on scale)

- **Diatom-poor** (**DP**, from 13.01 to 6.5 mcd, representing ~5850 years of deposition).

- **Diatom-rich** (**DR**, from 6.5 to 3.56 mcd, representing ~4550 years of deposition).

The percent-abundances of the diatom species at each sample depth are summarised below in Table 5.2. The percent-abundance data has been used to distinguish the biosiliceous deposition into five zones: four Diatom Zones and one Cyst Zone. Depths that have insufficient diatom data to be statistically valid (yellow bands) have been classified as Barren Zones.

All diatom species found in the HMC M1-2 lake sediments are of the benthic variety, living attached to substrates such as rocks (epilithic), sand (episammic), or submerged macrophytes (epiphytic) in the photic zone. In both biofacies, the dominant diatom species is *Encyonema mesianum* (>97%). It is a cosmopolitan benthic species found in oligotrophic waters and a wide range of temperate

conditions. Only in the sediments at the base of the lake is a different diatom species dominant (*Staurosirella lapponica*, from 12.91-11.36 mcd). Otherwise, Diatom Zones are distinguished by the percent-abundance of the diatom species that is secondarily abundant after *E. mesianum*. The zones are labelled by genus, as follows. Depth range and years since deposition began are provided in parentheses for each zone.

- Diatom Zone 1 (DZ1): *Staurosirella* (12.91-11.36 mcd; ~50 to 1750 years)
- Diatom Zone 2 (DZ2): *Encyonema* and *Gomphonema* (10.61-9.88 mcd; ~2250 to 2900 years)
- Diatom Zone 3 (DZ3): *Encyonema* and *Rossithidium* (8.17-6.64 mcd; ~4300 to 5850 years)
- Diatom Zone 4 (DZ4): *Encyonema* and *Sellaphora* (6.45-3.95 mcd; ~5850 to 9950 years)

Chrysophycean cysts are a minor contributor until they increase sharply across the top ~40 cm of the lake sediments (Figure 4.22). Chrysophyceae which generate the cysts are typically planktonic and tend to be most common in cool oligotrophic lakes that are somewhat acidic (Sandgren *et al.*, 1995; Smol *et al.*, 2002; Cohen, 2003).

Peaks of sponge spicule abundance are present across all physical and biological facies, in both Barren and Diatom Zones, but they appear most commonly between ~9.7 and 5.7 mcd, which is in the upper part of the physical DLCS facies, (Figure 4.25). 9.7 mcd corresponds to the beginning of a Barren Zone after DZ2 in the DP biofacies, while 5.7 mcd is in the lower half of the DR biofacies (Table 5.2). Spicules also increase across the top ~30 cm of the lake sediments. Freshwater sponges are generally intolerant of turbidity as it inhibits their ability to filter-feed (Cohen, 2003). A decline in sponge spicules has been correlated with deterioration in lake water quality (Yang *et al.*, 1993). Cumming *et al.* (1993) showed that freshwater sponges have a very low tolerance for salinity.

Table 5.2: Summary of biosiliceous organisms surveyed throughout the HMC M1-2 lake sediment deposit. Yellow bands indicate depths at which survey counts were insufficient to be statistically valid, labelled Barren Zones. Only percent-diatom abundances >2% were used to classify the four Diatom Zones. There is also one Cyst Zone. The DP and DR biofacies transition at the dashed line between 6.447 and 6.64 mcd.

= Not statistically valid

Depths (mcd)	M1-2 Sample Number	Percent Abundance of Diatoms						Cysts per view	Spics per view	Zones	
		Ency	Stsrella	Sella	Rossi	Gomph	Achnan				
3.57	1	98.6	0.0	0.3	0.9	0.0	0.0	117.2	3.7	Cyst Zone	Diatom-Rich
3.767	2	96.3	0.0	1.9	0.0	0.0	0.0	33.8	3.5		
3.951	3	98.9	0.0	1.0	0.0	0.0	0.0	21.1	0.1	Diatom Zone 4 Max Ency / Sellaphora	
4.143	4	99.0	0.0	1.0	0.0	0.0	0.0	0.0	0.0		
4.387	5	99.9	0.0	0.1	0.0	0.0	0.0	0.0	0.0		
4.545	6	98.7	0.0	1.0	0.0	0.0	0.0	2.9	1.2		
4.721	7	99.7	0.0	0.3	0.0	0.0	0.0	6.3	0.0		
4.905	8	99.5	0.0	0.2	0.2	0.2	0.0	2.0	0.3		
5.101	9	99.8	0.0	0.2	0.0	0.0	0.0	4.0	0.2		
5.302	10	99.8	0.0	0.2	0.0	0.0	0.0	4.4	0.9		
5.502	11	98.6	0.0	1.3	0.0	0.0	0.0	0.0	0.1		
5.699	12	99.4	0.0	0.5	0.0	0.0	0.2	1.7	0.0		
5.961	13	99.2	0.0	0.5	0.3	0.0	0.0	0.0	0.8		
6.084	14	98.1	0.0	1.3	0.2	0.5	0.0	4.4	5.4		
6.251	15	98.4	0.0	0.8	0.6	0.0	0.2	2.9	1.6		
6.447	16	93.8	0.0	3.0	1.8	0.7	0.3	4.4	1.9		
6.64	17	95.6	0.0	0.0	3.1	0.3	0.7	1.9	0.9	DZ3 Ency /	Diatom-Poor
6.834	18	91.6	0.0	0.0	4.7	0.9	2.2	1.7	0.8		
7.033	19	100.0	0.0	0.0	0.0	0.0	0.0	0.4	5.9	Barren Zone	
7.232	20	94.5	0.0	0.0	2.6	0.8	1.1	8.7	0.8	Diatom Zone 3 Ency / Rossi	
7.411	21	97.7	0.0	0.0	0.8	0.8	0.2	0.3	1.7		
7.574	22	99.7	0.0	0.0	0.1	0.0	0.0	1.5	1.6		
7.788	23	98.4	0.0	0.0	0.6	0.6	0.0	1.0	0.2		
7.968	24	99.5	0.0	0.0	0.5	0.0	0.0	1.8	0.2		
8.168	25	98.9	0.0	0.0	0.5	0.5	0.0	5.9	3.1		
8.368	26	100.0	0.0	0.0	0.0	0.0	0.0	0.1	3.2	Barren Zone	
8.555	27	100.0	0.0	0.0	0.0	0.0	0.0	0.0	0.9		
8.754	28	93.9	0.0	0.0	4.1	2.0	0.0	0.1	0.2		
8.964	29	100.0	0.0	0.0	0.0	0.0	0.0	0.1	0.4		
9.156	30	100.0	0.0	0.0	0.0	0.0	0.0	1.6	2.2		
9.336	31	100.0	0.0	0.0	0.0	0.0	0.0	0.0	0.7		
9.507	32	100.0	0.0	0.0	0.0	0.0	0.0	0.0	1.8		
9.685	33	100.0	0.0	0.0	0.0	0.0	0.0	0.1	1.0		
9.883	34	98.0	0.0	0.0	0.3	1.0	0.0	2.6	0.4	Diatom Zone 2 Ency / Gomph	
10.071	35	98.9	0.0	0.0	0.7	0.2	0.2	1.4	0.6		
10.267	36	98.0	0.0	0.0	0.9	0.3	0.0	4.3	0.8		
10.432	37	95.0	0.0	0.0	0.7	2.7	0.0	2.0	0.5		
10.61	38	91.8	0.0	0.0	2.3	4.9	0.7	4.1	0.7		
10.79	39	93.3	0.0	0.0	0.0	0.0	6.7	0.3	0.3	Barren Zone	
10.975	40	100.0	0.0	0.0	0.0	0.0	0.0	0.0	0.1		
11.168	41	70.0	0.0	0.0	20.0	10.0	0.0	0.1	0.3		
11.363	42	50.1	41.5	0.0	6.2	0.5	1.8	1.0	0.9	DZ1 Stauro	
11.558	43	100.0	0.0	0.0	0.0	0.0	0.0	0.0	0.7	Barren Zone	
11.75	44	90.9	7.3	0.0	0.0	0.0	1.8	0.0	0.3		
11.988	45	7.4	85.8	0.0	2.3	0.0	3.4	2.3	0.7	Diatom Zone 1 Staurosirella	
12.162	46	38.4	54.0	0.3	3.5	1.3	1.8	19.0	0.2		
12.348	47	18.9	74.6	0.0	2.1	0.6	2.6	6.8	0.3		
12.536	48	40.0	50.0	0.0	0.0	0.0	0.0	0.3	0.3	Barren Zone	
12.722	49	0.0	0.0	0.0	0.0	0.0	0.0	0.0	0.1		
12.905	50	55.8	26.4	0.0	0.0	17.2	0.0	0.6	0.1	DZ1 Stauro	
12.965	51	45.5	31.8	0.0	0.0	4.5	0.0	0.5	0.1	Barren Zone	
	% of Total	97.3	1.3	0.7	0.3	0.2	0.1				

5.4.1 Diatom-Poor

The DP biofacies includes Diatom Zones 1-3 (Table 5.2) and is characterised by low abundance of diatomaceous phytoplankton. Four notable increases in diatom abundance occur across the DP biofacies, but never to the values found in the DR facies above. The increases peak at 12.16 and 11.36 mcd (DZ1), 10.27 mcd (DZ2), and from 8.17 to 7.41 mcd (DZ3). Each DZ will be examined, then a discussion about the DP depositional environment will follow. Refer to Table 5.2 throughout.

There are also several Barren Zones throughout the DP. The Barren Zones consist almost exclusively of carbonaceous organic material (i.e. DLCS facies). They have a scarcity of diatoms or cysts but do have sponge spicules in varying abundances, from very few to major peaks in occurrence (Figure 4.25). I interpret the Barren Zones to be the result of shifts from diatomaceous algal assemblages to non-diatomaceous ones. This could occur by a lack of available silica/silicic acid for the continuous development of diatom valves, acidic water (low pH), limited nutrient availability, or by freshwater sponges out-competing diatoms for nutrients and/or for silicic acid to form their spicules.

Where Barren Zones are discussed, an estimate for the deposition interval will be provided in parentheses. The calculations will be based on the average lamina-couplet thickness (Table 4.2) for the specific core section(s) in which the Barren Zone sediments occur. Because the calculations can be based on different lamina-couplet thicknesses, Barren Zones of the same estimated thickness may have slightly different deposition periods.

Diatom Zone 1: Staurosirella (12.91-11.36 mcd; ~50 to 1750 years since lake sedimentation began)

DZ1 deposition followed the initial accumulation of a Barren Zone (~50 years). The dominant diatom species in this zone is *Staurosirella lapponica* (4.5.2). It is an episammic, alkaliphilous species that can tolerate elevated temperature (up to 40°C), pH (optimum 8.6), and conductivity (up to 500 μScm^{-1}). The secondary diatom species is *E. mesianum*, which has a broad tolerance range but is generally found in weakly acidic waters. Within this zone there are tertiary diatom species that change in abundance throughout the zone. *Gomphonema affine* (4.5.5) is the main tertiary species at the base of the zone (~12.91 mcd). It has lower tolerance for elevated pH (circumneutral; 7.0±0.5 pH) and conductivity. A Barren Zone ~40 cm thick (~380 years of deposition) accumulated before DZ1 re-established. There is a cyst peak at 12.16 mcd, where *S. lapponica* decreased while *E. mesianum* increased sharply. This shift in diatom assemblage probably reflects a decrease in pH, as *E. mesianum* prefers weakly acidic water vs. the alkaline water that *S. lapponica* prefers. Another ~40 cm thick Barren Zone (~400 years of deposition) interrupted the DZ1 deposition. At the top of this zone (~11.36 mcd), DZ1 re-established again, this time with increased *Rossithidium nodosum* (4.5.4) compared to *Achnanthes exigua var. elliptica* (4.5.6). Of the two species, *A. exigua var. elliptica* has a much higher tolerance for pH and conductivity (up to 9.2 pH and >10,000 μScm^{-1}). *R.nodosum* occurs in cold oligotrophic circumneutral waters.

From the average lamina-couplet thickness for the DZ1 core sections, DZ1 sediments themselves took ~920 years to deposit over three separate time intervals (180, 560, and 180 years), while the two inter-DZ1 Barren Zones took a total of ~780 years. The total time then to accumulate the DZ1 and inter-Barren Zone sediments was ~1700 years.

Diatom Zone 2: Encyonema and Gomphonema (10.61-9.88 mcd; ~2250 to 2900 years)

Deposition of DZ2 began following a ~60 cm-thick Barren Zone (~500 years) accumulated after DZ1. *E. mesianum* showed its dominance for the first time in this deposit. *G. affine* was most abundant at the beginning of DZ2 and generally declined as deposition continued through DZ2. By the end of DZ2, cysts were increasing in abundance, which in an indication that acidity was increasing in the surface water and nutrients may have been decreasing. As mentioned previously, *E. mesianum* is found in a wide range of environmental conditions, but *G. affine* constrains the environmental parameters somewhat. Water conditions where the diatom assemblage included both species would likely have been weakly acidic (pH 5.88-6.93) with low conductivity (~50-55 μScm^{-1}) (Murakami *et al.*, 2009).

Using the average lamina-couplet thickness in the DZ2 core sections, DZ2 was deposited over an interval of ~650 years.

Diatom Zone 3: Encyonema and Rossithidium (8.17-6.64 mcd; ~4250 to 5850 years)

Following deposition of a ~1.4 metre-thick Barren Zone (~1350 years of accumulation), the DZ3 deposit began with a near mono-culture of *E. mesianum* and an uptick in cyst abundance, much the way DZ2 deposition ended. Sponge spicule abundance is high at the boundary of the underlying Barren Zone and DZ3 (Figure 4.25, at 8.37 and 8.17 mcd). As the spicules decreased, *E. mesianum* increased in abundance between ~7.97-7.57 mcd. *R. nodosum* established in amounts >2%-occurrence at ~7.23 mcd, coincident with an increase in chrysophycean cysts just before a narrow Barren Zone at ~7.03 mcd. This inter-DZ3 Barren Zone (~150 years of deposition) includes sponge spicules at their greatest abundance in the HMC M1-2 lake sediment deposit. Immediately following this Barren Zone, *E. mesianum* and *R. nodosum* re-established in the lake, along with a population of *A. exigua var. elliptica*, indicating an increase in pH to weakly alkaline.

Using average lamina-couplet thickness for the DZ3 core, the DZ3 sediments accumulated in two intervals across the span of ~1450 years (~1050 and 400 years) with a ~150-year inter-DZ3 Barren Zone between them for a total of ~1600 years.

Sand lenses and Terrigenous Sediment Clasts

Recall the core attributes of sand lenses and terrigenous sediment clasts (DLCS Core Attributes, above). Most of the sand lenses (38/40) were observed below ~7.6 mcd, which coincides more with the biological facies boundary at 6.5 mcd than the physical one at 5.7 mcd (Table 5.1). As mentioned previously, these sand lenses have been associated with faecal matter from waterfowl (Lee *et al.*, 2009; Kaulfuss & Moulds, 2015). The prevalence of them in the DP biofacies therefore indicates that there was more waterfowl activity in the lake during the deposition time of the DP biofacies than the DR biofacies. Ecological studies in lake systems have found that when a lake shifts from turbid phytoplankton-dominated conditions to clear submersed macrophyte-dominated conditions, waterfowl increase in density (Hanson & Butler, 1990, 1994; Hargeby *et al.*, 1994). Lakes dominated by submersed macrophytes are typically clear and provide habitat for a highly diverse assemblage of macroinvertebrates and fish (Hargeby *et al.*, 1994; Hansson *et al.*, 2010). Phytoplankton-dominated lakes are typically turbid and support a simpler trophic web with a lower diversity of macroinvertebrates (Hanson & Butler, 1990, 1994; Hargeby *et al.*, 1994). Clear lakes dominated by submerged macrophytes attract waterfowl whose preferred food sources are invertebrates and fish living amongst the macrophytes as well as the macrophytes themselves (Hargeby *et al.*, 1994; Hansson *et al.*, 2010). Reduction in the preferred macrophyte food source in lakes has been shown to result in decline of the waterfowl that feed on them (Fox *et al.*, 2011). I accept these findings as a working hypothesis to explain the change in the prevalence of sand lenses in the HMC M1-2 lake sediment deposit, as the lenses reduce in number around the transition zone from the DP to the DR (i.e. phytoplankton-rich) biofacies.

The terrigenous sediment clasts (as described in Chapter 4 Core Attributes) are too large to have undergone aeolian transport. They are also too isolated (interbedded as individuals between laminae) to have been involved in mass flow events into the lake. The isolated terrigenous sediment clasts are generally associated with the presence of sand lenses (Table 5.1). This points towards waterfowl activity as a possible mechanism for deposition of these coarse minerogenic clasts into the lake sediments. Perhaps these clasts were dropped by waterfowl while feeding on macrophytes or benthic invertebrates.

The DP Depositional Environment

The Diatom-Poor depositional environment was generally one in which clear waters of the lake received a high input of organic material relative to biosiliceous sediments. Included in the organic detritus were pollen grains from the surrounding forests (4.4.4 Pollen). Regarding the biosiliceous organisms present in the DP biofacies, changes in their assemblages upcore indicate that there were subtle changes in the temperature, pH, and conductivity in the surface waters of the lake. The initial post-eruption maar lake water inventory was alkaline but transitioned through circumneutral until it became somewhat acidic after DZ1. The pH of the lake surface water remained <7.0 throughout the rest of the DP biofacies. The acidity was strong enough to keep biosiliceous algae from becoming dominant, at times reducing them to near extinction and resulting in Barren Zone accumulation.

Lake water acidity is tolerated by waterfowl and some species of submerged macrophytes, so low pH would not completely inhibit their presence in a lake such is described above for HMC M1-2 (DesGranges & Rodrigue, 1986; Brouwer *et al.*, 2002). The deposition of waterfowl faecal matter and organic input from submerged macrophytes would continue in such conditions, as evidenced the distribution of sand lenses (Table 5.1) and continued thick organic lamina-couplets (Figure 4.3).

The increased abundance of chrysophycean cysts before and after several Barren Zones leads me to conclude that acidification of the surface water is responsible for the lack to diatomaceous material in those zones. Once diatom zones became established the cysts reduced in abundance as chrysophyte algae are poor competitors in high nutrient conditions. Changes in spicule abundance (Figure 4.25) are independent of the Barren Zones. From this I infer that the spicules originated from porifera species with slightly higher tolerance of low-pH conditions than the diatoms and they proliferated or decreased depending on nutrient availability or pH-values lower than diatoms could endure.

The profundal environment was alkaline enough at times for a measure of dissolution to take place, transferring silica from the biosiliceous sediments into solution. The long-term establishment of acidic surface and basic profundal waters throughout the DP biofacies deposition is evidence the depositional environment was a meromictic lake with a well-established chemocline. Nutrients and dissolved silica remained in the monimolimnion and likely increased in concentration as deposition continued. To maintain meromixis, the environment would have to be warm with little seasonality, and with insufficient wind energy at the lake surface to mix nutrients up from the chemocline.

Towards the end of the DP biofacies, conditions changed enough for diatoms to sustain a presence. Diatom abundance increased beyond that of previous concentrations, perhaps by more nutrients becoming available or by less competition from non-siliceous algal organisms or submerged macrophytes. I interpret the diatom peaks in DZ3 to be consequent to nutrients (or silica in solution from diatom valves partially dissolved earlier) that had been sequestered in the monimolimnion becoming available in the mixolimnion through the chemocline. The climate may have cooled, allowing the chemocline to degrade somewhat and rise closer to the surface. Convective turbulence in the mixolimnion could have then 'shaved' nutrients from the chemocline to sustain the diatom population during that time. By the end of the DP biofacies, pH of the surface waters was rising toward circumneutral (pH 7.0±0.5).

5.4.2 Diatom-Rich

The DR biofacies includes DZ4 and the Cyst Zone (Table 5.2). It is characterised by a high abundance of biosiliceous material (peak abundance is ~6 times greater than in the DP biofacies). *Encyonema mesianum* is the primary source of BioSi (Figure 4.20). The DR biofacies also has decreased organic input relative to the DP biofacies. The uppermost ~30 cm of sediments host the highest concentration of chrysophycean cysts in the HMC M1-2 deposit and have thus been labelled the Cyst Zone. There are diatoms in the Cyst Zone, but they are significantly decreased in abundance from those in DZ4.

Diatom Zone 4: Encyonema and Sellaphora (6.45-3.95 mcd; ~5850 to 9950 years)

DZ4 begins with the first occurrence of *Sellaphora saugerresii* in numbers >2% of the total diatom valves surveyed. *S. saugerresii* is associated with a slightly alkaline pH range (~7.1-8.0) and moderate conductivity (as high as 400 μScm^{-1}) (DPDC, 2017). It has also been found in cool distal geothermal waters of alkaline springs (Owen *et al.*, 2008). Otherwise, deposition continues as it had at the end of DZ3, with *R. nodosum* still present but rapidly decreasing in number. After the initial ~20 cm of accumulation, the diatom assemblage becomes a near-monoculture of *E. mesianum* with residual *S. saugerresii*. The abundance of diatoms increases sharply from the DP biofacies (Figure 4.19), although at 6.08 mcd there is a decrease in diatoms that coincides with a peak in sponge spicules. Between ~5.3 and 4.4 mcd the diatom abundance decreases to less than half of the peak values that occur before and after. The FTIRS composition analysis shows a small increase in terrigenous material between those depth values (Figure 4.16).

Comparison of normalised diatom abundance and FTIRS schist component datasets shows that, above 5.7 mcd in the DR biofacies, there is something of an inverse correlation between terrigenous material and diatom abundance (Figure 5.7). By the end of DZ4, diatom abundance decreases sharply.

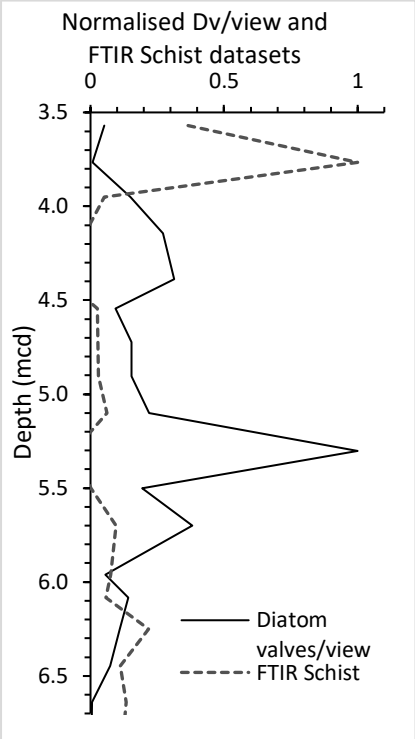

Figure 5.7: Normalised datasets for the FTIRS schist component (dashed line) and diatom valves/view in the Diatom-Rich biofacies.

Cyst Zone: (3.77-3.56 mcd; ~9950 to 10400 years)

The Cyst Zone begins with a sharp increase in cysts at 3.77 mcd. This coincides with an increase in terrigenous material (Figure 5.7 and Figure 4.16). Sponge spicule abundance increases in the Cyst Zone, as well. At the end of the Cyst Zone at the top of the lake sediment deposit, cyst abundance has increased by a factor of 3.5, terrigenous material has decreased, and diatoms increase in abundance.

Figure 4.23 shows that the earliest cyst morphotype to increase in abundance is Cyst #384, just before the narrow Barren Zone. Cyst #384 has been associated with cold circumneutral waters (mean pH 6.9) (Wilkinson *et al.*, 2002). Cyst #384 abundance is in decline when the other three most abundance cyst morphotypes (#1, #9, and #156) are increasing. Cysts #1 and #9 are cosmopolitan and associated with a breadth of ecological ranges, while Cyst #156 has not yet been associated with ecological data (Duff *et al.*, 1995). As cysts typically increase in slightly acidic surface waters, I infer that the lake surface was changing from generally weakly alkaline through DZ4 to weakly acidic as it was in DZ2 and early in DZ3.

Lamina-couplet thickness through the Cyst Zone indicates that it represents ~450 years of sediment accumulation.

The DR Depositional Environment

The Diatom-Rich depositional environment was one in which primary production via biosiliceous phytobenthos dominated, while organic input was greatly reduced from the level that characterised the earlier history of the lake. The lake had become weakly alkaline and perhaps higher in conductivity by the end of the DP biofacies, allowing a population of *S. saugerresii* to initially establish itself in notable abundance and subsequently maintain a small presence throughout the rest of the depositional period. High primary production in lakes typically results in a rise in pH. During photosynthesis the phytobenthos fixes carbon by taking up the dissociated constituents of dissolved CO_2 (H^+ and HCO_3^-), which would otherwise contribute to acidity in the lake (Pedersen *et al.*, 2013). High primary productivity allowed the lake to maintain an alkaline pH which is preferred by *S. saugerresii*.

Diatom abundance was reduced for a time (~1100 years) to about half of the peak values. Diatom productivity may have been nutrient-limited during that interval. Warmer climate conditions may have strengthened the chemocline in the HMC M1, sequestering nutrients from the surface waters, or nutrient input to the lake may have been reduced.

A major source of organic input to the lake was absent in during deposition of the DR biofacies, as the dark laminae were substantially reduced in thickness. The high concentration of benthic diatoms may have outcompeted macrophytes for nutrients, reducing the contribution of the macrophytes to the organic input. Deciduous forests surrounding the lake were contributors of organic material in the form of leaf detritus, as well. Decreases in leaf detritus could be caused by a retreat of the forests from the region due to cooling climate or reduction in precipitation.

A change which caused diatom abundance to decrease and cyst abundance to increase occurred late in the lake depositional period. Chrysophyte algae tend to tolerate environmental perturbances and oligotrophy well, and have an affinity for slightly acidic lakes. Chrysophytes may have exploited a drop in lake pH resulting from reduced primary production. The increase in sponge spicules at the top of the lake sediments, and concomitant decrease in diatoms and near extinction of alkaliphilic *S. saugerresii*, points towards a trophic change in the lake at that time. It is difficult to expound on what may have been contributing to those effects with the palaeoclimate archive being unconformably truncated at that point by overlying sediments.

5.5 Evolution of the Lake Environment

During the early part of the mid-Miocene climate transition (MMCT), the oceanic Antarctic Circumpolar Current (ACC) was further south at higher latitudes, allowing the climate of Zealandia to be influenced more by warm subtropical ocean currents and also to some extent by the atmospheric circumpolar westerlies (Reichgelt *et al.*, 2016a). The mid-latitude Hindon region had a warm and wet subtropical climate with MAT up to 10°C warmer than present day (Prebble *et al.*, 2017).

A Southern beech forest ecosystem with podocarps and mixed broadleaf understory covered the landscape (Pole, 2014; Möller *et al.*, 2017; Kaulfuss *et al.*, 2018). The Hindon region was overlying an aquifer hosted in Otago Schist (Craw *et al.*, 2016). During the formation of the Waipiata Volcanic Field, rising basaltic magma exploited regional NE-trending faults, forming dykes that intersected the aquifer (Németh, 2001). The resulting phreatomagmatic eruptions formed the Hindon Maar Complex.

Post-eruption, the deep sub-circular crater of Hindon Maar #1 was inundated with alkaline ground water from the aquifer. Mass flows of volcaniclastic material from the inner slopes of the tephra ring and the steep upper slopes of the crater initially added fill to the upper diatreme. The warm wet climate facilitated the breakdown of juvenile material in the tephra ring into nutrients that were exploited by the subtropical deciduous forests surrounding the maar. Pollen evidence in the DIC microscopy surveys (Figure 4.26) indicate that the forests re-established proximal to the maar lake and provided prodigious detrital leaf litter to the closed-basin lake every season.

There was a lack of seasonal temperature variation (Prebble *et al.*, 2017), and there would have been a lack of wave action in the maar lake within the shelter of the tephra ring. This, combined with the cold groundwater being supplied to the maar lake due to intersection with the aquifer, led to the maar lake quickly becoming meromictic (permanently stratified) with a well-developed chemocline. This is evident in the undisturbed organic laminae at the base of the lake sediments. Nutrients washed and blown into the lake by rain and wind would be sequestered below the chemocline in the cold monimolimnion. With a strong chemocline impeding the transfer of nutrients into the mixolimnion, the concentration of nutrients and soluble silica would increase below the chemocline over time (Boehrer *et al.*, 2017).

Subsequent lack of readily available nutrients in the warm surface waters of the mixolimnion kept the water clear of algae. I infer this from the lack of diatoms or

chrysophyte algal remains in the lake sediments. The seasonality of the deciduous forest defoliation was likely driven by annual changes in insolation as there was little seasonal variation in temperature or precipitation at that time (Prebble *et al.*, 2017).

After ~1750 years, low net photosynthesis in the oligotrophic mixolimnion combined with the continued addition of dissolved CO_2 from the high annual rainfall caused the mixolimnion to become acidic. Any macrophytes and macrofauna that inhabited them (e.g. freshwater sponges, aquatic arthropods) would have been acidophilic species.

FTIRS results indicate the presence of weathered Otago Schist from 10.4-10.0 mcd (between ~2300 and 2500 years after background lake sediments began accumulating), coincident with increasing GAD and MS at that depth range. The flux of terrigenous sediments to the maar lake evidently increased during the interval. Rainfall may have increased during that time and washed in more sediments. Alternatively, an increase in seismic activity may have caused terrigenous material to become incorporated with the lake sediments.

The lake maintained conditions of high organic input, oligotrophic clear water, and low pH until ~4500 years after the deposit began. The DIC slide surveys, FTIRS, and BioSi wet chemistry analyses indicate that diatomaceous benthic algae became established at that time. Recognising that processes influencing lake dynamics are inherently complex, I propose that colder regional temperatures at the HMC may have raised the chemocline enough to allow some nutrients and soluble silica to become available in the mixolimnion for biosiliceous phytobenthos to take advantage of. Wind speeds may have increased as well, resulting in turbulence in the lake that transferred nutrients and silica across the chemocline. Northward movement of the Antarctic Circumpolar Current (ACC) may have influenced the climate in Zealandia, as the Antarctic Ice Sheet (AIS) was prone to advance and retreat during the MMCT (Levy *et al.*, 2016). A northward shift of the ACC would also influence the latitude at which the circumpolar westerlies would be incident upon the vestigial land mass that was Zealandia in the mid-Miocene, perhaps placing them near the HMC region. This proposed climate cooling event lasted ~650 years, after which time conditions appear to have returned to what they had been before the cooling episode, i.e. a warm subtropical climate. The effect of warm wet climate conditions on the lake would have been to increase the depth of the chemocline and make nutrients unavailable to the mixolimnion again, resulting in the collapse of the diatom population as seen in the aforementioned analyses results near the end of DZ3 (Table 5.2).

Approximately 700 years later (or ~5800 years after background lake sediment deposition began) the lake underwent a change from clear oligotrophic to more turbid mesotrophic or eutrophic status in which the diatom population proliferated. From this I infer that another windy climate cooling episode occurred at that time, but with more intensity than the previous cooling event. As a result, the lake surface temperatures cooled, weakening the strength of the chemocline and reducing its depth. Convective turbulence and perhaps wind waves mixed the nutrients into the mixolimnion and 'shaved' them off of the chemocline. Nutrients and silica that had been concentrating below the chemocline would have become available in great quantities. The increase in diatom primary production would raise the pH of the mixolimnion (Pedersen *et al.*, 2013). The appearance of *Sellaphora saugerresii* at ~6.5 mcd (Table 5.2) is an indication that the pH of the mixolimnion rose above neutral.

Organic sediment input to the lake was greatly decreased during this cooling episode. The average lamina-couplet thickness is 60% of what it was in the earlier sediments. Also, only approximately half of the couplet thickness is comprised organic material, whereas all but a fine-sand-grain-diameter is organic material in the earlier sediment couplets. I interpret this to mean that the cooler climate caused the range of the deciduous forests to shift northward away from the HMC, leaving only a proximal broadleaf assemblage around the lake margin, as seen by (Möller *et al.*, 2017; Kaulfuss *et al.*, 2018).

From the FTIRS composition results, there was less terrigenous input to the lake at this time. Based on that information, I propose that annual precipitation was reduced in the colder climate as well during this inferred cool episode, as the capacity of the atmosphere to hold moisture decreases as temperature decreases. An additional consequence of reduced annual precipitation is that trees in the marginal broadleaf forest may have been smaller and more sparsely distributed, providing less organic detritus to the lake. Palaeobotanical evidence led Pole (2014) to the conclusion that there were arid fire-prone periods in the HMC region during the mid-Miocene.

The windy dry cooling episode endured for ~4100 years. The transition from one ecological state to the other was gradual at the beginning, as is evident in the steady increase in diatom concentration from 6.5 mcd (biofacies boundary) to peak at 5.7 mcd. Lake sediment lamina-couplet thickness is reduced through the transition, but light laminae are not prevalent in the core until above 5.7 mcd (lithofacies boundary), when slide surveys show diatom concentrations are peaking in this deposit. The increase in variability of the spectrophotometric results

(L*a*b* and RGB) above 5.7 mcd coincides with the high diatom concentrations, particularly the b* yellow hue. The transition from diatom paucity to peak spans ~1200 years.

In the middle of peak diatom abundance (5.1-4.7 mcd), slide DIC surveys and FTIRS show that the diatom concentration was reduced by approximately half and flux of terrigenous material increased to the lake. An episode of warmer temperatures and increased precipitation may have occurred. Ocean currents influenced by retreat of the AIS may have shifted south, such that the influence of the cold ACC on the circumpolar westerlies and Zealandia was reduced (Levy *et al.*, 2016). During this proposed warming period, transfer of nutrients across the chemocline would be impeded, limiting diatom primary production somewhat. After ~1100 years, the DIC surveys and composition analyses indicate that the diatom concentrations peaked once again and terrigenous input decreased to nil. Those were similar conditions to what they had been prior to the proposed warm episode. I interpret this to mean that windy cool dry conditions returned to the HMC region.

Core observations of the sections with light laminae show that at least 13 diatomaceous turbidite mass flow events occurred during the cool dry period. The diatom assemblage consists of exclusively benthic species. Upon death their remains would accumulate in the littoral zone. At the high concentrations present during the cool dry period, the diatom frustules would likely build up until the frustule accumulations collapsed as underwater gravity flows, initiated by inherent instability of thick accumulations, or perhaps due to storm wave energy or seismic activity.

Approximately 9900 years after the beginning of background lake sediment accumulation (~3.9 mcd), the lake experienced a perturbance. Slide DIC surveys indicate a large decrease in diatom concentration concomitant with the appearance of relatively abundant chrysophycean cysts and the re-emergence of freshwater sponges. The FTIRS and BioSi compositional analyses mirror the reduction in diatomaceous BioSi wt%, and the FTIRS results also show a large increase in terrigenous (Schist) input. The trophic status of the lake may have been returning to the condition it had maintained during the warm wet subtropical climate which characterised the first ~5800 years of deposition. Contraction of the AIS and poleward shift of the ACC would have allowed the warm subtropical ocean currents to have an increased influence on the climate in Zealandia and the circumpolar westerlies to have less influence. Warming temperatures and increased precipitation would have again strengthened the nutrient-isolating chemocline and added dissolved CO_2 to the lake. This would explain both the increased flux of

terrigenous material into the lake and the decrease of diatoms. As the diatom primary production decreased, the pH of the surface waters would drop below neutral, into a slightly acidic pH range preferred by chrysophyte algae and tolerated by the sponge species.

The warm wet climate was maintained for ~500 years. MS, GAD and L* luminosity increased during this time as minerogenic terrigenous material washed into the lake and biogenic silica input was reduced. The b* yellow hue decreased, reflecting the reduction in diatomaceous input. FTIRS, MS, GAD, and the spectrophotometric data increase sharply across the final 5-10 cm of the lake sediments, where drilling caused an intrusion of terrigenous overlying sediments into the lake sediment deposit.

After an estimated ~10,400 years, deposition of laminated lake sediments ends where the lake appears to have been inundated with an alluvial mass flow deposit. A seismic event may have destabilised part of the tephra ring or crater rim. When the forests were proximal to the lake their roots would have bound the sediments and chemically converted some of them to soil, providing stability. Retreat of the forests during the ~4100 year cool dry episode would have left the sediments at the lake margin less stable and more susceptible to mass movement. It can't be known how much capacity remained in the lake to accumulate continued sedimentation. What is known is that the HMC M1 lake sediment deposit remains after over 14 Ma of burial and subaerial erosion for us to study and add to the paucity of global knowledge regarding the effects of climate change in the Southern Hemisphere on a high resolution mid-latitude terrestrial deposit.

Chapter 6

Conclusion

This chapter presents a summary of the research findings and their significance. It then identifies opportunities for future research related to the Hindon Maar Complex.

6.1 The Hindon Maar Lake Sediments

The HMC was formed ~14.6±0.1 Ma by phreatomagmatic eruptions as part of the Waipiata Volcanic Field at the beginning of the mid-Miocene climate transition (MMCT), just after the mid-Miocene climate optimum (MMCO) (Kaulfuss *et al.*, 2018). Two maar lakes accumulated laminated organic sediments in an anoxic environment. Maar #1 yielded one ~18.5 m core containing ~9.5 m of lake sediments above basal volcaniclastic silts and sands, and unconformably overlain by a mass flow of alluvial silts, sands, and pebbles.

The lake sediment core sections were split and processed using a Geotek MSCL, then mm-scale surveys were completed using high-resolution digital images of the core split surfaces. One large (3.5 to 5.5 cm thick) representative sample was taken from each of the 10 lake sediment core sections to develop an age-depth model for the lake sediment deposit based on lamina-couplet thickness. High-magnification SEM images of biosiliceous microfossils were taken from 10 lake sediment samples, as well. Finally, 51 small representative samples (~0.8 cm^3) were taken at equidistant intervals (~20 cm) throughout the lake sediments to be processed for FTIRS and BioSi wet chemical compositional analyses, and to make microscope smear slides with which to conduct surveys of biosiliceous microfossils.

6.2 Lithological Facies

The core sections were split and processed to determine MS, GAD, and spectrophotometric L*a*b* and RGB colour data on the Geotek MSCL at 0.5 cm intervals. High resolution RGB digital images were taken of the core split surfaces as well. The core split images were visually surveyed at mm-scale to record features observed at the core split surfaces such as: black laminae; light laminae; isolated terrigenous sediment clasts; wavy bedding; black homogenous core; (wavy bedding and black homogenous core were features of turbidite mass flow deposits).

The results of the above analyses and observations identified two lithofacies with a boundary at 5.7 mcd:

- A **Dark Laminated Carbonaceous Sapropel** (DLCS) lithofacies at the base of the lake sediment deposit, from 13.0 to 5.7 mcd (7.3 m thick). The DLCS lithofacies is high in organic matter with very thin interbedded terrigenous sediments and occasional isolated terrigenous sediment clasts.
- A **Dark Laminated Diatomite** (DLDA) lithofacies that consists of the upper lake sediment deposit from 5.7 to 3.56 mcd (2.15 m thick). The DLDA lithofacies is characterised by the presence of light laminae amongst the dark laminae, turbidite mass flow deposits, and lack of discernible terrigenous sediments.

6.3 Biological Facies

Small subsamples of the 51 core samples were used to conduct compositional analyses and microfossil microscopy surveys. Dried homogenised samples were analysed using FTIRS to characterise the sediments as a three-component mixture; organic carbon, BioSi, and schist. Dried homogenised samples were also used to determine the absolute BioSi wt% composition of the lake sediments using chemical dissolution, reagents, and spectrophotometry. Microscope smear slides were made with the biosiliceous remains of samples after hydrogen peroxide digestion of organic material. Abundance surveys of the microfossils were done to species-level when possible, and other material such as pollen grains were recorded on the surveys as well. The dominant diatom species (>90%), *Encyonema mesianum*, tolerates a wide range of environmental parameters, so the second and sometimes third-most abundant species were used to infer lake surface water conditions during their time of deposition.

The sum of the above results identified two biological facies with a boundary at 6.5 mcd:

- A **Diatom Poor** (DP) biofacies at the base of the lake sediments, from 13.0 to 6.5 mcd (6.5 m thick). The DP biofacies is characterised by high TOC with low biogenic silica and low terrigenous schist material (as per FTIRS). The few microfossils surveyed are of alkaliphilous species at the base of the lake sediments, then transition to more acidophilous species upcore.
- A **Diatom Rich** (DR) biofacies in the upper lake sediments, from 6.5-3.56 mcd (~2.95 m thick). The DR biofacies is distinguished by the abundance of diatoms in the sediments, corroborated by high biogenic silica in the compositional analyses. Organic matter is still high while the presence of

terrigenous schist material (as per FTIRS) is very low. The diagnostic diatom microfossils in the DR biofacies are alkaliphilous.

6.4 Age-Depth Model

The lamina-couplet thickness measurements were taken on segments of the core immediately upon removal from the liner, then the samples were dried to make the laminae more visible before manually counting the couplets. With regards to the total composite length of core that was intact (excludes core catcher intervals and fragmented core section breaks), ~5% of the laminae were measured and enumerated.

The survey revealed a change in lamina-couplet thickness in the vicinity of the biofacies boundary at 6.5 mcd. Core sections in the DP biofacies below 6.5 mcd had comparatively thick (~1.09 mm) black organic laminae interbedded with very thin bands of very fine sands. Lamina couplets in DR core sections above 6.5 mcd were ~60% of the thickness as those in the DP biofacies (~0.66 mm). The organic component comprised less of the DR couplets as well, as the diatomaceous component in the DR core sections was thicker than the very fine sand interbeds in the DP core section.

The age-depth model estimates that the DP biofacies represents ~5850 years of deposition while the DR biofacies represents ~4550 years of deposition. In total, it is estimated that the lake sediment deposition occurred across 10,400 years.

6.5 Depositional Environments

When the Hindon Maar Complex formed in the mid-Miocene the landmass of Zealandia was heavily eroded and of low relief (Landis *et al.*, 2008). The climate was warm wet subtropical, as much as 10°C warmer than present day and with little seasonality (Prebble *et al.*, 2017). The Hindon region was covered in mature forests of deciduous Southern Beech, podocarps and associated understory brush and shrubs (Pole, 2014; Möller *et al.*, 2017; Kaulfuss *et al.*, 2018). When the eruptive activity ceased after Hindon Maar #1 formed, the crater would have soon been inundated with cold groundwater and meteoric water. Dark laminated sediments in the DLCS and DLDA lithofacies are an indication of quiescent deposition in an anoxic environment. The deep cold lake must have become meromictic and developed a strong chemocline, sustaining that characteristic throughout the deposition history.

Deposition during the DLCS/DP facies accumulation consisted of a high annual flux of leaf litter rain-washed in from the proximal forests. Some terrigenous

material was washed in as well, likely from the tephra ring, considering the ubiquitous presence of muscovite flecks from fragmented and weathered Otago Schist country rock as evidence. The increased presence of acidophilic diatom species as the deposit accumulated as well as the lack of abundant diatom algal remains are indicators that the lake had low productivity. Low net photosynthesis in the lake and the continued addition of dissolved CO_2 from rainfall likely led the pH to decrease below neutral in the surface waters of the lake. The lake remained clear due to its oligotrophic status, as the warm temperatures allowed the lake to maintain a strong deep chemocline that impeded nutrients from reaching the surface water where they would have been utilised for primary production. This depositional environment indicates that warm wet conditions that existed when the HMC was formed persisted afterwards, maintaining the density and distribution of the forests in the region.

During the interval from ~5850 to 7150 years after background lake sedimentation began (6.5-5.7 mcd; biofacies to lithofacies boundaries), the deposit environment transitioned to the DLDA/DR facies accumulation. Deposition of organic detritus in the profundal zone was greatly reduced, as was the terrigenous material. However, the abundance of diatomaceous silica increased substantially and was variable at times throughout this depositional period. The sediment composition and the alkaliphilic diatom species assemblage indicate that the productivity in the lake increased substantially while input of allochthonous organic detritus and terrigenous material decreased. The increase in productivity is likely due to weakening of the chemocline, allowing nutrients sequestered below to be exploited by the diatom algae. This occurs when the temperature of the surface water decreases, reducing the depth of the chemocline. It is aided by increased wave energy, resulting in sub-surface turbulence that can sweep nutrients from the top of the chemocline and distribute them in the surface waters. The reduction in organic input may be due to a shift of the forests away from the HMC region, or a reduction in the density of trees in the forests. Such a scenario could be caused by cooler temperatures and less precipitation. Less precipitation would also explain the lack of terrigenous material being transported into the lake. I propose that the climate transitioned to relatively windy cool dry conditions of varying intensities throughout the DLDA/DR facies deposition.

6.6 Climate Drivers Influencing the Accumulation of HMC Lake Sediments

Mid-Miocene warm wet conditions in the HMC region would indicate that warm subtropical ocean currents from the north were influencing the climate as the

DLCS/DP facies deposition accumulated. This is evidence that the oceanic Antarctic circumpolar current (ACC) and the atmospheric circumpolar westerlies (ACW) were more distant from Zealandia. It would seem they had contracted back to higher latitudes towards Antarctica, likely during an episode of Antarctic ice sheet (AIS) retreat.

The windy cool dry climate that can account for the DLDA/DR facies deposition can occur when the ACC and ACW latitudinally shift north to a position in which the ACW are incident upon the eroded mid-Miocene landmass of Zealandia. To shift ACC and ACW current north against the subtropical ocean currents, the AIS would likely have undergone an episode of expansion.

Variability in the extent of the AIS during the MMCO/MMCT has been interpreted from multi-proxy evidence (Flower & Kennett, 1994; Lewis *et al.*, 2008; Tripati *et al.*, 2009; Levy *et al.*, 2016). Drivers that the AIS responds to have been identified as the cumulative effect of the three primary Milankovitch cycles on solar insolation and atmospheric pCO_2 levels (Levy *et al.*, 2016).

6.7 Significance of the Research

Atmospheric pCO_2 during the MMCT has been reported as ~400 ppm, very similar to those of present day (Tripati *et al.*, 2009). Palaeoclimate studies on a Southern Hemisphere mid-Miocene climate archive, such as the HMC M1-2 lake sediment deposit, can be beneficial in predicting the response of the Antarctic ice sheets in an environment of elevated pCO_2. Adding to the significance of this study is the oceanic connection and lack of continental interference between New Zealand and the AIS, a global climate-driver.

The Hindon Maar lake sediment deposits are already unique in their global location and temporal occurrence. Furthermore, the laminated HMC lake sediments are of very high resolution compared to coeval low resolution marine sediment records used for pre-Quaternary climate studies. It is hoped that the findings of this study add to the understanding of climate change over geologically short time scales during in the MMCT.

6.8 Future Research Opportunities

The Hindon Maar Complex lake sediment deposits have only recently begun to be scientifically investigated. Most of the studies have been palaeontological in nature. Opportunities to extend global knowledge of ecological, environmental and climate information in the mid-Miocene abound.

6.8.1 Geochemical Analyses

Geochemical analysis of the Hindon Maar lake sediments has yet to be carried out. Findings may provide greater detail on the chemistry of the monimolimnion as sediments accumulated.

6.8.2 Climate Cycles

Within the two main depositional environments discussed here, there are smaller intra-depositional events (small diatom peaks in the DP facies, an interval of reduced diatom productivity in the DR facies) that may by associated with a known cyclicity pattern, perhaps sub-Milankovitch cycles or solar cycles.

6.8.3 Dating

The dates for the HMC cited in this study are an $^{40}Ar/^{39}Ar$ radiometric date on a basanite and a pollen-based maximum age constraint. Corroborative radiometric dates from the volcaniclastic deposits underlying the lake sediments would be beneficial.

References

Adams, C., Korsch, R., & Griffin, W. (2013). Provenance comparisons between the Nambucca Block, Eastern Australia and the Torlesse Composite Terrane, New Zealand: connections and implications from detrital zircon age patterns. *Australian Journal of Earth Sciences, 60*(2), 241-253.

Barinova, S., Yehuda, G., & Nevo, E. (2010). Comparative analysis of algal communities in the rivers of northern and southern Israel as bearing on ecological consequences of climate change. *Journal of Arid Environments, 74*(7), 765-776.

Battarbee, R. W., Jones, V. J., Flower, R. J., Cameron, N. G., Bennion, H., Carvalho, L., & Juggins, S. (2002). Diatoms. In *Tracking environmental change using lake sediments* (pp. 155-202). Springer.

Battarbee, R. W., Charles, D. F., Bigler, C., Cumming, B. F., & Renberg, I. (2010). Diatoms as indicators of surface-water acidity. In J. P. Smol & E. F. Stoermer (Eds.), *The diatoms: applications for the environmental and earth sciences (2nd ed.)* (pp. (pp. 98-121)). Cambridge, UK: Cambridge University Press.

Beddow-Twigg, H. (2016). *Orbital forcing and climate response: astronomically-tuned age models and stable isotope records for the Oligocene-Miocene.* Doctor of Philosophy thesis, Utrecht University, Zutphen, Netherlands.

Bere, T., & Mangadze, T. (2014). Diatom communities in streams draining urban areas: community structure in relation to environmental variables. *Tropical Ecology, 55*(2), 271-281.

Birge, E. A. (1904). The Annual Address of the President: The Thermocline and Its Biological Significance. *Transactions of the American Microscopical Society, 25*, 5-33.

Bishop, D. G., & Turnbull, I. M. (Cartographer). (1996). Geology of the Dunedin area.

Blaikie, T. N., Ailleres, L., Betts, P. G., & Cas, R. A. F. (2014). A geophysical comparison of the diatremes of simple and complex maar volcanoes, Newer Volcanics Province, south-eastern Australia. *Journal of Volcanology and Geothermal Research, 276*, 64-81.

Boehrer, B., von Rohden, C., & Schultze, M. (2017). Physical features of meromictic lakes: Stratification and circulation. In *Ecology of Meromictic Lakes* (Chapter 2, pp. 15-34). Springer.

Bowie, E. (2015). *Geophysical characterisation of the Hindon Maar Complex.* thesis, University of Otago, Dunedin, New Zealand.

Brauer, A., & Negendank, J. (1993). Paleoenvironmental reconstruction of the Late-and postglacial sedimentary record of Lake Weinfelder Maar. In *Paleolimnology of European maar lakes* (pp. 223-235). Springer.

Brouwer, E., Bobbink, R., & Roelofs, J. G. M. (2002). Restoration of aquatic macrophyte vegetation in acidified and eutrophied softwater lakes: an overview. *Aquatic Botany, 73*(4), 405-431.

Christie, T., Barker, R., & Vidanovich, P. (2012). *Publicly available airborne geophysical survey data in New Zealand*. (Vol. 1).

Cohen, A. S. (2003). *Palaeolimnology: the history and evolution of lake systems*. New York: Oxford University Press, Inc.

Conley, D. J., & Schelske, C. L. (2002). Biogenic silica. In *Tracking environmental change using lake sediments* (pp. 281-293). Springer.

Cooke, P. J., Nelson, C. S., & Crundwell, M. P. (2008). Miocene isotope zones, paleotemperatures, and carbon maxima events at intermediate water - depth, Site 593, Southwest Pacific. *New Zealand Journal of Geology and Geophysics, 51*(1), 1-22.

Coombs, D. S., Adams, C. J., Roser, B. P., & Reay, A. (2008). Geochronology and geochemistry of the Dunedin Volcanic Group, eastern Otago, New Zealand. *New Zealand Journal of Geology and Geophysics, 51*(3), 195-218.

Coxall, H. K., & Wilson, P. A. (2011). Early Oligocene glaciation and productivity in the eastern equatorial Pacific: Insights into global carbon cycling. *Paleoceanography, 26*(2).

Craw, D., Upton, P., Walcott, R., Burridge, C. P., & Waters, J. M. (2012). Tectonic controls on the evolution of the Clutha River catchment, New Zealand. *New Zealand Journal of Geology and Geophysics, 55*(4), 345-359.

Craw, D., Craw, L., Burridge, C. P., Wallis, G. P., & Waters, J. M. (2016). Evolution of the Taieri River catchment, East Otago, New Zealand. *New Zealand Journal of Geology and Geophysics, 59*(2), 257-273.

Cumming, B., Wilson, S., & Smol, J. (1993). Paleolimnological potential of chrysophyte cysts and scales and of sponge spicules as indicators of lake salinity. *International Journal of Salt Lake Research, 2*(1), 87-92.

DeMaster, D. J. (1981). The supply and accumulation of silica in the marine environment. *Geochimica et Cosmochimica acta, 45*(10), 1715-1732.

DesGranges, J.-L., & Rodrigue, J. (1986). Influence of acidity and competition with fish on the development of ducklings in Quebec. In *Acidic Precipitation* (pp. 743-750). Springer.

DPDC. (2017). *DPDC Taxon Search*. 2018.

Dräger, N., Theuerkauf, M., Szeroczyńska, K., Wulf, S., Tjallingii, R., Plessen, B., Kienel, U., & Brauer, A. (2016). Varve microfacies and varve preservation record of climate change and human impact for the last 6000 years at Lake Tiefer See (NE Germany). *The Holocene, July*.

Duff, K. E., Zeeb, B. A., Smol, J. P., & Wilkinson, A. N. (1995). Atlas of chrysophycean cysts. *1*.

EDDI. *European Diatom Database*. from http://craticula.ncl.ac.uk/Eddi/jsp/index.jsp.

Emiliani, C., & Geiss, J. (1959). On glaciations and their causes. *Geologische Rundschau, 46*(2), 576-601.

Fallu, M.-A., Allaire, N., & Pienitz, R. (2002). Distribution of freshwater diatoms in 64 Labrador (Canada) lakes: species–environment relationships along latitudinal gradients and reconstruction models for water colour and alkalinity. *Canadian Journal of Fisheries and Aquatic Sciences, 59*(2), 329-349.

Fellman, J. B., Hood, E., & Spencer, R. G. (2010). Fluorescence spectroscopy opens new windows into dissolved organic matter dynamics in freshwater ecosystems: A review. *Limnology and Oceanography, 55*(6), 2452-2462.

Field, B., Crundwell, M., Lyon, G., Mildenhall, D., Morgans, H., Ohneiser, C., Wilson, G., Kennett, J., & Chanier, F. (2009). Middle Miocene paleoclimate change at Bryce Burn, southern New Zealand. *New Zealand Journal of Geology and Geophysics, 52*(4), 321-333.

Flower, B. P., & Kennett, J. P. (1994). The middle Miocene climatic transition: East Antarctic ice sheet development, deep ocean circulation and global carbon cycling. *Palaeogeography, palaeoclimatology, palaeoecology, 108*(3-4), 537-555.

Foster, G. L., Lear, C. H., & Rae, J. W. (2012). The evolution of pCO 2, ice volume and climate during the middle Miocene. *Earth and Planetary Science Letters, 341*, 243-254.

Fox, A. D., Cao, L., Zhang, Y., Barter, M., Zhao, M. J., Meng, F. J., & Wang, S. L. (2011). Declines in the tuber - feeding waterbird guild at Shengjin Lake National Nature Reserve, China‐a barometer of submerged macrophyte collapse. *Aquatic Conservation: Marine and Freshwater Ecosystems, 21*(1), 82-91.

Fox, B. R. S. (2014). *Climate change at the Oligocene/Miocene boundary.* thesis, University of Otago, Dunedin, New Zealand.

Fox, B. R. S., Wartho, J., Wilson, G. S., Lee, D. E., Nelson, F. E., & Kaulfuss, U. (2015). Long-term evolution of an Oligocene/Miocene maar lake from Otago, New Zealand. *Geochemistry Geophysics Geosystems, 16*(1), 59-76.

Fox, B. R. S., Wilson, G. S., & Lee, D. E. (2016). A unique annually laminated maar lake sediment record shows orbital control of Southern Hemisphere midlatitude climate across the Oligocene-Miocene boundary. *Geological Society of America Bulletin, 128*(3-4), 609-626.

Fox, B. R. S., D'Andrea, W. J., Wilson, G. S., Lee, D. E., & Wartho, J. A. (2017). Interaction of polar and tropical influences in the mid-latitudes of the Southern Hemisphere during the Mi-1 deglaciation. *Global and Planetary Change, 155*, 109-120.

Frost, T. M. (2002). Freshwater sponges. In *Tracking environmental change using lake sediments* (pp. 253-263). Springer.

Garrity, F. D. A. (2017). *Paleoenvironmental Variability during the Middle Miocene Climatic Optimum Reconstructed using a Lake Sediment Record from the Otago Region, New Zealand.* Masters thesis, The University of Waikato, Hamilton, New Zealand.

Gasse, F. (1994). Lacustrine diatoms for reconstructing past hydrology and climate. In *Long-Term Climatic Variations* (pp. 335-369). Springer.

Geotek (Compiler) (2012). *Geotek Multi-Sensor Core Logger Manual*. Daventry, Northamptonshire, UK: Geotek Ltd.

Guiry, M. D., & Guiry, G. M. (Compiler) (2018). *Algaebase*. World-wide electronic publication. Galway: National University of Ireland. Accessed March 21, 2018 from http://www.algaebase.org.

Hall, R. I., & Smol, J. P. (2010). Diatoms as indicators of lake eutrophication. In J. P. Smol & E. F. Stoermer (Eds.), *The diatoms: applications for the environmental and earth sciences (2nd ed.)* (pp. (pp. 122-151)). Cambridge, UK: Cambridge University Press.

Hamon, N., Sepulchre, P., Lefebvre, V., & Ramstein, G. (2013). The role of eastern Tethys seaway closure in the Middle Miocene Climatic Transition (ca. 14 Ma). *Climate of the Past, 9*(6), 2687-2702.

Hanson, M. A., & Butler, M. G. (1990). Early responses of plankton and turbidity to biomanipulation in a shallow prairie lake. In *Biomanipulation Tool for Water Management* (pp. 317-327). Springer.

Hanson, M. A., & Butler, M. G. (1994). Responses to food web manipulation in a shallow waterfowl lake. *Hydrobiologia, 279*(1), 457-466.

Hansson, L.-A., Nicolle, A., Brönmark, C., Hargeby, A., Lindström, Å., & Andersson, G. (2010). Waterfowl, macrophytes, and the clear water state of shallow lakes. *Hydrobiologia, 646*(1), 101-109.

Hargeby, A., Andersson, G., Blindow, I., & Johansson, S. (1994). Trophic web structure in a shallow eutrophic lake during a dominance shift from phytoplankton to submerged macrophytes. *Hydrobiologia, 279*(1), 83-90.

Harrison, F. W. (1988). Utilization of freshwater sponges in paleolimnological studies. *Palaeogeography, Palaeoclimatology, Palaeoecology, 62*(1), 387-397.

Haworth, E. Y. (1972). Diatom succession in a core from Pickerel Lake, northeastern South Dakota. *Geological Society of America Bulletin, 83*(1), 157-172.

Henry, G. (1913) On the vertical distribution of the plankton in Winona Lake. In *Proceedings of the Indiana Academy of Science* (Vol. 23, pp. 77-92).

Herrmann, M. (2010). Palaeoecological reconstruction of the late Oligocene Maar Lake of Enspel, Germany using lacustrine organic walled algae. *Palaeobiodiversity and Palaeoenvironments, 90*(1), 29-37.

Holbourn, A., Kuhnt, W., Kochhann, K. G., Andersen, N., & Sebastian Meier, K. (2015). Global perturbation of the carbon cycle at the onset of the Miocene Climatic Optimum. *Geology, 43*(2), 123-126.

Hu, J., Zhou, H., Peng, P. a., Yang, X., Spiro, B., Jia, G., Wei, G., & Ouyang, T. (2015). Reconstruction of a paleotemperature record from 0.3–3.7 ka for subtropical South China using lacustrine branched GDGTs from Huguangyan Maar. *Palaeogeography, Palaeoclimatology, Palaeoecology, 435*, 167-176.

Hurd, D., & Theyer, F. (1977). Changes in the physical and chemical properties of biogenic silica from the central equatorial Pacific; Part II, Refractive index, density, and water content of acid-cleaned samples. *American Journal of Science, 277*(9), 1168-1202.

Hutton, J. (1788). X. Theory of the Earth; or an Investigation of the Laws observable in the Composition, Dissolution, and Restoration of Land upon the Globe. *Earth and Environmental Science Transactions of The Royal Society of Edinburgh, 1*(2), 209-304.

Ito, M., Aita, Y., & Hada, S. (2000). New radiolarian age information for the Chrystalls Beach Complex, southwest of Dunedin, New Zealand. *New Zealand Journal of Geology and Geophysics, 43*(3), 349-354.

Jakobsson, M., Løvlie, R., Al-Hanbali, H., Arnold, E., Backman, J., & Mörth, M. (2000). Manganese and color cycles in Arctic Ocean sediments constrain Pleistocene chronology. *Geology, 28*(1), 23-26.

Jones, D. A., Wilson, G. S., Gorman, A. R., Fox, B. R. S., Lee, D. E., & Kaulfuss, U. (2017). A drill-hole calibrated geophysical characterisation of the 23 Ma Foulden Maar stratigraphic sequence, Otago, New Zealand. *New Zealand Journal of Geology and Geophysics, 60*(4), 465-477.

Jordan, S. C., Cas, R. A. F., & Hayman, P. C. (2013). The origin of a large (>3km) maar volcano by coalescence of multiple shallow craters: Lake Purrumbete maar, southeastern Australia. *Journal of Volcanology and Geothermal Research, 254*, 5-22.

Juggins, S. (2013). Quantitative reconstructions in palaeolimnology: new paradigm or sick science? *Quaternary Science Reviews, 64*, 20-32.

Kamenik, C., & Schmidt, R. (2005). Chrysophyte resting stages: a tool for reconstructing winter/spring climate from Alpine lake sediments. *Boreas, 34*(4), 477-489.

Kaulfuss, U., Lee, D. E., Lindqvist, J. K., Bannister, J. M., & Conran, J. G. (2010). *Geological setting, lithofacies and biota of the early Miocene Foulden Maar, southern New Zealand*. Presented at the New Advances in Maar-Diatreme Research in Hungary, Germany and New Zealand.

Kaulfuss, U., & Moulds, M. (2015). A new genus and species of tettigarctid cicada from the early Miocene of New Zealand: Paratettigarcta zealandica (Hemiptera, Auchenorrhyncha, Tettigarctidae). *Zookeys*(484), 83-94.

Kaulfuss, U., Lee, D. E., Wartho, J.-A., Bowie, E., Lindqvist, J. K., Conran, J. G., Bannister, J. M., Mildenhall, D. C., Kennedy, E. M., & Gorman, A. R. (2018). Geology and palaeontology of the Hindon Maar Complex: A Miocene terrestrial fossil Lagerstätte in southern New Zealand. *Palaeogeography, Palaeoclimatology, Palaeoecology*.

King, P. R. (2000). Tectonic reconstructions of New Zealand: 40 Ma to the present. *New Zealand Journal of Geology and Geophysics, 43*(4), 611-638.

Knorr, G., & Lohmann, G. (2014). Climate warming during Antarctic ice sheet expansion at the Middle Miocene transition. *Nature Geoscience, 7*(5), 376.

Krammer, K., Lange-Bertalot, H., Krammer, K., Lange-Bertalot, H., Bate, N., Podzorski, A., & Bukowska, J. (2000). *Süsswasserflora von Mitteleuropa: Bacillariophyceae*. Süsswasserflora von Mitteleuropa. Stuttgart [etc.]: Fischer Verlag [etc.].

Kristiansen, J., & Preisig, H. (2011). Phylum Chrysophyta (Golden Algae) Pp. 290–294 In: John, DM, Whitton, BA & Brook, AJ. *The Freshwater Algal Flora of the British Isles*.

Kuerten, S., Parolin, M., Assine, M. L., & McGlue, M. M. (2013). Sponge spicules indicate Holocene environmental changes on the Nabileque River floodplain, southern Pantanal, Brazil. *Journal of paleolimnology, 49*(2), 171-183.

Landis, C., Campbell, H., Begg, J., Mildenhall, D., Paterson, A. M., & Trewick, S. (2008). The Waipounamu Erosion Surface: questioning the antiquity of the New Zealand land surface and terrestrial fauna and flora. *Geological magazine, 145*(2), 173-197.

Laskar, J., Robutel, P., Joutel, F., Gastineau, M., Correia, A., & Levrard, B. (2004). A long-term numerical solution for the insolation quantities of the Earth. *Astronomy & Astrophysics, 428*(1), 261-285.

Last, W. M., Smol, J. P., & Birks, H. J. B. (2001). *Tracking environmental change using lake sediments*. Dordrecht ; Boston: Dordrecht ; Boston : Kluwer Academic Publishers.

Lee, D. E., Lindqvist, J. K., Mildenhall, D. C., Bannister, J. M., & Kaulfuss, U. (2009). *Paleobotany, palynology and sedimentology of late Cretaceous-Miocene sequences in Otago and Southland*. Presented at the Geosciences 09 Conference.

Lee, D. E., Kaulfuss, U., Conran, J. G., Bannister, J. M., & Lindqvist, J. K. (2016). Biodiversity and palaeoecology of Foulden Maar: an early Miocene Konservat-Lagerstätte deposit in southern New Zealand. *Alcheringa: An Australasian Journal of Palaeontology, 40*(4), 525-541.

Levy, R., Harwood, D., Florindo, F., Sangiorgi, F., Tripati, R., von Eynatten, H., Gasson, E., Kuhn, G., Tripati, A., & DeConto, R. (2016). Antarctic ice sheet sensitivity to atmospheric CO2 variations in the early to mid-Miocene. *Proceedings of the National Academy of Sciences, 113*(13), 3453-3458.

Lewin, J. C. (1961). The dissolution of silica from diatom walls. *Geochimica et Cosmochimica Acta, 21*(3), 182-198.

Lewis, A. R., Marchant, D. R., Ashworth, A. C., Hedenäs, L., Hemming, S. R., Johnson, J. V., Leng, M. J., Machlus, M. L., Newton, A. E., & Raine, J. I. (2008). Mid-Miocene cooling and the extinction of tundra in continental Antarctica. *Proceedings of the National Academy of Sciences, 105*(31), 10676-10680.

Liebrand, D., Lourens, L. J., Hodell, D. A., de Boer, B., van de Wal, R. S. W., & Palike, H. (2011). Antarctic ice sheet and oceanographic response to eccentricity forcing during the early Miocene. *Climate of the Past, 7*(3), 869-880.

Lindqvist, J. K., & Lee, D. E. (2009). High-frequency paleoclimate signals from Foulden Maar, Waipiata Volcanic Field, southern New Zealand: An Early Miocene varved lacustrine diatomite deposit. *Sedimentary Geology, 222*(1-2), 98-110.

Lorenz, V. (1986). On the growth of maars and diatremes and its relevance to the formation of tuff rings. *Bulletin of Volcanology, 48*, 265-274.

Lorenz, V. (2003). Maar-diatreme volcanoes, their formation, and their setting in hard-rock or soft-rock environments. *Geolines, 15*, 72-83.

Lorenz, V. (2007). Syn- and posteruptive hazards of maar-diatreme volcanoes. *Journal of Volcanology and Geothermal Research, 159*(1-3), 285-312.

Maier, D. B., Rydberg, J., Bigler, C., & Renberg, I. (2013). Compaction of recent varved lake sediments. *GFF, 135*(3-4), 231-236.

Manconi, R., & Pronzato, R. (2002). Suborder Spongillina subord. nov.: freshwater sponges. In *Systema Porifera* (pp. 921-1019). Springer.

Martin, A. P., Rattenbury, M. S., & Cox, S. C. (2013). *Geophysics-aided geological interpretation of the Otago Schist: new insights for mineral exploration and geological mapping*. Presented at the 46th New Zealand Branch annual conference on exploration, mining and New Zealand's mineral resources.

Martínez-Carreras, N., Udelhoven, T., Krein, A., Gallart, F., Iffly, J. F., Ziebel, J., Hoffmann, L., Pfister, L., & Walling, D. E. (2010). The use of sediment colour measured by diffuse reflectance spectrometry to determine sediment sources: Application to the Attert River catchment (Luxembourg). *Journal of Hydrology, 382*(1), 49-63.

Meyer-Jacob, C., Vogel, H., Boxberg, F., Rosén, P., Weber, M. E., & Bindler, R. (2014a). Independent measurement of biogenic silica in sediments by FTIR spectroscopy and PLS regression. *Journal of paleolimnology, 52*(3), 245-255.

Meyer-Jacob, C., Vogel, H., Gebhardt, A., Wennrich, V., Melles, M., & Rosén, P. (2014b). Biogeochemical variability during the past 3.6 million years recorded by FTIR spectroscopy in the sediment record of Lake El'gygytgyn, Far East Russian Arctic. *Climate of the Past, 10*(1), 209-220.

Milankovitch, M. (1941). History of radiation on the Earth and its use for the problem of the ice ages. *K. Serb. Akad. Beogr*.

Miller, K. G., Wright, J. D., & Fairbanks, R. G. (1991). Unlocking the ice house: Oligocene-Miocene isotopes, eustasy, and margin erosion. *Journal of Geophysical Research-Solid Earth and Planets, 96*(B4), 6829-6848.

Miller, K. G., Kominz, M. A., Browning, J. V., Wright, J. D., Mountain, G. S., Katz, M. E., Sugarman, P. J., Cramer, B. S., Christie-Blick, N., & Pekar, S. F. (2005). The Phanerozoic record of global sea-level change. *science, 310*(5752), 1293-1298.

Mingram, J., Schettler, G., Nowaczyk, N., Luo, X., Lu, H., Liu, J., & Negendank, J. F. (2004). The Huguang maar lake—a high-resolution record of palaeoenvironmental and palaeoclimatic changes over the last 78,000 years from South China. *Quaternary International, 122*(1), 85-107.

Möller, A. L., Kaulfuss, U., Lee, D. E., & Wappler, T. (2017). High richness of insect herbivory from the early Miocene Hindon Maar crater, Otago, New Zealand. *PeerJ, 5*, e2985.

Morales, E. A., Wetzel, C. E., & Ector, L. (2010). Two short-striated species of Staurosirella (Bacillariophyceae) from Indonesia and the United States. *Polish Botanical Journal, 55*(1), 107-117.

Mortimer, N. (1993). Jurassic tectonic history of the Otago schist, New Zealand. *Tectonics, 12*(1), 237-244.

Mortlock, R. A., & Froelich, P. N. (1989). A simple method for the rapid determination of biogenic opal in pelagic marine sediments. *Deep Sea Research Part A. Oceanographic Research Papers, 36*(9), 1415-1426.

Mucciarone, D. (2003). Biogenic silica analysis procedure. In *Stanford University Stable Isotope Laboratory Standard Operating Procedure Manual* (pp. 93-105). Stanford University Department of Geological and Environmental Sciences Stanford, CA.

Murakami, E., Bicudo, D., & Rodrigues, L. (2009). Periphytic algae of the Garças Lake, Upper Paraná River floodplain: comparing the years 1994 and 2004. *Brazilian Journal of Biology, 69*(2), 459-468.

Naish, T. R., Woolfe, K. J., Barrett, P. J., Wilson, G. S., Atkins, C., Bohaty, S. M., Bucker, C. J., Claps, M., Davey, F. J., Dunbar, G. B., Dunn, A. G., Fielding, C. R., Florindo, F., Hannah, M. J., Harwood, D. M., Henrys, S. A., Krissek, L. A., Lavelle, M., van der Meer, J., McIntosh, W. C., Niessen, F., Passchier, S., Powell, R. D., Roberts, A. P., Sagnotti, L., Scherer, R. P., Strong, C. P., Talarico, F., Verosub, K. L., Villa, G., Watkins, D. K., Webb, P. N., & Wonik, T. (2001). Orbitally induced oscillations in the East Antarctic ice sheet at the Oligocene/Miocene boundary. *Nature, 413*(6857), 719-723.

Németh, K. (2001). *Phreatomagmatic Volcanism at the Waipiata Volcanic Field, Otago, New Zealand: A Thesis Submitted for the Degree of Doctor of Philosophy in Geology at the University of Otago, Dunedin, New Zealand.* thesis, University of Otago.

Németh, K., & White, J. D. (2003). Reconstructing eruption processes of a Miocene monogenetic volcanic field from vent remnants: Waipiata Volcanic Field, South Island, New Zealand. *Journal of Volcanology and Geothermal Research, 124*(1-2), 1-21.

Nesje, A., Olaf Dahl, S., Andersson, C., & Matthews, J. A. (2000). The lacustrine sedimentary sequence in Sygneskardvatnet, western Norway: a continuous, high-resolution record of the Jostedalsbreen ice cap during the Holocene. *Quaternary Science Reviews, 19*(11), 1047-1065.

Newnham, R. M., Lowe, D. J., Green, J. D., Turner, G. M., Harper, M. A., McGlone, M. S., Stout, S. L., Horie, S., & Froggatt, P. C. (2004). A discontinuous ca. 80 ka record of Late Quaternary environmental change from Lake Omapere, Northland, New Zealand. *Palaeogeography, Palaeoclimatology, Palaeoecology, 207*(1), 165-198.

Nichols, G. (2009). *Sedimentology and stratigraphy*. John Wiley & Sons.

Nowaczyk, N. R. (2002). Logging of magnetic susceptibility. In *Tracking environmental change using lake sediments* (pp. 155-170). Springer.

Nygaard, G. (1956). Ancient and recent flora of diatoms and chrysophyceae in Lake Gribso. Studies on the humic acid lake Gribso. *Folia limnologica scandinavica, 8*, 32-94.

Ohta, N., & Robertson, A. (2006). *Colorimetry: fundamentals and applications*. John Wiley & Sons.

Ojala, A. E. K., Francus, P., Zolitschka, B., Besonen, M., & Lamoureux, S. F. (2012). Characteristics of sedimentary varve chronologies - A review. *Quaternary Science Reviews, 43*, 45-60.

Owen, R. B., Renaut, R. W., & Jones, B. (2008). Geothermal diatoms: a comparative study of floras in hot spring systems of Iceland, New Zealand, and Kenya. *Hydrobiologia, 610*(1), 175-192.

Pälike, H., Norris, R. D., Herrle, J. O., Wilson, P. A., Coxall, H. K., Lear, C. H., Shackleton, N. J., Tripati, A. K., & Wade, B. S. (2006). The heartbeat of the oligocene climate system. *Science, 314*(5807), 1894-1898.

Pedersen, O., Colmer, T. D., & Sand-Jensen, K. (2013). Underwater photosynthesis of submerged plants–recent advances and methods. *Frontiers in Plant Science, 4*, 140.

Penney, J., & Racek, A. (1968). Comprehensive revision of a worldwide collection of freshwater sponges (Porifera: Spongillidae). *United State National Museum Bulletin, 272*, 1-184.

Piątek, J., Piątek, M., Zeeb, B. A., & El Shahed, A. (2009). Chrysophyte stomatocysts in Africa: the first description of an assemblage in the recent sediments of a thermo-mineral spring in Egypt. *Phycologia, 48*(1), 13-23.

Pirrung, M., Fischer, C., Buchel, G., Gaupp, R., Lutz, H., & Neuffer, F. O. (2003). Lithofacies succession of maar crater deposits in the Eifel area (Germany). *Terra Nova, 15*(2), 125-132.

Pirrung, M., Buchel, G., Lorenz, V., & Treutler, H. C. (2008). Post-eruptive development of the Ukinrek East Maar since its eruption in 1977 AD in the periglacial area of south-west Alaska. *Sedimentology, 55*(2), 305-334.

Poirrier, M. A. (1969). Louisiana Freshwater Sponges: Taxonomy, Ecology and Distribution.

Pole, M. (2014). The Miocene climate in New Zealand: estimates from paleobotanical data. *Palaeontologia Electronica, 17*(2), 1-79.

Prebble, J. G., Reichgelt, T., Mildenhall, D. C., Greenwood, D. R., Raine, J. I., Kennedy, E. M., & Seebeck, H. C. (2017). Terrestrial climate evolution in the Southwest Pacific over the past 30 million years. *Earth and Planetary Science Letters, 459*, 136-144.

Ragueneau, O., Leynaert, A., Tréguer, P., Demaster, D. J., & Anderson, R. F. (1996). Opal studied as a marker of paleoproductivity. *Eos, Transactions American Geophysical Union, 77*(49), 491-491.

Reichgelt, T. (2015). *Reconstructing southern New Zealand Miocene terrestrial climate and ecosystems from plant fossils.* thesis, University of Otago, Dunedin, New Zealand.

Reichgelt, T., D'Andrea, W. J., & Fox, B. R. S. (2016a). Abrupt plant physiological changes in southern New Zealand at the termination of the Mi-1 event reflect shifts in hydroclimate and pCO2. *Earth and Planetary Science Letters, 455*, 115-124.

Reichgelt, T., Kennedy, E. M., Jones, W. A., Jones, D. T., & Lee, D. E. (2016b). Contrasting palaeoenvironments of the mid/late Miocene Dunedin Volcano, southern New Zealand: Climate or topography? *Palaeogeography, Palaeoclimatology, Palaeoecology, 441*, 696-703.

Rosén, P., Vogel, H., Cunningham, L., Hahn, A., Hausmann, S., Pienitz, R., Zolitschka, B., Wagner, B., & Persson, P. (2011). Universally applicable model for the quantitative determination of lake sediment composition using Fourier transform infrared spectroscopy. *Environmental science & technology, 45*(20), 8858-8865.

Round, F. E., Crawford, R. M., & Mann, D. G. (1990). *The Diatoms : biology & morphology of the genera*. Cambridge {England} ; New York: Cambridge {England} ; New York : Cambridge University Press.

Ruengsawang, N., Sangpradub, N., Artchawakom, T., Pronzato, R., & Manconi, R. (2017). *Rare freshwater sponges of Australasia: new record of Umborotula bogorensis (Porifera: Spongillida: Spongillidae) from the Sakaerat Biosphere Reserve in Northeast Thailand*. (Vol. 2017).

Rull, V., & Vegas-Vilarrúbia, T. (2000). Chrysophycean stomatocysts in a Caribbean mangrove. *Hydrobiologia, 428*(1), 145-150.

Rybak, M., Rybak, I., & Nicholls, K. (1991). Sedimentary chrysophycean cyst assemblages as paleoindicators in acid sensitive lakes. *Journal of Paleolimnology, 5*(1), 19-72.

Ryves, D. B., Battarbee, R. W., Juggins, S., Fritz, S. C., & Anderson, N. J. (2006). Physical and chemical predictors of diatom dissolution in freshwater and saline lake sediments in North America and West Greenland. *Limnology and Oceanography, 51*(3), 1355-1368.

Ryves, D. B., Battarbee, R. W., & Fritz, S. C. (2009). The dilemma of disappearing diatoms: Incorporating diatom dissolution data into palaeoenvironmental modelling and reconstruction. *Quaternary Science Reviews, 28*(1), 120-136.

Sabel, M., Bechtel, A., Püttmann, W., & Hoernes, S. (2005). Palaeoenvironment of the Eocene Eckfeld Maar lake (Germany): implications from geochemical analysis of the oil shale sequence. *Organic Geochemistry, 36*(6), 873-891.

Sandgren, C. D. (1991). Chrysophyte reproduction and resting cysts: a paleolimnologist's primer. *Journal of Paleolimnology, 5*(1), 1-9.

Sandgren, C. D., Smol, J. P., & Kristiansen, J. (1995). *Chrysophyte algae : ecology, phylogeny, and development*. Cambridge ; New York: Cambridge ; New York : Cambridge University Press.

Schnurrenberger, D., Russell, J., & Kelts, K. (2003). Classification of lacustrine sediments based on sedimentary components. *Journal of Paleolimnology, 29*, 141-154.

Selby, M. J. (1993). *Hillslope Materials and Processes*. Oxford University Press.

Shackleton, N. (1967). Oxygen isotope analyses and Pleistocene temperatures re-assessed. *Nature, 215*(5096), 15.

Smith, T. M., & Smith, R. L. (2014). *Elements of ecology (8th ed.)*. Harlow, England: Pearson Education Limited.

Smol, J. P. (1988). Chrysophycean microfossils in paleolimnological studies. *Palaeogeography, Palaeoclimatology, Palaeoecology, 62*(1-4), 287-297.

Smol, J. P., Birks, H. J., & Last, W. M. (2002). *Tracking Environmental Change Using Lake Sediments: Volume 3: Terrestrial, Algal, and Siliceous Indicators*. Springer Netherlands.

Smol, J. P., & Stoermer, E. F. (2010). *The diatoms: applications for the environmental and earth sciences (2nd ed.)*. Cambridge, UK: Cambridge University Press.

Soroczki-Pinter, E., Pla-Rabes, S., Magyari, E. K., Stenger-Kovacs, C., & Buczko, K. (2014). Late Quaternary Chrysophycean stomatocysts in a Southern Carpathian mountain lake, including the description of new forms (Romania). *Phytotaxa, 170*(3), 169-186.

Spaulding, S., & Edlund, M. (2008). *Encyonema* Diatoms of the United States. from http://westerndiatoms.colorado.edu/taxa/genus/Encyonema.

Spaulding, S., Lubinski, D. J., & Potapova, M. (2010a). *Diatoms of the United States*. from http://westerndiatoms.colorado.edu.

Spaulding, S. A., Lubinski, D. J., & Potapova, M. (2010b). *Diatoms of the United States*. Retrieved 27 April, 2018, from http://westerndiatoms.colorado.edu/.

Suhr, P., Goth, K., & Lorenz, V. (2006). Long lasting subsidence and deformation in and above maar-diatreme volcanoes - a never ending story. *Zeitschrift der Deutschen Gesellschaft für Geowissenschaften, 157*, 491-511.

Tripati, A. K., Roberts, C. D., & Eagle, R. A. (2009). Coupling of CO2 and ice sheet stability over major climate transitions of the last 20 million years. *science, 326*(5958), 1394-1397.

Upton, P., Craw, D., & Walcott, R. (2014). Far-field deformation resulting from rheologic differences interacting with tectonic stresses: an example from the Pacific/Australian plate boundary in southern New Zealand. *Geosciences, 4*(3), 93-113.

Valentine, G. A., & White, J. D. L. (2012). Revised conceptual model for maar-diatremes: Subsurface processes, energetics, and eruptive products. *Geology, 40*(12), 1111-1114.

Van Eaton, A. R., Harper, M. A., & Wilson, C. J. (2013). High-flying diatoms: Widespread dispersal of microorganisms in an explosive volcanic eruption. *Geology, 41*(11), 1187-1190.

Wehr, J., & Sheath, R. (2003). Freshwater algae of North America: Ecology and classification.

Wetzel, C. E., Ector, L., Van de Vijver, B., Compere, P., & Mann, D. G. (2015). Morphology, typification and critical analysis of some ecologically important small naviculoid species (Bacillariophyta). *Fottea, 15*(2), 203-234.

White, J. D. L., & Ross, P. S. (2011). Maar-diatreme volcanoes: A review. *Journal of Volcanology and Geothermal Research, 201*(1-4), 1-29.

Wilkinson, A. N., Zeeb, B. A., & Smol, J. P. (2002). *Atlas of chrysophycean cysts*. (Vol. 2). Springer Science & Business Media.

Yang, J.-R., Duthie, H. C., & Delorme, L. D. (1993). Reconstruction of the recent environmental history of Hamilton Harbour (Lake Ontario, Canada) from analysis of siliceous microfossils. *Journal of Great Lakes Research, 19*(1), 55-71.

Zachos, J. C., Flower, B. P., & Paul, H. (1997). Orbitally paced climate oscillations across the Oligocene/Miocene boundary. *Nature, 388*(6642), 567-570.

Zachos, J. C., Pagani, M., Sloan, L., Thomas, E., & Billups, K. (2001). Trends, rhythms, and aberrations in global climate 65 Ma to present. *Science, 292*(5517), 686-693.

Zeeb, B., Smol, J., & Horn, S. P. (1996). Chrysophycean stomatocysts from Costa Rican tropical lake sediments. *Nova Hedwigia, 63*(3), 279-300.

Zeeb, B., & Smol, J. P. (2002). Chrysophyte scales and cysts. In *Tracking environmental change using lake sediments* (pp. 203-223). Springer.

Zhang, Y. G., Pagani, M., Liu, Z., Bohaty, S. M., & DeConto, R. (2013). A 40-million-year history of atmospheric CO2. *Phil. Trans. R. Soc. A, 371*(2001), 20130096.

Zolitschka, B., Mingram, J., Van Der Gaast, S., Jansen, J. F., & Naumann, R. (2002). Sediment logging techniques. In *Tracking environmental change using lake sediments* (pp. 137-153). Springer.

Zolitschka, B., Francus, P., Ojala, A. E. K., & Schimmelmann, A. (2015). Varves in lake sediments - a review. *Quaternary Science Reviews, 117*, 1-41.